Fermilab FERMILAB-THESIS-2002-14

THE LIMITING BACKGROUND IN A DARK MATTER SEARCH AT SHALLOW DEPTH

by

THUSHARA PERERA

Submitted in partial fulfillment of the requirements
For the degree of Doctor of Philosophy

Thesis Advisor: Daniel S. Akerib

Department of Physics

CASE WESTERN RESERVE UNIVERSITY

January, 2002

To my parents

Table of Contents

Dedication . . . iii
Table of Contents . . . iv
List of Tables . . . viii
List of Figures . . . ix
Acknowledgments . . . xiii
Abstract . . . xvi

1 WIMP Dark Matter **1**
1.1 Introduction . . . 1
1.2 Present-Day Cosmology . . . 2
1.2.1 Theoretical Framework . . . 2
1.2.2 Constraints on Ω_m and Ω_Λ . . . 4
1.3 Evidence for Non-Baryonic Cold Dark Matter . . . 5
1.3.1 Dark Matter . . . 5
1.3.2 Baryonic and Non-Baryonic Dark Matter . . . 10
1.3.3 Hot and Cold Dark Matter . . . 11
1.4 Weakly Interacting Massive Particles . . . 11
1.5 WIMP Detection . . . 13
References . . . 16

2 The CDMS I Experiment **19**
2.1 Introduction . . . 19
2.2 Backgrounds and Shielding . . . 20
2.2.1 Photon Backgrounds . . . 23
2.2.2 Neutron Backgrounds . . . 25
2.3 CDMS Detectors . . . 28
2.3.1 The Phonon Measurement . . . 30
2.3.2 Charge Measurement . . . 35
2.4 Cryogenics and Electronics . . . 45
2.4.1 The Icebox . . . 45
2.4.2 Mounting of Detectors and Cold Electronics . . . 46

2.4.3 Room Temperature Electronics and Data Acquisition . 50
2.5 The Future of CDMS 52
References 54

3 Monte Carlo Tools and Their Use in Interpreting Calibration Data 56
3.1 The Need for Detailed Monte Carlo Simulations 57
3.2 Monte Carlo transport code used in CDMS 58
3.2.1 Specialized tools for GEANT in CDMS Simulations . . 59
3.3 Geometry Definition for Monte Carlos 63
3.4 Output of the Monte Carlo 65
3.5 Neutron Calibration 65
3.5.1 Introduction 65
3.5.2 Setup for Simulation 66
3.5.3 Results 68
3.5.4 Interesting Features in the Neutron Calibration Data and Monte Carlo 80
3.6 Veto-Coincident Neutrons 93
3.6.1 Introduction 93
3.6.2 Monte Carlo Setup 93
3.6.3 Results 95
3.7 Photon Calibration 99
References 111

4 Data and Results from CDMS I 114
4.1 Introduction 114
4.2 Run 19 Data Set and Analysis 115
4.2.1 Trigger, Charge Search, and Analysis Thresholds . . . 118
4.3 Software Cuts and Their Efficiencies 119
4.3.1 Introduction 119
4.3.2 Trace Quality Cuts 120
4.3.3 Physics Cuts 125
4.4 Veto-Coincident Data 130
4.5 Veto-Anticoincident Data 133
4.6 Dark Matter Analysis 137
4.6.1 Veto-Anticoincident Nuclear Recoils 137
4.6.2 The Neutron Interpretation 140
4.6.3 Upper Limits on WIMP Dark Matter 143
References 149

5 The Neutron Background in CDMS I **150**
5.1 Introduction 150
5.2 Possible Sources of External Neutrons 152
5.2.1 Neutrons from Cosmic-ray Muons 152
5.2.2 Neutrons from Natural Radioactivity 156
5.2.3 Rates and Spectra of External Neutrons 157
5.3 Studies of Neutron Shielding and Detection in CDMS I 158
5.3.1 Importance of Neutrons from Hadron Showers 158
5.3.2 Spectrum Independence of Results 161
5.4 Predictions of External Neutron Monte Carlo and Comparisons with Data 165
5.5 Additional Shielding of External Neutrons in CDMS I 171
5.6 Neutron Background for CDMS II 172
5.7 Direct Simulation of External Neutrons Through Muon Transport in Rock 175
5.7.1 Monte Carlo Setup 178
5.7.2 Results 180
References 183

6 Tests of a Z-sensitive Ionization and Phonon mediated Detector **186**
6.1 Introduction 186
6.2 The ZIP Phonon Technology 187
6.2.1 Transition Edge Sensors 187
6.2.2 Voltage Bias and Electrothermal Feedback 189
6.2.3 Production and Trapping of Quasiparticles 191
6.2.4 Biasing and Readout Scheme 193
6.2.5 Design Considerations for ZIP Detectors 195
6.2.6 Advantages of Using ZIP Detectors 199
6.3 Tests of a CDMS II ZIP Detector 200
6.3.1 Detector Characterization at C.W.R.U. 200
6.3.2 Diagnostics and Testing of a ZIP Detector 202
6.3.3 SQUID and QET biasing 210
6.3.4 Description of Data 213
6.3.5 Position Dependent Phonon Energy Calibration 217
References 222

7 Conclusion **224**
References 227

A Output of the GEANT Based Monte Carlo **228**
A.1 Event-by-event Quantities 229
A.2 Hit-by-hit Quantities 231

Bibliography **233**

List of Tables

3.1 Results of fiducial volume calculation. 72
3.2 Comparison of data and Monte Carlo for neutron calibrations. 81
3.3 Information on the ^{73}Ge nuclear excitations. 86
3.4 Comparison of data and Monte Carlo for veto-coincident neutrons. 98

5.1 Production rates, fluxes and detection rates for the three possible sources of external neutrons. 158
5.2 Comparison of rates and ratios between the external neutron Monte Carlo and the veto-anticoincident nuclear recoils. . . . 168

6.1 Transition temperature, normal resistance, and critical current at base temperature for the four phonon sensors. 203

List of Figures

1.1 Rotation curves of spiral galaxies. 7
1.2 Measurements of mass-to-light ratio as a function of dynamical scale. 9

2.1 The Stanford Underground Facility (SUF). 21
2.2 The CDMS I shield. 22
2.3 Nuclear- vs. electron-recoil discrimination used in CDMS. . . . 31
2.4 BLIP detector. 32
2.5 The NTD thermistor based phonon readout circuit. 33
2.6 Approximate band structure of intrinsic Ge crystals used in CDMS. 36
2.7 Simplified version of the ionization readout circuit. 38
2.8 The readout circuitry of a BLIP detector. 40
2.9 Cartoon of blocking electrodes. 43
2.10 The CDMS I cryostat. 44
2.11 Detector mounts and tower 47
2.12 Block diagram of the CDMS data acquisition system 51

3.1 Schematic depicting the definition of "clumps". 61
3.2 Average clump size vs. energy deposited for Ge and Si. 63
3.3 Geometry definition used in Run 19 simulations. 64
3.4 Charge Yield versus Recoil energy in the first neutron calibration. 69
3.5 Radii of BLIP5 inner and outer contained events from Monte Carlo. 74
3.6 Detector-by-detector comparison of data and Monte Carlo spectra for the first neutron calibration. 76
3.7 Comparison of summed spectra from the first neutron calibration. 77
3.8 Detector-by-detector comparison of data and Monte Carlo spectra for the second neutron calibration. 78

3.9 Comparison of summed spectra from the second neutron calibration. 79
3.10 Charge versus recoil energy from the second neutron calibration. 82
3.11 Energies of photon scatters in the neutron calibration. 85
3.12 Proposed method for measuring the high-energy neutron flux. 90
3.13 Detector-by-detector comparison of data and Monte Carlo spectra for veto-coincident neutrons. 97
3.14 Comparison of summed spectra between data and Monte Carlo for veto-coincident neutrons. 98
3.15 Charge yield vs. recoil energy for inner and shared events in the 6 V photon calibration data. 100
3.16 Charge yield in BLIP1 from Run 18 data. 103
3.17 Charge yield for BLIP1 in Run 18 as estimated by the Monte Carlo. 104
3.18 Distributions of low charge yield events in the Run 18 photon calibration Monte Carlo. 106
3.19 BLIP4 charge yield vs. BLIP3 charge yield for electron-calibration data. 109

4.1 Cumulative raw livetime for low-background data in Run 19. . 115
4.2 Phonon trigger efficiencies in BLIPs 3 through 6. 117
4.3 Phonon χ^2 vs. phonon energy for typical low-background data form Run 19. 123
4.4 Charge-yield distributions for 10-100 keV veto-anticoincident inner events in BLIPs 3 through 6. 127
4.5 Distribution of veto-trigger times relative to charge triggers. . 128
4.6 Distribution of veto-trigger times relative to the inferred charge pulse time for phonon triggers. 129
4.7 Recoil-energy spectra for veto-coincident inner events. 131
4.8 Recoil-energy spectra for veto-coincident shared events. 132
4.9 Ionization yield vs. recoil energy for veto-anticoincident single scatters in BLIPs 4 through 6. 134
4.10 Single-scatter photon and electron spectra for veto-anticoincident inner events. 135
4.11 Single-scatter photon and electron spectra for veto-anticoincident shared events. 136
4.12 Recoil energy distribution of inner nuclear-recoil candidates. . 137
4.13 Scatter plot of ionization yields for veto-anticoincident double scatters in BLIPs 4 through 6. 139

4.14 Ionization yield vs. recoil energy for veto-anticoincident events in the Run 18 Si ZIP detector. 141
4.15 Schematic comparison of simulated and observed numbers of nuclear-recoil events. 142
4.16 Spin-independent σ vs. M limit plot. 147

5.1 Flux-normalized neutron spectra at the SUF from simulations of neutron production mechanisms external to the shield. . . . 157
5.2 Penetration and detection probability of neutrons as a function of neutron energy outside the shield. 159
5.3 Spectra of neutrons incident on detectors for a range of initial neutron energies. 162
5.4 The dependence of mean recoil energy and multiples fraction on initial neutron energy. 164
5.5 Production (dark) and ambient (light) spectra of external neutrons at the SUF. 166
5.6 The neutron spectra incident on detectors due to external and internal neutrons. 167
5.7 Recoil energy spectra from the veto-anticoincident germanium data set and the corresponding external neutron Monte Carlo. 170
5.8 Comparison of observed and predicted cumulative spectra for veto-anticoincident neutrons. 171
5.9 Geometry setup for the FLUKA Monte Carlo. 177
5.10 Muon spectra at ground level and at the SUF tunnel from FLUKA simulations. 179
5.11 Ambient neutron spectra inside the SUF tunnel from GEANT and FLUKA simulations. 180

6.1 Resistance versus temperature for a Transition Edge Sensor (TES). 187
6.2 Pictorial representation of quasiparticle trapping and diffusion in ZIP detectors. 192
6.3 The biasing and readout scheme for phonon sensors in ZIP detectors. 194
6.4 Present aluminium fin and TES design in ZIP detectors. . . . 197
6.5 Phonon side of a ZIP detector. 199
6.6 IbIs data from sensor A. 205
6.7 IbIs data from sensor B. 206
6.8 IbIs data from sensor C. 207
6.9 IbIs data from sensor D. 208

6.10 The noise power spectral density for the four phonon channels and two charge channels of a ZIP detector. 212
6.11 Ionization energy versus phonon energy from detector *G6* before applying the position dependent phonon energy calibration. 215
6.12 Histogram of ionization energy in *G6*. 215
6.13 $Ydelay$ vs. $xdelay$ for ^{241}Am and ^{137}Cs photons in *G6*. 216
6.14 Position dependence of phonon pulse height. 218
6.15 $<P/Q> \times 100$ for a grid in $xdelay$ and $ydelay$ 219
6.16 Ionization energy vs. *calibrated* phonon energy. 220

7.1 Projected sensitivity of CDMS II and WIMP upper limits from recent experiments. 225

A.1 Raw output of GEANT based Monte Carlo. 229

Acknowledgments

The time I have spent working on CDMS has been a very enjoyable and exciting one. In addition to the wide variety of physics problems and challenges that have come my way, my life has been enriched by the people I have associated with during this time. Of these people, I mention first Dan Akerib, my thesis advisor. I have benefitted immensely from Dan's broad knowledge of physics, perspective on issues, his ability to quickly grasp and explain new concepts, and his talent for separating the essentials from the details. Before long, I realized how fortunate I was to have an advisor like Dan. I am proud to be his first graduate advisee. I hope that many more young physicists will have the opportunity to experience the leadership, humility, encouragement, and friendship that he brings as a thesis advisor.

I thank the two research associates I have worked with in the CWRU-CDMS group, Alex Bolozdynya and Richard Schnee, for their guidance and friendship. I thank Alex for giving me a feel for the practical, hardware-oriented side of experimental physics which I now relish. I also treasure the many conversations we have had on more esoteric topics. I have learned much from Richard on subjects ranging from poker to data analysis. I admire his overall knowledge of the experiment, and had a good opportunity to make use of it during the last few months of thesis writing. Special thanks to him for helping me out in many ways during the last few months. Don Driscoll was my first office mate and colleague at CWRU. I have greatly enjoyed talking physics and solving problems with him. I have happily become addicted to his

humor and optimism as well as the wonderful company of his family, Diana and Astra. Gensheng Wang, the next graduate student to join the group has been a pleasure to work with. In addition to the general comradery we have developed, I have enjoyed and learned much from our interesting and often lively discussions. I also thank him and his family for treating me on many occasions to the best Chinese food I have ever tasted. In the last year, I have had the pleasure of working with Sharmila Kamat. Her hard work, and questions have been very helpful to me. I hope I have done a decent job of answering some of those questions. I would also like to thank the undergrads, Matt, Mo, Tim P, Peter, Aaron, and Tim J for their tireless work and for making the lab a fun and lively workplace. Thanks also to Cheshana Marshal, and Mike Stamatikos for their excellent company.

I would like to thank all the secretaries in the physics department for making my life much easier than it could have been. I also thank my thesis committee for their interest and patience. I am grateful to Lawrence Krauss for pointing me in the direction of Dan and CDMS when I started looking for research work a while back.

I thank Bernard Sadoulet and Blas Cabrera for welcoming me to the CDMS collaboration. My exposure to the rest of the CDMS collaboration occurred mainly over the month-long visits I made to Stanford. During these stays and later, I have had the opportunity of working closely with Rick Gaitskell whose guidance and encouragement have been valuable to me. I am also grateful to Tom Shutt for his help and patient explanations during my first days in CDMS. I also thank Angela Da Silva whose work was the starting point for many of the studies described here. I was fortunate to have been paired with Steve Eichblatt on most of these studies. I have greatly enjoyed his company and friendship. I have enjoyed many interesting and informative

discussions with Dan Bauer, Sae Woo Nam, Andrew Sonnenschein, Roland Clarke, and Sunil Golwala during my visits to Stanford. I am especially thankful to Sunil for his perseverance and hard work in making Run 19 the success that it was. I thank Steve Yellin, Dennis Seitz, Laura Baudis, Maria Isaac, Paul Brink, Patrizia Meunier, Tarek Saab, and Vuk Mandic for helping me with much of the work described in this dissertation. Although I haven't worked on specific projects with many of the other members of CDMS, I owe all of them a big thank you because I have benefitted from all of their hard work.

I thank all my friends and relatives all over the world! Special thanks to Chaminda, Kathy and the kids, and my friend Bala for their encouragement and support during the last few months of thesis writing. I am grateful to Christine for her company, and friendship. I also thank my brother Gehan for his support and words of encouragement during trying times. Finally but most importantly, I thank my parents. I would not be who I am or where I am if not for the love, freedom, and opportunities they have given me. Thank you.

The Limiting Background in a Dark Matter Search at Shallow Depth

Abstract

by

Thushara Perera

A convincing body of evidence from observational and theoretical astrophysics suggests that matter in the universe is dominated by a non-luminous, non-baryonic, non-relativistic component. Weakly Interacting Massive Particles (WIMPs) are a proposed particle candidate that satisfy all of the above criteria. They are a front-runner among dark matter candidates because their predicted contribution to matter in the universe is cosmologically significant and because they may arise naturally from supersymmetric (SUSY) models of particle physics. The Cryogenic Dark Matter Search (CDMS) employs advanced detectors sensitive to nuclear recoils caused by WIMP scatters and capable of rejecting ionizing backgrounds.

The first phase of the experiment, conducted at a shallow site, is limited by a background of neutrons which are indistinguishable from WIMPs in terms of the acquired data. By accounting for and statistically subtracting these neutrons, CDMS I provides the best dark matter limits to date over a wide range of WIMP masses above 10 GeV/c^2. These results also exclude the signal region claimed by the DAMA annual modulation search at a >71% confidence level.

The second phase of the experiment, located at a deep site, is scheduled to begin data acquisition in 2002. Due to longer exposures, larger detector mass, and low background rates at this site, data from CDMS II are expected to improve on present WIMP sensitivity by about two orders of magnitude.

Emphasized in this work are the research topics in which I have been directly involved. These include the work described in Chapters 3 and 5 with regard to the development and use of simulation tools, detailed studies into the limiting neutron background, and the present understanding of this background in relation to CDMS I and CDMS II. I was also involved in several detector development projects in preparation for CDMS II. Analysis of test data from a ZIP detector, planned for use in CDMS II, is presented in Chapter 6.

Chapter 1

WIMP Dark Matter

1.1 Introduction

Much of the theoretical and observational work in present-day astrophysics revolves around the dark matter problem. Particle physics also plays an integral role in research into this subject. The Cryogenic Dark Matter Search (CDMS) is designed for the direct detection of Weakly Interacting Massive Particles (WIMPs), a strongly motivated dark matter candidate. In this chapter, I will briefly outline the reasoning and evidence behind the dark matter problem, the need for non-baryonic cold dark matter, the motivation for WIMPs, and some specifics regarding their detection.

The dark matter problem refers to the lack of luminous matter for explaining certain astronomical observations under the framework of conventional gravity. This discrepancy between theory and observation may be explained by a "dark" component of matter in the universe. The discussion in this chapter is phrased in terms of this assumption. Another solution to the dark matter problem may be the discovery of a new theory of gravity and inertia that does not require additional matter to reconcile theory and observation. Several such theories have been proposed. However, none of them have gained widespread acceptance due mainly to

aesthetic reasons[1]. In either case, experimental searches for dark matter, like CDMS, serve an important purpose. They are useful for detecting or setting limits on several proposed dark matter candidates.

1.2 Present-Day Cosmology

1.2.1 Theoretical Framework

The development below follows several standard text books on cosmology [3, 4, 5]. The details may be found in these references.

The Robertson-Walker metric, which is the outcome of assuming that the universe is homogeneous and isotropic on large scales, is given by

$$ds^2 = dt^2 - R^2(t)\left\{\frac{dr^2}{1-kr^2} + r^2 d\theta^2 + r^2 \sin^2\theta d\phi^2\right\} \tag{1.1}$$

where $R(t)$ is a scale factor with units of length. It is scaled to give k the values $+1$, -1, or 0, for positively curved, negatively curved, and flat universes. The Einstein equations for this metric simplify to the Friedmann equations given below.

$$\left(\frac{\dot{R}}{R}\right)^2 + \frac{k}{R^2} = \frac{8\pi G}{3}\rho + \frac{\Lambda}{3} \tag{1.2}$$

$$\frac{\ddot{R}}{R} = -\frac{4\pi G}{3}(\rho + p) + \frac{\Lambda}{3} \tag{1.3}$$

Here, units with $c = 1$ have been used. The matter density and pressure of the "fluid" filling the universe are given by ρ and p respectively. Newton's constant is represented by G while k is the curvature index as given above. Terms involving the cosmological constant Λ can be absorbed into the first term of each r.h.s. above, if it is viewed as a "fluid" component having energy density $\rho_\Lambda = \Lambda/8\pi G$ and pressure $p_\Lambda = -\rho_\Lambda$. For matter and radiation the pressure p is given by 0 and $\rho/3$, respectively.

[1] Several authors have recently claimed that the predictions of one such theory, MOdified Newtonian Dynamics (MOND) compare unfavourably with existing data. [1, 2]

The Hubble parameter is given by

$$H = \frac{\dot{R}}{R}. \tag{1.4}$$

According to equation 1.2, a flat universe ($k = 0$) implies that $\rho_{\text{total}} = \rho + \rho_\Lambda = 3H^2/8\pi G$. This value of ρ_{total} is referred to as ρ_c, the critical density. Using this definition, equation 1.2 may be rewritten as

$$1 + \frac{k}{H^2 R^2} = \Omega_m + \Omega_\Lambda = \Omega \tag{1.5}$$

where the Ω's are obtained by dividing the respective densities (ρ and ρ_Λ) by ρ_c. Note that both Ω's are functions of R. Also note that a Ω geater than, less than, or equal to unity correspond to positively-curved, negatively-curved, and flat universes, respectively. The Hubble constant H_0 is the present value of H. It is usually quoted to be [6]

$$H_0 = 71 \pm 7 \text{ km/sec/Mpc} = 100h \text{ km/sec/Mpc} \tag{1.6}$$

where the dimensionless parameter h is useful for expressing the uncertainty in H_0 when quoting cosmological parameters. For example, using this value, the current critical density is estimated at $1.1 \times 10^{-6} h^2$ GeV/cm^3.

Light emitted in the past is *redshifted* by a factor $1 + z$ given by

$$1 + z = \frac{R_0}{R} \tag{1.7}$$

where R_0 is the present value of the scale factor while R is the value of the scale factor at the time that light was emitted. According to equation 1.5, the r.h.s. of equation 1.7 is a function of the curvature k, Ω_m, and Ω_Λ. The redshift (z) in the l.h.s. is a measurable.

When a disk and a point are separated by a large distance, the solid angle subtended by the disk at the point depends on the curvature of space. Light rays from the point to the edges of the disk will be convergent, divergent, and straight for positive-curvature, negative-curvature and flat

universes respectively. Curvature-measurement experiments where the point is an observer and the disk is the a far-away object of known size are called *standard ruler* tests. *Standard candle* tests, where the redshift of an object is recorded against its luminosity distance, also yield information on curvature.

1.2.2 Constraints on Ω_m and Ω_Λ

Distance versus redshift measurements on high-redshift supernovae Ia [7, 8] and measurements of the first-Doppler-peak angular size in the Cosmic Background Radiation (CBR) [9, 10], are highly successful instances of the two methods outlined above. Since z is a measurable and the r.h.s of equation 1.7 depends on curvature and the Ω's, measuring curvature using these methods puts constraints on specific functions of Ω_m and Ω_Λ. Experimental constraints on Ω_m and Ω_Λ are obtained using measurements at several redshifts. While to first order, the angular size of the first CBR peak is only sensitive to $\Omega = \Omega_m + \Omega_\Lambda$, the shape of the angular power spectrum of temperature anisotropy and positions of other peaks in that spectrum can be used to obtain possible ranges in Ω_m and Ω_Λ [11, 12]. These experiments, together with other observations [13] have in recent years provided accurate evidence in favor of a particular cosmological model. This model is described by

$$\Omega \simeq 1, \quad \Omega_m \simeq 0.3, \quad \Omega_\Lambda \simeq 0.7. \tag{1.8}$$

This model is contrary to previous expectations that $\Omega = 1$ and $\Omega_m \geq 0.9$. In recent years, the above model has lead to a concentrated effort to find a good particle physics motivation for a non-zero Λ.

A theoretical prejudice for $\Omega = 1$ exists for two reasons. Equations 1.2 and 1.3 can be used to show that $\Omega = 1$ is the only static solution for Ω. Furthermore, values of Ω different from unity will lead to

large deviations from unity in a very short time. Therefore, in the early universe, Ω must have been extremely close to unity in order to be consistent with the present observation of a nearly flat universe. Therefore, if Ω is not exactly unity, a mechanism for extreme fine tuning is required to explain its minute deviation from unity in the early universe. This is the first theoretical reason for expecting that $\Omega = 1$. The other is due to a popular class of theories known as inflation. These theories were first developed to explain the absence of magnetic monopoles. Soon thereafter, it was realized that they also explain the startling homogeneity of the cosmic microwave background radiation which is incident on the earth today from a large number of causally disconnected parts of the universe. In inflation theories, an exponential expansion of a previously-small causally-connected patch of space is used to explain this homogeneity. The exponential expansion drives the scale factor R to a large value, thus making the second term on the l.h.s. of equation 1.5 negligibly small. Therefore, even if the curvature k is non-zero, Ω is driven to unity.

1.3 Evidence for Non-Baryonic Cold Dark Matter

1.3.1 Dark Matter

The galaxy luminosity density in the nearby universe is measured to be [14]

$$L_g = 3.3 \times 10^8 h L_\odot/\mathrm{Mpc}^3. \tag{1.9}$$

where $L_\odot$ refers to the sun's luminosity. Given this luminosity density, the matter density will equal ρ_c when the mass to luminosity ratio is

$$\frac{M}{L} \simeq 1400h\frac{M_\odot}{L_\odot} \tag{1.10}$$

where $M_\odot$ refers to the solar mass. Thus, the matter density in the universe cannot be equal to the critical density or a significant fraction of it, if most

of the matter in the universe is in objects like like stars ($M/L < 10 M_{odot}/L_{odot}$).

It addition to the above argument, there are several direct measurements that support the existence of a dark matter problem. The most familiar of these are from the rotation curves of spiral galaxies and observations of galaxy clusters.

Galactic Rotation Curves

The tangential velocity of stars in the plane of a spiral galaxy can be measured using redshifts of stellar absorption lines. About 83% of the luminous matter in a typical spiral galaxy is contained within a radius $R_{\rm opt}$ of about 10 kpc. The radio emission line of neutral hydrogen can be used to trace velocities beyond this point to about $2R_{\rm opt}$ [16]. A set of velocity curves obtained in this way for several typical spiral galaxies is shown in figure 1.1. The crucial feature of these plots is that the velocity curve flattens beyond $r > R_{\rm opt}$. According to Newtonian gravity, which is applicable in this case, the tangential velocities are governed by

$$\frac{V^2}{r} = \frac{GM(r)}{r^2} \tag{1.11}$$

If most matter in the galaxy were luminous, the velocity curve beyond $R_{\rm opt}$ is therefore expected to vary as $1/\sqrt{r}$. The observed rotation curves clearly indicate the presence of a non-luminous component. The expected rotation curve due to the luminous matter is also displayed in figure 1.1. The dashed curve indicates the rotation curve due to a particular "dark halo" model used by the authors of [15]. Surveys of spiral-galaxy rotation curves typically yield mass-to-light ratios greater than 10 $hM_\odot/L_\odot$.

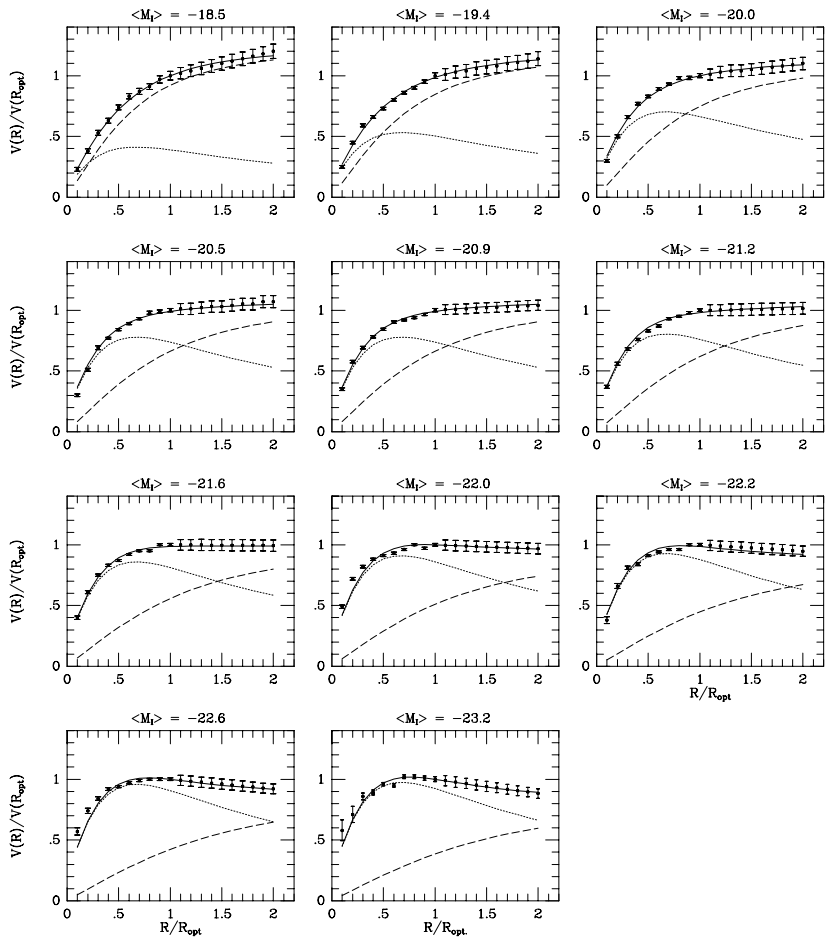

Figure 1.1: Rotation curves of spiral galaxies. The radius is given in units of $R_{\rm opt}$. The velocities are normalized to the velocity at $R_{\rm opt}$. Data are shown with error bars. The dashed curve is the velocity contribution due to an assumed dark halo, which is modeled to have a density distribution proportional to $r^3/(r^2+a^2)$ where a is a constant [15]. The dotted and solid curves represent the expected rotation curves due to luminous matter and the combination of dark and luminous components. Figure taken from [15]

Clusters of Galaxies

Galaxy clusters are gravitationally bound systems of up to several thousand galaxies. Because of their large size, galaxy clusters are expected be a fair sampling of the universe. Mass-to-light measurements on galaxy clusters can therefore be used to estimate Ω_m for the universe.

Mass-to-Light Ratios

Several methods are used to extract mass-to-light ratios from galaxy clusters. The first method uses the peculiar velocities of galaxies to estimate gravitational potential energy in a cluster [17]. The gravitational potential is obtained from peculiar velocities through the virial theorem which states that

$$<T> = -\frac{1}{2}<V> \tag{1.12}$$

where $<T>$ and $<V>$ are the average values of kinetic and potential energy respectively. This method is valid as long as the cluster is in a state of dynamic equilibrium. The "first" discovery of the dark matter problem is attributed to Zwicky, who in 1933 used this method on the Coma cluster.

X-ray emission from hot intracluster gas can also be used for mass-to-light estimates. Hydrostatic equilibrium is assumed for gas in the central part of the cluster. The observed x-ray maps are then fit to models of temperature and density distributions of the gas [18, 19]. Gravitational lensing of background galaxies by clusters has also been used to measure the dark matter content of clusters [20]. Most mass-to-light estimates obtained from galaxy clusters lie in the range $(250 - 450)hM_\odot/L_\odot$. This implies that Ω_m is in the range 0.18 to 0.32.

Cluster Baryon Fraction

As with mass-to-light ratios, the ratio of baryon density to matter density in galaxy clusters is expected to be a fair sampling of the baryon

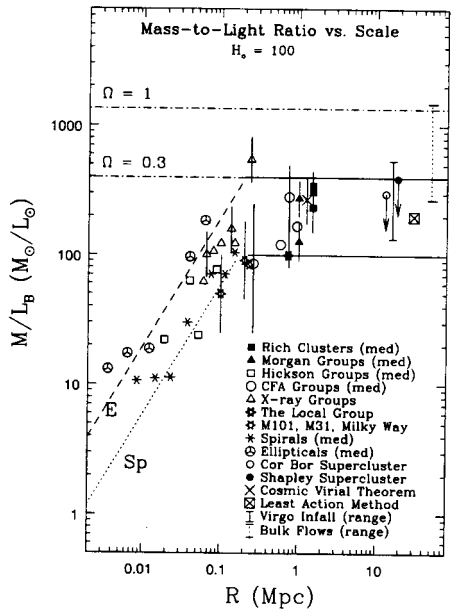

Figure 1.2: Measurements of mass-to-light ratio as a function of dynamical scale. Figure taken from [22]

fraction of the universe. Once the baryon fraction of a cluster is measured, it can be combined with constraints on baryon density provided by Big Bang nucleosynthesis, discussed below, to obtain Ω_m. These estimates are in good agreement with mass-to-light estimates from galaxy clusters, with typical quoted Ω_m s of about 0.4±0.1 [21].

Consistency of Evidence

The above methods and other studies (eg. large scale flows, Virgo infall) yield a coherent picture of matter density in the universe. All estimates of Ω_m from large scale structures, with fair sampling of the universal matter density, give values consistent with the picture described by equation 1.8. Figure 1.2 shows the light to mass ratios from a large number of measurements carried out at different length scales [22].

1.3.2 Baryonic and Non-Baryonic Dark Matter

The amount of baryonic dark matter in the universe is powerfully constrained by Big Bang Nucleosynthesis (BBN) [23, 24, 25]. It predicts the relative abundance of the light elements ^{2}H, ^{3}He, ^{4}He, ^{7}Li, to photons in the early universe within the framework of the hot big bang. Of the input parameters used in these calculations, only the baryon density has a significant uncertainty. Therefore, the observed light-element abundances can be used to constrain it. In recent years, BBN constraints on Ω_b, the baryon density, have become stronger due to new data on the ^{2}H abundance in high-redshift clouds [26]. Present observations yield

$$0.018 < \Omega_b h^2 < 0.022. \tag{1.13}$$

According to the evidence presented in earlier sections, the most likely value of Ω_m is about 0.3. Therefore this constraint on the baryon density implies the presence and dominance of non-baryonic dark matter. On the other hand, the BBN constraint also hints at a baryonic dark matter problem because the observed baryonic matter density in stars and gas in galaxies and clusters of galaxies is estimated at about 0.0033 for $h = 0.65$ [27].

At high redshift, Ω_b is believed to be dominated by clouds of ionized hydrogen (HII). The measured density is within the range indicated by equation 1.13 [28]. In the nearby universe, the composition of the baryonic dark matter is less certain. Searches, for MAssive Compact Halo Objects (MACHOs) using microlensing of background stars [29] indicate that no more than 20% of the galactic halo is composed of objects with mass less than $0.03\mathrm{M}_\odot$. Non-observation of stellar remnants impose an upper limit on more massive compact objects [30].

1.3.3 Hot and Cold Dark Matter

Present limits on neutrino masses indicate that the neutrino contribution to Ω_m is small. In the early universe, neutrinos will decouple from thermal equilibrium at relativistic speeds. Therefore, they are classified as "hot" dark matter. The pressure of hot dark matter will inhibit the gravitational collapse of protogalaxies during the epoch when galaxy-sized density fluctuations become important. Therefore, a significant hot dark matter component is incompatible with observations of structure formation. However, a small admixture of hot dark matter is helpful for reducing the small scale power to the observed levels [3]. However, the dominant component must arise from non-relativistic or "Cold" dark matter in order to be consistent with the observed power spectrum of density fluctuations.

1.4 Weakly Interacting Massive Particles

Weakly Interacting Massive Particles (WIMPs) are a non-baryonic cold dark matter candidate. Together with axions which were first proposed as a solution to the strong CP problem in particle physics [31], they are favored dark matter candidates that may account for most of the matter density in the universe. The Cryogenic Dark Matter Search (CDMS), which this dissertation is based on, is designed to detect or set limits on the interaction rate of WIMPs with nuclei.

WIMPs are a generic type of particle that would be created in the Big Bang. The argument for a relic abundance of such particles is also generic and is called the "freeze-out" argument [32]. In the early universe, the temperature density is high enough to keep WIMPs in kinetic and chemical equilibrium through various creation and annihilation channels. As the universe expands and cools, the falling equilibrium density will be dominated by a Boltzmann suppression of the WIMP number density,

which goes as $\exp(-m_\chi/k_B T)$ where m_χ is the WIMP mass and $k_B T$ is the thermal energy at the time. However, as the universe expands further, the WIMP number density will become too low for WIMP annihilations to maintain the number density in thermal equilibrium. This occurs when the average WIMP-annihilation mean free path grows due to the Hubble expansion faster than the average WIMP velocity at the time. The relic abundance of WIMPs is therefore determined by their mass and annihilation cross-section, which enter through the Boltzmann factor and mean free path. For masses of a few GeV, which are allowed by present constraints from particle physics, the annihilation cross-section (σ_A) times velocity (v) is given by [33]

$$\sigma_A v = \frac{10^{-26}}{\Omega_\chi h^2} \mathrm{cm}^3/\mathrm{sec} \tag{1.14}$$

Therefore, a WIMP density close to the critical density ($\Omega_\chi \sim 1$) naturally implies a typical weak interaction rate. Since the weak interaction scale is not assumed for the above estimate, this may be a hint that particle physics at the W and Z scale are intimately related to the dark matter problem.

Although WIMPs are a generic class of particle, leading WIMP candidates at present are provided by supersymmetry (SUSY) [34]. Supersymmetry is a particle physics model that predicts bosonic partners for all known fermions and fermionic partners for all known bosons. It provides a natural mechanism to prevent the Higgs boson from acquiring a large mass compared to the electroweak scale. Another feature of supersymmetry is that its inclusion in Grand Unified Theories (GUTs) usually ensures the exact unification of coupling constants at the GUT scale. Current experimental constraints require that the as-yet-undiscovered half of the supersymmetric particle spectrum does not decay to known particles. Therefore, the Lightest Supersymmetric Particle (LSP) must be stable. In minimal supersymmetric extensions to the

standard model (MSSM), the lightest "neutralino" is regarded as an ideal WIMP candidate. The interaction rate of these particles with ordinary matter is determined by several model dependent parameters. Measurable event rates are predicted by a large range of MSSM models.

1.5 WIMP Detection

Direct and indirect detection techniques are used in WIMP searches. Indirect detection uses annihilation products of WIMPs, such as neutrinos, to constrain WIMP masses and cross-sections. The CDMS experiment is designed for the direct detection of WIMP scatters in detector material. For completeness, I include here some of the standard assumptions used by the WIMP search community for setting dark matter limits.

The WIMP interaction rate per nucleus is given by

$$R = n\sigma<v> = \frac{\rho_0}{m_\chi}\sigma<v> \tag{1.15}$$

where n is the WIMP number density, σ is the WIMP-nucleus cross-section, $<v>$ is the average relative velocity between a WIMP and the nucleus, ρ_0 is the local halo density, and m_χ is the WIMP mass. Although ρ_0 is uncertain by a factor of a few at present, a standard value of 0.3 GeV/cm^3 is often used. The WIMP-nucleus cross-section is related to the WIMP-*nucleon* cross-section through the assumption of coherent ($\sim$ A^2) scattering. Only the spin-independent WIMP-nucleon cross-section is used and therefore constrained in the results presented here. For calculating the relative velocity, a mean earth velocity of 230 km/sec relative to the galactic rest frame and a Maxwellian WIMP-velocity distribution with a characteristic dispersion (v_0) of 220 km/sec are used [35].

Given the rate of interactions in a detector, the above information may be used to constrain possible ranges of WIMP mass and

spin-independent WIMP-nucleon cross-section. However, the resulting recoil energy spectrum must first be calculated in order to account for energy thresholds of detectors. The observed recoil-energy spectrum can also improve constraints on parameter space. The recoil energy spectra as functions of WIMP mass are calculated according to the methods outlined in [35]. The Woods-Saxon (Helm) form factor is used in these calculations to account for nuclear structure. For germanium, the main target material used in CDMS, the mean recoil energy is about 20 keV for a WIMP mass of 100 GeV. The expected event rate of WIMPs is less than 1 per kg-day. Detecting such low event rates at keV energies presents significant challenges for WIMP seach experiments, given the presence of radioactive backgrounds.

The first generation of WIMP search experiments which made use of conventional technologies, such as NaI and Ge diode detectors, are ultimately limited by radioactive backgrounds. On the other hand, rejection of such radioactive backgrounds is an inherent property of the advanced detector technologies used by CDMS. Therefore, CDMS has the potential to achieve much better sensitivity to WIMPs. The detectors and the experimental apparatus used in CDMS I, the first phase of CDMS, are described in Chapter 2. In Chapter 3, I discuss the development, testing, and subsidiary uses of the simulation tools used for studying backgrounds in CDMS I. In Chapter 4, I present a brief description of the analysis and results from the latest CDMS physics run. This run provided clear evidence of a limiting neutron background at the CDMS I site. In Chapter 5, I will describe detailed studies into this background and the conclusions drawn. The CDMS II experiment, scheduled to begin data taking in 2002, is expected to yield a two-orders-of-magnitude improvement over present WIMP sensitivity. I was fortunate to have been involved in the detector

development program for CDMS II. In Chapter 6, I describe test results from a Z-sensitive Ionization and Phonon (ZIP) mediated detector planned for use in CDMS II.

References

[1] A. Aguirre, J. Schaye, and E. Quataert. astro-ph/0105184. Submitted to Astrophys. J., 2001.

[2] D. Scott et al. astro-ph/0104435. Submitted to Mon. Not. R. Astron. Soc., 2001.

[3] E.W. Kolb and M.S. Turner. *The Early Universe*. Addison-Wesley, 1990.

[4] P.J.E. Peebles. *Principles of Physical Cosmology*. Princeton University Press, 1993.

[5] J.A. Peacock. *Cosmological Physics*. Cambridge University Press, 1999.

[6] M. Fukugita and C.J. Hogan. *Euoro. Phys. J. C, Review of Particles and Fields*, 15:136, 2000.

[7] S. Perlmutter et al. *Astrophys. J.*, 517:565, 1999.

[8] A.G. Riess et al. *Astron. J.*, 116:1009, 1998.

[9] P. de Bernardis et al. *Nature*, 404:955, 2000.

[10] S. Hanany et al. *Astrophys. J.*, 545:L5–L9, 2000.

[11] E.M. Leitch et al. astro-ph/0104488. Submitted to Astrophys. J., 2001.

[12] C.B. Netterfield et al. astro-ph/0104460, 2001.

[13] L.M. Krauss. In N.J.C. Spooner and V. Kundryavtsev, editors, *Proceedings of the Second International Workshop on The Identification of Dark Matter*, 1999. hep-ph/9807376.

[14] P. Coles and G.F.R. Ellis. *Is the Universe Open or Closed*. Cambridge University Press, 1997.

[15] P. Salucci and M. Persic. In P. Salucci and M. Persic, editors, *Dark and Visible Matter in Galaxies*, 1997. asto-ph/9703027.

[16] R. Sancisi and T.S. van Albada. Dark Matter in the Universe. Dordrecht, Holland, 1987.

[17] R.G. Carlberg et al. *Astrophys. J.*, 462:32, 1996.

[18] A.E. Evrard, A Metzler, and J.F. Navarro. *Astrophys. J.*, 469:494, 1996.

[19] L.P. David et al. *Astrophys. J.*, 445:578, 1995.

[20] I. Smail et al. *Astrophys. J.*, 479:70, 1996.

[21] J.E. Carlstrom. astro-ph/9905255, 1999.

[22] N.A. Bahcall, L.M. Lubin, and V. Dorman. *Astrophys. J.*, 447:L81–L85, 1995.

[23] A.M. Boesgaard and G. Steigman. *Ann. Rev. Astron. Astro.*, 23:319, 1985.

[24] T. Walker et al. *Astrophys. J.*, 376:51, 1991.

[25] C.J. Copi, D.N. Schramm, and M.S. Turner. *Science*, 276:192, 1995.

[26] S. Burles et al. *Astrophys. J.*, 483:778, 1997.

[27] B. Carr. *Ann. Rev. Astron. Astro.*, 32:531, 1994.

[28] D.H. Weinberg et al. *Astrophys. J.*, 490:564, 1997.

[29] C. Alcock et al. astro-ph/0001272, 2000.

[30] B.D. Fields, K. Freese, and D.S. Graff. *Astrophys. J.*, 534:265, 2000.

[31] R.D. Peccei and H.R. Quinn. *Phys. Rev. Lett.*, 38:1440, 1977.

[32] B.W. Lee and S. Weinberg. *Phys. Rev. Lett.*, 38:165, 1977.

[33] K. Griest and B. Sadoulet. Model Independence of Constraints on Particle Dark Matter, Erice, Italy. In *Second Particle Astrophysics School on Dark Matter*, 1988.

[34] G. Jungman, M. Kamionkowski, and K. Griest. *Phys. Rep.*, 267:195, 1996.

[35] J.D. Lewin and P.F. Smith. *Astropart. Phys.*, 6:87, 1996.

Chapter 2

The CDMS I Experiment

2.1 Introduction

In this chapter, I discuss the design and methodology of the CDMS I experiment. Much of the infrastructure described here was in place when I joined the experiment in 1996. For details on the subjects described below, I will cite the "definitive" works on each topic. However, to avoid inadvertent omissions, I have refrained from listing the individuals who spearheaded each front. Suffice it to say that I and others in my position owe a great deal to the efforts of these individuals.

The CDMS collaboration consists of over 50 researchers and technicians from 11 institutions throughout the U.S. The collaborating institutions are Case Western Reserve University, Fermi National Accelerator Laboratory, Lawrence Berkeley National Laboratory, National Institute of Standards and Technology, Princeton University, Santa Clara University, San Francisco State University, Stanford University, University of California at Berkeley, University of California at Santa Barbara, and the University of Colorado. The full list of 50 or so authors can be found in [1].

CDMS I is located at the Stanford Underground Facility (SUF). The SUF consists of three tunnels and a loading dock at the south end of Hansen Experimental Physics Laboratory's End Station III which is located

on the Stanford University campus in Stanford, California. Figure 2.1 displays side and top views of the SUF. The experiment is housed in tunnel A which has been extended and widened. Tunnel B houses the pumps and high pressure gas cylinders necessary for operating the dilution refrigerator. Tunnel C is used as a "clean" storage area particularly for materials that need to be shielded from cosmic rays at the surface.

As explained in the previous chapter, WIMP search experiments strive to identify a signal that is smaller than 1 event per kg-day. As will become clear in the next section, this is an extremely difficult task given the backgrounds that all experiments are subject to. The signal is also expected to deposit energies smaller than 100 keV with a steeply falling exponential shape (see Chapter 1). Therefore, there is a constant effort to lower energy thresholds and increase energy resolution. A WIMP search experiment in general, and CDMS in particular, is defined by the strategies it employs to address these challenges.

In the case of CDMS, the choice of detector technology which introduces the cryogenic aspect, the shielding scheme, and the electronics all have their origin in these issues. I will first discuss backgrounds and the methods used to reduce them. This will naturally lead to the CDMS detectors which play an important role in rejecting backgrounds, in addition to providing low thresholds and good energy resolution. Then, I will briefly mention the technical aspects of implementing the desired schemes. Finally, the future of CDMS and its physics reach will be briefly mentioned.

2.2 Backgrounds and Shielding

Figure 2.2 contains a schematic of the CDMS I shield. Most of the work described here, that went into the the CDMS I shield design is thoroughly documented by Angela Da Silva in her Ph.D. dissertation [2]. I only

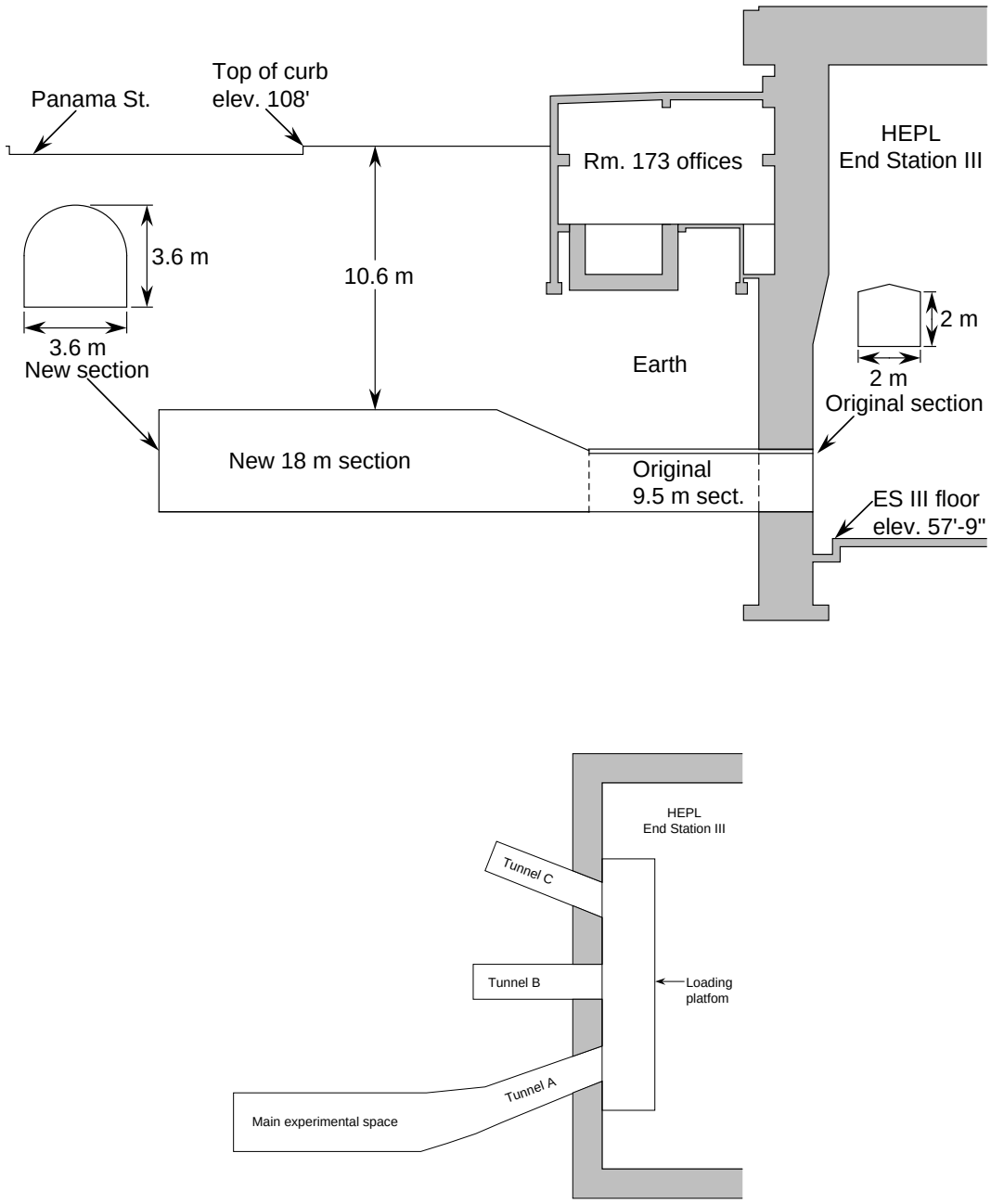

Figure 2.1: The Stanford Underground Facility (SUF).

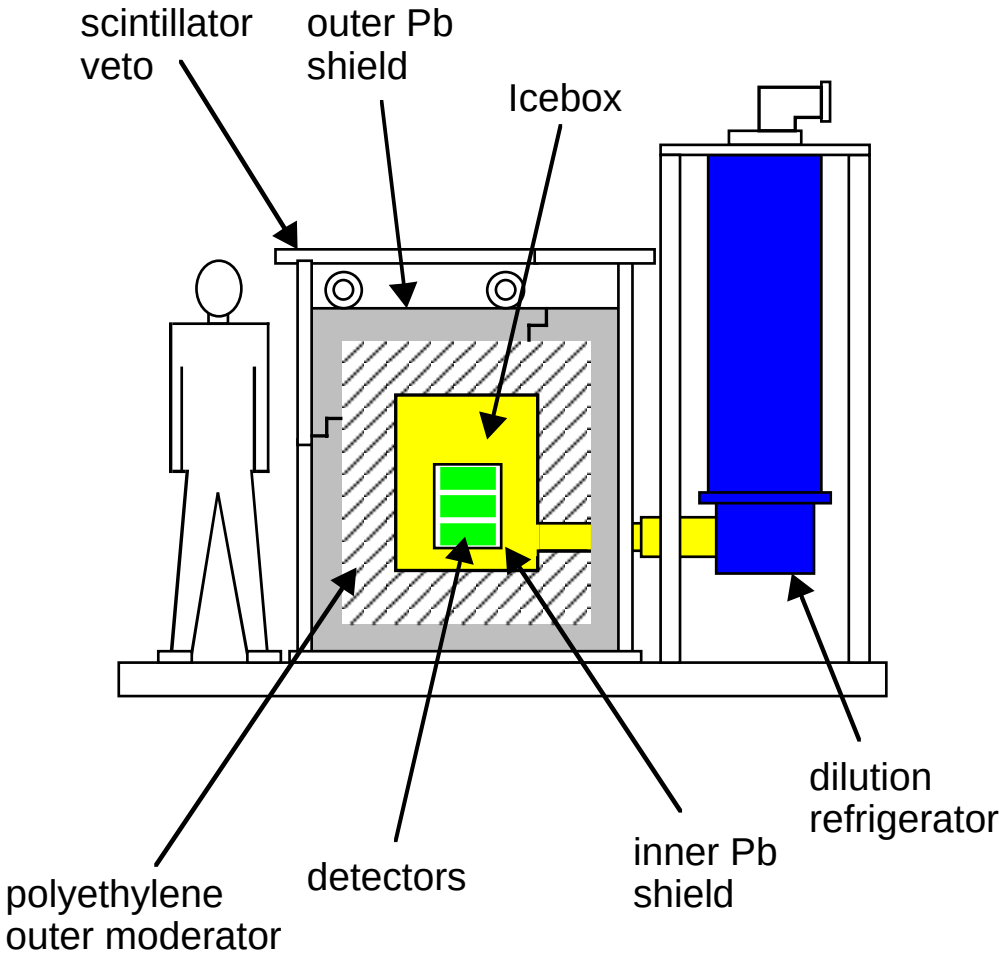

Figure 2.2: The CDMS I shield.

mention here the essential ideas for the sake of completeness. In Chapter 5, I will elaborate on some of these backgrounds, especially neutron backgrounds, as they relate to the data from CDMS I.

2.2.1 Photon Backgrounds

At sea level, a 1 kg germanium detector with a 10 keV energy threshold will typically see an event rate in excess of 50 Hz. This rate is primarily due to photons from the uranium and thorium chains and the decay of ^{40}K . These radioactive nuclides are present in the earth's crust and man-made structures. In the uranium and thorium chains, secular equilibrium is reached when all daughter nuclides reach equilibrium concentrations due to the much longer life time of the parent isotopes (^{238}U and ^{232}Th). In this state, all nuclides (parent and daughter) decay at the same rate. The decay chains, the relative intensities of different photon lines, and their abundance in different types of rock can be found in [2, 3, 4]. Typical activities of each chain in rock, are of the order 50 Bq per kg of rock. The other common source of gamma radiation is ^{40}K which undergoes beta decay and electron capture. The 1460 keV photon resulting from electron capture is its main contribution to backgrounds in low-rate experiments.

Photon backgrounds can be attenuated effectively by high-Z materials such as lead. The CDMS detectors are surrounded by both Pb and Cu which serve as gamma attenuators. The ^{238}U , ^{232}Th , and ^{40}K activities in these materials are low because these isotopes and their daughters are removed efficiently during the smelting and refining processes. The outer layer of the CDMS I shield consists of 15 cm of lead (figure 2.2). The thickness of the lead and the types of lead used were decided based on measurements made with a high-purity germanium (HPGe) detector[2]. The outer 10 cm of lead is comprised of "Stanford

lead" bricks which are known to have relatively high radioactive contamination[2] from the decay chains mentioned above. The inner 5 cm is made of "Glover lead" bricks which were measured to have lower activity. The lead shield attenuates the ambient gamma background by about three orders of magnitude. Increasing the lead thickness beyond 15 cm does not reduce the photon background, because at this thickness, the dominant source of radiation is radioactive contamination in lead itself. Even though the smelting and refining of lead is efficient for most isotopes, ^{210}Pb is not removed because it is chemically inseparable. Unfortunately, this isotope has a long lifetime ($T_{1/2}$ = 22.3 years). It beta decays to ^{210}Bi which subsequently decays to ^{210}Po with a beta endpoint of 1.162 MeV. In a high-Z material like lead, these electrons will yield substantial amounts of bremsstrahlung photons. In Run 13 of CDMS I, these residual backgrounds from the lead shield were a serious concern especially since the charge contacts were performing poorly. To shield detectors from this background, a 1-cm-thick layer of ancient lead ("Nantes" lead) has since been placed inside the cryostat (see figure 2.2). In this lead, the ^{210}Pb isotope has decayed away. In copper, no harmful isotopes are left after purification. However, the copper cans that make up the cryostat and other materials internal to the lead shield are carefully screened for radiopurity.

Another harmful isotope from the ^{238}U chain is ^{222}Rn because it is airborne[1]. About 6×10^8 ^{222}Rn atoms are released from the earth's surface per square-meter per day. Although ^{222}Rn decays with a half-life of 3.82 days, it leads to the long lived ^{210}Pb . In CDMS I, boil-off from Liquid Nitrogen which is free from ^{222}Rn is used to purge the insides of the shield. In the shielding studies described in [2], this was found to reduce the gamma rate by more than a factor of two.

[1] Although ^{220}Rn is also airborne it is present at much lower levels due to its very short half life ($T_{1/2}$ = 55.6 sec).

Photons will also arise from cosmic ray interactions in the detector surroundings. The CDMS I experiment is located at a depth of 10.6 m (see figure 2.1). Using cosmic ray muon intensities, this location was determined to be at 16 $\pm$ 1 meters of water equivalent (m.w.e.) [2]. At this depth, the absolute muon flux is reduced by a factor of about four. The hadronic component of cosmic rays, however, is completely removed in the first 2 m.w.e. Cosmic-ray muons reaching the "tunnel" will interact in the shielding material producing many background particles. Photons produced in this way are by far the dominant source of events in CDMS I. The scintillator paddles that surround the CDMS shield (figure 2.2) are viewed by photomultiplier tubes via light guides. Signals from the photomultiplier tubes are used to veto these events. As described in Chapter 5, the muon veto is measured to have an efficiency greater than 99.99 %. Details of the design and maintenance of the veto can be found in Andrew Sonnenschein's Ph.D. dissertation[5].

Radionuclides produced from cosmic ray interactions are also a source of background. Radionuclides of this type in the atmosphere as well as the shielding and detector materials can contribute to backgrounds. One reason for the 10.4 keV photon line seen in Ge-detector data is the cosmic ray spallation interaction that results in the production of ^{68}Ga. This is an example of radionuclide production by cosmic rays, clearly evident in CDMS I data.

2.2.2 Neutron Backgrounds

In CDMS, neutrons pose a more immediate background problem than photons because the event-by-event discrimination technique described above does not distinguish neutrons from WIMPs. At 16 m.w.e., neutron production is dominated by cosmic ray interactions. The neutron flux also

contains neutrons from (α,n) reactions induced by alpha decay in the uranium and thorium chains, and neutrons from spontaneous fission of ^{238}U and ^{232}Th .

As mentioned earlier, the hadronic component of cosmic rays is insignificant at 16 m.w.e. Interactions of cosmic-ray muons are the main sources of neutron production. There are two types of interaction. First, slow negative muons are captured by nuclei to form muonium. Subsequent muon capture by the nucleus leads to neutron production. Second, electromagnetic interactions between muons and nuclei, mediated by real or virtual photons, can lead to neutron production. Both these production mechanisms, and corresponding rates and spectra are discussed in detail in Chapter 5. Here, I will concentrate more on the design and effectiveness of the CDMS I shield with regard to neutrons.

Muon induced neutron production processes take place in the surrounding rock and the shielding material. Neutrons produced by these mechanisms in the shielding material can be rejected using the muon veto. Muon coincident neutrons identified in this way provide a convenient "neutron calibration" spanning the entirety of a data run. Since no vetoing is available for neutrons produced by muons in the surrounding rock, it is important to shield the detectors from these neutrons. The combined muon-induced neutron production rate from rock is estimated to be about 60 neutrons per day per kg of rock[2, 4]. These neutrons have typical energies in the range 1 to 10 MeV.

Neutrons from (α,n) interactions produce about 30 neutrons/kg/day in rock[2, 4]. The alphas emitted by the uranium and thorium series are of too low an energy (E $<$ 8.78 MeV) to yield neutrons from common elements in rock like O, Si, and Ca which make up about 79% of the earths crust. Neutrons are produced mainly from interactions of alphas with

elements like Al, and Na. Neutrons from spontaneous fission are even rarer with a typical production rate of 4.1 neutrons/kg/day in rock[2]. Neutrons from (α,n) and spontaneous fission reactions are negligible in the shielding materials which have low concentrations of the uranium and thorium series. The spectrum of neutrons from both these processes can be characterized by a fission spectrum which falls exponentially, with a characteristic energy of 1.29 MeV[2].

The ambient neutron flux at the SUF was measured to be $(8.1 \pm 0.6) \times 10^5$ neutrons/cm^2/sec. The 25 cm thick polyethylene layer in the CDMS I shield (see 2.2) attenuates this neutron flux by a factor of almost 1000. Given the neutron cross sections in polyethylene for the energies quoted above, all neutrons that are incident on the shield from outside (produced in rock) are moderated by the polyethylene, save one important exception. Included in the category "neutrons from electromagnetic muon-nuclear interactions", are high energy neutrons (E > 50 MeV) in hadronic showers resulting from nuclear interactions of fast muons. These neutrons are energetic enough to penetrate the polyethylene. The limiting background of CDMS I, seen in Run 19, is believed to be from neutrons caused by these rare events. I will spend most of Chapter 5 on these neutrons. The details regarding measurements and simulations that went into the design of the polyethylene shield can be found in [2]. These measurements were carried out using a BF_3 counter.

Due to the attenuation of muons with depth, neutron production from sources of "natural radioactivity" such as (α,n) and fission starts to dominate at deeper sites. However, the harder muon spectrum at these depths can give rise to high energy neutrons that are capable of penetrating usual shielding schemes. These neutrons and their impact on the design of the CDMS II shield will be discussed in Chapter 5.

In summary, both natural radioactivity and interactions of cosmic-ray mouns contribute to the neutron flux at the SUF. The polyethylene moderator is very effective at shielding low energy neutrons from natural radioactivity. Neutrons produced in muon interactions within the shield can be rejected using the muon veto. As discussed in Chapter 5, highly penetrative neutrons produduced by muons outside the shield present problem in terms of backgrounds.

2.3 CDMS Detectors

CDMS detectors are made from large crystals of Ge and Si. They are disk shaped with typical diameters of 6 cm, typical thicknesses of 1 cm, and typical masses in the 100-250 kg range. Two types of detector have been used in CDMS. They are the Berkeley Large Ionization and Phonon mediated (BLIP) detectors developed by Bernard Sadoulet's group at Berkeley and the Z-sensitive Ionization and Phonon mediated (ZIP) detectors which use the phonon detection technology developed by Blas Cabrera's group at Stanford. Most of the data described here was acquired using BLIP detectors. I will briefly describe the operation of BLIP detectors in the following sections. More detailed accounts can be found in Tom Shutt's [6] and Sunil Golwala's [7] dissertations.

When a particle interacts in a crystal of Ge or Si, the energy deposited goes mainly into phonon excitations and the liberation of electron-hole pairs. The CDMS detectors extract signals from both these processes. In BLIP detectors, the phonon signal appears as a change in detector temperature measured by thermistors mounted on the crystal. ZIP detectors measure the phonon signal before phonons thermalize using a different technology. I will discuss the ZIP phonon technology in more detail in Chapter 6. The charge signal is measured by drifting electron-hole

pairs in the crystal using a constant applied electric field. The charge measurement is identical in both types of detector. The quantity measured is the the total external charge needed to maintain a constant electric field during the drifting process. I will show that this is equal to the total charge liberated by the interaction.

The phonon or heat signal consists of two parts: the initial energy given to the phonon system and the kinetic energy deposited in the crystal by electron hole-pairs in motion. Part of the electron-hole kinetic energy is supplied by the constant electric field across the crystal while the other part is due to the original particle interaction. The total measured heat can then be written as,

$$P = E_r + eN_{eh}V. \tag{2.1}$$

Here, P is the measured heat and E_r is the "recoil energy". The recoil energy is the total energy deposited in the crystal by the particle interaction. N_{eh} is the the number of electron-hole pairs, and V is the voltage bias across the detector. The second term, known as the Neganov-Trofimov-Luke term[8, 9], can be subtracted from the heat to obtain the recoil energy. This subtraction is possible because the ionization circuit measures $Q = eN_{eh}$.

As opposed to the phonon signal, the number of electron-hole pairs liberated in a scatter depends on the the type of interaction. When a particle scatters off an electron, the energy fraction utilized to liberate electron-hole pairs is higher than the corresponding fraction for a scatter off a nucleus. Therefore, measuring both phonon and charge signals allows one to distinguish between nuclear and electron recoils. The charge energy is calibrated using known photon lines, such as the feature at 511 keV due to positron annihilation. Since charge calibration is performed using electron recoils, the charge measurement is given in "electron recoil equivalent"

energy. From now on, I will refer to it simply as the "charge energy" or "ionization energy".

Figure 2.3(a) shows the excellent separation of nuclear-recoils from electron recoils in a plot of charge energy versus recoil energy. We will also refer to the "charge yield" which is simply the charge energy divided by the recoil energy. Figure 2.3(b) is a plot of charge yield versus recoil energy. We use this type of plot in many of the discussions in Chapters 3 and 4 because it better reflects the quality of the electron-recoil/nuclear-recoil separation as a function of energy. Note that a constant charge threshold appears as a hyperbola in the charge yield versus recoil energy plot.

The separation of electron and nuclear recoils is a very powerful tool for rejecting backgrounds. Using this technique more than 99% of events due to photons and 95% of events due to electrons can be rejected.

I now describe the phonon and charge measurements. Figure 2.4 displays the BLIP detector design. The amplifiers mentioned below, with regard to both the phonon and charge circuits, have JFETs as their inputs. these JFETs are mounted on the 4 K stage of the cryostat in order to minimize noise. The operating temperature of the JFETs is about 130 K. The rest of the amplifier circuit is at room temperature.

2.3.1 The Phonon Measurement

Particle interactions in crystalline detectors result in high energy phonons which thermalize on millisecond time scales. Thus, the temperature of the detector rises on this time scale. The temperature rise is significant due to the T^3 dependence of heat capacity in insulating crystals at low temperatures. A 10 keV energy deposition will increase the temperature of a 165 g germanium BLIP detector at 20 mK by 2.4 μK[7]. This temperature rise is measured using Neutron Transmutation Doped (NTD)

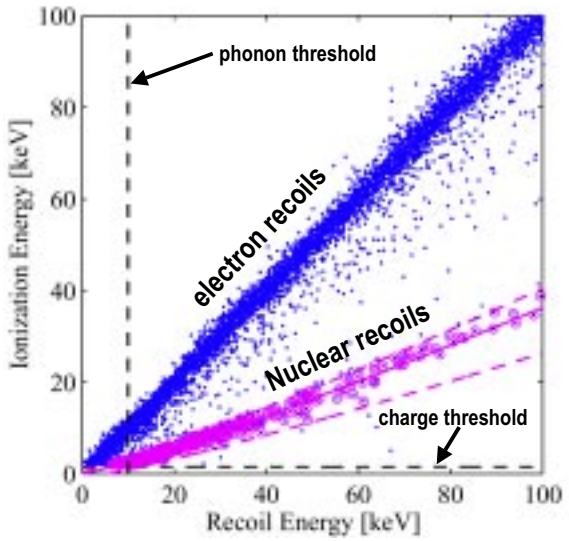

(a)

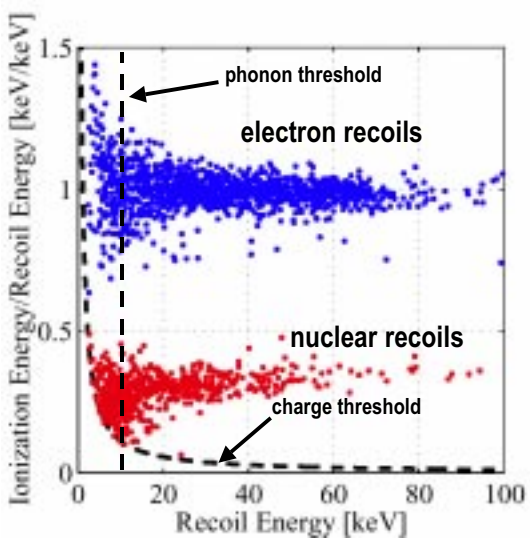

(b)

Figure 2.3: Nuclear- vs. electron-recoil discrimination used in CDMS. (a) Nuclear-recoils and electron recoils are clearly separated in a plot of charge energy vs. recoil energy. The nuclear-recoil band is identified by the dashed lines. (b) A plot of charge yield versus recoil energy. Typical charge and phonon thresholds are shown in both plots. These data were obtained by exposing detectors to gamma and neutron sources.

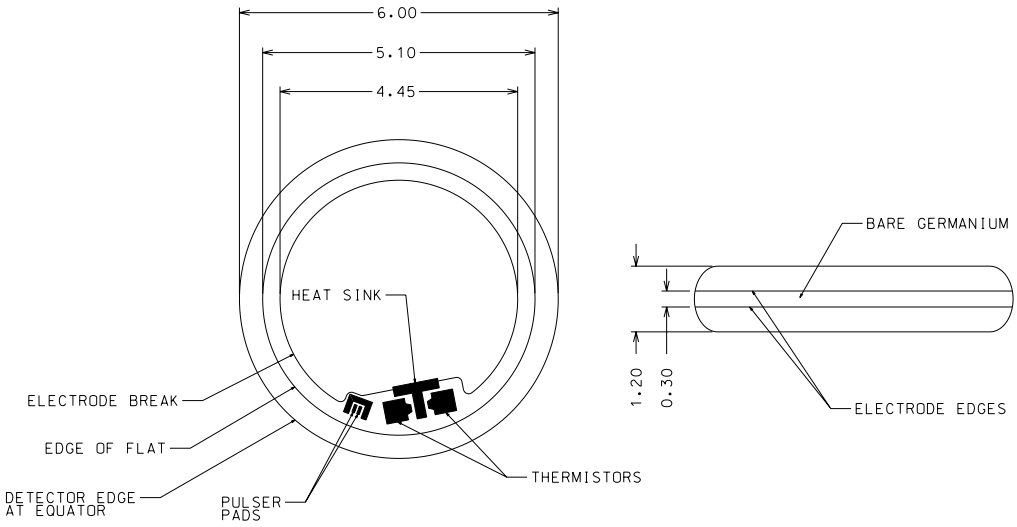

Figure 2.4: BLIP detector. The dimensions are in centimeters. The second circle on the left indicates the start of the curved region. The innermost circular shape is the break between the inner and outer electrodes. The thermistors, pulser, and heat sink pad are not shown in the side view on the right.

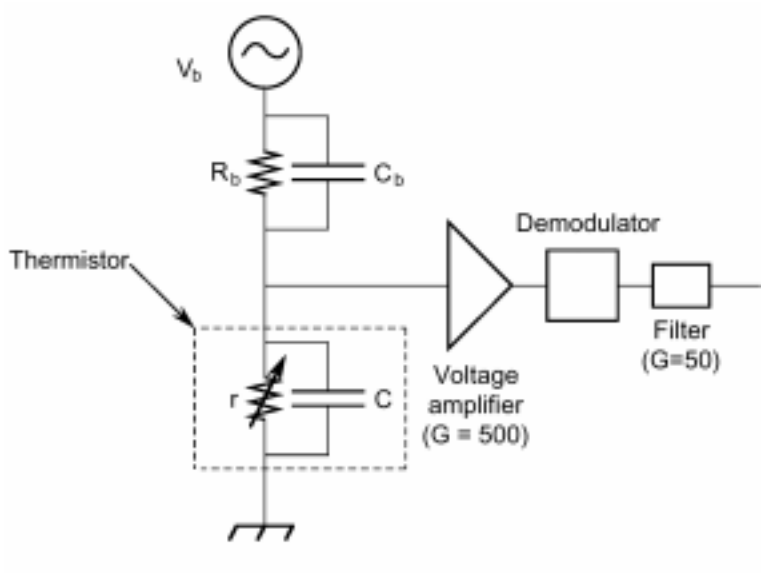

Figure 2.5: The NTD thermistor based phonon readout circuit.

thermistors. NTD germanium is made by exposing intrinsic germanium (Z = 32) crystals to a neutron beam of high enough energy that neutrons will scatter homogeneously in the crystal. A high concentration of gallium (Z = 31) impurities results from nuclear transmutations induced by these neutrons. Hopping of electrons between these acceptor sites causes conduction. The $3.1 \times 3.1 \times 2.6$ mm^3 NTD thermistors (see figure 2.4) are eutectically bonded to the detectors. The efficient transmission of phonons across this interface and the closeness of the specific heats of thermistors and detectors cause thermistor temperatures to vary with detector temperature. The resulting resistance change is the signal measured by the readout system (figure 2.5). Two thermistors are deployed to enable rejection of particle interactions that occur within a thermistor, which occur at a rate of a few per hour.

Since heat aids hopping conduction in the thermistors, the resistance

drops as temperature increases. Therefore, the thermistor must be current biased for stability. At low temperatures, the electron and phonon systems of an NTD are not closely coupled. Injection of bias current into the NTD causes the electron temperature to be offset from the phonon temperature according to the formula

$$P_{in} = I_b^2 R = \Sigma V \left(T_e^6 - T_\phi^6 \right) \tag{2.2}$$

where T_e is the electron temperature, T_ϕ is the phonon temperature, Σ is a material dependent constant, and V is the volume of the thermistor. Heat flow into the thermistor causes T_ϕ to increase, which in turn causes T_e to increase by the same amount. The resistance change in the thermistor is then measured as a voltage change. On a longer time scale of order 50 ms, the heat from the interaction is conducted from the detector-thermistor system to the refrigerator via a gold wirebond.

The rise time and fall time of the phonon signal are determined by the phonon thermalization time and the thermal relaxation time respectively. Therefore, the signal lies in the 20–1000 Hz frequency range. This frequency range has a high noise level due to microphonics and $1/f$ noise from the JFETs used in the measurement. The modulation-demodulation scheme illustrated in figure 2.5 is used to shift this noise to high frequencies. A 1 kHz sine wave is used to bias the thermistor. Since the thermistor's thermal time constants are much slower than the 1 kHz modulation, it effectively sees only the average current bias. A slow resistance change in the thermistor due to an event will cause the sinusoidal voltage drop across the crystal to be amplitude modulated. On the other hand, the dominant noise sources (1/f noise and microphonics), will appear as additive terms. The sum of the AM signal and the noise is amplified and then mixed with (multiplied by) a square wave with the exact same frequency and phase as the signal. In the resulting output, half

of the signal is retrieved at its original frequency. The rest appears as amplitudes of higher harmonics of the 1 kHz modulation. Meanwhile, the low frequency noise is shifted to the range around 1 kHz. Filters before and after the demodulator remove high frequency noise and higher harmonics of the 1 kHz bias, leaving the signal at low frequency.

A 1 kHz bias frequency is chosen because it is above the low frequency noise and below the bandwidth of the circuit. The low frequency noise falls off around 500 Hz. The bandwidth of the circuit is set by the components shown in figure 2.5. The usual values of these components are[7],

$$\begin{aligned} R_b &\approx 40M\Omega \\ C_b &\approx 1pF \\ r &\approx 2M\Omega \\ C &\approx 50pF. \end{aligned} \tag{2.3}$$

The thermistor capacitance C, is dominated by the FET gate-wire capacitance. Bias currents in the range 6.5–8 nA are used. Typical heat pulse heights of 160 nV/keV before amplification are observed[7]. The zero-point resolution and the resolution at 30 keV are measured to be about 0.6 keV and 1.4 keV, respectively[7].

2.3.2 Charge Measurement

Particle interactions will also cause the excitation of electrons across the band gap into the conduction band. The band gaps of Ge and Si are approximately 0.7 eV and 1.2 eV at 20 mK. In Ge, an energy of 3 eV is required on average to produce an electron-hole pair since the deposited energy goes into a continuous distribution of electron kinetic energies. As mentioned earlier, the energy that goes into the electron system is highly

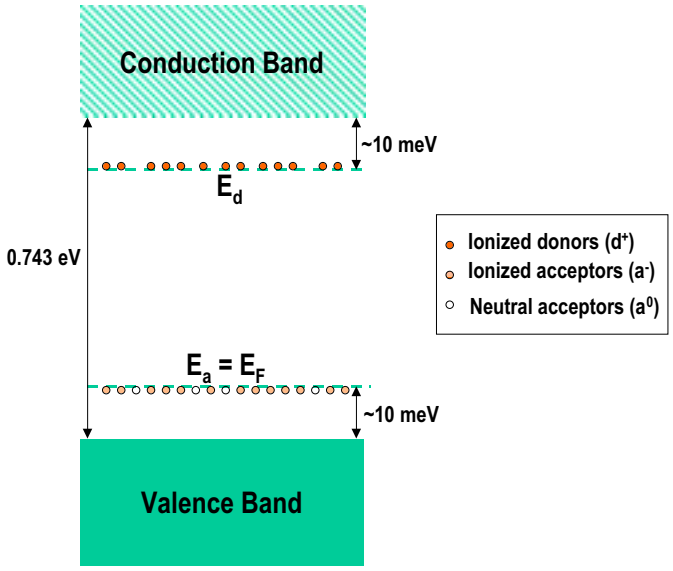

Figure 2.6: Approximate band structure of intrinsic Ge crystals used in CDMS.

dependent on the target (electron or nucleus). An electric field drifts electrons and holes through the crystal to electrodes on the detector surface. As indicated in figure 2.4, the electrodes are radially segmented and read out separately to enable the discrimination of events in the outer region from those in the inner region.

The intrinsic Ge crystals used in CDMS are mildly p-type with N_a - $N_d \sim 10^{-11}$. Figure 2.6 shows the approximate band structure of Ge at 20 mK. The acceptor and donor levels are both about 10 meV removed from the valence and conduction bands, respectively. The thermal energy at 20 mK corresponds to 1.7 μeV. Due to the very low temperatures and the p-type nature of the crystal, the Fermi energy lies very close to the acceptor level. In this situation, all donors and an equal number of acceptors will be ionized. This is the minimum-energy equilibrium

configuration. The detector is in this condition when it is first cooled down. Due to the trapping of drifting electrons and holes by ionized impurities, the ionization signal is initially very small. However, as trapping continues, more impurities are neutralized. This neutralization results in better charge yield. Before data taking begins, the detectors are completely neutralized by flashing an infra red LED that has enough energy to generate electron hole pairs. Even though this neutralized state is not the lowest energy configuration (described above), the thermal excitations needed for reaching the lowest energy configuration are unavailable at these temperatures. Therefore the neutralized condition is a stable one. Although other trapping mechanisms (eg. neutral impurities, deep impurities) persist even after neutralization[6], the charge yield is sufficient to discriminate between nuclear and electron recoils (see figure 2.3).

However, reduced charge yield can reappear due to infra-red photons from the FET card and other heat sources re-ionizing the crystal. Therefore special precautions must be taken to shield against infra-red sources. The build up of space charge within the crystal also results in poor charge collection. This process occurs due to the trapping of drifting charges in regions of the crystal with high impurity densities. Grounding the detector removes this space charge. In CDMS data runs, the detectors are grounded approximately every 30 minutes to ensure good charge collection. The data acquisition system is paused during this time. Detectors need to be grounded more often in the test facilities where event rates are higher.

A simplified version of the charge readout circuit is given in figure 2.7. The applied electric field does work in drifting the charge pairs. If no external current were allowed to flow to the electrodes, the electric field will decrease as a result, producing a measurable voltage change across the detector. Determining the complete charge from an event using such a

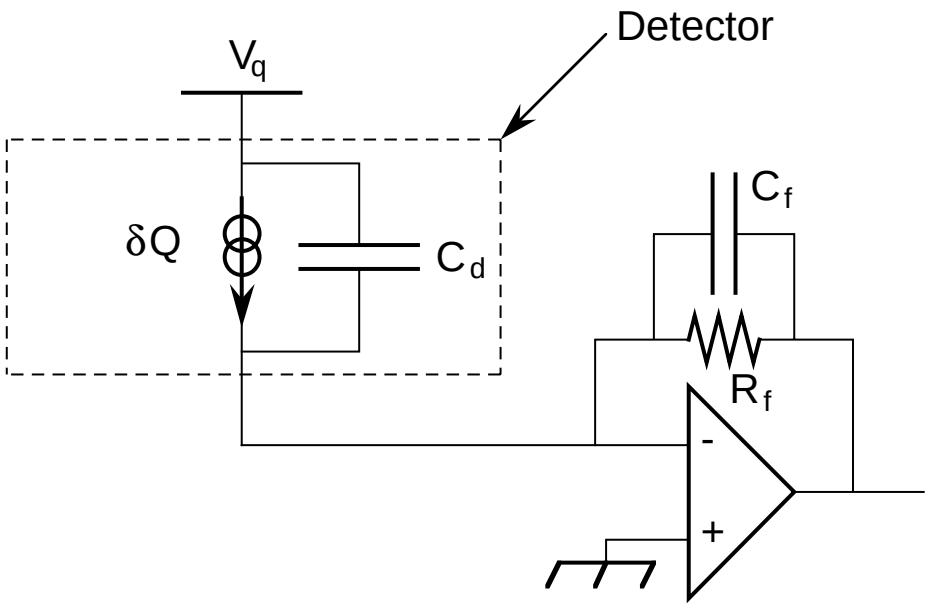

Figure 2.7: Simplified version of the ionization readout circuit.

measurement involves knowing the exact capacitance of the detector in spite of temperature drifts that cause the crystal dielectric constant to change. To circumvent this problem, CDMS detectors use a current-amplifier method for the ionization measurement. In this method, the "current" from an event (see figure 2.7) is made to flow through C_f, the feedback capacitor, instead of discharging the detector capacitance C_d as in the aforementioned scenario. The large gain-bandwidth of the the amplifier ensures this. Current from the event is thus integrated on C_f. The resulting voltage change, when multiplied by C_f, yields the total charge.

The charge drift process occurs on nanosecond time scales. However, the rise time of charge pulses are limited to about 1 μsec by the amplifier. This is done in order to prevent oscillations that would take place due to phase shifts in the feedback scheme. Phase shifts will occur because of the 650 pF stripline capacitance between the 4 K and room-temperature parts

of the discrete amplifier. The fall time of the pulse is $R_f C_f$ and is chosen to be 40 μsec. In reality, the charge circuit is connected to the "biased" side of the detector because the phonon circuit makes use of the ground side. A coupling capacitor C_c, which acts as an open circuit for DC and a short circuit for AC, connects the charge integrator circuit to the biased side. Figure 2.8 displays the complete scheme.

Typical values of the charge circuit components are,

$$\begin{aligned} R_b &\approx 40M\Omega \\ C_d &\approx 50pF \\ C_c &\approx 300pF \\ C_p &\approx 50pF \\ R_f &\approx 40M\Omega \\ C_f &\approx 1pF. \end{aligned} \tag{2.4}$$

Again, the FET gate-wire dominates C_p. Pulse heights of $\sim$ 50 nV/keV are expected at the output of the first stage amplifier shown in figures 2.7 and 2.8. The zero-point resolution and the resolution at 10 keV are measured to be about 0.6 keV and 1 keV respectively[7].

The Surface Electron Problem

Prior to Run 19, CDMS detectors suffered from poor charge collection for events close to detector surfaces. In particular, electrons incident on the detector result in events with poor charge yield because they scatter close to the surface. For instance, in Ge, a 10 keV electron has a range of 0.5 μm while a 60 keV electron has a range of 10 μm. As explained in Chapter 3, a significant fraction of photon interactions with energy depositions below about 100 keV will also happen close to the surfaces. The resulting reduction in charge yield may cause these events to be misidentified as

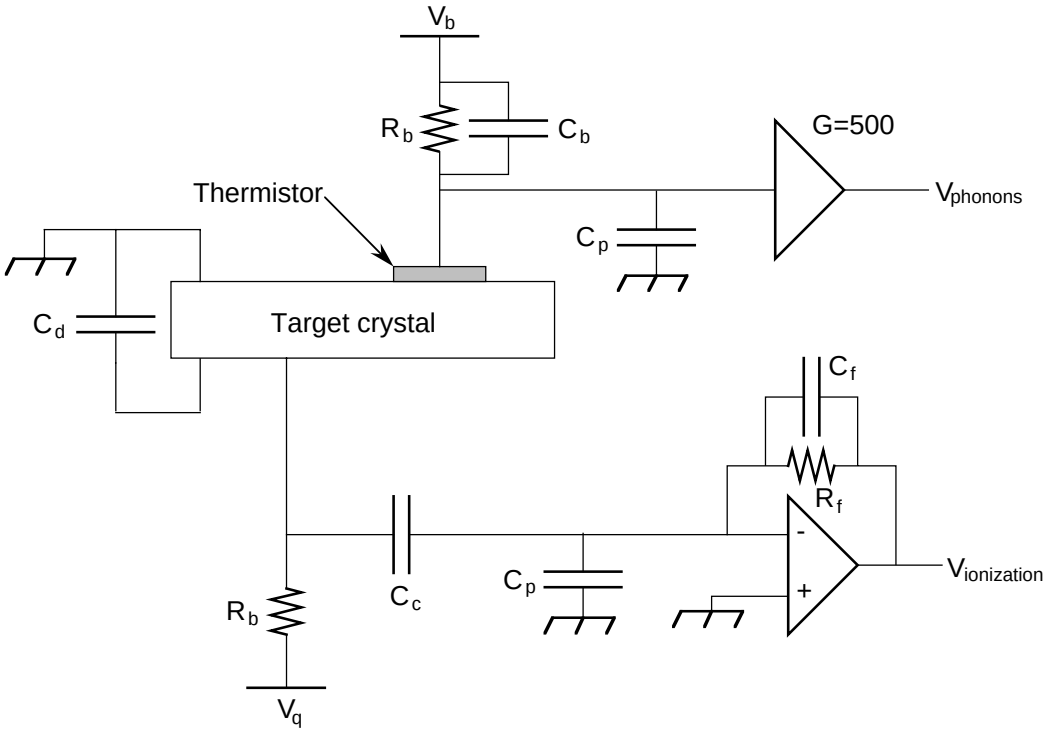

Figure 2.8: The readout circuitry of a BLIP detector.

nuclear recoils. Since some of these particles are due to localized sources of background near detectors, the muon veto does not help. Before Run 19, progress in increasing our sensitivity to dark matter was slow due to this problem.

Reduction in ionization yield near the surface of a semiconductor detector is a well known problem even in conventional detectors operated at 77 K. It is referred to as the "dead-layer problem". Two processes contribute to this effect. First, charge pairs liberated in a particle interaction will initially have high kinetic energies and, therefore, move in all directions before reacting to the applied electric field. This process is known as "back-diffusion". Second, when back-diffusion occurs close to an electrode, some of the back-diffusing charges are trapped in the electrodes. Originally, the electrodes on CDMS detectors were made from degenerate doping of the detector surface with boron ions. The resulting p-type electrode has an acceptor density of $10^{19}/\mathrm{cm}^3$. Attempts to mitigate the loss mechanism at the electrodes by lowering the acceptor concentration were unsuccessful[6, 10]. The successful solution to the dead-layer problem, implemented in Run 19 detectors, involves reduction of back-diffusion, as described below.

For Run 19, a four-pronged strategy was developed to solve the surface electron problem.

1. Use newly developed electrodes that minimize back-diffusion (see below).

2. Minimize electron contamination in detectors and materials close to them through clean and careful handling.

3. Close packing of detectors (see figure 2.11) with about 3 mm spacing in order to shield the inner electrode fiducial region from less

penetrating backgrounds like electrons.

4. Use a new phonon technology that allows the rejection of surface events.

The fourth item above is implemented in ZIP detectors. This new technology is described in Chapter 6. Due to the successful implementation of the first three steps in the above plan, Run 19 detectors are mostly free of the surface electron problem. Although charge yield is still low for surface events relative to bulk events, misidentification of electron recoils as nuclear recoils is very unlikely, as demonstrated in Chapter 4. Here, I will briefly describe the workings of the new electrodes. Due to their success, future CDMS detectors will incorporate this new design. The most recent account on this topic is a paper by Tom Shutt *et.al.*[11].

With the degenerately doped p-type electrodes, a strong electric field of the order 15 V/cm pointing in the direction of the surface is expected very close to the electrodes. This field would appear as a result of free holes from the electrodes de-ionizing the acceptors close to the electrode. Since the positively ionized donor impurities remain, charge will build up in these regions until the electric field is strong enough to oppose further diffusion of free holes from the electrode. This field would extend about 10-20 μm into the crystal. The strong built in field at the electrodes was expected to provide a barrier against back-diffusion. Given an applied electric field in a particular direction, the built in field would align with it at one of the electrodes. Therefore, little back-diffusion is expected especially on that side of the detector. However, tests indicated that the built in field is insignificantly small. Again, this is due to the low thermal energies available at 20 mK. For instance, the neutralization process described above can occur near the positively charged region next to the electrodes yielding a neutral stable state.

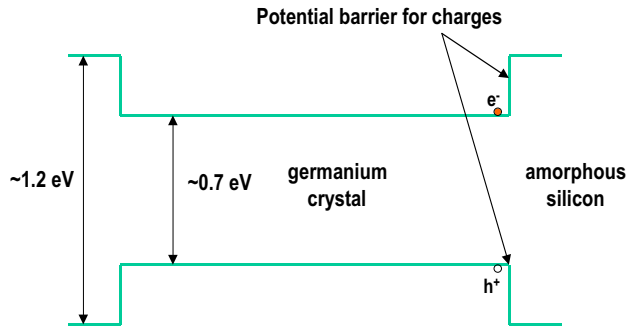

Figure 2.9: Cartoon of blocking electrodes.

The new electrodes in BLIP detectors consist of a 27.5-nm-thick amorphous Si layer followed by a 250-nm-thick Al layer deposited on the crystal. If the larger Si band gap aligns with the band gap of Ge as indicated in figure 2.9, electrons and holes are blocked at the point of entry to the electrodes. Charges that remain next to the electrode due to the applied electric field are eventually be conducted to the Al layer through hopping conduction in the amorphous Si. However, due to the external field, back-diffusing charges do not remain at the "wrong" electrode long enough for hopping conduction to take place. Therefore, back-diffusion is minimized with this scheme.

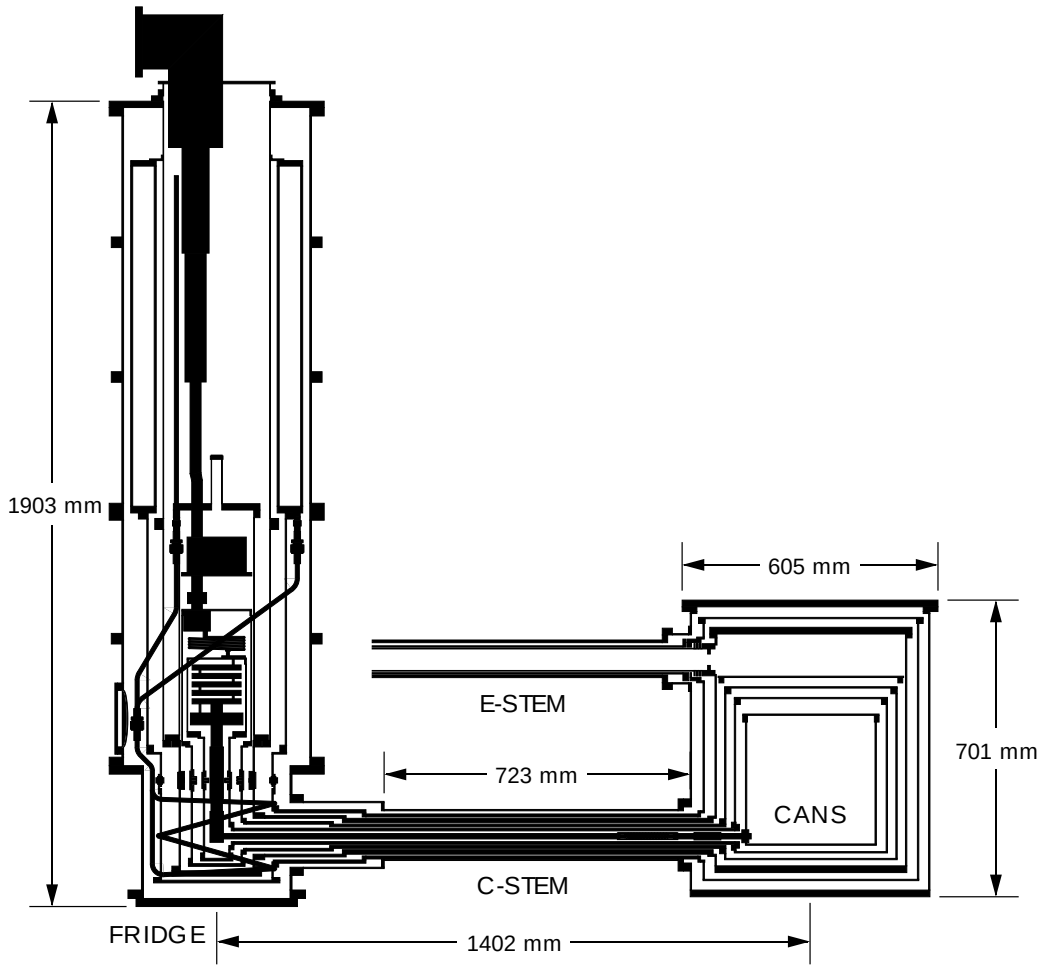

Figure 2.10: The CDMS I cryostat. The refrigerator, stems, and icebox are in order from left to right. Note the 30 l volume of cold detector space on the right which can be shielded from backgrounds.

2.4 Cryogenics and Electronics

2.4.1 The Icebox

The low temperatures required for detector operation are obtained with a Kelvinox 400 dilution refrigerator made by Oxford Instruments. Because the refrigerator materials do not have the radiopurity required of near-detector materials, the detectors and the shield must be separated from the refrigerator. In CDMS, a separate cryostat made from oxygen-free electronic (OFE) copper, called the "icebox" is used to house detectors. The OFE copper was deemed sufficiently pure after radiopurity screening at Lawrence Berkeley National Laboratory (LBNL). Figure 2.10 is a side-view schematic of the icebox. A complete description of the icebox and relevant design issues can be found in Peter Barnes' Ph.D. dissertation[12]. Here I will briefly mention some key points.

The icebox consists of six concentric copper cans corresponding to the six temperature stages in the dilution refrigerator. The six layers are the room temperature layer, the 77 K liquid nitrogen layer, the 4 K liquid helium layer, the 600 mK still layer, the 50 mK cold plate layer, and the 10 mK base temperature mixing chamber layer. The temperatures indicated above may vary slightly. Usually, only the mixing chamber temperature is carefully controlled. The icebox cans are suspended from each other using kevlar loops. Brass screws are used as fasteners. The kevlar and brass were also screened for radiopurity. Each of the six layers are connected through the "cold-stem" (C-stem) to the corresponding layers of the refrigerator, as shown in figure 2.10. The striplines used for detector control and readout go from the room temperature hermetic feedthrough (not shown) to the icebox via the "electronics stem" (E-stem). The striplines are heat sunk at the room temperature, liquid nitrogen, and liquid helium layers of the icebox. All cryogenic seals are made with copper gaskets. A complete

temperature monitoring system is installed on the icebox and refrigerator for diagnostic purposes.

The heat loads at each temperature layer are due to radiation, heat sinking of cables, and power dissipation by components in the FET card (see below). The heat loads are particularly significant for the liquid nitrogen and liquid helium layers. A 20-layer superinsulation shield and gold plating are used for thermal isolation of the liquid nitrogen layer. The C-stem and E-stem joints at each end are made flexible to accommodate differences in thermal contractions at each temperature stage. The maintenance of good thermal conductivity between these flexible thermal joints, isolation of the cans from fridge vibrations, development of the copper gaskets, and other challenging design aspects are described in [12].

2.4.2 Mounting of Detectors and Cold Electronics

The detector and low temperature electronics are mounted on a hexagonal "tower", as indicated in figure 2.11. The tower is a modular assembly which provides removable mounts for detectors and cold electronics components. The part of the tower that houses detectors is known as the tower "basement". Each tower can house up to six detectors. I will describe the parts in figure 2.11 from bottom to top.

Not all detector housing and mounting components are shown on figure 2.11. Following the close-packing scheme mentioned above, detector surfaces are separated by only 3.5 mm. The insides of the copper detector housing are covered with detector-grade germanium to shield against electron backgrounds emanating from the copper. The detector housing and electrical connections through it are "light-tight". Wirebonds from the detector are connected to the patterned copper-kapton Detector Interface Boards (DIB) labeled as Q DIB and P DIB in figure 2.11 for the phonon

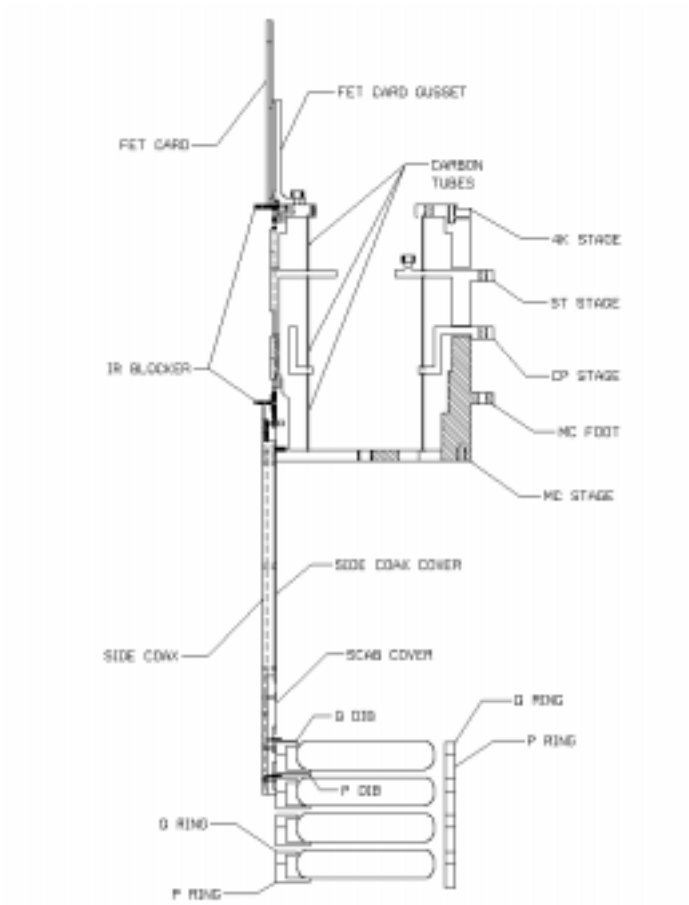

Figure 2.11: Detector mount and tower.

and charge channels, respectively. The infra red LEDs used for neutralizing detectors are the only electronic components inside the detector housing. They are attached to the DIBs. Details of the detector housing and mounting are presented in Sunil Golwala's dissertation[7].

The "side-coax" boards are connected to the DIBs via connections that are impenetrable to infra red radiation. These "IR blocker connectors" are also described in [7]. Each detector has its own side-coax and tower face. The lower part of the side-coax contains some low temperature circuitry. In the side-coax, a special design is used for the signal wires in order to minimize the capacitance to ground and reduce microphonics noise. Dielectric materials between signal wires and the ground plane increase capacitance. The triboelectric effect resulting from the difference in work functions of materials will give rise to microphonics noise when vibrations are present. These effects are particularly damaging for high impedance measurements using FETs. Therefore, no insulating materials are placed between the signal wires and the ground plane. These "vacuum-coaxes" are made by tensioning each wire inside its channel. The side-coax connects to the mixing chamber (MC) stage of the tower.

Each face of the tower can be considered a continuation of the side-coax with the same vacuum-coax design. However, inside the tower, the signal wires are heat sunk at every temperature stage except the cold plate. Effective heat sinking of wires within the small distance allowed by the icebox design is a challenging task. NbTi wires which superconduct below 9.5 K are used as the signal wires in order to lower heat conduction between stages. Thermal stages of the tower which correspond to different icebox cans are thermally isolated from one another through the thin graphite tubes shown in figure 2.11. The mixing chamber stage of the tower is bolted firmly to the mixing chamber can. The other stages are heat sunk

to icebox cans using flexible joints. Details of the tower design are contained in Walter Stockwell's dissertation [13].

Finally, the signal wires connect to the FET cards atop the tower (see figure 2.11). The JFETs that make up the first part of both the phonon and charge amplifiers must be kept close to the detector to reduce the gate-to-ground capacitance. They also have low noise at low temperatures. Therefore, they are mounted at the 4 K stage. The FET cards are made of many layers of kapton and adhesive with several layers of patterned copper in between. Kapton is used instead of fiberglass because of the relatively high content of ^{40}K in the latter. Only low-activity solder is used close to the detector volume [14]. The FETs are mounted on a thermally well-separated "window" within the card. This allows them to self-heat to a temperature of around 120 K. A heater and a temperature sensor are also mounted on the window. The heater is used to pre-heat the FETs before operation.

The FET cards are read out and biased via striplines which connect to the room temperature electronics through a hermetic feedthrough box. The striplines are made of kapton and copper. They are approximately 3 m long, 2.5 cm wide and 0.5 mm thick. Each stripline contains 50 traces 0.13 mm wide and 0.018 mm thick with an average trace-separation of 0.25 mm. Ground lines which comprise about half of the traces are interleaved with signal lines to decrease cross-talk. Two 1 μm copper layers on each side of the traces make up the shield of the stripline. The stripline is designed to minimize electrical resistance and thermal conductance given the length constraint imposed by the shield and E-stem. Each trace has a resistance of approximately 20 Ω and deposits a heat load of roughly 12 mW at the liquid helium layer of the icebox. Both these parameters are acceptable in terms of noise and heat considerations. However, the bandwidth of the

charge measurement circuit has to be artificially reduced to to about 1 MHz due to the non-negligible stripline capacitance of approximately 650 pF[15]. The striplines connect to the inside of a hermetically sealed feedthrough unit at the room temperature end. The room temperature front-end electronics are connected to this feedthrough from the outside.

2.4.3 Room Temperature Electronics and Data Acquisition

The readout, biasing, and pulsing lines of each detector are connected from the hermetically sealed feedthrough to the front-end electronics through 50-wire twisted-pair "Detector I/O" cables which are roughly 1 ft long. The front-end electronics consists of an 18-slot subrack which houses custom-built 9U size boards containing IC components. Each detector has its own stripline, detector I/O cable, and front-end board. Most of the amplifiers, switches, and DACs needed for reading out, biasing, and pulsing detectors are contained on the front-end board. After processing by the front-end board, signals are transported through a 50 ft long 25-wire cable to the Receiver-Trigger-Filter (RTF) rack. The RTF boards, one for each detector, perform some minimal conditioning and anti-alias filtering of the signals. Each RTF board also outputs phonon and charge triggers at two different discriminator levels ("Hi" and "Low"). The front-end and RTF boards are computer controlled through a custom made GPIB interface.

The data acquisition system is presented in block diagram form in figure 2.12. The "Trigger Logic Board" which is also plugged into the the RTF rack takes triggers from individual RTF boards and outputs a global OR trigger to inform the data acquisition system (DAQ) that an event has occurred. The front panel outputs of the RTF boards which carry the conditioned, filtered signals are connected to the inputs of waveform digitizers housed in a VXI-mainframe. Although the digitizers are VME

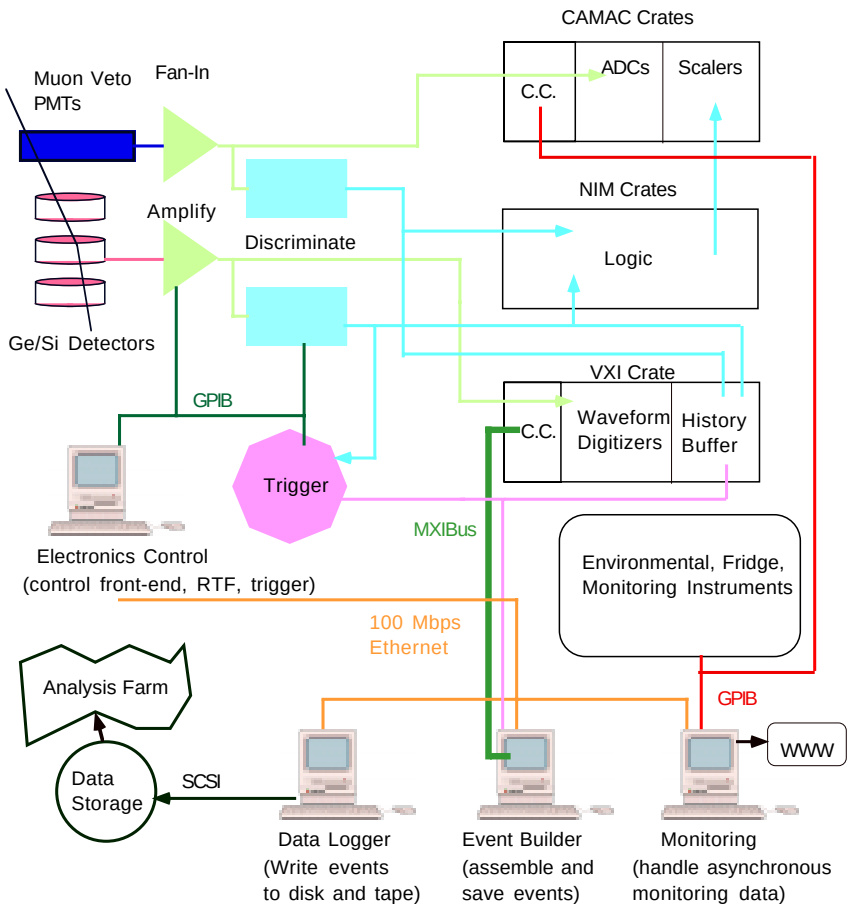

Figure 2.12: Block diagram of the CDMS data acquisition system

modules, they are housed inside a VXI-crate for better noise performance. The global trigger causes the 12-bit, 10 MHz waveform digitizers to stop digitization after the pre-set number of post-trigger samples are acquired. The computer then downloads the pre-trigger and post-trigger samples. Further triggers are disabled until the download is complete and a minimum number of pre-trigger samples for the next event has been acquired by the digitizers.

The muon veto signals from the photomultiplier tubes are recorded and saved at 1 μsec intervals after processing by NIM logic and discriminator modules. When a trigger occurs, the "veto history buffer" which forms a window around the trigger time, is also downloaded. This information allows the rejection of muon related events in the software. The DAQ software is written in LabVIEW and runs on a Power Macintosh. The acquired data are written over a 100 Mbps Ethernet network to disks mounted via fast SCSI to Linux and Unix workstations. The raw data are analyzed on these machines using Matlab-based analysis code. Raw data and reduced data output by the analysis code are stored on DLT tapes.

Cryostat temperatures and information regarding performance of the veto and trigger systems are recorded at regular intervals on another Power Macintosh for diagnostic purposes.

2.5 The Future of CDMS

The sensitivity of CDMS I is limited by the neutron background observed in Run 19. More statistics and further shielding of these neutrons should enable CDMS to further lower its dark matter limits[2]. However, lower background rates are required in order to rule out significant regions of

[2]The neutron background and the proposed shielding scheme are discussed in detail in Chapters 4 and 5.

unexplored parameter space. The CDMS II experiment located at the Soudan mine outside Tower, Minnesota is now under construction with first data taking planned for 2002. This site is 2350 ft below the surface, which is equivalent to 2090 m.w.e. The ZIP detectors described in Chapter 6 will be used for this experiment. The large reduction in cosmic-ray muon-related backgrounds at this site is expected to increase the sensitivity of CDMS by approximately 2 orders of magnitude. Shielding considerations and expected event rates for CDMS II are discussed briefly in Chapter 5. Further details can be found in the CDMS II proposal [16] which was approved by the National Science Foundation and the Department of Energy in 1999. The general principles described in this chapter will apply to CDMS II and any other future incarnations of CDMS.

References

[1] R. Abusaidi et al. Exclusion Limits on the WIMP-Nucleon Cross-Section from the Cryogenic Dark Matter Search. *Physical Review Letters*, 84:5699, 2000.

[2] Angela Da Silva. *Development of a Low Background Environment for the Cryogenic Dark Matter Search*. PhD thesis, The University of British Columbia, April 1996.

[3] Glenn F. Knoll. *Radiation Detection and Measurement*. John Wiley and Sons, second edition, 1989.

[4] T. Florkowski, L. Morawska, and K. Rozanski. Natural Production of Radionuclides in Geological Formations. *Nuclear Geophysics*, 2:1, 1988.

[5] Andrew Sonnenschein. *A Search for Weakly Interacting Dark Matter Particles with Low Temperature Detectors Capable of Simultaneously Measuring Ionization and Heat*. PhD thesis, University of California, Santa Barbara, July 1999.

[6] Thomas A. Shutt. *A Dark matter Detector Based on the Simultaneous Measurement of Phonons and Ionization at 20 mK*. PhD thesis, The University of California at Berkeley, 1993.

[7] Sunil Golwala. *Exclusion Limits on the WIMP-Nucleon Elastic-Scattering Cross-Section from the Cryogenic Dark Matter Search*. PhD thesis, The University of California at Berkeley, Fall 2000.

[8] B.B. Neganov and V.N. Trofimov. *JETP Letters*, 28:328, 1978.

[9] P.N. Luke. *Journal of Applied Physics*, 64:6858, 1988.

[10] T. Shutt et al. In *Proceedings of the Seventh International Workshop on Low Temperature Detectors*, 1997.

[11] T. Shutt et al. *Nucl. Instrum. Methods Phys. Res., Sect A*, 444:340, 2000.

[12] P.D. Barnes. PhD thesis, The University of California at Berkeley, 1996.

[13] W.K. Stockwell. PhD thesis, The University of California at Berkeley, 1996.

[14] D.S. Akerib et al. *Nucl. Instr. Meth. Phys. Res., Sect. A*, 400:181, 1997.

[15] Dennis Seitz. Private communication.

[16] The Cryogenic Dark Matter Search Collaboaration. Proposal for a Second Generation Experiment to Search For Cold Dark Matter: CDMS II. February 1997.

Chapter 3

Monte Carlo Tools and Their Use in Interpreting Calibration Data

Over six million particle interactions were recorded in CDMS detectors during Run 19. I will argue that all these events are consistent with backgrounds, not WIMPs. Crucial to such an argument is the study and understanding of backgrounds. This process begins with the identification of likely background mechanisms and good models for the types of particle produced, the rate, spectrum, originating positions, and directions of these particles. To obtain the effect of these backgrounds on detectors, one must consider the probability and characteristics of all possible interactions in detectors and the experimental setup. In the presence of complex geometries and backgrounds, it is best to to use Monte Carlo techniques for the transport of particles. These techniques have been used extensively in CDMS. I will first discuss these Monte Carlo techniques and the tools developed for their effective use. With this machinery in hand, we will examine several "calibration" data sets that have helped assess detector performance as well as the reliability of the Monte Carlos themselves.

3.1 The Need for Detailed Monte Carlo Simulations

The uses of Monte Carlos in CDMS can be divided into several broad categories.

1. Identifying dominant backgrounds.

   When data indicates the presence of a background, various hypotheses about the cause can be tested with Monte Carlos. These tests lead to the elimination of unimportant processes and eventual identification of the dominant background.

2. Testing the effectiveness of different shielding schemes.

   Monte Carlos have been useful in designing and planning improvements to the CDMS I shield and in the design of the CDMS II shield.

3. Subtracting backgrounds

   The final analysis of Run 19 data involves the subtraction of a neutron background based on the data and predictions of Monte Carlos.

4. Verifying that detector behavior is well understood.

   For instance, in a calibration run, agreement between the detected spectrum and Monte Carlo prediction indicates energy response linearity of the detector. Other instances will follow.

5. Estimating cut efficiencies in data analysis.

   Knowing the probability of a particular type of event (eg. events that occur under the inner charge electrode) from a Monte Carlo allows us to estimate the efficiency of a cut that selects those events.

3.2 Monte Carlo transport code used in CDMS

The GEANT [1] Monte Carlo particle-transport code has been used extensively in CDMS. The MICAP [2], FLUKA [3], and GHEISHA [4] packages that are included with GEANT have been used to simulate hadronic interactions. Use of "standalone" FLUKA [3] (independent of GEANT), is described in Chapter 5. It is used to simulate the production of hadron showers from high-energy muon interactions in rock.

First, the geometry of the the experimental setup must be specified in the GEANT framework. Next, the user specifies the initial positions and 3-momenta of the particles to be propagated. During transport, GEANT makes use of elemental tabulated cross-sections and kinematics derived from theory or measured in experiments. It is the use of this vast knowledge base that makes Monte Carlo transport codes like GEANT and FLUKA so powerful. During transport, the user can collect information about processes of interest.

GEANT offers two options for the transport of neutrons. The use of GEANT-GHEISHA for neutrons of all energies or the use of FLUKA + MICAP. If the latter is chosen, neutrons with kinetic energies above 20 MeV are propagated using GEANT-FLUKA while neutrons of lower energy are handled by GEANT-MICAP. In the past, CDMS simulations were done with GEANT-GHEISHA [5]. Since most of these Monte Carlos are designed for use with accelerator experiments, transport algorithms are not very accurate at low energy. Therefore, special modifications were made to the GHEISHA code for accurate handling of low energy neutrons [5]. However, the accurate handling of low energy neutrons is incorporated directly in the MICAP package. Therefore, all the simulations presented here were carried out using GEANT-FLUKA above 20 MeV and

GEANT-MICAP below 20 MeV. A further discussion of Monte Carlo transport codes used in CDMS can be found in [5].

3.2.1 Specialized tools for GEANT in CDMS Simulations

For the sake of clarity, I will adhere strictly to the following definitions of the words event, scatter, and hit. An event includes all processes that take place between successive "throws" of user specified primary particles. Production and interaction of secondaries as well as multiple interactions of the same particle are therefore included in this definition. The words scatter and hit refer to individual interactions of particles. These definitions will apply in general throughout this dissertation. In later sections and chapters, I will use the term "detector hit" to include all interactions occurring in one detector.

We are often interested in occasions when an external particle penetrates the shield. These instances are rare due to the effectiveness of the CDMS I shield. Because they are rare, the Monte Carlo may require a forbiddingly-long CPU time to generate acceptable statistics on such events. We have used "cloning" (also known as "splitting") as a way around this problem. In this method, the positions and 3-momenta of particles that reach a certain stage in the shield (cloning boundary) are saved. In a subsequent iteration, the Monte Carlo cycles through these saved "vertices" many times, using them as the starting conditions for new events. If the distribution of particles reaching the cloning boundary are sampled well, and if different random seeds are used with the same parent vertex over different iterations, reasonable results can be expected.

In situations where the shield is very effective for the population of particles considered, it is possible to do this in several steps. However, a significant amount of shielding must be present between successive cloning

boundaries. Otherwise, the use of different random seeds will not have an effect due to the lack of interactions, and thus, the secondary vertices resulting from the same parent vertex will be similar if not exactly the same. In addition, the last cloning boundary should not be placed very close to the detector unless the interaction probability (in the detectors) of the particles considered is very small. Otherwise, all interactions from the same parent vertex will yield similar positions of interaction. This is the case for electrons which usually have very small penetration depths in detectors. When good statistics are available for particles reaching a particular cloning boundary, correlated histograms of position and momentum can be used as starting distributions for the next iteration of the Monte Carlo instead of using the saved vertices. Cloning was not used in most of the simulations presented here. The places where it was used will be mentioned explicitly.

"Clumping" is another specialized tool used in CDMS simulations. In simulations involving photon and electron transport, energy is deposited in detectors through electron tracks. GEANT and other Monte Carlo packages approximate these continuous tracks as a large collection of discrete points. Since CDMS detectors have some position sensitivity (even BLIPs use the segmented electrode structure for coarse position sensitivity), which is useful for the study of backgrounds, it is important to obtain position information from the Monte Carlo. Therefore, the Monte Carlo is programmed to output the position and energy of each scatter during an event. However, in the case of electron tracks, it is cumbersome to save information about each of the large number of discrete points. Therefore, for electrons, we have devised a way of grouping energy deposition in "clumps" (see figure 3.1).

A clump is initiated by either an interaction of any particle other

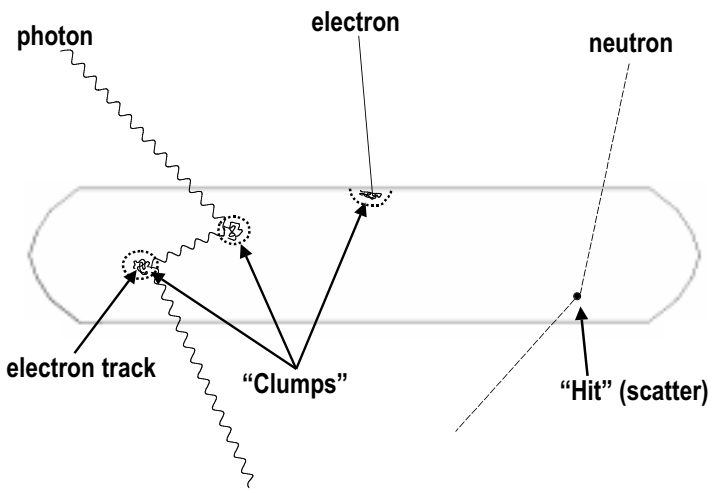

Figure 3.1: Schematic depicting the definition of "clumps". The grey outline represents the detector. Note that electrons incident on the detector initiate clumps while internal electron tracks do not. Clumps and individual hits of particles (eg. neutrons) are treated on the same footing.

than an electron or by the interaction of an electron incident on a detector. Electron tracks that result from a clump-initiating interaction belong to that clump. Other secondary electron tracks induced by parent electron tracks also belong to the same clump. Any non-electrons that results from this interaction or subsequent electron transport will initiate a separate clump if it interacts in a detector. An electron is allowed to initiate a clump only when it is incident on a detector (i.e. the track did not start within the detector). For instance, electrons from electron sources will initiate clumps. Accordingly, electron tracks belonging to a certain clump can also cause new clumps if they exit the present detector and interact in another. In summary, only electrons incident from outside the detector, and non-electrons initiate clumps.

Note that these conditions allow for overlapping clumps in the same event. The position of the clump is defined to be the mean values of x,y, and z, weighted by the energy deposited at each point. The size of a clump is taken to be the distance from the clump position (energy centroid) to the furthest point where an associated electron track deposited energy. Average clump size versus deposited energy are shown in figure 3.2. Above 100 keV, the shapes of these curves are identical to the shapes of electron range versus energy in these materials as given in [6]. The numbers are different by a constant multiplicative factor (4.7 for Ge and 3.3 for Si) because the range is defined as the total length of a track. At lower energy the clump size does not decrease as much as the range taken from [6]. This disagreement may be due to inaccuracies in GEANT electron transport at energies below 100 keV [7].

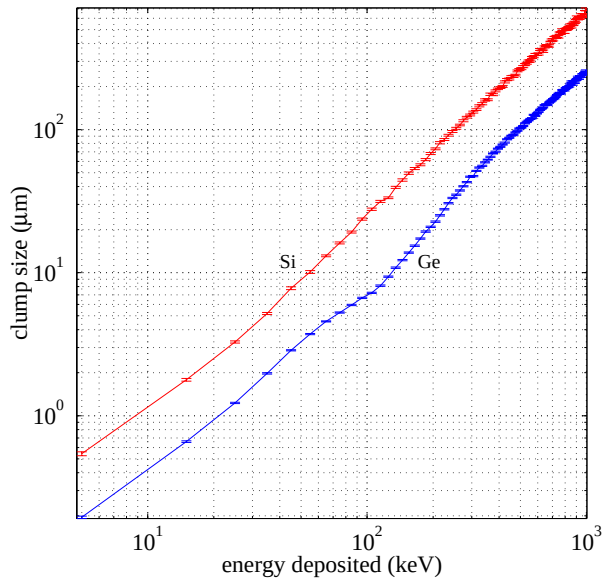

Figure 3.2: Average clump size vs. energy deposited for Ge and Si. This gives the typical spread of an electron recoil event in detectors as a function of energy. However, below 100 keV the size seems to be overestimated by GEANT [6, 7].

3.3 Geometry Definition for Monte Carlos

For the most part, the geometry definition included in GEANT simulations accurately reflects the true geometry. Certain details like rounded edges are sometimes omitted. Hexagonal cross sections are usually approximated with circular shapes. However, the total volume of a region is usually accurate. Detectors and nearby regions are defined more accurately. Figure 3.3 depicts the geometry definition used in Run 19 simulations. Note that the curved edges of the BLIP detectors, their copper housings and the passive Ge shielding are represented accurately. However, the tower and side coaxes were not included in these Monte Carlos. These approximations are reasonable when considering gamma and neutron backgrounds originating far away from detectors, as is the case for the simulations presented here. On the other hand, a more accurate nearby geometry must

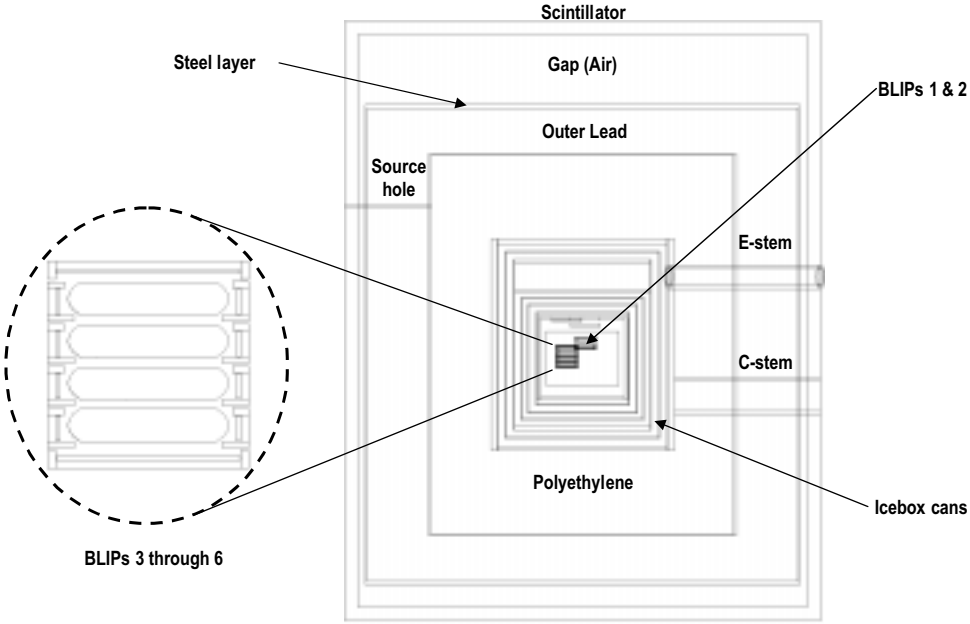

Figure 3.3: Geometry definition used in Run 19 simulations.

be used when considering low-energy localized sources of background close to the detectors.

3.4 Output of the Monte Carlo

If any energy is deposited in detectors during an event, some information is saved to a file at the end of the event. This output is called an "ntuple". A detailed description of the output can be found in Appendix A. We mention here the most commonly used quantities output by the Monte Carlo. For each saved event, the identity, energy, and position of the primary particle are saved. For all detectors present, the total nuclear recoil energy (neutron scatters only) and electron recoil energy (all other particles) are saved on an event by event basis. Several hit-by-hit quantities are also saved. A hit is defined as one scatter of a particle inside a detector, or a whole clump when transporting electrons. For each hit, the identity, energy , and direction of the incident particle are saved. The position, energy deposited, and the type of interaction (nuclear/electron recoil) of each hit are also recorded.

3.5 Neutron Calibration

3.5.1 Introduction

Every CDMS data run, detector response is calibrated using a ^{252}Cf neutron source. In addition to the daily gamma energy calibrations, neutron events provide information about nuclear recoils, where a WIMP signal would lie. We gain confidence in GEANT-FLUKA and GEANT-MICAP neutron Monte Carlos by testing predictions against the neutron calibration data. Once performance is established, information from the Monte Carlo is used in data analysis. The "neutron subtraction" described in Chapter 4 is a prime example. Establishing trust in the accuracy of simulations is essential

for this. Besides providing a test of the neutron transport code, the neutron calibration Monte Carlo is useful for understanding and interpreting data from the calibration. For instance, given the cuts in use, the fiducial volume for WIMPs is obtained from the Monte Carlo as explained below.

3.5.2 Setup for Simulation

Both alpha decay and spontaneous fission are present in ^{252}Cf . On average, four neutrons are emitted in each spontaneous fission event. The 3.1% fission fraction combined with the neutron multiplicity yields 0.116 neutrons-per-decay when all decays (including alpha decays) are taken into account [8]. In the simulation, each neutron is treated separately and can give rise to a separate event. Inaccuracies like underestimating the number of multiple-scatters can result, if in reality, two or more neutrons from the same fission event contribute to detector hits. However, this effect should be negligible because individual neutrons have low interaction probabilities: According to the Monte Carlo only one out of 14 000 neutrons cause detector hits. The half-life of the source is 2.65 years. Of the many fission products, only neutrons and gammas escape the encapsulation of the source. The neutron spectrum can be approximated by the expression [8]

$$\frac{dN}{dE} = \sqrt{E}e^{-E/1.3MeV}. \tag{3.1}$$

Only the primary neutrons and their secondaries are transported in the simulation. Therefore, only events in the data containing neutrons should be compared with the Monte Carlo output. The source is placed almost vertically above the detector volume on top of the scintillator (see figure 3.3). Layers of polyethylene are removed down to the top surface of the icebox cans in order to increase the rate to 3-4 Hz, a good rate given the pulse duration and trace download time. The odds of detecting a neutron

and a photon from the same decay are negligible due to the lead's effectiveness in shielding gammas. In this configuration, a 5 MeV photon emitted in the direction of the detectors will produce a detector hit less than 4.8×10^{-8} of the time for 1 kg of Ge. Therefore, "gamma–neutron multiples" of this type can be ignored in the calibration data sets, which contain fewer than 100 000 events.

According to the Monte Carlo, over half the detector hits due to the neutron source are accompanied by various interactions in the scintillator. Neutron scatters comprise most of these. Ten percent of neutron interactions in the scintillator deposit energies in excess of 2 MeV. Therefore, in the interest of keeping as many events as possible, the muon veto is usually not applied when analyzing neutron calibration data (it *is* applied in the analysis for estimating fiducial volumes, as described below). This introduces the possibility of muon coincident backgrounds contaminating the data set. However, restricting the analysis to events with at least one nuclear recoil removes most of the contamination. When the top polyethylene is removed, although the resulting veto-coincident neutron rate of 15±3 per hour is about 20 times its usual value, it is still insignificant compared to the event rate due to the source. The neutron rate from the source is about 9 000 per hour. Misidentification of muon related backgrounds as multiple scatter partners of neutron events is also a possibility. Since most muon induced events are high energy gammas ($>$ 100 keV), these will appear as gamma–neutron multiple scatters. Given the 350 μsec window for accepting multiple scatters, and taking 3 Hz and 1 Hz as the neutron and muon coincident rates respectively, the probability of an accidental multiple scatter is roughly 0.001, much smaller than the fraction of actual multiple scatters.

Two neutron calibrations were carried out during Run 19. Only the

top polyethylene, as described above, was removed in the the first neutron calibration performed in early April of 1999. A further 1 cm of polyethylene was removed in the September neutron calibration. Thus, two separate geometries and Monte Carlos were used to simulate these neutron calibrations. The change in source rate due to the time elapsed between the two data sets is taken into account when calculating expected event rates. Each neutron calibration lasted about half a day.

The experiment should not be exposed to the neutron source for long periods of time because of the resulting activation of detectors and cryostat copper. For instance, according to the Monte Carlo, a one-hour exposure to a 14 μCi ^{252}Cf source increases the ^{60}Co rate in the icebox copper by 5×10^{-9} Bq/kg. This increase is about 0.004% of the equilibrium activity at the earth's surface from cosmic-ray induced spallation. Therefore, the veto-anticoincident gamma rate in detectors will not increase by more than this fraction due to one hour of exposure to the neutron source. The geometry of the first neutron calibration is used in the above estimate. The rate increase is given for the OVC lid of the icebox.

3.5.3 Results

I will first cover estimation of fiducial volumes, which is a useful application of the neutron calibration Monte Carlo. This will be followed by comparisons of Monte Carlo predictions to data. Finally, some interesting effects seen in the Monte Carlo and the data will be discussed.

Estimating Fiducial Volumes

Charge yield and resolution are poor for events contained under the outer electrodes of detectors. Evidence of this and possible reasons are provided in [9] and [10]. A brief description can be found here in Chapter 4. Because accurate charge measurement is essential for correctly identifying nuclear

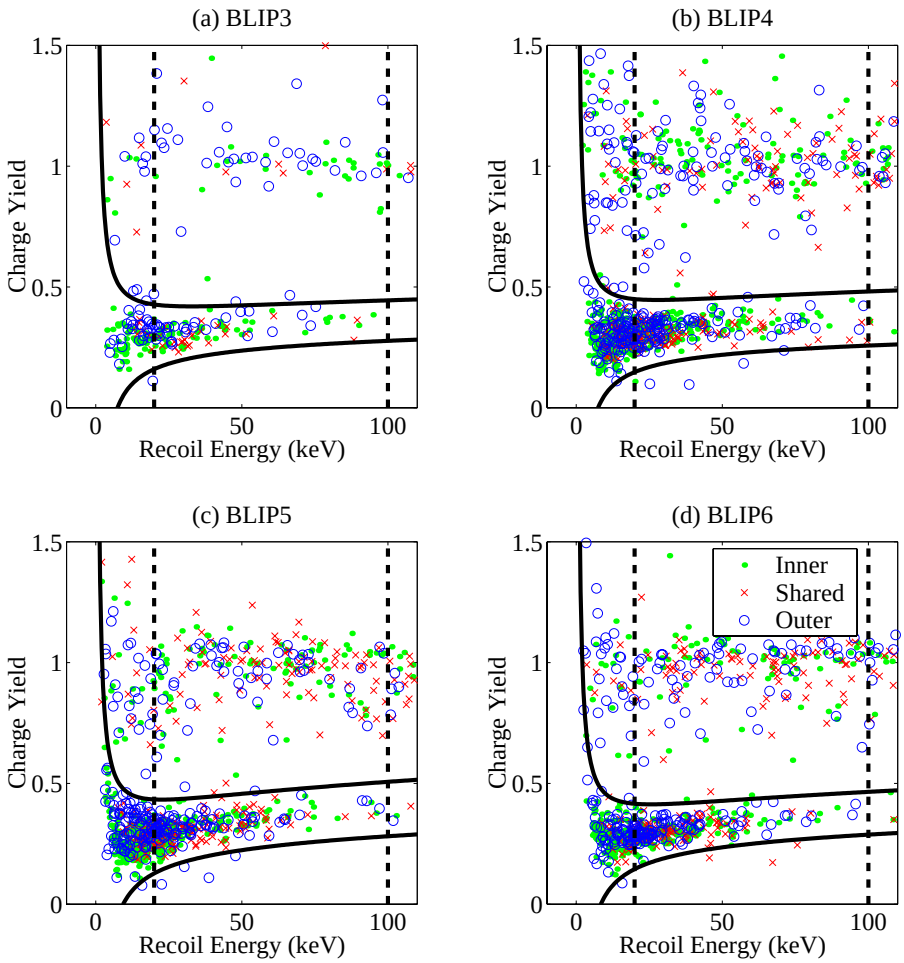

Figure 3.4: Charge Yield versus Recoil energy in the first neutron calibration for events passing cuts used in the fiducial volume estimate. The legend in (d) applies to all four plots. Solid lines indicate the boundaries of the nuclear-recoil cut. Only events in the energy range indicated by dashed lines (20-100 keV) were used in the calculation to ensure an almost 100% efficiency for the shown nuclear-recoil cut. Note that BLIP3 has poor statistics because its charge bias was *off* during most of the first neutron calibration.

recoils, such "outer" events are excluded from the final data analysis. For the WIMP limits set in [9, 11], only events with a charge signal in the inner electrode alone were included. The final analysis of Run 19 data presented in [10] uses all but the events with charge only in the outer electrode. These two data sets are different because some events have charge in both electrodes. Such events are not included in the former data set but are present in the latter. To estimate our exposure to WIMPs in kg days, the fiducial volumes selected out by these cuts must be calculated. It is best to use nuclear recoil data for this purpose. The neutron calibration is the only such data set with sufficient statistics.

Events with charge in both electrodes are due to the charge drift patterns at work near the gap in the electrodes as well multiple scatters that span both electrodes. The Monte Carlo can be used to estimate the contribution from the latter. The fraction of neutrons that scatter close enough to the electrode gap to result in charge sharing can be estimated from this information. This fraction, together with the inner and outer fractions, is sufficient to find the regions of the detector that result in inner, shared, and outer events. Since WIMP multiple scatters are negligible, the volumes of these regions are the fiducial volumes of the inner, shared, and outer cuts.

If neutrons incident on detectors have large interaction lengths compared to detector dimensions, uniform "illumination" of detectors will result. In this case, the fraction of neutrons with inner, shared, and outer charge can be trivially used to estimate the volumes of the three regions, as outlined above. However, interacting neutrons in this data set have energies of the order 1-2 MeV (according to the simulation) and interaction lengths of order 6 cm, comparable to the detector diameter. Therefore, the density of events will not be completely uniform within a detector. However,

position information from the Monte Carlo can be used to carry out the calculation.

Figure 3.4 shows the charge yield versus recoil energy from the first neutron calibration for all detectors. Events in these plots, which are used in the analysis described below, are required to pass all data-quality cuts [9, 10]. In this case, the veto-anticoincidence cut is also applied because the charge-yield distribution of veto-coincident events is less well resolved, presumably due to muon-induced electron events which suffer from poor charge collection (see below). These events are also required to pass the inner, outer, or charge-share cut. In figure 3.4 these three types are indicated separately. The only non-pathological events excluded by this requirement will have energies lower than a few keV. This is not a problem since only events with recoil energy in the range 20-100 keV (dashed lines in figure 3.4) are used in what follows. The solid lines define the borders of the nuclear-recoil cut used to select neutrons. It is based on the *charge sum* and recoil energy. To correctly estimate the inner, shared, and outer neutron fractions, neutrons from all three regions should have equal nuclear recoil cut efficiencies. In other words, they should have an equal probability of being identified as neutrons, and therefore an equal probability of being included in this analysis. Since this may not be true for the usual 90% acceptance-charge-sum cut [9], a less restrictive cut is used here[1]. By inspection, it is clear this cut is nearly 100% efficient for all three types of events. Misidentification of electron recoils is a small effect due to the fair charge-yield separation of the nuclear recoil band.

For neutrons passing the above cuts, the inner, shared, and outer fractions from data are given in the first row of table 3.1. Using the mean

[1]The 90% acceptance specification for of the usual cut applies when *all* nuclear recoils are considered together. The acceptance is different from 90% when inner, shared, and outer events are considered separately.

	BLIP3	BLIP4	BLIP5	BLIP6
Data fractions $\times$ 1000	505:178:318	451:232:317	477:227:296	490:185:325
MC fractions $\times$ 1000	517:091:391	519:090:391	518:094:387	526:086:389
Adjusted fractions $\times$ 1000	555:095:350	495:156:349	526:147:327	536:109:355
Inner R (cm)	$2.10 \pm 0.16^{+0.02}_{-0.01}$	$1.96 \pm 0.09^{+0.06}_{-0.02}$	$2.02 \pm 0.08^{+0.05}_{-0.02}$	$2.04 \pm 0.09^{+0.04}_{-0.01}$
Outer R (cm)	$2.31 \pm 0.12^{+0.02}_{-0.04}$	$2.31 \pm 0.06^{+0.03}_{-0.03}$	$2.34 \pm 0.06^{+0.03}_{-0.04}$	$2.29 \pm 0.07^{+0.03}_{-0.03}$
Mean inner radius = 2.015 $\pm$ 0.040 cm				
Mean outer radius = 2.311 $\pm$ 0.020 cm				

Table 3.1: Results of fiducial volume calculation. The first three rows contain the inner, shared, and outer events (separated by colons) in each detector for the indicated categories. Rows 4 and 5 contain the radii infered from the above numbers. Rows 6 and 7 give the best-fit radii for the inner and inner+shared fiducial volumes. A full description is given in the text.

charge for nuclear recoils as a function of recoil energy, obtained from the data, the charge energy under each electrode is calculated for Monte Carlo events. The second row of table 3.1 is obtained by applying the same inner, shared, and outer cut definitions used in the data, to the charge generated for Monte Carlo events. Note that the shared fraction from the Monte Carlo is smaller than that from the data because internal-multiple scatters are the only mechanism through which a Monte Carlo event enters this category. As mentioned above, charge sharing between the electrodes for events close to the gap also contribute to the shared fraction in detectors. The shared fraction from the simulation is then subtracted from the shared fraction seen in the data. The inner fraction, the residual shared fraction, and the outer fraction are given in the third row after normalizing to make the sum of these equal to unity. The shared fractions in this row represent the contribution due only to charge drift patterns near the electrode gap. The radii that yield these fractions for Monte Carlo events with scatters under only one electrode are shown in the fourth and fifth rows. The integral distribution of radius for the typical case of BLIP5 is shown in figure 3.5. Since all detectors have the exact same design, and since the same electric field was applied in all of them, we expect these numbers to be the same for all detectors. The values and uncertainties given in rows 4 and 5 show that the results are consistent with this expectation. Therefore, the statistics-weighted mean radii given at the bottom of table 3.1 are used for all detectors in the Run 19 data. A similar analysis of data from the second neutron calibration shows a higher but statistically consistent variance of results between detectors. As expected, the mean radii are in excellent agreement with those in table 3.1. Note that the true radius of the electrode gap is 2.133 cm.

The first uncertainty quoted next to radii in rows 4 and 5 as well as

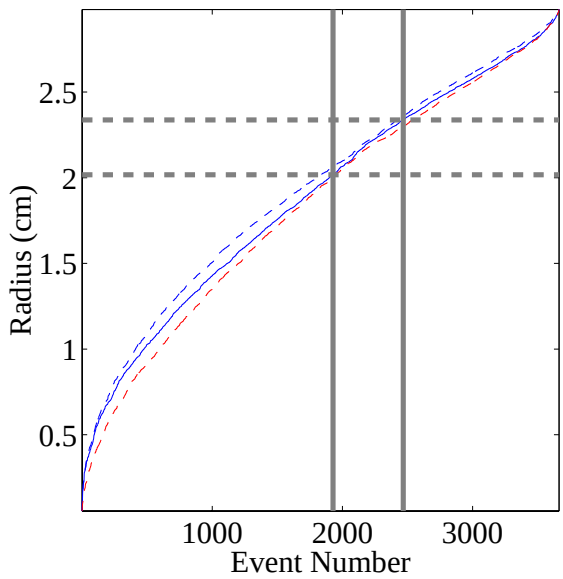

Figure 3.5: Radii of BLIP5 inner and outer contained events from Monte Carlo. Event numbers are ordered according to radius. Solid vertical lines correspond to adjusted inner, shared and outer fractions. The horizontal dashed lines are the corresponding radii given in table 3.1.

the only uncertainties given for the average values in rows 6 and 7 are statistical. Because it has lower statistics than other detectors (as evident in figure 3.4), results from BLIP3 have larger statistical uncertainties. BLIP3 has low statistics because it was "Off" during a large part of the first neutron calibration. The second set of uncertainties appearing in rows 4 and 5 are upper limits on the error inherent in the method used to determine the fiducial volumes. The method described above would be perfect if no internal multiple scatters are present after removing events that scatter under both electrodes. However, since this is not the case, the *average* radii of Monte Carlo internal multiple scatters are used when calculating the radii given in table 3.1. An upper limit on this error can be estimated by calculating the radii that would result if the minimum or maximum radius in an internal multiple scatter is used instead. The second set of uncertainties in table 3.1 correspond to these radii. A further

iteration of the above method, taking into account internal multiple scatters, will not improve on the above estimates because statistical uncertainties are comparable to these upper limits on systematic error. The lower and upper dashed curves in figure 3.5 represent the integral distributions of radii if the minimum and maximum radii respectively are used for internal multiple scatters.

Comparison of Data and Monte Carlo

After obtaining the correct volumes of the "inner" and "all but outer" fiducial volumes, the Monte Carlo results can be compared with data passing the inner and shared cuts. The purpose of this comparison is to test the reliability of the Monte Carlo and verify that cut efficiencies and live-times in the data are well understood. The crucial comparison is between neutrons seen in the data and neutrons predicted by the Monte Carlo. Since the final analysis of CDMS data involves only nuclear recoils, other predictions like the neutron-photon multiple-scatter rate are not as important. I will briefly mention some of these secondary features in the following section.

Comparisons of neutron rate, energy spectrum, and fraction of multiple-scatters are given below on a detector-by-detector basis for both neutron calibrations. Spectra and ratios averaged over detectors are also given for both calibrations.

As mentioned earlier, the Monte Carlo output contains information on deposited energy, positions of hits, and the type of particle involved in each scatter. Several efficiency corrections must be performed on this output before it can be compared with data. A detailed calculation is needed especially for correctly estimating the rate of multiple-scatters predicted by the Monte Carlo. For instance, given a *true* neutron multiple scatter in BLIP4 and BLIP5, there are non-zero probabilities for that event

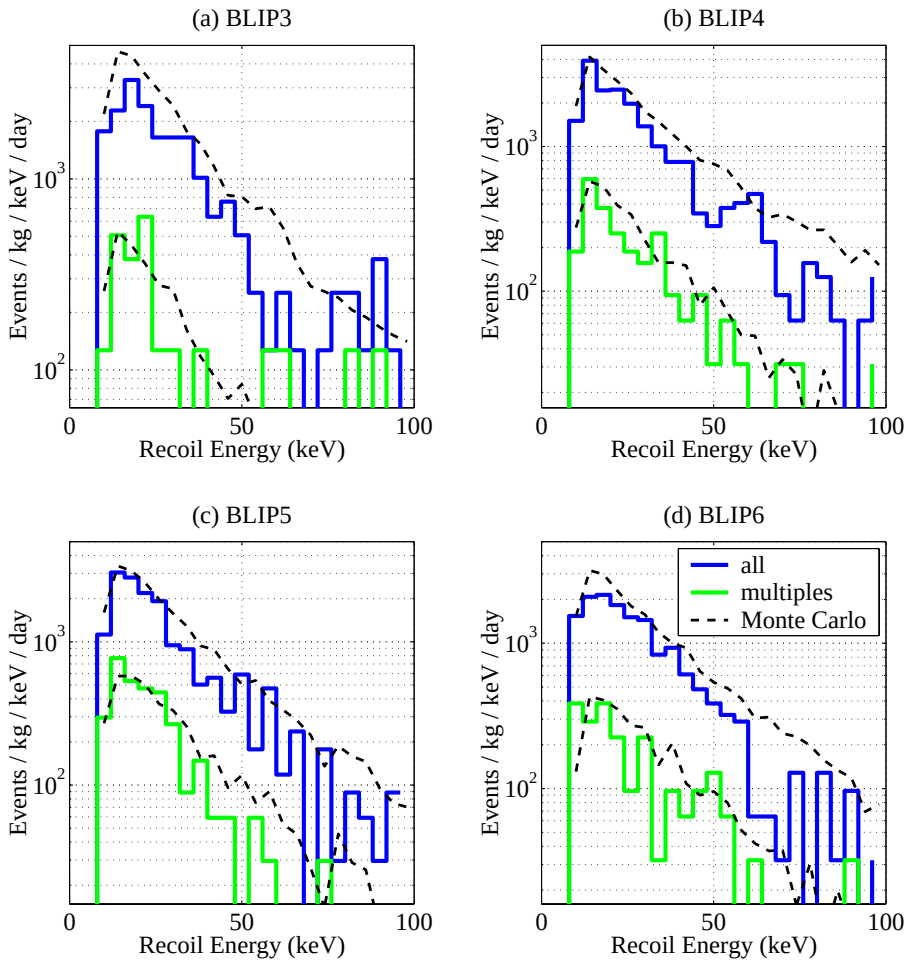

Figure 3.6: Detector-by-detector comparison of data and Monte Carlo spectra for the first neutron calibration. Solid lines represent data while the dashed lines represent the Monte Carlo. "All" stands for every neutron scatter in a particular detector including hits associated with multiple-scatter events. Multiple-scatters shown here belong to events with at least one nuclear recoil passing the inner or shared cut. Note that BLIP3 has poor statistics because it was *off* during most of the first neutron calibration.

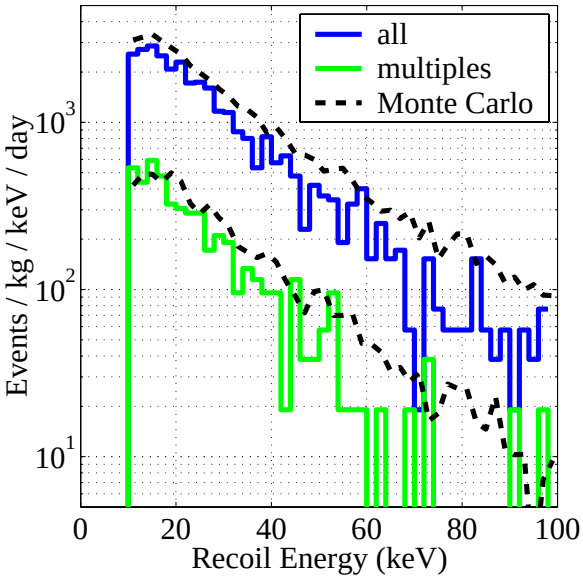

Figure 3.7: Comparison of summed spectra from the first neutron calibration.

appearing in the data as a multiple-scatter, a BLIP4-only event, a BLIP5-only event, or not appearing in the data at all. The probability of this event appearing as a multiple scatter is not unity because in both detectors it must pass a sequence of cuts whose efficiencies are less than 100%. This event has a probability for appearing as a single scatter in either BLIP4 or BLIP5 if during some periods, only one of the these detectors was *on*. Passing all cuts in one detector and failing cuts in the other will also give the same result. Failing cuts in both detectors can result in not seeing this neutron in the data at all. Using knowledge of cut efficiencies in each detector and the fractions of time that each particular detector combination was *on*, the probability of all possible outcomes is calculated for each Monte Carlo event. The data and code needed for this calculation was put together by Richard Schnee and Sunil Golwala. A discussion of the method can be found in [12].

In figures 3.6-3.9, I show comparisons of data and Monte Carlo for events passing the inner or shared cut. As explained before, this is the less

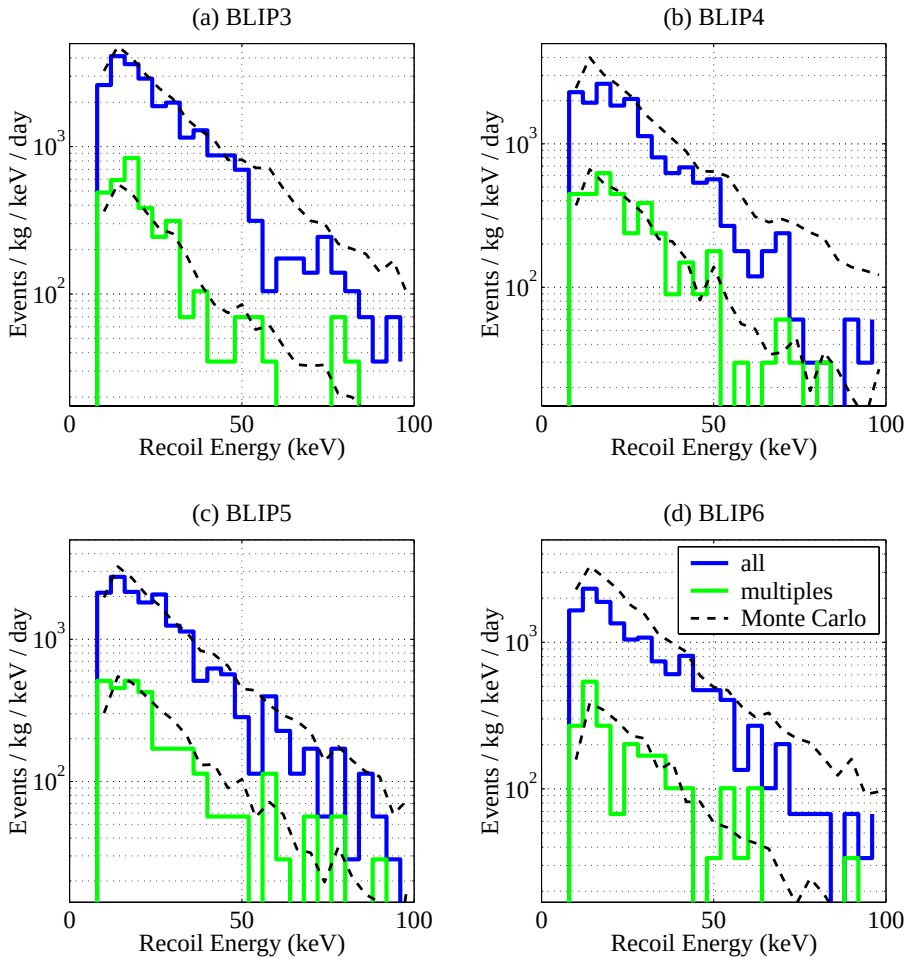

Figure 3.8: Detector-by-detector comparison of data and Monte Carlo spectra for the second neutron calibration.

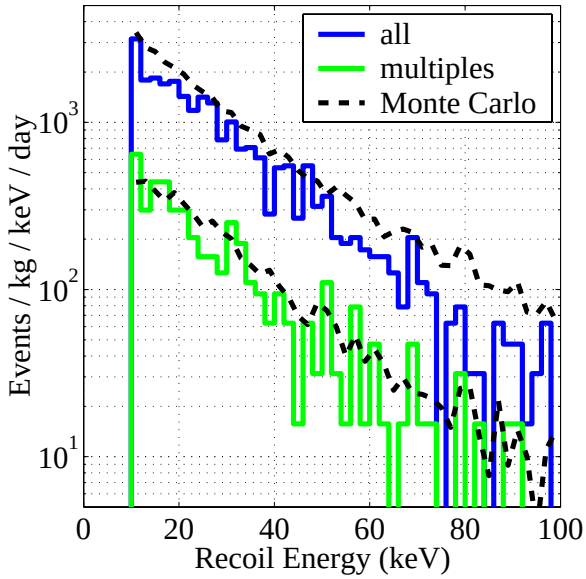

Figure 3.9: Comparison of summed spectra from the second neutron calibration.

restrictive cut that includes hits in the inner and shared fiducial volumes, as well as "internal" multiple-scatters which deposit energy under both electrodes. In each of these plots, the solid lines correspond to the data. Dashed lines correspond to Monte Carlo predictions. The higher-rate spectrum in each case is obtained from all neutron scatters in detectors. The multiple-scatter spectra are also displayed. Two types of multiple-scatter are defined. The lower-rate spectra in each plot correspond to events with a neutron passing the inner or shared cut in at least one detector. The other nuclear recoil(s) is not required to pass either of these cuts. The second multiple-scatter definition requires all hits to pass the inner or shared cut. To avoid clutter, the latter class of multiple-scatters is not shown on the plots. However, the rate of these multiple-scatters are given in table 3.2. Defining two types of multiples-scatter allows one to further test the understanding of fiducial volume cuts and the overall performance of the Monte Carlo.

Figure 3.6 shows spectra in each detector from the first neutron calibration. Figure 3.7 shows the same spectra averaged over detectors. Figures 3.8,3.9 are the corresponding plots for the second neutron calibration. Only the 10-100 keV energy range is shown. This is the important region to understand since the CDMS I WIMP sensitivity calculations only use data in this range. Table 3.2 gives numbers for neutrons in the 10-100 keV range. The first row has Monte Carlo rates after efficiency corrections. The second row has corresponding rates from the data. Only statistical uncertainties from the data are included because low statistics in the data dominate the uncertainty in the comparison. The rates in the first two rows include single-scatters and multiple-scatters. Each hit from a multiple-scatter is counted. The third row has the predicted ratio of the first type of multiple-scatter to all hits. The corresponding ratio and statistical uncertainty from the data is in the fourth row. The fifth and sixth rows contain the same information about the second type of multiple-scatter.

The plots indicate that the Monte Carlo predicts the spectra with reasonable accuracy. A small deviation between data and Monte Carlo spectra is seen at energies above 60 keV. The discrepancy between absolute rates given in table 3.2 is more significant. The source of this discrepancy is not yet understood. However, the multiple-scatters to single-scatters ratio is well predicted by the Monte Carlo.

3.5.4 Interesting Features in the Neutron Calibration Data and Monte Carlo

Hydrogen-Capture Gammas

In both neutron calibrations, about 4% of neutrons seen in the 10-100 keV range in one detector are associated with a gamma scatter, typically above 100 keV, in another detector. The Monte Carlo predicts this rate to be less

	First Calibration	Second Calibration
Efficiency corrected MC hit rate (hits/kg/day)	9.70×10^4	9.62×10^4
Data hit rate (hits/kg/day)	$(6.5 \pm 0.2) \times 10^4$	$(7.2 \pm 0.2) \times 10^4$
MC multiples fraction 1	0.150	0.156
Data multiples fraction 1	0.157 ± 0.009	0.185 ± 0.010
MC multiples fraction 2	0.098	0.102
Data multiples fraction 2	0.104 ± 0.008	0.106 ± 0.008

Table 3.2: Comparison of data and Monte Carlo for neutron calibrations. In the first multiple-scatter fraction, only one hit is required to pass the inner or shared cut. The second multiple-scatter fraction refers to events in which two or more hits passed the inner or shared cut. Note that rates and fractions are in terms of hits. i.e. each hit in a multiple-scatter is counted.

than 0.5%. The deficiency of such events in the Monte Carlo is probably due to the 10 keV cut-off energy for neutron propagation. While this cut-off is more than sufficient to simulate all detectable neutron scatters in detectors, effects arising from thermal neutron interactions are not treated by the Monte Carlo. The neutron propagation threshold is applied in the Monte Carlo to save CPU time. Thermal neutron capture by ^{1}H atoms in the polyethylene results in the formation of ^{2}H nuclei which relax to the ground state by emitting a photon with the binding energy of the two nucleons. Most of the electron recoils seen in coincidence with neutrons are probably due to Compton scattering of these 2.2 MeV photons. Typical neutron capture times of about 150 μsec have been observed [5]. Capture gammas appear as multiple-scatters due to the 300 μsec window used to identify multiple-scatters. Since high-energy photons coming from the

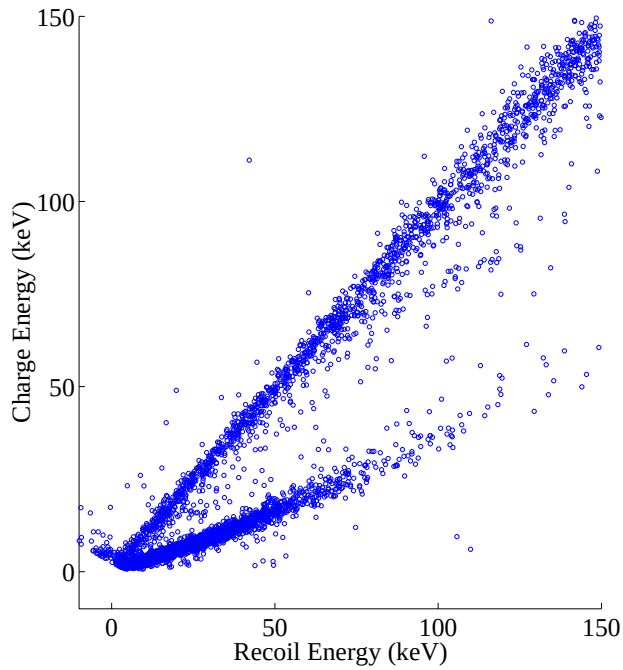

Figure 3.10: Charge versus recoil energy from the second neutron calibration. Includes data from BLIP3 through BLIP6.

polyethylene will scatter in each detector with roughly equal probabilities, about 1.3% of 10-100 keV neutrons are expected be followed by a high-energy-gamma scatter in the same detector. These events will fail either the post-trigger pile-up and shape (χ^2) cuts or the the nuclear recoil cuts. The resulting decrease in efficiency for neutron detection is small (1.3%) and therefore not incorporated into the data-to-Monte Carlo comparisons given above. Details of the multiple-scatter-acceptance window and post-trigger pile-up and shape cuts are given in Chapter 4.

Features in Data Due to ^{73}Ge Nuclear Excitations

Nuclear excitations followed by gamma emission can lead to other types of gamma-neutron events. These events are of interest because they provide additional insights into background issues, detector behavior, and the

performance of Monte Carlos. These features were first noticed and explained by Rick Gaitskell [13] and Andrew Sonnenschein [14] during Run 18.

I will first present evidence for these events in the data. Figure 3.10 is a plot of ionization energy versus recoil energy in all detectors for the second neutron calibration. The electron and nuclear recoil bands are clear. The dark (upper) curve of figure 3.11 is a recoil-energy histogram of events in the electron-recoil band.

One feature I will discuss below is the peak in this histogram around 65-70 keV. Some points in figure 3.10 between the electron and nuclear recoil bands may be due to simultaneous electron and nuclear recoils in the same detector. Two energy depositions that happen in quick succession compared to the pulse digitization sampling time will appear to be simultaneous in the data. Assuming that all points with intermediate charge yield are due to gamma-neutron coincidences, these points can be projected along loci parallel to the nuclear recoil band to find the associated electron-recoil energy. The lighter (lower) curve in figure 3.11 is a histogram of the electron recoil energy computed for these events. There appear to be at least two definite gamma energies associated with such events: one at around 13 keV and the other between 65-70 keV. The feature between 65-70 keV can also be seen in figure 3.10 as a locus of points parallel to the nuclear recoil band, which intersects the electron-recoil band between 65-70 keV. Of course, not all events between the electron and nuclear recoil bands are due to mixed gamma-neutron scatters. Some of them are due to noise in the phonon and charge measurements. Others are due to poor charge collection from electron recoils which occur close to detector surfaces (see Chapter 2). These events appear as a continuous background to the two features seen in the lower histogram of figure 3.11.

The background rates around the two peaks must be subtracted when estimating the rates of these peaks.

The two features in the lower histogram of figure 3.11 and the peak in the upper hitogram are due to nuclear excitations of ^{73}Ge which has a 7.8% abundance in natural germanium. They are related to the first three nuclear excitations in ^{73}Ge at 13.3 keV, 66.7 keV, and 68.8 keV, also shown in figure 3.11. Possible mechanisms for producing these states are

1. **Th72** : Thermal neutron capture on ^{72}Ge, which has a natural abundance of 27.7%. A total of 6.8 MeV is released through gammas in the subsequent de-excitation of the ^{73}Ge nucleus.

2. **In73** : Inelastic neutron scattering off ^{73}Ge which has a natural abundance of 7.8%.

3. **Hi74** : High energy neutron scattering off ^{74}Ge which results in two free neutrons and an excited ^{73}Ge nucleus, usually represented by ^{74}Ge (n,2n)^{73}Ge*. The threshold energy for this interaction is approximately 10.1 MeV.

In what follows, I will refer to these processes by the shortened forms given in this list. The energies, spin-parities and relaxation times of the first three excited states of ^{73}Ge as well as the processes that populate these states are given in table 3.3. Note that the ground state of ^{73}Ge has a spin-parity of $9/2^{+}$. The 66.7 keV state has a long half-life due to the large mismatch between its spin and the spins of the states below. Half-lives of the other two states are also related to their spin-parities relative to the ground state. Note that In73 does not contribute significantly to the 66.7 keV state, again due to the large difference between its spin and that of the ground state.

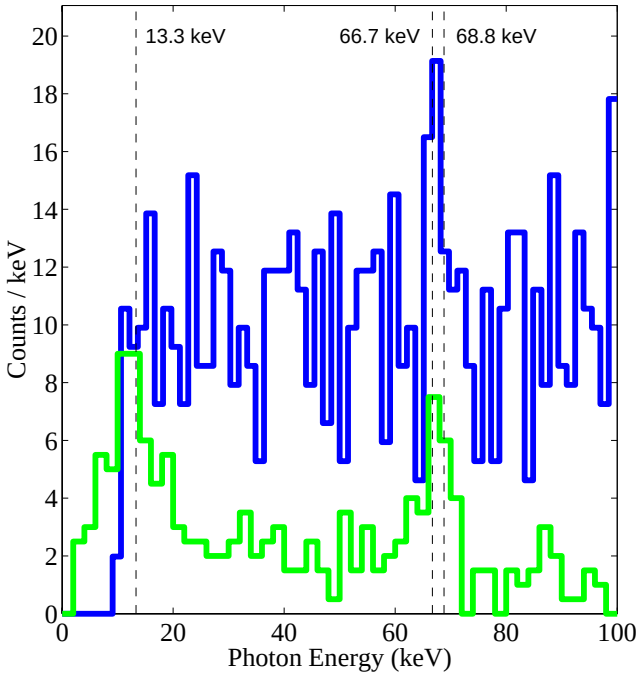

Figure 3.11: Energies of photon scatters in the neutron calibration. The upper histogram is a spectrum of events in the electron recoil band. It is simply a *recoil-energy* histogram for electron recoils, obtained *directly* from figure 3.10. On the other hand, the lower histogram shows to a *computed* energy. It corresponds to the gamma energy contained in mixed gamma-neutron events that appear between the electron and nuclear recoil bands in figure 3.10. For each event in this region, the gamma energy is obtained by finding a curve "parallel" to the nuclear recoil band that goes through that data point. The gamma energy is the recoil energy at which this curve intersects the electron-recoil band. The dashed vertical lines indicate the excitation levels of ^{73}Ge. As explained in the text, the 66.7 keV excitation should be associated with the upper histogram, while the 13.3 keV and 68.8 keV lines are expected for the lower histogram.

Energy of excited state	13.3 keV	66.7 keV	68.8 keV
Spin-parity	$5/2^+$	$1/2^-$	$7/2^+$
Decay	E2 to ground	M2 to $5/2^+$ state (53.4 keV release) then E2 to ground (53.4 keV release)	M1+E2 to ground
Half-life	3 μsec	500 msec then 3μsec	1.7 nsec
Processes	Th72, In73	Th72, In73, Hi74	Th72, In73

Table 3.3: Information on the ^{73}Ge nuclear excitations. The energies given correspond to the total energies of the excited states relative to the ground state. As indicated, the 66.7 keV state decays to the ground state in two steps.

Even though it is listed in table 3.3, Hi74 should be insignificant in neutron calibrations due to the low energy of neutrons from ^{252}Cf (see Eq. 3.1). The possibility of measuring the contribution from this process to estimate the high-energy neutron flux at the detectors during low-background data taking will be discussed below.

Gamma-Neutron Events

I will first discuss the mixed neutron-gamma events seen in the data at gamma energies of about 13 keV and 68 keV. I will argue that the 66.7 keV excitation is not related to these events and that Th72 contributes negligibly to these events. This argument is important for the linear reduction scheme presented in the next section for measuring the high-energy neutron flux. The phonon and charge digitization rates used in Run 19 correspond to 64 μsec and 6.4 μsec respectively. Mixed neutron-gamma events occur due to a neutron and photon scatter in the same detector being integrated as one event in the digitizers. This will occur mainly for the 13.3 keV and 68.8 keV states due to their short decay

times compared to the charge digitization rate. Due to its long decay time, mixed gamma-neutron events associated with the 66.7 keV state are expected to be less than 0.1% of the 66.7-keV-line intensity seen in the upper histogram of figure 3.11. Therefore, essentially all ^{73}Ge-related gamma-neutron *merged* events are due to the 13.3 keV and 68.8 keV excitations; the 66.7 keV events trigger the DAQ as separate events distinct from the associated neutron.

In73 is expected to be the main contributor to these states. Th72 will contribute only if a neutron, after scattering in a detector, is later captured in the same detector as a thermal neutron. For such an event to appear in a neutron-gamma band, the neutron must thermalize in a few microseconds and the 6.8 MeV relaxation must proceed through one of the short-lived states. Furthermore, Th72 can contribute only when none of the other gammas associated with the nuclear relaxation cause energy deposition in the same detector. For these reasons, the contribution from Th72 to neutron-gamma events is expected to be very small, implying that neutron-gamma events are associated with the two short-lived states produced by In73.

The Monte Carlo can be used to check this because In73 is modeled by GEANT-MICAP. In the Monte Carlo, inelastic scatters can be identified by checking if the neutron energy loss is equal to the recoil energy of the nucleus. If the nuclear recoil energy is less, the deficit in energy is the energy of the nuclear excitation. The subsequent gamma emission however, is not simulated by GEANT-MICAP since it does not model nuclear physics. For the second neutron calibration, the predicted rates of 13.3 keV and 68.8 keV excitations are 275±21 per day and 1058±42 per day respectively. The observed rates in these two bands are 161±58 per day and 299±92 per day, respectively. The large excess of 68.8 keV events in

the Monte Carlo may be due to an inaccuracy in the simulation of inelastic scatters.

As an interesting aside, these short-lived states may also be used for WIMP detection. Such an experiment using a purified ^{73}Ge target is described in [15]. The threshold energy needed to produce nuclear excitations in an inelastic scatter is given by

$$E_t = \frac{m+M}{M}E \tag{3.2}$$

where m is the mass of the projectile, M is the mass of the target, E is the the excitation energy, and E_t is the required threshold energy. The kinetic energies required of a 50 GeV WIMP to produce the 13.3 keV state and 68.8 keV state are 22.6 keV and 117 keV, respectively. The average kinetic energy of a 50 GeV WIMP in the galactic halo is 0.82 keV. Therefore, the 13.3 keV state is expected to be more likely even though the 68.8 keV state is closer in spin to the ground state. Neutron backgrounds, which have typical energies in excess of 1 MeV will excite the 68.8 keV state more often. This feature may be used to discriminate between neutrons and WIMPs. However, preliminary cross section estimates [16] for production of the 13.3 keV state by WIMPs indicate that the event rate, using a pure ^{73}Ge detector, is smaller by about 6×10^{-5} than that of a conventional Ge WIMP detector of the same mass with a 10 keV threshold.

Estimating the High-Energy Neutron Flux Using the Long-Lived ^{73}Ge State

The 66.7 keV line appears in the data due to integration of the two gammas (53.4 keV and 13.3 keV) emitted in the de-excitation of the 66.7 keV state of ^{73}Ge. During normal running (not during calibrations), 66.7 keV events are observed due to processes Th72 and Hi74; Th72 is expected to dominate. As mentioned before, it may be possible to measure the

high-energy neutron flux at the detectors during normal running by measuring the contribution of Hi74 to the long-lived (66.7 keV) excited state of ^{73}Ge. Here, "high-energy neutrons" refer to neutrons with energy above the 10.1-MeV threshold needed for Hi74. This method is based on information in Andrew Sonnenschien's dissertation [14]. It requires the use of a photon line at 10.4 keV observed in the low-background data (see [9] or [14] for example).

These 10.4 keV X-rays arise from two processes associated with the production of gallium isotopes. When detectors are above ground, cosmic ray induced spallation results in the production of some ^{68}Ge nuclei. These decay to ^{68}Ga by electron capture with a 270.8 day half-life. Alternatively, neutron capture on ^{70}Ge (natural abundance 21.2%) produces ^{71}Ge which decays to ^{71}Ga by electron capture with a 11.4 day half-life. Since, in both cases, the captured electron comes from the K-shell, the resulting gallium atom has a vacant K-shell. The subsequent filling of the vacated K-shell state causes a 10.4 keV X-ray . If the contribution to the 10.4 keV line from cosmic-ray induced spallation can be estimated, the residual rate may be used to calculate the thermal neutron flux at the detectors. Knowing the thermal neutron flux allows one to deconvolve the two contributions to the 66.7 keV events, thus providing an estimate of the high-energy neutron ($>$ 10.1 MeV) flux. This method is schematically outlined in figure 3.12.

The statistical viability of this method can be checked using a rough estimate of the expected high-energy neutron flux. There are several processes that yield neutrons with energies greater than 10.1 MeV. The rate we want to measure is that due to muon induced high energy neutrons from the rock, which is believed to be the limiting background for CDMS I (see Chapter 4). Using the Monte Carlo methods described in Chapter 5, the neutron flux above 10.1 MeV from this process can be calculated.

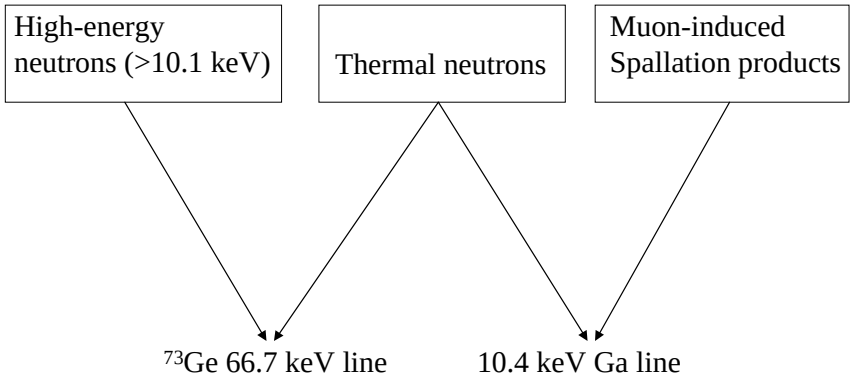

Figure 3.12: Proposed method for measuring the high-energy neutron flux. The object is to estimate the high-energy neutron flux indicated in the upper left-hand box. The thermal neutron contribution must first be subtracted using information about 10.4 keV gallium line. The other contribution to the gallium line from muon-induced spallation must also be estimated in this calculation.

Neutrons from muon interactions within the shield will also contribute. Note that a veto cut is of no use here, because of the long half-life of the 66.7 keV state. Extending the veto-coincidence window to hundreds of milliseconds is not feasible due to the 5.6 kHz veto trigger rate. Thus, in addition to high-energy external neutrons, the high energy neutron flux from muon interactions in the shield is also obtained from the Monte Carlo for the following calculation.

Convolving the incident energy spectra at the detectors from all the above sources with $\sigma(E)$ for Hi74, gives an expected event rate of 2.63±0.06 neutrons/kg/day. The cross-section ($\sigma(E)$) was obtained from ENSDF files from the National Nuclear Data Center's web site [17]. It is between 1-1.2 barns above 14 MeV. Here, I have assumed that all ^{74}Ge (n,2n)^{73}Ge* reactions (Hi74) lead to the 66.7 keV state. The whole detector mass is used to get the above rate with no allowance for self-shielding because the interaction length of high-energy neutrons is larger than the detector dimensions. Combining this estimate with the integrated exposure in kg-days for good data from Runs 18 and 19 predicts 69±1 events at 66.7 keV from Hi74. The contribution to this number from high-energy external neutrons is estimated at 10±1 neutrons. The observed total number of events in the 66.7 keV line from Runs 18 and 19 is about 270±16 [14]. While the contribution from Hi74 is probably measurable, using this method to measure the high-energy *external neutron* flux is not yet statistically feasible. However, I will outline the steps needed to statistically subtract the contribution from Th72.

The thermal-neutron-capture cross-section of ^{72}Ge is 0.8±0.2 barns. This and capture cross sections of other Ge isotopes implies a thermal neutron diffusion length larger than 10 cm in natural Ge. Since the diffusion length is large compared to detector dimensions, no self shielding

is expected. Given a thermal neutron flux ϕ (in neutrons/cm^2/day) and the above cross-section, the neutron capture rate on ^{72}Ge is estimated to be (1.8±0.5)ϕ /kg/day. A Monte Carlo of a relaxing ^{73}Ge nucleus indicates that (64±1)% of decays will proceed through the 66.7 keV state. Data on branching ratios for simulating the 6.8 MeV cascade were also taken from on-line ENSDF files [17]. Using this estimate, the rate of 66.7 keV events is (1.2±0.3)ϕ /kg/day.

If gammas in the decay chain prior to the 66.7 keV state trigger any of the detectors, the subsequent 66.7 keV deposition may be lost in the resulting post-trigger dead time. Given a typical dead time of 250±25 msec in Run 19, and the 500 msec half-life of the excited state, and assuming a hard 2 keV trigger threshold for BLIPs 3 through 6 (no triggers from BLIPs 1 and 2 are used), the fraction of surviving 66.7 keV events is 0.79±0.08 [2]. Finally, if the thermal neutron flux ϕ, is known, the observed rate of 66.7 keV events from Th72 will be (0.8±0.3)ϕ /kg/day. Similarly, using Andrew Sonnenschein's numbers for DAQ dead time, the Run 18 rate is estimated at (0.8±0.2)ϕ /kg/day.

As mentioned above, ϕ must be estimated using 10.4 keV gallium x-ray line. This can be done by fitting the observed rate of 10.4 keV gammas over time with two decaying exponentials and a constant term. One of the exponentials is due to the 270.8 day half-life of the decaying ^{68}Ge . The other exponential is due to the 11.4 day half-life of ^{71}Ge following thermal neutron capture. The second decaying exponential is necessary due to the sharp increase in the thermal neutron capture rate during neutron calibrations. The constant term reflects the equilibrium thermal neutron flux that we intend to measure. Once the constant term is

[2] For high-energy events, the true dead time may be longer than the DAQ dead time because the trace remains above the baseline for a longer period of time. However, since most energy depositions in the 6.8 MeV gamma cascade are below 300 keV, this effect is negligible.

estimated, the thermal neutron flux can be calculated using the capture cross-section (2.9 barns) and the mass fraction of ^{70}Ge (21.2%). Therefore, the Hi72 contribution to the 66.7 keV line can be isolated.

3.6 Veto-Coincident Neutrons

3.6.1 Introduction

During regular running, cosmic-ray muon interactions in the shield provide another neutron data set. This data set consists of events with a nuclear recoil in at least one detector and an associated veto trigger. The nuclear recoil bands are identified using the ^{252}Cf neutron calibration described above. Because they occur at a steady rate during the run, these veto-coincident neutrons can be used to check the stability of trigger and software-cut efficiencies as a function of time. With all data quality cuts applied, the rate of these events does indeed appear to be constant over the entirety of Run 19. The total rate of neutrons in BLIPs 3 through 6 in the 10-100 keV range is about 22$\pm$1 per live day [10]. Because it is relatively simple to model the majority of neutrons resulting from muon interactions, Monte Carlo simulations of these neutrons have been performed. This gives us an opportunity to compare data against Monte Carlo to establish that the veto-coincident neutron background is well understood.

3.6.2 Monte Carlo Setup

As explained in detail in Chapter 5, muon interactions in matter can proceed through two basic mechanisms: muon capture and electromagnetic interactions of muons with matter. GEANT does not simulate neutron production from muon capture. Therefore, the Monte Carlo is programmed to start with rates and spectra of neutrons from various materials rather than the primary muons. Since muon-induced neutron production occurs

mainly in the lead, polyethylene, and copper of the shield and cryostat, we must consider the rates and spectra of neutrons from each material for each mechanism. However, several simplifications are made. The contribution from the outer lead shield and the polyethylene is neglected due to the high efficiency for these neutrons being stopped by the polyethylene. Estimates of neutron rates from the outer lead and polyethylene indicate that their contribution to the total rate is 3% [18] and 1% [19] respectively. Therefore, only neutrons from the cryostat cans and inner lead shield are modeled. The spectrum resulting from electromagnetic muon interactions is approximated by the better known muon-capture neutron spectrum [5]. The high energy tail in the spectrum from electromagnetic interactions due to electromagnetic and nuclear showers (see Chapter 5) is not reproduced accurately by this method. However, the neutron rates from these processes are expected to be a small fraction of the total neutron rate. As discussed in Chapter 5, the high energy tail is more important when considering neutrons from outside the shield. Since the cryostat and inner lead are not shielded from detectors by layers of polyethylene, the high energy component does not have added significance here. Actually, the low energy neutrons are more important here, due to the increase in cross-section at low energy. Therefore, only the low energy part of the neutron spectrum from electromagnetic interactions is simulated, using the spectrum for muon capture. Due to the high rate of muon interactions in the outer lead shield, the contribution from the high energy tail of outer-lead neutrons may be important. This high energy component is not included in the 3% contribution estimated above. I plan to include the high energy component in future simulation using input from the FLUKA simulations described in Chapter 5.

Using measurements made at the SUF with a BF_3 counter, the

combined neutron production rate from muon capture and electromagnetic processes in lead is estimated to be (243±9) neutrons/kg/day [5]. The muon-capture neutron production spectrum is calculated to be [5]

$$\frac{dN}{dE} = \begin{cases} 0.812E^{(5/11)}\exp(-E/1.22), & \text{for } E < 4.5 \text{ MeV} \\ 0.018\exp(-E/9.0), & \text{for } E > 4.5 \text{ MeV} \end{cases} \tag{3.3}$$

where all energies are in MeV. In the simulation, all neutrons from the lead are produced at the above rate according to this spectrum. Since separate measurements of the muon induced neutron spectrum for copper is not available in the literature, the above spectrum is also used for copper with a production rate of 100 neutrons/kg/day [5]. Due to the assumptions and simplifications made above, predictions of this Monte Carlo are expected to be less accurate than those of the Monte Carlo used in the ^{252}Cf neutron calibration. Also note that gammas resulting from muon capture and electromagnetic interactions producing neutrons are not simulated. Therefore, the gamma-neutron multiple scatter fraction will be underestimated by the Monte Carlo.

3.6.3 Results

Figure 3.13 shows comparisons of spectra between data and Monte Carlo for veto-coincident neutrons. Figure 3.14 is a comparison of spectra summed over BLIPs 4 through 6. Solid lines represent the data while the dashed lines represent the Monte Carlo. No overall normalization is performed to match the data and Monte Carlo spectra. All histograms contained in these figures are for events passing the inner cut. Events passing the shared cut are not included because shared events show signs of electron contamination, especially in BLIP3. Although not clear for inner events, BLIP3 is also excluded from the summed plots because of possible contamination of the nuclear recoil band by electrons. Note that only

BLIPs 4 through 6 are used in the final analysis of veto-anticoincident data, as described in Chapter 4.

Unlike in figures 3.6-3.9 where the darker solid lines represent all events passing the nuclear recoil cut, the darker solid lines here are the single-scatter recoil spectra. Events with triggers in other detectors are excluded because of cross-talk problems seen in the data. A high energy event (> 1 MeV) in one detector causes negative charge cross-talk in other detectors. Thus, a lower energy electron recoil in another detector may suffer from a diminished charge signal due to this. The nuclear-recoil band is clearly contaminated by such events especially at low energy. Requiring events to be single scatters in both the data and Monte Carlo removes this problem when comparing spectra and rates. Since the inner electrodes seem to be less susceptible to the cross-talk problem, the multiple scatters shown in figures 3.13 and 3.14 are required to pass the inner cut in at least two detectors. These correspond to the second type of multiple scatter defined in the previous section (see table 3.2). However, in table 3.2 both hits are required to pass either the shared or inner cuts. Here, the requirements are more stringent (inner only). Rates and multiples fractions from the data and Monte Carlo in the 10-100 keV range are given in table 3.4. The sums and averages in this table are again over BLIPs 4 through 6 only.

There is another source of discrepancy between data and Monte Carlo that has not been accounted for in the comparisons in figures 3.13,3.14 and table 3.4. When a nuclear recoil and an electron recoil occur in the same detector, that event will most likely be removed from the nuclear recoil band. The Monte Carlo is not expected to yield the correct rate of gamma-neutron coincidences because the Monte Carlo does not model gammas from the muon captures or electromagnetic interactions of muons which produce neutrons. As pointed out in the section on the ^{252}Cf

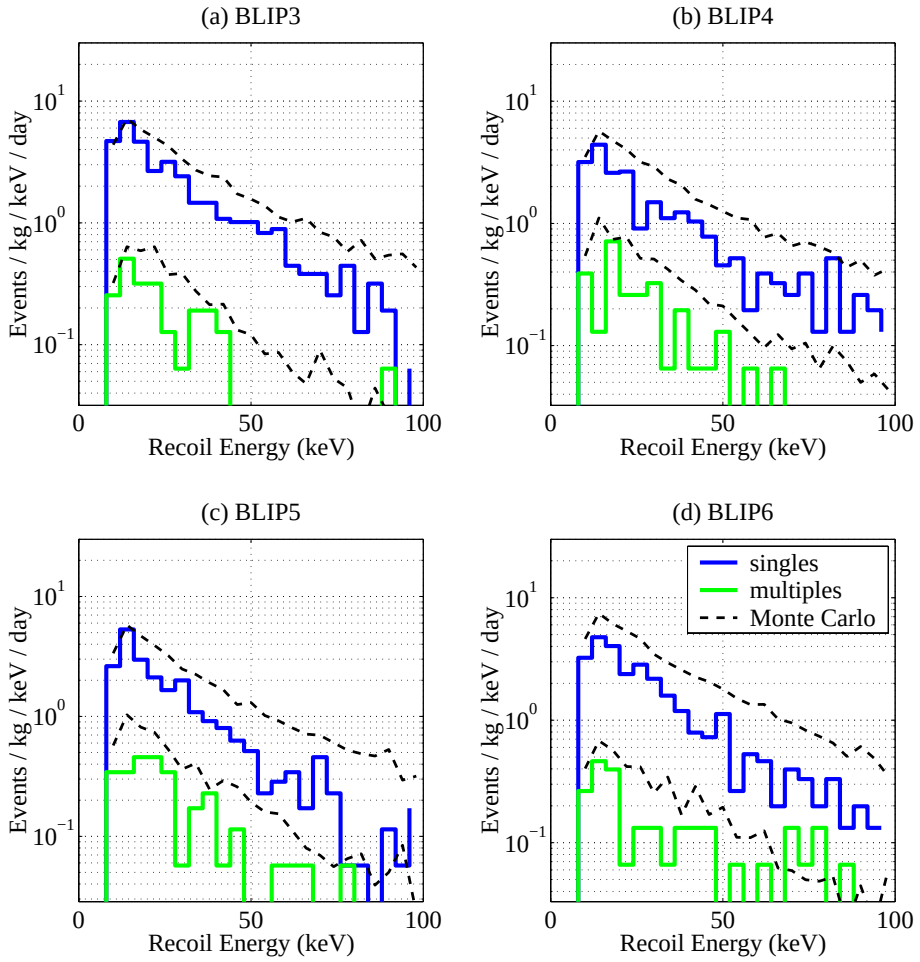

Figure 3.13: Detector-by-detector comparison of data and Monte Carlo spectra for veto-coincident neutrons. Solid lines represent data while the dashed lines represent the Monte Carlo. "Singles" stand for single scatter neutrons passing the inner cut. Multiple scatters shown here are required to pass the inner cut and the nuclear-recoil cut in at least two detectors.

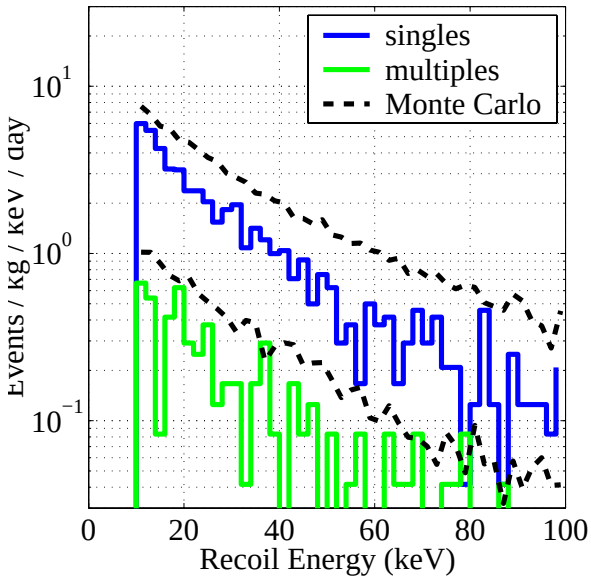

Figure 3.14: Comparison of summed spectra between data and Monte Carlo for veto-coincident neutrons. The sum is taken over BLIPs 4 through 6.

	Veto-Coincident neutrons
Efficiency corrected MC singles rate (events/kg/day)	160.8
Data singles rate (events/kg/day)	98.7 ± 2.8
MC multiples fraction 2	0.135
Data multiples fraction 2	0.108 ± 0.009

Table 3.4: Comparison of data and Monte Carlo for veto-coincident neutrons.

neutron calibration, the Monte Carlo also does not simulate gammas from thermal neutron capture. The only gammas propagated in this Monte Carlo are those that arise as secondaries from neutron interactions in the detectors and shielding material. Therefore the Monte Carlo will overestimate the rate of nuclear recoils passing cuts in each detector. In the ^{252}Cf neutron calibration, we were able to estimate the magnitude of this effect using the gamma-neutron multiple scatter rate between detectors. It is difficult to apply this method for veto-coincident neutrons because of the cross-talk problem described above. When considering multiple scatters in which only one of the hits is required to be a nuclear recoil, one cannot assess whether the nuclear recoil cut is passed due to that hit being a true nuclear recoil or due to cross-talk from hits in other detectors. In the ^{252}Cf neutron calibration, the reduction in nuclear recoil efficiency due to this effect was estimated to be small ($< 2\%$). Because most muon interactions producing neutrons will also yield gammas [20, 21, 22], this effect is expected to be larger in the veto-coincident data set. Also note that the singles rate will be overestimated in the Monte Carlo due to the deficiency of simulated gamma-neutron multiple scatters. Future simulations with appropriate production of gammas are necessary for checking whether the non-inclusion of gammas is the main source of discrepancy between the predicted and observed absolute rates.

3.7 Photon Calibration

The photon calibration is performed using a ^{60}Co source inserted through a small hole on the side of the lead shield. The ^{60}Co nucleus emits a 1173 keV photon and a 1332 keV photon in quick succession. Since these high energy gammas have interaction lengths larger than detector dimensions, the full energy of primary photons is rarely observed in a single

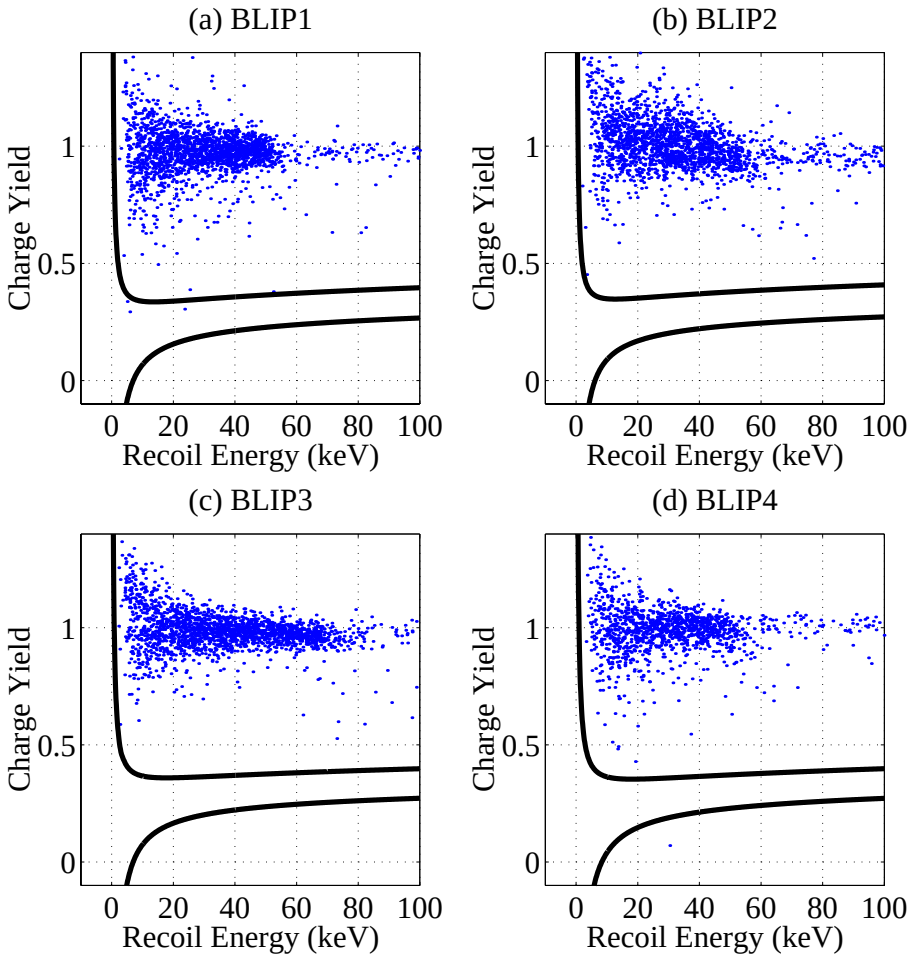

Figure 3.15: Charge yield vs. recoil energy for inner and shared events in the 6 V photon calibration data. See text for details on cleaning cuts.

detector. However, a high rate of electron recoils is generated due to compton scatters of high energy gammas and energy deposition by photons that have down-scattered in the shielding material.

During Run 19, two gamma calibrations were performed, one in July 1999 and the other in September 1999. Data were acquired at a 1 V charge bias as well as the usual 6 V charge bias. Figure 3.15 shows ionization yield versus recoil energy for all four detectors at a 6 V bias. The main use of this data set is to estimate the level at which photons are misidentified as

nuclear recoils. Figure 3.15 contains data passing the inner and shared cuts. These plots clearly indicate that, at the 6 V bias which was used for most of the "physics" data taken during Run 19, photon misidentification is a small effect for events passing the inner and shared fiducial volume cuts. The sudden drop in event rate between 40-60 keV seen in the data is due to vetoing of high energy events by the triggering system used during the photon calibration. Such a veto was applied to limit the data to the recoil energy range of interest. Several "cleaning" cuts have also been applied to the data shown in figure 3.15. In particular,

- A veto anticoincidence cut is used to remove muon-induced electrons.
- All events with at least one detector showing charge saturation have been excluded. This cut removes contamination due to the cross-talk effect described in the previous section.

However, both single and multiple scatters appear in figure 3.15. The photon misidentification parameter used in the Feldman-Cousins statistical analysis is calculated for each detector using these data. The misidentification parameter is simply the ratio of the number of photons appearing in the nuclear recoil band to the number of photons above the nuclear recoil band. The relevant fractions and 90% CL intervals are given in Sunil Golwala's dissertation [9]. For inner and shared events, the 90% CL interval of the photon misidentification parameter is conservatively estimated to be below 0.5% in all detectors. The misidentification parameter is significantly higher for the outer electrodes, and is estimated to be around 1-2%. This clearly indicates that the gap between the top and bottom electrode affects charge collection in the outer electrode.

The cleaning cuts mentioned above do not unfairly improve the estimate of photon misidentification because similar or more stringent

requirements are made on the data included in the final physics analysis. For instance, data included in the dark matter analysis are required to be veto-anticoincident single scatters. When identifying multiple-scatter nuclear recoils for the neutron subtraction (see Chapter 4), all scatters in an event are required to be nuclear recoils in the 10-100 keV recoil energy range. Therefore, events with charge saturation and associated veto signals are also excluded from the final analysis.

Actually, the photon misidentification parameters are overestimated above due to the presence of electrons in the photon calibration data set. Since electrons interact mostly in the dead-layer (see chapter 2), they are expected to contribute to events seen below the "gamma" band in figure 3.15. Several interesting effects pertaining to this population of low-charge-yield events were uncovered during Run 18. I will use the Run 18 data and simulations to illustrate these effects. These events are due to interactions that occur in the dead-layer. During Run 18 the dead-layer problem was more significant because the improved electrodes containing amorphous silicon were not implemented at the time. Therefore, dead-layer events had lower charge yield and were much more likely to be misidentified as nuclear recoils. However, the arguments presented here will also apply to detectors with the new electrodes because the nature and extent of the dead layer are qualitatively the same as before. However, the the reduction in charge yield is smaller now due to the improved electrodes.

In the Run 18 photon calibration, over 3% of events between 10-100 keV were observed to lie below the gamma band (figure 3.16). Furthermore, the fraction of low charge-yield events appears to be flat over the 10-100 keV range. To estimate the expected fraction of such events from the Monte Carlo, a simple charge-collection model for the dead-layer obtained from [23], was incorporated into the Monte Carlo. The charge

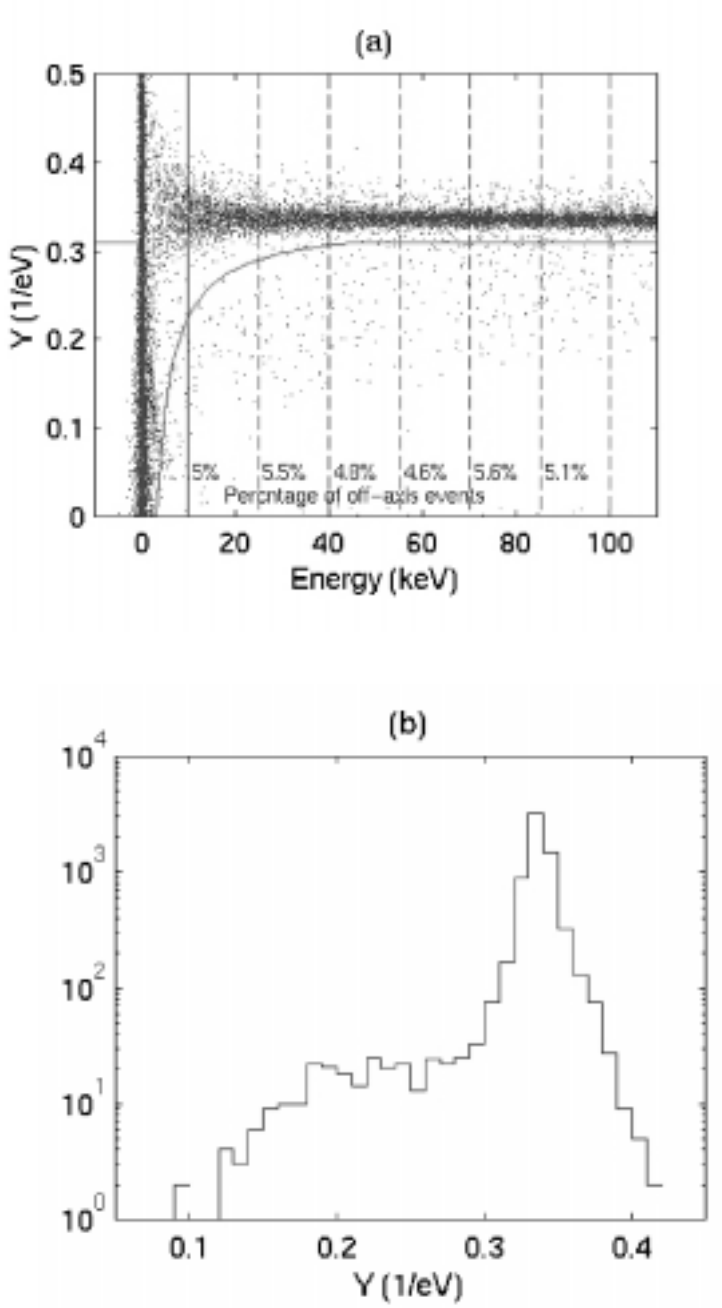

Figure 3.16: (a) Charge yield vs. recoil energy and (b) the integrated charge yield distribution over the 10-100 keV range for BLIP1 data from Run 18. The percentages quoted in (a) are the fractions of events below the solid curve in each energy range indicated by the dashed lines. Note that the photon band in these plots lie at around 0.33, not 1. This is because, during Run 18, the charge yield was normalized differently. It was quoted in terms of the number of electron-hole pairs liberated per 1 eV of energy. For electron recoils a electron-hole pair is created per every 3 eV of energy on average.

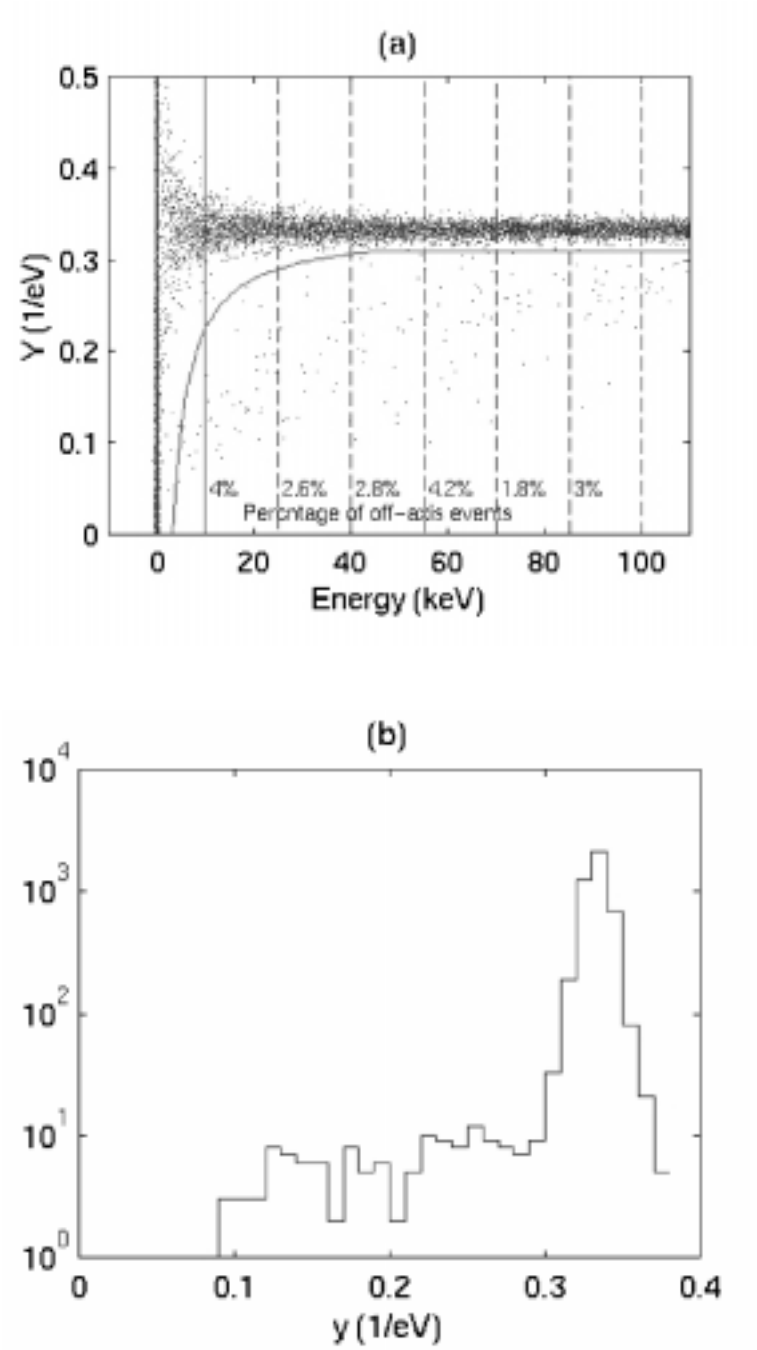

Figure 3.17: (a) Charge yield vs. recoil energy and (b) the integrated charge yield distribution over the 10-100 keV range for BLIP1 as estimated by the Monte Carlo.

collection efficiency $q(x)$ was modeled as

$$q(x) = 1 - 0.7e^{-x/\lambda} \tag{3.4}$$

where x is the distance to the event from the closest detector surface and λ is set to 15 μm. Thus, only scatters occurring in the 40 μm outer layer of the detector will experience charge collection efficiencies less than 95%. The resulting charge data from the Monte Carlo are shown in figure 3.17. Figures 3.16 and 3.17 indicate that the Monte Carlo is in reasonable agreement with data in terms of the fraction of "low charge-yield events". The solid curves in these figures are empirically obtained 95% charge yield contours.

However, according to the Monte Carlo only 0.7% of events in the 10-100 keV range are due to electrons and low-energy photons. All photons with energies below 50 keV have been included in the 0.7% estimate. Actually, a 50 keV photon in Ge has an attenuation length of 560 μm. But, including all photons below 50 keV in the "expected low-charge-yield" set does not introduce a significant error because such photons are very rare. They are rare because of the Cu shields around each detector[3]. Thus, the 0.7% consists mainly of electrons. According to the Monte Carlo, the majority of low charge-yield events are induced by high energy photons ($>$ 100 keV) with energies extending up to the 1.3 MeV cut-off of the ^{60}Co source. Assuming that all such photons scatter uniformly within the detectors, the random fraction of events that fall within the 40 μm outer layer is calculated to be 0.9%. The solid-line histogram in figure 3.18 shows the fraction of events with less than 95% charge yield as a function of incident energy of the interacting photon. This plot verifies that the 0.9% estimate is valid for incident energies above 200 keV. Finally, the initial

[3]Similar shielding is present in Run 19. In Run 19, the Cu housing is lined on the inside with passive Ge shielding (see Chapter 2).

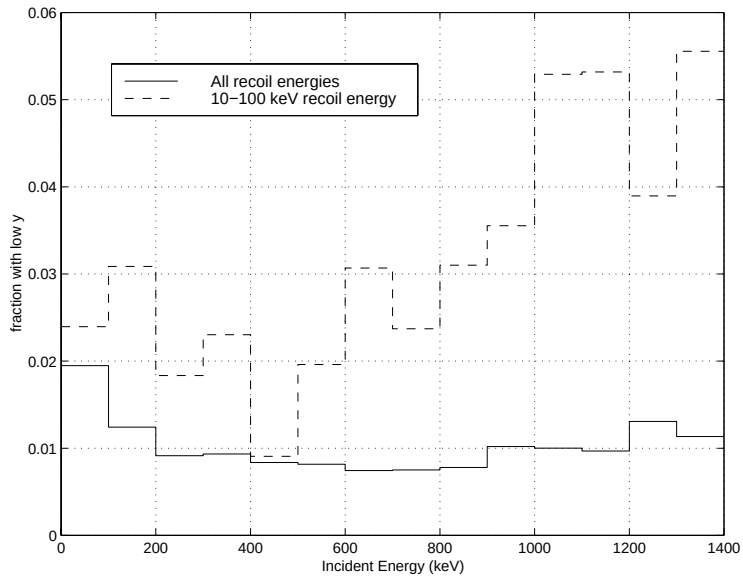

Figure 3.18: The solid line shows the fraction of events with poor charge collection (less than 95%) as a function of the incident energy, regardless of the energy deposited. The dashed line indicates the same fraction for the same incident energies when the deposited energy is restricted to the range 10–100 keV.

guess at the fraction of expected low-charge-yield events is $0.7\% + 0.9\% = 1.6\%$. The fractions given in figures 3.16 and 3.17 are greater by about a factor of three.

The majority of low charge-yield events are due to selection effects introduced when studying low recoil energies (10-100 keV). Of photons that deposit 10-100 keV in the detector, the fraction with poor charge collection ($< 95\%$) is given by the dashed-line histogram in figure 3.18. According to figure 3.18, the fraction of poor charge yield events is higher in general for energy depositions in the 10-100 keV. This trend indicates that low charge yield events are more likely to deposit low energies in the detector. Running the Monte Carlo with an event display finally shed some light on the mechanisms responsible for the majority of low charge-yield events. Some high energy photon interactions will eject the recoiling electron from

the detector. In this case only a fraction of the energy imparted to the electron in the interaction will be deposited in the detector. This is one mechanism through which high-energy photons can deposit 10-100 keV energies in a detector. Since this scenario involves an electron traversing the dead-layer, poor charge collection will result. When examining low energy data from a high energy photon source, this is the dominant mechanism for leading to poor charge yield. The rise of the dashed-line histogram of figure 3.18 above 400 keV is due to the decrease in the fraction of 10-100 keV energy transfers in scatters of high-energy photons. Therefore, for low energy depositions, the electron ejection mechanism becomes more important with increasing photon energy.

Both the solid-line and dashed-line histograms of figure 3.18 have different shapes at low energy (below ∼400 keV). The *total* low charge-yield fraction (solid-line) is higher than the predicted 0.9% fraction at low energy simply because low energy photons do not scatter uniformly within a detector because they have short interaction lengths. The fraction of low charge-yield events among 10-100 keV depositions (dashed-line) is even higher because the relevant interaction length here is that of the photon after the 10-100 keV energy deposition.

In Run 18, the ejected electron in the process described above for high energy photons would stop in the Cu shield surrounding each detector. However, in Run 19 and future detector stacks, the detectors are close packed with no material between them. Therefore most poor charge yield events from the above process will appear as multiple scatters with one scatter due to a high energy photon and the other due to the ejected electron. Low charge-yield scatters due to high energy photons form a broad flat distribution in charge yield (see figures 3.16 and 3.17). On the other hand, data from tests of charge implants [24] indicate that incident

electrons form a narrow band at low charge yield.

Misidentification of electrons as nuclear recoils must also be considered in the final dark matter analysis. Although electron calibrations have been performed on small devices with electrodes similar to those on the Run 19 detector stack [24], no direct electron calibration on Run 19 detectors has been performed. Electron events in the photon calibration cannot be clearly separated from other low charge-yield events which have a broad charge yield distribution. However, a relatively clean electron data set is available in the "low background" data due to electron contamination on the surface of BLIP3. This data can only yield information about electron contamination in BLIPs 3 and 4. However, the results should be applicable to the other two detectors as well because they are of the exact same design. The cuts used to isolate these events and the methods used in the electron misidentification estimate are presented in Sunil Golwala's dissertation [9]. Once the proper cuts are applied an "electron band" is discernible in plots of charge yield versus recoil energy. This band lies between the photon and nuclear-recoil bands. The electron misidentification parameter is the ratio of the number of electrons in the nuclear recoil band to the the number of electrons above the nuclear recoil band.

Figure 3.19 shows ionization yield in BLIP 4 versus ionization yield in BLIP 3 for the electron calibration data set. The two circled events pass the nuclear-recoil cut in both detectors while the boxed event passes the BLIP 4 nuclear-recoil cut. Because these data are gathered over the whole run, these events are consistent with being true veto-anticoincident nuclear recoils. The circled events are consistent with being neutron double scatters while the boxed event is probably a gamma-neutron multiple scatter. However, to obtain a conservative estimate, these events are counted as misidentified electrons. With this assumption, the 90% CL interval on the

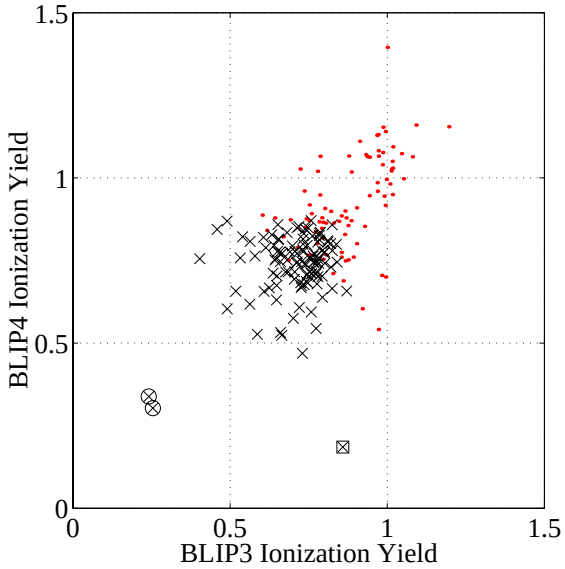

Figure 3.19: BLIP4 charge yield vs. BLIP3 charge yield for electron calibration data. Circles indicate events tagged as nuclear recoils in both detectors; squares indicate events tagged as nuclear recoils in BLIP4. This set consist of all veto-anticoincident double-scatter events between BLIP3 and BLIP4 with both hits in the 10-100 keV range, and at least one inner hit. Figure taken from [9].

electron misidentification parameter is estimated to be below 10.2% for inner and shared events. This large fraction is due in part to the limited statistics available in the electron calibration. The true level of misidentification is expected to be much lower.

References

[1] Geant version 3.21.04, released March 1995. Copyright CERN, Geneva.

[2] J. O. Johnson and T. A. Gabriel. Micap: A Monte Carlo Ionization Chamber Analysis Package, February 1993.

[3] A. Fassò, A. Ferrari, J. Ranft, and P.R. Sala. Fluka: present status and future developments. In Menzione and A. Scribano, editors, *Proc. IV Int. Conf. on Calorimetry in High Energy Physics*, pages 493–502, La Biodola, Italy, 21-26 September 1993. World Scientific.

[4] H. C. Fesefeldt III. Gheisha version 7.03, released September 1985.

[5] Angela Da Silva. *Development of a Low Background Environment for the Cryogenic Dark Matter Search*. PhD thesis, The University of British Columbia, April 1996.

[6] L. Pages, E. Bertel, H. Joffre, and L. Sklavenitis. Energy loss, range, and bremsstrahlung yield for 10-keV to 100-MeV electrons in various elements and chemical compounds. *Atomic Data*, 4:1–127, 1972.

[7] Josef Jochum. Spectrum of deposited energies from Tritium beta decay. In cdmsnotes (cdmsnote 9705005)., May 1997.

[8] Glenn F. Knoll. *Radiation Detection and Measurement*. John Wiley and Sons, second edition, 1989.

[9] Sunil Golwala. *Exclusion Limits on the WIMP-Nucleon Elastic-Scattering Cross-Section from the Cryogenic Dark Matter Search*. PhD thesis, The University of California at Berkeley, Fall 2000.

[10] D. Abrams et al. Exclusion Limits on the WIMP-Nucleon Cross-Section from the Cryogenic Dark Matter Search. Will appear in Physical Review D., 2001.

[11] R. Abusaidi et al. Exclusion Limits on the WIMP-Nucleon Cross-Section from the Cryogenic Dark Matter Search. *Physical Review Letters*, 84:5699, 2000.

[12] Richard Schnee. Calculation of Neutron Multiple Scatter Fraction. Memo to the CDMS collaboration, July 2001.

[13] Rick Gaitskell. Observation of Inelastic Neutron Scattering and thermal Neutron Capture in Ge BLIP data from First Neutron Calibrations of Run 18. In cdmsnotes (cdmsnote 9805001)., May 1998.

[14] Andrew Sonnenschein. *A Search for Weakly Interacting Dark Matter Particles with Low Temperature Detectors Capable of Simultaneously Measuring Ionization and Heat*. PhD thesis, University of California, Santa Barbara, July 1999.

[15] A.A. Klimenko et al. *JETP Letters*, 67:837, 1998.

[16] J. Engel and P. Vogel. *Phys. Rev.*, D61:63503, 2000.

[17] http://www.nndc.bnl.gov. National Nuclear Data Center.

[18] Richard Schnee. Private communication.

[19] Steve Eichblatt. Estimating the Neutron Background for SUF Run 18. In cdmsnotes (cdmsnote 9802001)., February 1998.

[20] P. Singer. *Springer Tracts in Modern Physics*, 71:38, 1974.

[21] G. Backenstoss et al. *Nuclear Physics*, A162:541, 1971.

[22] G.G. Harris and T.J.B. Shanley. *Physical Review*, 85(5):983, 1952.

[23] T. Shutt et al. In *Proceedings of the Seventh International Workshop on Low Temperature Detectors*, 1997.

[24] T. Shutt et al. *Nucl. Instrum. Methods Phys. Res., Sect A*, 444:340, 2000.

Chapter 4

Data and Results from CDMS I

4.1 Introduction

After several icebox runs to test the cryogenic and electronics chains, physics data from CDMS were first acquired in icebox Run 13 in 1996. It was soon realized that further developments in shielding, reduction of backgrounds, and the ionization measurement were necessary. The four step strategy outlined in Chapter 2 and other improvements came to fruition during CDMS Run 19 which took place between October 1998 and September 1999. The data obtained during Run 19 and their analysis are described in this chapter. More detailed discussions on many of the topics below can be found in Sunil Golwala's dissertation [1] and some recent publications [2, 3].

A total of 99.4 raw live-days worth of data were taken in Run 19. This number corresponds to the time that the data acquisition system was waiting for a trigger with the experiment in "low-background" mode. Low-background data consists of all data excluding detector calibrations and periods with known problems. As described below, this livetime will be reduced due to the application of software cuts. Figure 4.1 shows how the above livetime was aggregated. The x-axis represents real time in days. The dark solid line depicts the total time that the DAQ was operating in

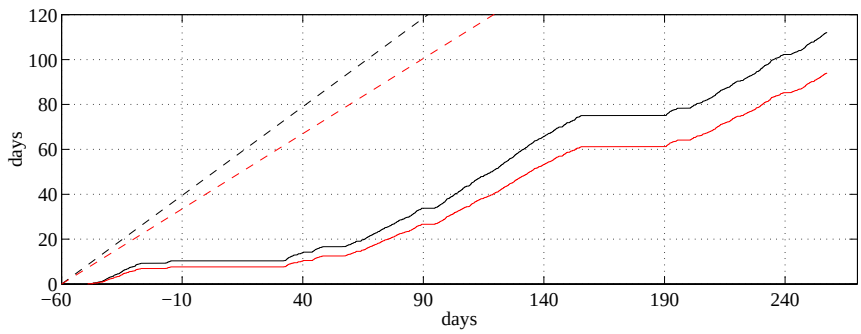

Figure 4.1: Cumulative raw livetime for low-background data in Run 19. The dark solid line shows the cumulative time of operation of the DAQ. The light solid line is the time spent waiting for a trigger. The dark and light dashed lines are the corresponding maximum expected slopes. Figure taken from [1].

low-background mode. The light solid line indicates the time that the DAQ was waiting for a trigger. The 99.4 live-days quoted above is the high-point of this curve. Periods of slow increase in raw exposure are due to calibration data taking, electronics and detector troubleshooting, problems with the DAQ, and cryogenics system failure and maintenance. During other times, the slope of the dark solid line is not unity because of cryogen transfers, detector grounding, and phonon pulser calibrations. The light solid line has a slightly smaller slope because of DAQ deadtime. The maximum expected slopes of the these two curves are also shown as dashed lines in figure 4.1.

4.2 Run 19 Data Set and Analysis

The triggering and DAQ employed in Run 19 as well as the cryogenics and electronics chains are described in Chapter 2. The phonon and charge pulses are digitized at 15.625 kHz and 156.25 kHz respectively. In both cases, a downloaded trace consists of 2048 samples. The traces correspond to 131 msec and 13.1 msec for the phonon and charge channels respectively. The phonon and charge pulse durations are roughly 85 msec and 45 μsec

respectively. Charge traces are much longer than the charge pulse duration because a large pretrigger window is needed in the charge search for phonon-trigger events (see below). Raw data from Run 19 consists of phonon and charge pulses from BLIPs 3 through 6 and a "history buffer" corresponding to each event. The history buffer contains veto and trigger information for a number of veto hits and detector triggers before and after the current trigger. Although BLIPs 1 and 2 were also inserted into the icebox for Run 19, they were only operated during the first part of Run 19 mainly for the purpose of confirming hypotheses about tritium contamination seen in previous runs.

The DAQ is triggered by phonon and charge pulser events, random triggers, as well as real events in detectors. The raw data is put through "Dark Pipe," a Matlab based analysis program, which writes out "reduced quantities" or RQs for each event. The RQs contain veto and trigger information regarding an event in addition to phonon and charge energy estimates, which are obtained using several pulse-fitting and optimal-filtering techniques. A second-pass analysis program "Pipe Cleaner", uses RQs to produce more reduced quantities called RRQs. The recoil energy is calculated in the second-pass analysis using the Luke correction mentioned in Chapter 2. Before calculating the recoil energy, better estimates of charge and phonon energy are obtained by correcting for fridge temperature drifts over time (see [1] for details). The non-linearity in charge energy, which appeared after a Stanford-wide power outage on April 3 1999, is also corrected for in the the RRQs. Other quantities saved by Pipe Cleaner include noise level estimates, which use the random trigger data, and some of the software cuts discussed below.

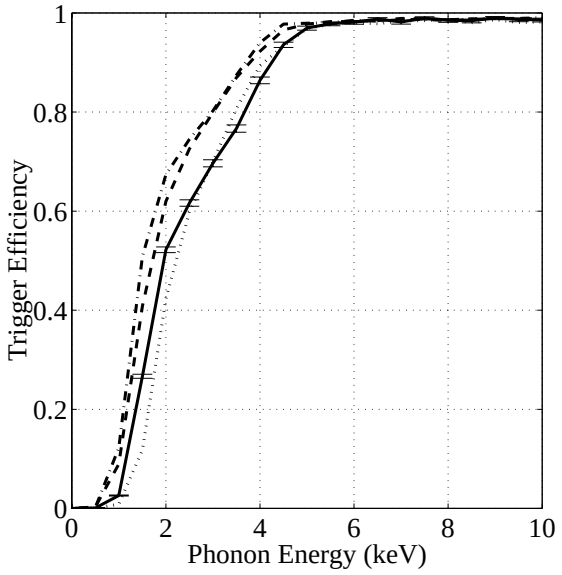

Figure 4.2: Phonon trigger efficiencies in BLIPs 3 through 6. Phonon energy is the heat generated from an event before applying the Neganov-Trofimov-Luke correction. The curves for BLIPs 3 through 6 are solid, dashed, dash-dotted, and dotted respectively. Statistical errors (1σ) are only shown for BLIP3. They are similar for the other detectors. Figure taken from [2].

4.2.1 Trigger, Charge Search, and Analysis Thresholds

The phonon and charge trigger efficiencies for each detector are estimated using events where another detector triggers the DAQ. When a trigger occurs, traces from all channels of all detectors are downloaded and later analyzed. The history buffer indicates whether the channel being studied caused a subsequent trigger. Therefore, the trigger efficiency for a particular channel at a given energy E, is the fraction of all "off-detector" triggers with energy E in the channel being studied, for which a trigger is recorded in the history buffer. Only events passing all data-quality cuts are included in the trigger-efficiency calculation. The phonon trigger efficiencies for all detectors are shown in figure 4.2. These trigger efficiencies are almost 100% above 5 keV. Only the phonon trigger efficiencies are given here because, for nuclear recoils, the phonon trigger turns on at a lower energy than the charge trigger.

For events with only a phonon trigger, the pretrigger part of the charge trace is searched to find the corresponding charge pulse. The charge pulse is in the pretrigger part because phonon pulses have slow risetimes and therefore late trigger times compared to charge pulses. The phonon and charge risetimes are approximately 5 msec and 2 μsec respectively. The charge search algorithm looks for the highest charge peak in a 1.6 msec time window determined by the phonon-pulse start time. Obtaining the correct charge signal is essential for performing event-by-event nuclear-recoil discrimination. Finding the correct charge pulse also helps set the event time more accurately. The time of the event is important for deciding whether the event is "coincident" with a veto hit. For events with low energy, especially nuclear recoils, the highest peak in the search window may be due to noise rather than the true charge pulse. To avoid

misidentification of noise as true charge, a charge search threshold is set on a daily basis using charge-channel noise levels estimated from random triggers. Events with no charge signal above this threshold are removed from the analysis. Note that misidentification of the charge signal can still occur if a random noise bump exceeds the charge search threshold. The charge yield for such events will be overestimated in the analysis. However, above 2 keV of ionization energy, this effect is negligible [1, 2].

Although the charge search threshold changes daily for each detector, it usually occurs between 1 keV and 2 keV in ionization energy. A 2 keV ionization energy corresponds to recoil energies of about 10 keV for nuclear recoils at the lower charge-yield limit of the nuclear-recoil acceptance band. Therefore, a 10 keV recoil energy threshold is applied when selecting events that enter the analysis. Leakage of the surface-electron band into the nuclear-recoil band at low energy is another reason for the 10 keV analysis threshold.

4.3 Software Cuts and Their Efficiencies

4.3.1 Introduction

Several periods with known detector, electronics, and DAQ problems are excluded from the data analysis. These "good times" cuts remove periods of high noise levels and trace baseline drift in addition to obviously corrupt data. Sometimes, only data from a subset of detectors is corrupt, for example due to a particular charge channel being unbiased. In such cases data from the other detectors are not excluded. Next, several cuts are applied to select events for which the energy estimates are reliable. In addition to the other benefits of having good energy resolution, accurate estimates of charge and phonon energy are crucial for the nuclear-recoil discrimination used in CDMS. Therefore, several cuts which discriminate

on trace properties, called "trace quality cuts," are applied. The first three cuts described below belong to this category. The rest of the cuts discussed below are based on information contained in the traces and history buffer. These are called "physics cuts." Finally, of course, artificially induced events such as phonon and charge pulser events as well as random triggers are also excluded from the physics analysis based on trigger status bits recorded in the history buffer.

For single-scatters, the combined efficiency of the cuts given below is the product of all the cut efficiencies. Calculating the combined efficiency for multiple scatters is more complicated because a matrix of possible outcomes must be considered, as explained in Chapter 3. The efficiency calculations are checked by applying them to the Monte Carlo output for the neutron calibrations and comparing to the corresponding data. These comparisons are presented in Chapter 3. The good agreement between data and Monte Carlo with regard to the multiple-scatter fraction indicates that the cut efficiencies are well understood. The constant rate of veto-coincident neutrons (see Chapter 3) throughout the run indicates that cut efficiencies remain stable.

4.3.2 Trace Quality Cuts

Cuts described below are presented in the usual order of their application.

Pretrigger Quality

The pulse analysis programs cannot be expected to perform well in the presence of high noise, baseline drifts, and pileup in the pretrigger trace. The pre-pulse baseline must also be in a certain range to ensure that events below 100 keV do not saturate the digitizers. Several requirements on the means and standard deviations of pretrigger traces are used to select acceptable events. The "DC-reference" voltages recorded during each event

indicate the temperature of the thermistors. In the second-pass analysis mentioned above, a correction to the phonon energy estimate is applied based on the DC-reference voltage. However, this correction can be reliably applied only for a certain range of DC-reference voltages. Therefore, the DC-reference voltage is required to be within this range. This cut is mentioned here because its efficiency is evaluated together with the pretrigger-trace quality cuts. In the analysis presented in this chapter and Chapter 3, all detectors passing "good times" cuts are required to pass the above cuts.

Charge-pulser events are used to assess the efficiency of the above cuts. The charge-pulser events are programmed to occur at random times, but with a uniform average rate. Charge pulsing consists of injecting a small amount of charge to the detector electrodes. These signals must then propagate through the usual electronics and DAQ chains in order to be recorded. Therefore, the cut efficiency can be simply evaluated as the ratio of charge pulser events passing the above cuts to the total number of charge puler events seen in the data. This ratio is consistently between 0.70 to 0.75 in the low-background data and lower for calibration data due to the higher rate of pileup.

Actually, the above ratio also accounts for a small inefficiency unrelated to the cuts given above. Triggers from particular channels are inhibited for very small periods of time following events in those channels. Therefore, the true trigger efficiency for a given event depends on the event rate and is less than 100% even at high energy. The trigger efficiency versus energy plot of figure 4.2 reaches 100% above 5 keV because only events passing data quality cuts, and in particular pretrigger-trace-quality cuts, were included in the analysis. Thus, the trigger-efficiency calculation does not include traces just recovering from previous events. However, the above

ratio accounts for this high-energy trigger inefficiency because charge pulser events almost always cause triggers, and therefore include traces recovering from previous events. The charge pulser events have high trigger efficiencies because they occur in the charge channels which have very small recovery times and because the pulses are chosen to be well above the charge trigger threshold.

Post-Trigger Quality

Post-trigger quality cuts attempt to remove pulses with pileup. In general, such pulses will yield poor energy estimates usually erring on the high side. In most cases only the phonon energy will be overestimated because phonon pulses are much more likely to have pileup due to their long $\sim$83 msec durations. These events are potentially troublesome because they may be misidentified as nuclear recoils due to the charge yield being underestimated. The first cut used to remove such events requires channels of a particular detector to be free of charge triggers 10 msec before and 10 msec after the trigger. However, triggers in a -50 μsec to 300 μsec window are allowed in order to accept "coincident" triggers. Another cut used to remove pileup is based on the time between the beginning and the highest point of the pulse. This time will be unusually high when a second superimposed pulse causes the highest peak. This cut is very effective for events below 100 keV in the low-background data because most events in this data set have higher energy. Therefore the combination of these two cuts is expected to remove most pulses with pileup. Since other events in a -10 msec to 83 msec window around the trigger are considered pileup, the combined efficiency of the above cuts can be calculated as

$$1 - \epsilon = 1 - \exp(-0.093/\tau) \tag{4.1}$$

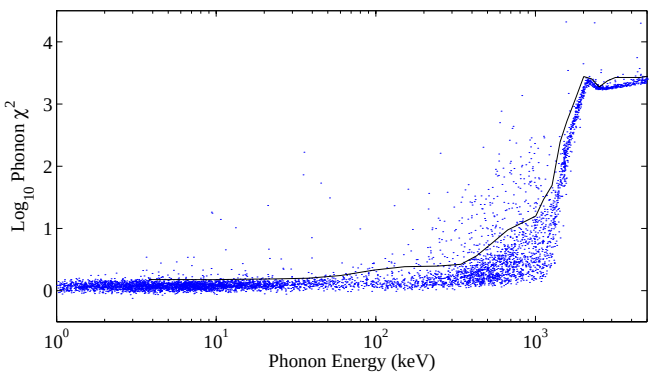

Figure 4.3: Phonon χ^2 vs. phonon energy for typical low-background data form Run 19. The solid line indicates the position of the empirically determined χ^2 cut. Figure taken from [1].

where ϵ is the cut efficiency and $1/\tau$ is the single-detector event rate. Note that post-trigger quality cuts remove only the contribution of particular detectors to an event. Using the typical single-detector low-background event rate of 0.33 Hz in equation 4.1, the efficiency is estimated at 0.97. This number is in good agreement with the fraction of low-background events passing post-trigger quality cuts.

χ^2 and Charge Delay Cuts

Cuts based on pulse-fit χ^2 values are used to remove pileup events which survive the post-trigger quality cuts, and pathological pulses which yield inaccurate energy estimates. The distribution of phonon pulse-fit χ^2 versus phonon energy for a typical low-background data set is displayed in figure 4.3. The χ^2 distribution rises at high energy because the templates used in the fit do not model the pulse shapes accurately at high energy [1]. The slow rise above 300 keV is due to pulse shape non-linearities that occur at these energies. The sudden change around 1 MeV coincides with digitizer saturation. The shape of the χ^2 distribution also changes with time, due to fridge temperature drifts. Due to these reasons an empirical

approach is adopted when placing cuts on χ^2 values. The second-pass analysis mentioned above automatically calculates the position of the cut at a particular energy based on the χ^2 distribution at that energy. The position of the cut is indicated by the solid line in figure 4.3. Because the ionization χ^2 distributions are much better behaved, a very liberal cut with nearly 100% efficiency is used for the charge channels.

The efficiency of the χ^2 cut at each energy is taken to be the fraction of events passing the cut. The combined χ^2 cut efficiency for many data sets is obtained by taking an average of the efficiencies weighted by the number of events in each data set before the χ^2 cut. Since, for well behaved data sets, the number of events is proportional to the livetime, this is a fair way of obtaining the combined χ^2 cut efficiency. On the other hand, if some data sets containing high-trigger-rate periods caused by excessive noise are not excluded by the previous cuts, weighting by the number of events underestimates the combined efficiency because events during such periods are less likely to pass χ^2 cuts. Therefore, the above method for estimating the χ^2 cut efficiency is conservative.

Another "cleaning cut" is applied before further analysis or the application of physics cuts. In some low-energy phonon-trigger events, the phonon trigger occurs so late that the true charge pulse is not in the downloaded charge trace. If the charge-search algorithm mistakenly finds a charge pulse in such cases, the position of the "inferred" pulse is likely to occur close to the beginning of the downloaded charge trace. Therefore, phonon-trigger events with inferred charge pulses too close to the beginning of the charge search window are discarded. For events with recoil energy above 10 keV and ionization energy above the search threshold, this cut has a negligible inefficiency.

4.3.3 Physics Cuts

Thermistor Events

Particle interactions that occur within the two thermistors are also recorded by the DAQ. These events cannot be included with the other data because they have little or no charge signal and anomalous phonon pulse shapes compared to regular data. These events can be easily removed by discriminating on the phonon energy partition of each event. Both thermistors will yield roughly equal pulse heights for events in detectors. However, the phonon energy estimates in two thermistors are clearly different for thermistor contained events. Therefore, reasonable phonon energy partitions are required of events entering the physics analysis. This cut is almost 100% efficient for events in detectors. Also note that only the detector mass is used when quoting exposure in kg-days.

Fiducial Volume Cuts

As described in Chapter 2, the detectors have radially segmented electrodes. Three types of events can be defined using the ionization signals contained in each electrode. "Inner-electrode-contained" events have inner-electrode signals 4σ above the noise mean and outer-electrode signals within $\pm 2\sigma$ of the noise mean. "Outer-electrode-contained" events have outer electrode signals above 2σ of the noise mean and inner-electrode signals below the noise mean plus 4σ. "Shared-electrode" events have inner-electrode signals above 4σ of the noise mean and outer electrode signals above 2σ of the noise mean. The mean and standard deviations of the noise used in the above definitions are calculated on a daily basis for each electrode, using random triggers. In the rest of this dissertation I will refer to these categories simply as inner, outer, and shared events. Although the thresholds given above are somewhat arbitrary, at energies above 10 keV

these three classes of events are clearly separated in their ionization signal partition between electrodes. The radial range within which a scatter occurs determines whether it will be classified as an inner, shared, or outer event. However, for particles with short interaction lengths compared to detector dimensions, an event may fall into the shared category due to an internal multiple scatter. This effect is negligible for WIMPs because the probability of a WIMP multiple scatter is negligibly small. Therefore, for WIMPS the above cuts identify three separate volumes within a detector. A calculation of the volumes corresponding to the inner, shared, and outer cuts, using the neutron calibration, is presented in Chapter 3.

As noted in Chapter 3 with regard to the photon calibration, a significant fraction of outer events suffer from poor charge collection efficiency. This is clearly evident in the electron calibration and low-background data as well. Poor charge collection in the outer electrode is presumably due to the gap between the top and bottom electrodes. Since the probability of misidentifying an electron recoil as a nuclear recoil is high for outer events, they are excluded from the dark matter analysis.

Exclusion of BLIP3

The rate of veto-anticoincident low-charge-yield events is a factor of four higher in BLIP3 compared to other detectors. These events are mostly due to electrons. Exposure to a ^{14}C electrons source, later found to be leaky, appears to have contaminated the surface of BLIP3. Since it was the prototype detector, BLIP3 underwent more processing and handling steps than other detectors. This may also have contributed to the electron contamination in BLIP3. Some of the low-charge-yield rate may be due to electrode problems which may also have been introduced during the repeated processing steps. For these reasons, events with any scatters in BLIP3 are excluded from the dark matter analysis. However, as explained

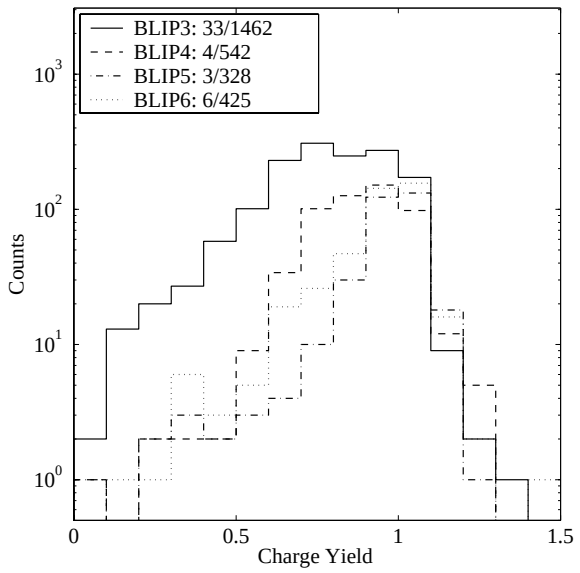

Figure 4.4: Charge-yield distributions for veto-coincident inner events in BLIPs 3 through 6. The legend indicates the ratio of events in the nuclear recoil band to the total number of events included in each histogram. The electron contamination in BLIP3 is clearly visible at low charge yield. Figure taken from [2].

in Chapter 3, multiple scatters between BLIPs 3 and 4 are used as an electron calibration data set.

Figure 4.4 displays the charge yield distribution of 10-100 keV veto-anticoincident inner events in all four detectors. As mentioned above, BLIP3 has an unusually large population of low-charge-yield events, even after applying the inner cut. However, BLIP4, which is exposed to electrons from BLIP3 has a well behaved charge-yield distribution and is therefore included in the dark matter analysis.

Veto-Anticoincidence Cut

A veto-anticoincidence cut is used to remove events induced by cosmic-ray muons. Due to the high veto rate, the veto-coincidence window must be chosen carefully. The distribution of veto trigger times relative to event

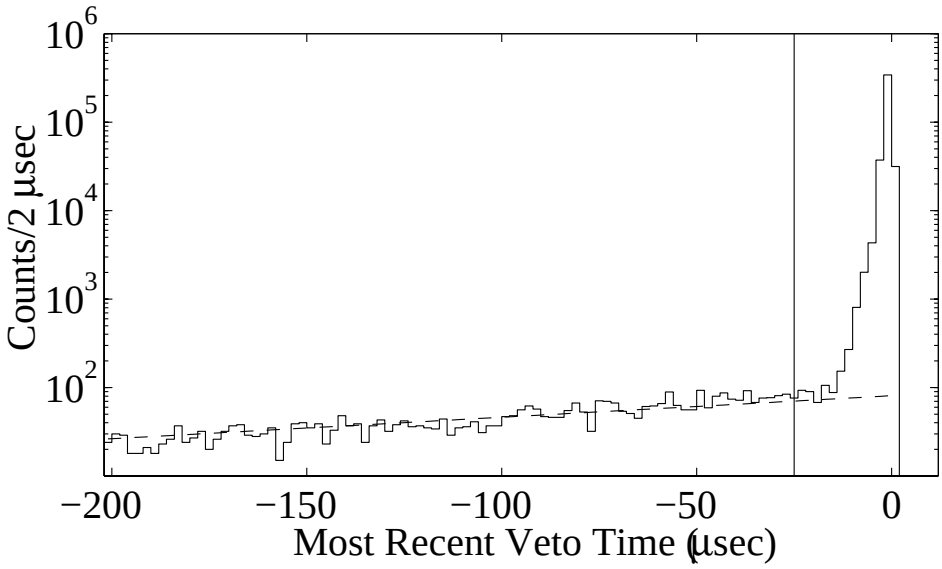

Figure 4.5: Distribution of veto-trigger times relative to charge triggers. The exponentially falling accidental distribution has a slope corresponding to 150 μsec (dashed line). The 25 μsec veto-coincidence window is also indicated. Figure taken from [2].

triggers is shown in figure 4.5 for events with charge triggers. The veto-coincidence window is chosen close to the point at which the slope of this distribution changes. All charge-trigger events with a veto trigger in the previous 25 μsec are excluded by the veto-anticoincidence cut. For phonon triggers the veto-coincidence window is defined differently. If a charge signal is found by the search algorithm, the time of the charge pulse can be compared to veto-trigger times. For phonon triggers, the distribution of closest veto trigger times to the inferred charge pulse time is shown in figure 4.6. Here, a veto coincidence window of ± 25 μsec is chosen.

The probability of an accidental veto coincidence is

$$1 - \epsilon = 1 - \exp(-T_w/\tau) \tag{4.2}$$

where T_w is the size of the veto-coincidence window and $1/\tau$ is the veto trigger rate, which was about 5.6 kHz during Run 19. Using the

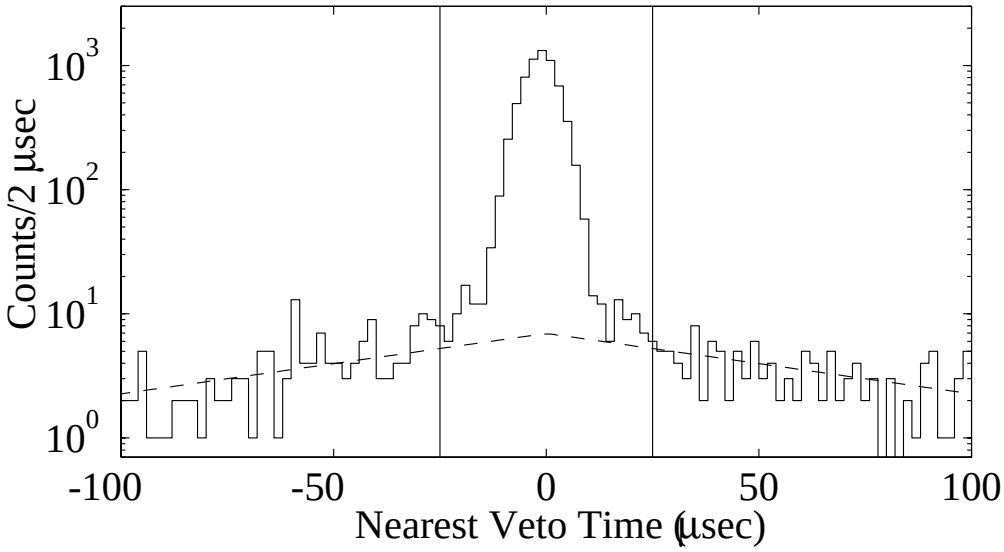

Figure 4.6: Distribution of veto-trigger times relative to the inferred charge pulse time for phonon triggers. The exponentially falling accidental distribution has a slope corresponding to 150 μsec (dashed line). The ± 25 μsec veto-coincidence window is also indicated. Figure taken from [2].

appropriate window sizes T_w, the veto-anticoincidence efficiency ϵ calculated in this way for charge and phonon triggers are 0.87 and 0.75, respectively. Although these estimates are in the correct range, a more detailed calculation is performed to account for trigger rate variations over time.

Nuclear Recoil Cut

The nuclear-recoil acceptance band is determined from the two neutron calibration data sets. Having two neutron calibration data sets proved to be useful because the position of the nuclear-recoil band appears to have shifted after the Stanford-wide power outage on April 3, 1999. This shift persists even after empirical corrections to the charge non-linearity that resulted from the power outage. Fortunately, the first neutron calibration occurred just before the power outage. Therefore, the two neutron calibrations are used to parametrize the nuclear recoil bands for data before

and after the power outage. For each detector, the mean position and standard deviation of the nuclear recoil band in charge energy is determined as a function of recoil energy. Next, the mean position Q_{NR} and standard deviation σ_{NR} are fit with a power law of recoil energy E_{R}. The nuclear-recoil-acceptance band is chosen to be $1.28\sigma_{\mathrm{NR}}(E_{\mathrm{R}})$ above and $3\sigma_{\mathrm{NR}}(E_{\mathrm{R}})$ below $Q_{\mathrm{NR}}(E_{\mathrm{R}})$. The nuclear-recoil cut efficiency is evaluated as

$$\epsilon_{\mathrm{NR}} = \int_{Q_{\mathrm{min}}(E_{\mathrm{R}})}^{Q_{\mathrm{max}}(E_{\mathrm{R}})} \frac{1}{\sigma_{\mathrm{NR}}\sqrt{2\pi}} \exp\left[\frac{(q - Q_{\mathrm{NR}})^2}{2\sigma_{\mathrm{NR}}^2}\right] dq \ . \tag{4.3}$$

Where the limits specified above are used as Q_{max} and Q_{min} except at low recoil energy (around 10 keV) where Q_{min} is set to the ionization search threshold. For the recoil-energy range not affected by the ionization-search threshold, the nominal cut efficiency $\epsilon_{\mathrm{NR}}(E_{\mathrm{R}})$ is 90% from the definition of the band. In the neutron calibrations, about 88% of "neutrons" pass the nuclear-recoil cut. This fraction is slightly lower than expected due to possible contamination of the event set identified as neutrons. However, the difference between these two percentages may be taken as a systematic uncertainty in $\epsilon_{\mathrm{NR}}(E_{\mathrm{R}})$.

4.4 Veto-Coincident Data

Most events acquired in CDMS I are due to cosmic-ray muons and their secondaries. The veto-coincident event rate in detectors is approximately 60 events/keV/kg/day in the 10-100 keV range. These events are dominated by electron recoils, mostly due to photons, but with a significant contribution from electrons. Figures 4.7 and 4.8 show the veto-coincident recoil energy spectra for inner and shared events in all detectors.

The event rate in BLIP3 is slightly higher because it is the top detector in the stack. Compared to veto-anticoincident and calibration data, the multiple scatter rate is higher in all detectors for these data.

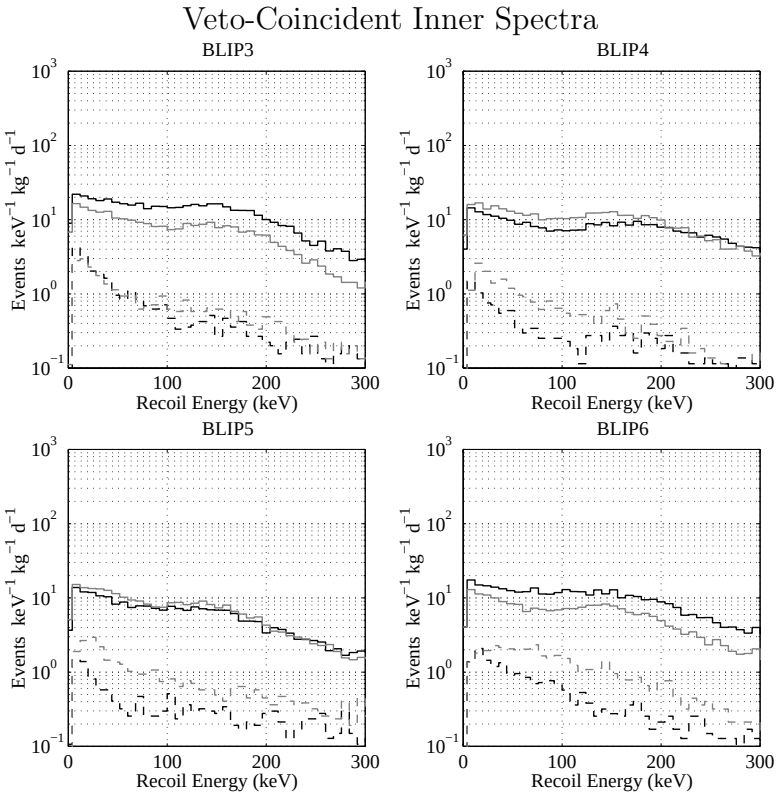

Figure 4.7: Recoil-energy spectra for veto-coincident inner events. Dark solid: single-scatter photons. Dark dashed: single-scatter electrons. Light solid: photons belonging to double scatters. Light dashed: electrons belonging to double scatters.

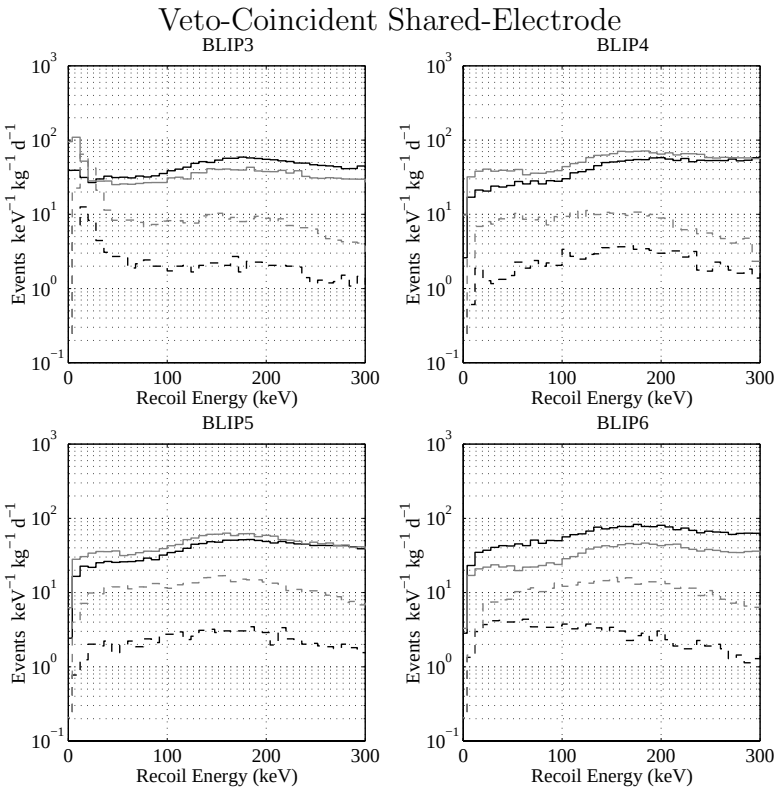

Figure 4.8: Recoil-energy spectra for veto-coincident shared events. Legend as in Figure 4.7.

Thus, most muon-induced interacting particles must be emitted in showers close to the detectors. The multiple scatter rates in BLIP4 and BLIP5 are higher than those in BLIP3 and BLIP6 because BLIP4 and BLIP5 are sandwiched between other detectors whereas BLIP3 and BLIP6 are at the ends of the stack.

The shapes of spectra for inner and shared events are different. The incident photon spectrum at the detectors is expected to drop at low energy due to the presence of many shielding layers. The shared events reflect the incident spectrum better because internal multiple scatters are included in this set. When several scatters are allowed, it is more likely for the full energy of photons to be deposited in a detector. On the other hand, inner events are dominated by single-scatters. Therefore, the spectrum rises at low energy due to Compton scattering of high energy photons.

4.5 Veto-Anticoincident Data

The veto-anticoincident spectra are dominated by electrons and photons from natural radioactivity in the near-detector materials. Figure 4.9 contains plots of charge yield versus recoil energy for veto-anticoincident single scatters. The two plots correspond to inner and outer events. In addition to the bulk electron-recoil band around a charge yield of unity, a surface-electron band is clearly visible around a charge yield of 0.75. As expected, this band rises with increasing recoil energy. However, below 10 keV, the electron band comes close to the nuclear recoil acceptance region, indicated by the light dashed lines. The possibility of electron misidentification at low energy is a major reason for placing the analysis threshold at 10 keV. This threshold is represented by the dark dashed lines in figure 4.9. As mentioned above, the nuclear-recoil-cut efficiency falls below 90% at low energy due to the ionization search threshold. This

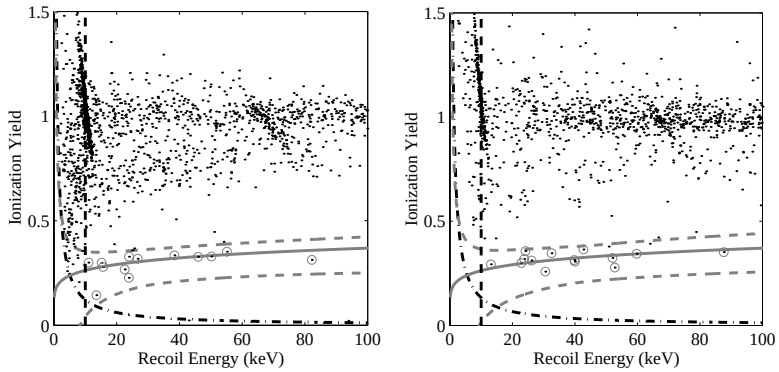

Figure 4.9: Ionization yield vs. recoil energy for veto-anticoincident single scatters in BLIPs 4 through 6 for the inner (left) and shared (right) data sets. Solid line: expected position of nuclear recoils. Light dashed lines: nominal 90% nuclear-recoil acceptance region. Dark dashed line: 10 keV analysis threshold. Dash-dotted line: ionization search threshold. Circled points: nuclear recoils. The non-circled points that appear within the nuclear-recoil band on the left hand plot are due to slight differences in nuclear-recoil cut definitions among detectors.

threshold is represented by the dash-dotted hyperbolae of figure 4.9. I will concentrate on the circled nuclear-recoil candidates in the next section.

The single-scatter veto-anticoincident electron and photon spectra are shown separately for inner and shared events in figures 4.10 and 4.11. The difference in shape between inner and shared spectra, described above, appears in these plots too. Even though the majority of photons arise from natural radioactivity, the two features in the photon spectra at 10 keV and 67 keV are due to the processes described in Chapter 3. These photon lines are also visible[1] in figure 4.9. The high rate of electrons in BLIPs 3 and 4 is

[1]These features appear as lines with a negative slope in charge yield vs. recoil energy plots. The slopes are due to charge noise affecting the estimate of Luke-Neganov-Trofimov (LNT) energy, and therefore recoil energy. If one is certain that a particular class of events is due to bulk electron recoils, a better recoil energy estimate can be obtained by substituting the recoil energy for the charge energy in the LNT term, and solving for recoil energy. This removes the poor resolution due to charge noise. The photon spectra in figures 4.10 and 4.11 are histograms of recoil energy obtained with this method. The line at 67 keV suffers from a further effect possibly due to the appearance of two pulses in the charge trace. The physics leading to this line is explained in Chapter 3.

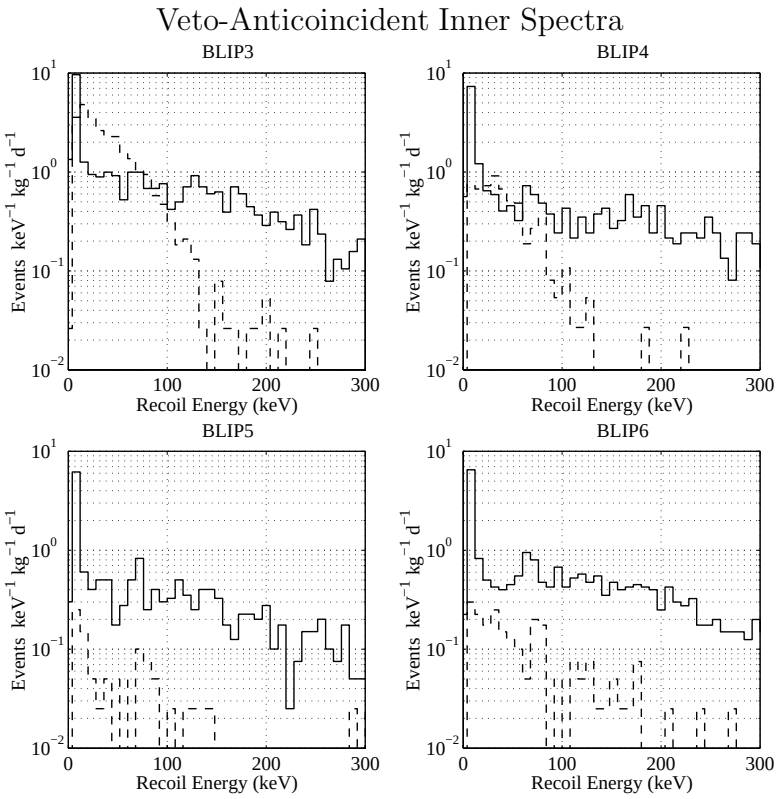

Figure 4.10: Single-scatter photon and electron spectra for veto-anticoincident inner events. Solid: photons. Dashed: electrons.

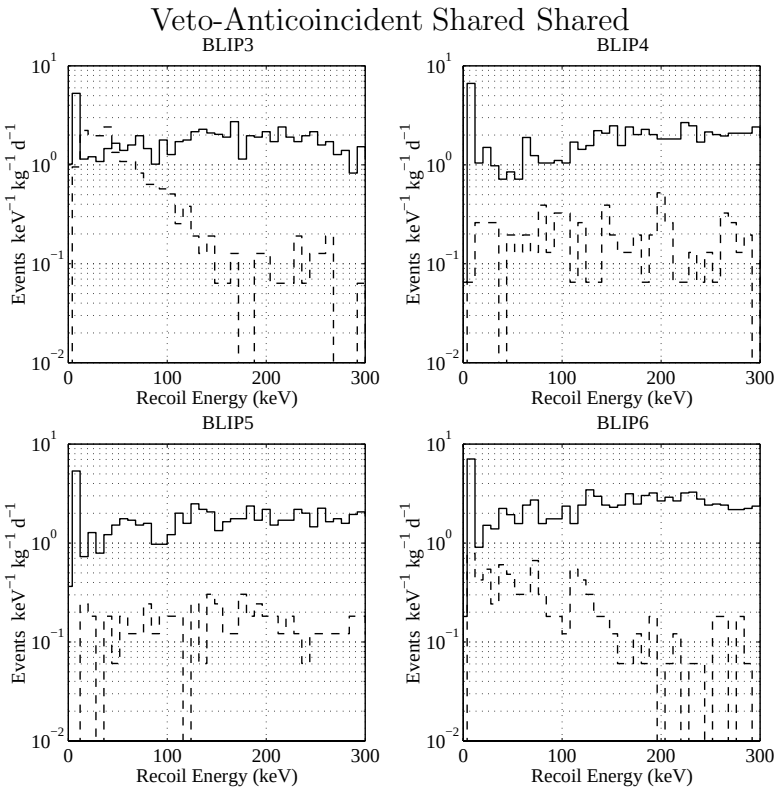

Figure 4.11: Single-scatter photon and electron spectra for veto-anticoincident shared events. Solid: photons. Dashed: electrons.

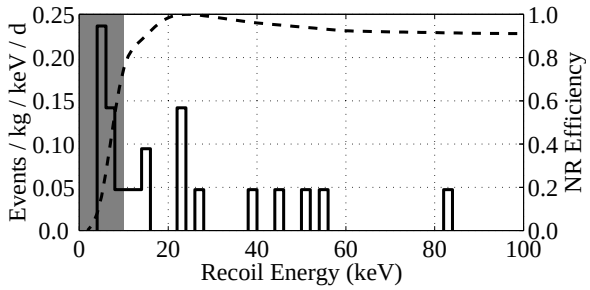

Figure 4.12: Recoil energy distribution of inner nuclear-recoil candidates. Shaded: 10 keV analysis threshold. Dashed curve: peak-normalized nuclear-recoil efficiency (right-hand scale).

due to the electron contamination on the surface of BLIP3.

4.6 Dark Matter Analysis

4.6.1 Veto-Anticoincident Nuclear Recoils

When both inner and shared events are considered, and all cut efficiencies are accounted for, the total exposure for nuclear recoils in Run 19 is 17.2 kg-days. The total number of nuclear-recoil candidates from the two plots in figure 4.9 is 27. Kolomogorov-Smirnov (KS) tests of the nearest veto-trigger times and event-times confirm that these events are consistent with a veto-anticoincident uniform-rate population. Figure 4.12 shows the energy distribution of nuclear-recoil candidates passing the inner cut. The dashed line indicating the nuclear-recoil-cut efficiency is calculated according to equation 4.3. The shaded region represents energies below the 10 keV threshold. A similar histogram for the inner+shared data set will soon be published in [2]. Before assuming that these events are indeed nuclear recoils, the possibility of contamination by misidentified electron recoils must be considered.

Using the photon misidentification parameters discussed in Chapter 3 and the number of photons in the veto-anticoincident data set,

the 90% CL upper limit on misidentified photons is 0.8, which is negligible compared to the above number of observed nuclear-recoil candidates. However, a similar estimate using surface electrons yields 20.6 as the 90% CL upper limit. In the following analysis, it is assumed that all 27 candidates are true nuclear recoils since this leads to conservative dark matter upper limits. However, there are several reasons to believe that most of these events are indeed nuclear recoils. First, the electron-misidentification parameters estimated from the electron calibration are statistics limited. Moreover, as noted in Chapter 3, two of the three events in the electron calibration that appear in the nuclear recoil band are clearly consistent with being neutrons rather than electrons. However, they are included in the analysis to arrive at a conservative estimate. Secondly, a clear charge-yield separation exists between surface electrons and the nuclear-recoil candidates as evident in figure 4.9. If surface-electron misidentification is the dominant effect a more uniform charge yield distribution is expected. A KS test of the nuclear-recoil candidate charge-yield distribution indicates that 70% of experiments will observe distributions with a higher deviation from the expected one.

The third reason to believe that electron misidentification is negligible comes from the veto-anticoincident multiple-scatter data set. Figure 4.13 shows ionization-yield versus ionization-yield for double scatters among BLIPs 4 through 6 in the veto-anticoincident data. The concentration of points at charge yields of 1 in both detectors correspond to photon multiple scatters. The points at slightly lower charge yield are consistent with surface electrons. The main feature to note in figure 4.13 is that the nuclear recoil candidates, which are circled, are clearly separated from the other points. If these four events are misidentified surface electrons, they have been misidentified in both detectors. Even with the

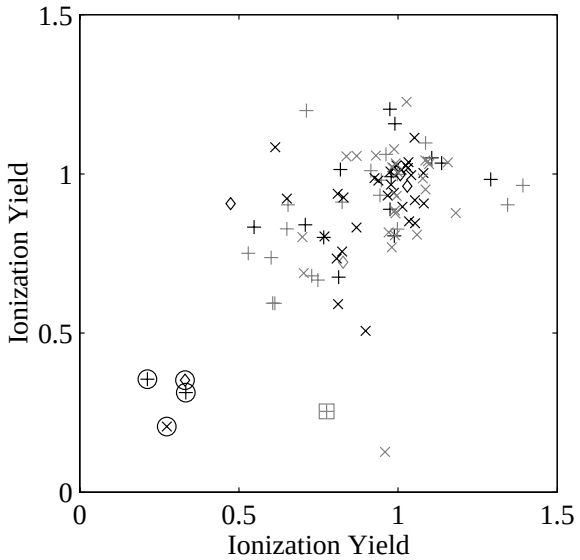

Figure 4.13: Scatter plot of ionization yields for veto-anticoincident double scatters in BLIPs 4 through 6. All points here are required to have at least one inner scatter (black) or shared scatter (grey). Both scatters are also required to be within 10-100 keV. Distribution among detectors: +: BLIP4/BLIP5; ◇: BLIP4/BLIP6; ×: BLIP5/BLIP6. Circled events are tagged as nuclear recoils in both detectors. The boxed event is tagged as a nuclear recoil in only BLIP4. Bulk electron-recoils and surface-electron events lie at charge yields of about 1 and 0.75, respectively. Non-nuclear-recoil candidates with low ionization yield (<0.6) in one of the two detectors have the low-yield hit in the outer electrode, consistent with the expectation of higher electron-recoil misidentification in outer events. Figure taken from [2]

high upper limit on surface-electron leakage, the probability of misidentification in two detectors is small: the 90% CL upper limit on misidentified surface-electron double scatters is 0.8. The presence of four multiple-scatter nuclear-recoils indicates that most of these are true nuclear recoils. As explained in the next section, the Monte Carlo prediction for the number of multiple scatters agrees with the number seen, under the assumption that all single-scatter nuclear recoils are due to neutrons.

4.6.2 The Neutron Interpretation

As argued in the previous sections, events passing the nuclear recoil cut are most likely due to true nuclear recoils. Therefore, multiple scatters passing nuclear-recoil cuts must be interpreted as true multiple-scatter nuclear recoils. Such an event set can only be attributed to a neutron background. Therefore, a certain fraction of single-scatters must also be due to this neutron background. The magnitude of this fraction is obtained from Monte Carlo simulations. Details of the simulation and expected background are given in Chapter 5. The dominant veto-anticoincident neutron background is expected to arise from high-energy muon interactions in the rock. As described below, Monte Carlo simulations of this background combined with the observed number of multiple-scatter neutrons indicate that all observed single-scatter nuclear recoils are consistent with neutron interactions.

There is another data set that lends credence to the neutron hypothesis. Figure 4.14 shows data from the Si ZIP detector operated during CDMS Run 18. Details regarding this data set can be found in Roland Clark's dissertation [4]. Four nuclear-recoil candidates are present in this data set which represents a total exposure of 1.5 kg-days after cuts. Since both spin-dependent and spin-independent WIMP-nucleon cross

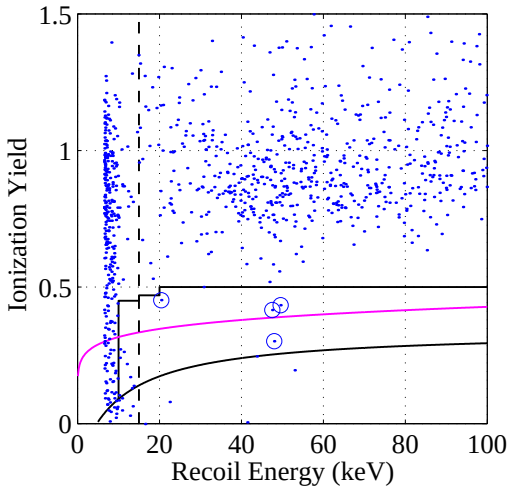

Figure 4.14: Ionization yield vs. recoil energy for veto-anticoincident events in the Run 18 Si ZIP detector. Light solid line: center of nuclear-recoil band. Dark solid lines: nuclear-recoil-acceptance region. Dashed line: nuclear-recoil analysis threshold (15 keV). Figure taken from [2].

sections are much smaller in silicon than in germanium, the probability of these events being WIMPs is negligible. If they are WIMPs, the implied rate of WIMPs in Ge BLIPs and other dark matter detectors worldwide is much higher than observed. Therefore, this data set measures the neutron background. The separation between nuclear and electron recoil bands is not very good in this data set. However, the circled points are likely to be true nuclear recoils. The confidence interval on the number of misidentified electrons is being calculated at present for inclusion in [2].

Since the final data set clearly includes neutron events, an estimate of the neutron background is used when setting dark matter limits. The absolute rate of veto-anticoincident neutrons predicted by the Monte Carlo is not used in the dark matter analysis due to the uncertainties involved. The nature of these uncertainties are explained in Chapter 5. The predicted fraction of multiple-scatters and the predicted rate for the Run 18 ZIP detector are used in the statistical "subtraction" of neutrons described in

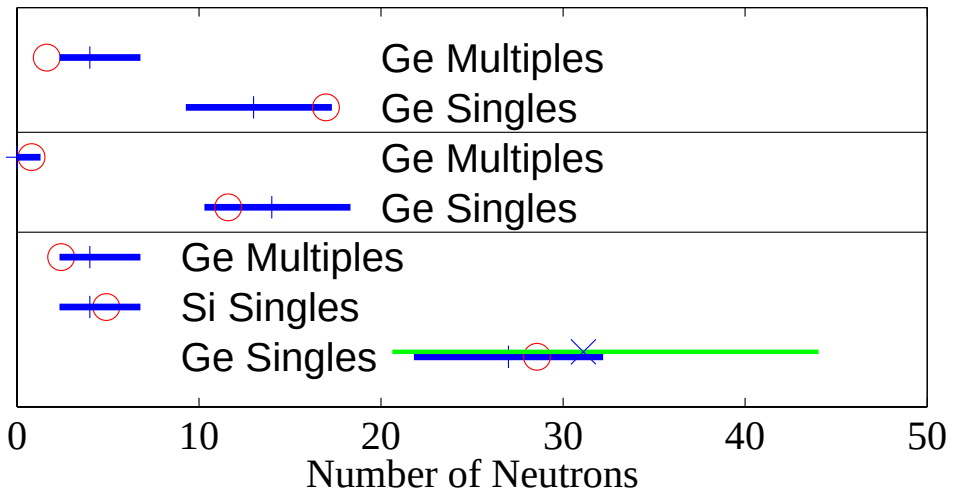

Figure 4.15: Schematic comparison of simulated and observed numbers of nuclear-recoil events for inner (top), shared (middle), and combined (bottom) data sets. The vertical marks and dark horizontal lines indicate the observed numbers of events and Feldman-Cousins 68% CL confidence intervals. The circles indicate the expected number of events when the simulated background is normalized to best fit the numbers of singles, multiples, and Si events jointly. The "×" and light line indicate the expected number of singles and corresponding 68% CL confidence interval when the simulated background is normalized to the simultaneous best fit of multiples and Si events. Figure taken from [2].

the next section. Figure 4.15 provides a convenient means for comparing predicted rates against the data. The upper, middle, and lower sections of figure 4.15 correspond to rate comparisons for inner, shared, and combined data sets. The vertical marks represent numbers of events obtained from the data. The dark lines around these marks represent the corresponding 68% Feldman-Cousins (FC) intervals [5]. The circles indicate the predicted rates when the Monte Carlo output is normalized to yield the best joint fit to the rates of single scatters, multiple scatters, and Si events. Except for the number of multiple scatters in the inner data set, all predictions fall within the indicated confidence intervals. Another comparison using only the Si and multiple scatter rate as input is shown for the combined (inner and shared) data. The "×" and the light line around it indicate the expected single scatter rate and its 68% FC interval, when the best fit to the Si and multiple scatter rates is used. This plot indicates that the observed rates are in good agreement with predicted rates under the neutron hypothesis. The predicted recoil energy spectrum is also in good agreement with the observed spectrum. For the combined data set, a KS test indicates that 69% of experiments would yield observed spectra with larger deviations from the prediction. The shape of the expected recoil energy spectrum due to high-energy external neutrons is given in Chapter 5.

4.6.3 Upper Limits on WIMP Dark Matter

The results of dark matter experiments are summarized in plots like figure 4.16. Before discussing the content of figure 4.16, I will outline the interpretation of such a plot and the analysis that went into making the CDMS contour. Each curve on figure 4.16 divides the WIMP-nucleon cross-section (σ) versus WIMP mass (M) plane into two regions. The regions above and below a curve are the excluded and allowed regions

respectively, at the 90% confidence level. Therefore, these curves represent the 90% CL upper limits on WIMP-nucleon cross section as functions of WIMP mass. Even though the definitions of the excluded and allowed regions may seem intuitively clear, it is important to explicitly state their definitions to avoid confusion.

Given a set of "theoretical" parameters θ, which in this case consists of M and σ, the probability of obtaining a set of measurements more "favorable" than the actual measurements X, is denoted $P(X|\theta)$. Here, "favorable" simply means more likely, given the theory θ. In a classical treatment, $P(X|\theta) > 0.9$ for points in the 90% CL excluded region. Thus, at least 90% of measurements made would be more likely than the current one for θ in the excluded region. Of course, the allowed region is the set of points about which the same cannot be said. In other words, the current measurement is in the top 90% of likely results for θ in the allowed region. This is precisely how figure 4.16 should be interpreted. A more commonly used and satisfying 90%-allowed region is the Bayesian one which has a 90% probability of containing the true theory. This definition does *not* apply to figure 4.16 because obtaining $P(\theta|X)$ from $P(X|\theta)$ using Bayes theorem requires knowledge of $P(\theta)$, the probability density of theories. Given the lack of consensus on which (M, σ) are more likely than others, we must be content with the classical confidence regions defined above. The two definitions become equivalent in the limit of high statistics and other requirements. This is not the case for CDMS at present.

To rank the likelihood of a particular result X, it is customary to use the likelihood ratio

$$R = \frac{\mathcal{L}(X|\theta)}{\hat{\mathcal{L}}(X|\hat{\theta})} \tag{4.4}$$

where $\mathcal{L}(X|\theta)$ is the likelihod for obtaining X given θ and $\hat{\mathcal{L}}(X|\hat{\theta})$ is the maximum likelihood for X which occurs at $\hat{\theta}$. Note that R is higher for

more likely outcomes. The Feldman-Cousins likelihood ratio [5], used in the method described below, is distinguished by the requirement that $\hat{\theta}$ lie within the physically allowed parameter space. The "neutron subtraction" amounts to including the neutron background n in the set of parameters θ. Here, n is the trial expectation value for the number of neutron events in the Run 19 data set. It is varied along with σ and M on a three dimensional grid of points to find the 90% CL allowed region in (σ, M, n) parameter space[2].

In the following, $\{E_i\}$ is the set of Ge-single-scatter recoil energies, N_{d} is the number of Ge multiple-scatters, and $N_{\mathrm{S}i}$ is the number of Si events. Consider a particular point on the (σ, M) plane. For that choice of σ and M, the likelihood ratio

$$R = \frac{\mathcal{L}(\{E_i\}, N_{\mathrm{d}}, N_{\mathrm{Si}} | \, \sigma, M, \tilde{n})}{\widehat{\mathcal{L}}(\{E_i\}, N_{\mathrm{d}}, N_{\mathrm{Si}} | \, \hat{\sigma}, \hat{M}, \hat{n})} \tag{4.5}$$

is evaluated, where the denominator is the global maximum of the likelihood as before and $\tilde{n}$ is the value of n that yields the maximum likelihood for the observed data given σ and M. Next, for a range of n at this particular σ and M, a series of experiments with Ge and Si exposures identical to CDMS I are simulated. An R value is calculated according to equation 4.5 for the outcome $(\{E_i\}, N_{\mathrm{d}}, N_{\mathrm{S}i})$ of each simulated experiment. Then, the R value of the *real* data R_0, is compared with the distribution of R values obtained from the simulations. If R_0 is in the top 90% of simulated R values, that point in (σ, M, n) space is allowed at the 90% confidence level. The parameter n is of no interest when setting dark matter limits. Therefore, it must be projected out. This is done conservatively by including the current choice of σ and M in the allowed region if any grid point along n is allowed for these σ and M. The CDMS

[2]In practice, a grid of points in (M, n) space is spanned to find the σ at the border between the allowed and excluded regions.

upper limit of figure 4.16 is obtained by repeating this process at all reasonable values of σ and M.

Details on calculating the likelihood function for points in (σ, M, n) parameter space are given in [6]. WIMP rates and recoil energy spectra in Ge and Si for particular values of σ and M are obtained from the standard methods outlined in [7]. In particular, the spin-independent Woods-Saxon (Helm) form factor and the assumption of coherent ($\sim$ A^2) scattering are used. Note that the upper limits shown in figure 4.16 apply only to the spin-independent cross-section. The standard values for characteristic WIMP velocity $v_0 = 220$ km/sec (where v_0 is the dispersion in the assumed Maxwell-Boltzmann velocity distribution relative to the galactic rest frame), galactic escape velocity $v_{esc} = 650$ km/sec, mean earth velocity relative to the galactic rest frame $v_E = 232$ km/sec, and local halo density $\rho = 0.3$ GeV/c^2/cm^3 are used [2]. All upper-limit curves in figure 4.16 have been obtained using these standard assumptions. A brief discussion on WIMP rates, spectra, and reasonable ranges for the above parameters is contained here in Chapter 1.

The Ge neutron spectrum, the Ge multiple-scatter fraction, and the Ge-to-Si ratio are obtained from the Monte Carlo simulation described in Chapter 5. Since the probability of WIMP multiple scatters is negligible, the shape of the Ge-multiple-scatter spectrum is independent of σ, M, and n. Therefore, it is not included in the likelihood function. Even though a small contribution from WIMPs is allowed to enter the Si event rate, the shape of the Si spectrum is not used in the likelihood function because its influence on the result would be negligible. Finally, the rates and spectra due to WIMPs and neutrons are combined with the efficiencies described in this chapter to obtain the final form of the likelihood function.

Neglecting photon and electron misidentification in the Ge data set

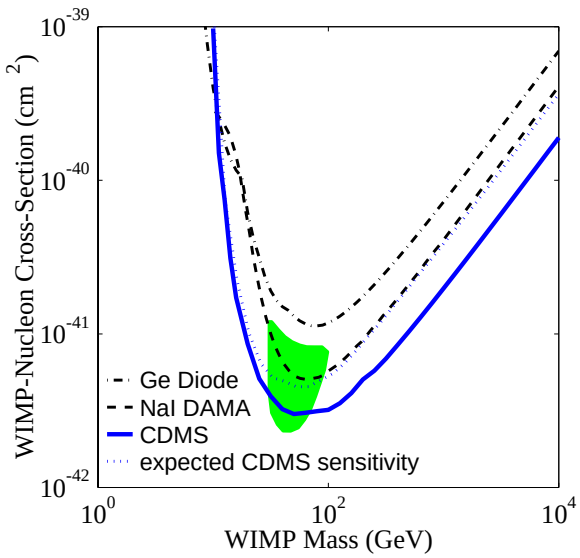

Figure 4.16: Spin-independent σ vs. M limit plot. The regions above the curves are excluded at 90% CL. Solid curve: limit from CDMS. Dashed curve: DAMA limit using pulse-shape analysis [8]. Dash-dotted curve: Ge diode limit, lead by Heidelberg-Moscow [9] and IGEX [10] groups. Shaded region: DAMA 3σ allowed region [11].

leads to conservative WIMP upper limits unless, contrary to expectation and data presented in the previous sections, the multiple-scatter data set is contaminated preferentially by photons and electrons. Therefore, electron-recoil misidentification in the Ge data set is ignored. However, since electron-recoil misidentification in Si would lead to a lower estimate of the neutron background and hence a larger contribution from WIMPs, it *is* considered when constructing the likelihood function. The number of misidentified electron-recoils in the Si data is set at 0.76, the 90% CL upper limit from a previous analysis.

Figure 4.16 contains 90% CL upper limits on the spin-independent WIMP-nucleon cross-section from CDMS data and other experiments. The CDMS limit included in this figure is from a previous analysis including only inner events. Exclusion limits based on a new analysis using the inner

and shared data sets are being calculated presently and will be published in [2]. As seen in figure 4.16, a significant part of the 3σ region allowed by the DAMA-NaI annual modulation experiments [11] is excluded by CDMS at the 90% confidence level. The whole region is ruled out at a 71% confidence level. More importantly, new regions of parameter space are ruled out by CDMS.

As mentioned above, the parameters recommended in [7] are used to obtain all the curves of figure 4.16. Some of these parameters have significant uncertainties. For instance, the halo density is known only upto a factor of a few due to the large uncertainty in the halo structure and lack of knowledge on the contribution of WIMPs to the halo density. The mean earth velocity is also not known to three significant figures, as qouted above, due to the uncertainty of the sun's velocity in the galactic rest frame. Therefore, the absolute positioning of curves in figure 4.16 are uncertain by a factor of a few. However, since all exclusion curves are obtaned from the same set of assumed parameters, this figure provides a fair comparison between the sensitivities of limit-setting experiments. On the other hand, results of an annual modulation search such as DAMA are more senitive to inaccuracies in velocity estimates and the particular halo model used. Therefore, the confidence level at which CDMS data rule out the DAMA claimed region is model dependent. Recent work by C. Copi *et.al* [12] indicate that CDMS and DAMA data are not incompatible under certain halo models.

References

[1] Sunil Golwala. *Exclusion Limits on the WIMP-Nucleon Elastic-Scattering Cross-Section from the Cryogenic Dark Matter Search*. PhD thesis, The University of California at Berkeley, Fall 2000.

[2] D. Abrams et al. Exclusion Limits on the WIMP-Nucleon Cross-Section from the Cryogenic Dark Matter Search. Will appear in Physical Review D., 2001.

[3] R. Abusaidi et al. Exclusion Limits on the WIMP-Nucleon Cross-Section from the Cryogenic Dark Matter Search. *Physical Review Letters*, 84:5699, 2000.

[4] Roland Clarke. *An Athermal Phonon Mediated Dark Matter Detector with Surface Event Discrimination*. PhD thesis, Stanford University, May 1999.

[5] G.J. Feldman and R.D. Cousins. *Physical Rev. D*, 57:3873, 1998.

[6] Richard Schnee. Calculating Limits Following Feldman and Cousins. Memo to the CDMS collaboration, April 2001.

[7] J.D. Lewin and P.F. Smith. *Astropart. Phys.*, 6:87, 1996.

[8] R. Bernabei et al. *Phys. Lett. B*, 389:757, 1996.

[9] L. Baudis et al. *Phys. Rev. D*, 59:022001, 1999.

[10] A. Morales et al. hep-ex/0002053. Submitted to Phys. Lett. B, 2000.

[11] R. Bernabei et al. *Phys. Lett. B*, 480:23, 2000.

[12] C. Copi. Private communication.

Chapter 5

The Neutron Background in CDMS I

5.1 Introduction

Evidence of a residual background in the CDMS I data was presented in Chapter 4. In this chapter, I will describe studies into this background and the conclusions drawn. Based on the arguments presented in Chapter 4, it is very unlikely that this background is due to leakage of photons or electrons into the nuclear recoil band. Therefore, the studies described below are based on the premise that the residual background is due to neutrons.

Direct use of Run 19 data indicates that the scintillator veto has an efficiency of about 99.9% [1] for muons. A somewhat higher efficiency was observed in Run 18 [2]. Because a significant number of muons that give rise to neutrons are captured within the shield by nuclei as explained below, and therefore pass through only one veto counter, the veto inefficiency is about a factor of three higher for muon induced neutrons (efficiency $\simeq$ 99.7%). Using this efficiency and the veto-coincident neutron rate, the expected veto-anticoincident neutron rate due to veto inefficiency is estimated to be smaller than 20% of the observed background rate [1]. Therefore, the majority of background neutrons are not related to muon

interactions within the shield. Neutrons unrelated to muons originating within the shield and neutrons from outside the shield, muon induced or otherwise, are the two possible sources of this background.

There are no muon-induced neutron production mechanisms that occur on timescales long as compared to the 25 μsec veto-coincidence window. Therefore, veto-anticoincident neutrons from within the shield may originate from (α,n) reactions and spontaneous fission associated with uranium and thorium chain contamination in the detector environment. Actually, alphas produced in these decay chains are below the threshold energy needed for (α,n) reactions in materials with atomic number (Z) greater than 16 [3]. Therefore, veto-anticoincident neutron production in the lead and copper surrounding the detectors is dominated by spontaneous fission. Because of their low energy (see below), only material within the polyethylene need be considered when calculating detection rate of fission neutrons. Given a 1 ppb uranium contamination in the approximately 500 kg of material within the polyethylene, the number of neutrons produced during the entire raw live-time of Run 19 is estimated to be about 70. Applying the detection to production ratio obtained from the Monte Carlo of muon-induced neutrons from copper and inner lead, this leads to an estimate of 0.7 neutrons or fewer in the entire Run 19 data. This is an overestimate since the true level of contamination in the high-purity near-detector materials is expected to be lower than 1 ppb [4]. Since the Run 19 data are consistent with several tens of neutrons, the dominant neutron background must originate from outside the shield.

5.2 Possible Sources of External Neutrons

5.2.1 Neutrons from Cosmic-ray Muons

Muons are produced high in the Earth's atmosphere mainly from the decay of pions and kaons produced by primary cosmic rays [5]. The flux of muons at the earth's surface is about 170 muons/m^2/sec [4] with an average energy of about 4 GeV [5]. For muons propagating through the earth, the energy loss mechanisms can be divided into two broad categories, ionization losses and radiative losses.

Ionization energy loss occurs due to the microscopic electric field in the material traversed by muons, and is given as a function of muon energy by the Bethe-Bloch formula [5]. Since most muons are relativistic, the energy loss per unit path length will be close to the minimum ionizing energy and depend only slightly on muon energy. The energy lost by muons will mainly be transferred to electrons in the traversed medium. Although this can be thought of as a continuous process for the most part, a large amount of energy can occasionally be imparted to an individual electron. These electrons which have enough energy to produce ionizing tracks of their own are called delta-rays.

The radiative losses result from muon-bremsstrahlung, direct pair production by muons, and muon-nuclear interactions. The average energy loss per unit path length from all three of these stochastic processes increases as a function of muon energy [5].

Muon-induced neutron production can proceed through three channels. They are,

1. Neutron emission following negative muon capture by a nucleus
2. Neutrons resulting from electromagnetic showers caused by the delta-rays, bremsstrahlung, and pair production

3. Neutrons from direct muon-nuclear interactions, which at high energy (energy transfer > 100 MeV) is dominated by secondaries in the resulting nuclear showers.

In general, the rate and relative importance of muon-induced neutron production mechanisms depend on muon energy. Therefore, shielding and background issues related to neutrons depend on site depth.

In the first process, slow negative muons can be captured by the Coulomb field of a nucleus to form *muonium*. On a time time scale of about 10^{-11} sec, the muon cascades down to the $1s$ atomic orbital and either decays to an electron, neutrino, and antineutrino, or gets captured by the nucleus [6] via

$$\mu^- + p \rightarrow n + \nu_\mu. \tag{5.1}$$

The resulting neutron may escape without interacting in the nucleus (direct emission) or cause a nuclear excitation which will eventually result in the emission of a few low-energy evaporation neutrons. The neutron spectrum in rock from these two processes is estimated using measurements in [6, 7] to be

$$\frac{dN}{dE} = \begin{cases} 0.38E^{5/11}\exp(-E/1.7) & \text{for } E < 4.5 \text{ MeV} \\ 0.1\exp(-E/7) & \text{for } E > 4.5 \text{ MeV} \end{cases} \tag{5.2}$$

where the energy E is in MeV [4]. Here, no normalization is implied by the constant pre-factors. They simply serve to make the spectrum continuous at 4.5 MeV. Later, an overall normalization is applied to give the estimated rate of neutrons following this spectrum. This spectrum is similar to the "internal production" spectrum in figure 5.5. This type of spectrum is generally called an "evaporative" spectrum, although only the part below 4.5 MeV is truly evaporative (neutrons emitted due to an increase in nuclear "temperature"). The average neutron multiplicity from muon capture depends on the material and ranges from 0.7 to 1.7 [8]. Although the

neutron contribution from muon capture is important for the CDMS I site, it is negligible for deeper sites where the muon spectrum is much harder.

In the second process, neutron production in electromagnetic showers proceeds mainly through (γ,n) and (γ,Xn) interactions of photons in these showers [9]. The spectrum of photons in electromagnetic showers falls of as $1/E^2$ [9, 10]. Therefore, most interactions proceed through the "giant dipole" resonance which occurs in most nuclei between 10-30 MeV [10, 11]. The resulting spectrum of neutrons can be approximated by equation 5.2 because they undergo similar process as the ones described for neutrons from negative muon capture. Therefore, in the following, neutrons from muon capture and electromagnetic showers are treated together, using the spectrum of equation 5.2. The combined production rate of evaporative neutrons in rock is estimated to be (41 ± 4) neutrons/kg/day [3, 4].

The third process, muon-nuclear interactions, are mediated by virtual photons. At low energies, this interaction proceeds through the giant dipole resonance yielding neutrons with roughly the same evaporation spectrum given above for the first two processes [10, 9, 11]. Therefore, a small contribution form these neutrons are also folded into the rate quoted above for evaporative neutrons. However, the spectrum of virtual photons goes as $1/E$ [10] and therefore becomes more important at high energy than real photons in electromagnetic showers. When the energy transfer exceeds the pion production threshold, these interactions give rise to hadron showers. The cross-section for this process and the resulting neutron multiplicity depends on muon energy [9, 12]. At a few hundred GeV of shower energy, the neutron multiplicity is about one hundred, an order of magnitude greater than the neutron multiplicity from an electromagnetic shower with the same energy [9]. For a shower with 2 GeV

of energy or more, the spectrum of primary neutrons is generic to all particles in the shower and is obtained from a compilation of measured spectra contained in [12]. This spectrum is parametrized as [13]

$$\frac{dN}{dE} = \begin{cases} 6.05\exp(-E/77) & \text{for } E < 200 \text{ MeV} \\ \exp(-E/250) & \text{for } E > 200 \text{ MeV} \end{cases} \tag{5.3}$$

Again, the energy E is given in MeV and the prefactor is used simply for continuity of the spectrum. As the number of particles in the shower multiplies, the neutron spectrum eventually approaches the evaporative form [9] given in equation 5.2. The neutron production rate in hadron showers does not decrease with depth as fast the muon intensity. An increased neutron multiplicity due to a higher mean muon energy at greater depths is responsible for this effect. In general, the multiplicity goes as $<E_s>^{0.7}$ where $<E_s>$ is the average shower energy at a given depth [9, 14].

Estimating the neutron production rate from hadron showers at the SUF depth is non-trivial. Most of the literature on the subject deals exclusively with deeper sites. We have used a neutron flux measurement carried out at the SUF by M. Chen *et al* [15] to estimate the neutron production rate. This measurement was confined to the neutron energy window between 11.5 MeV and 50 MeV. Since the evaporation spectrum of equation 5.2 still contributes to this energy range, the contribution from hadron showers must first be deconvolved. The authors of [15] conclude that 62% of the measured flux is due to this high energy neutron component. We have used a GEANT Monte Carlo with equation 5.3 as the input spectrum to generate neutrons isotropically in a 5 m shell of rock[1] in order to determine the resulting flux in the rock cavity in the 11.5-50 MeV range. The flux quoted in [15] is obtained at a neutron production rate of (4.14 ± 0.03) neutrons/kg/day in rock. Therefore, in the simulations

[1] Increasing the rock-shell size further does not alter the flux, which indicates that these neutrons have mean path-lengths smaller than 5 m.

discussed in section 5.7, this value is used as the neutron production rate from hadron showers. Extrapolations of measurements at deeper sites [9, 16] indicate that the above production rate is not unreasonable. Combining these extrapolations with the measurement error quoted in [15], the true production rate is estimated to be 5±3 neutrons/kg/day.

As argued below, the residual background of CDMS I is dominated by high energy neutrons from hadron cascades. Removing the large uncertainty associated with this production rate is a major motivation for the FLUKA based simulation discussed below. Note however, that the neutron subtraction described in Chapter 4 does not depend on correctly estimating the production rate. It is based on the normalization-independent Ge singles/multiples and Ge/Si ratios of neutrons. However, a more accurate estimate of absolute rates is desirable to assure ourselves that this background is indeed dominant.

5.2.2 Neutrons from Natural Radioactivity

As described in Chapter 2, the other neutron background external to the shield is due to natural radioactivity. These neutrons arise mainly from (α,n) reactions induced by α emission in the uranium and thorium radioactive chains. There is also a smaller contribution from spontaneous fission of uranium [3]. The combined neutron production rate in rock from these two processes is estimated to be (34 ± 3) neutrons/kg/day [3, 4]. Compared to other neutron production mechanisms discussed above, neutrons from natural radioactivity have a very soft spectrum, with a steep fall-off above 2 MeV. A typical fission spectrum [17] given by

$$\frac{dN}{dE} = E^{1/2} \exp(-E/1.29) \tag{5.4}$$

is used to model these neutrons. Again, the neutron energy E is in MeV.

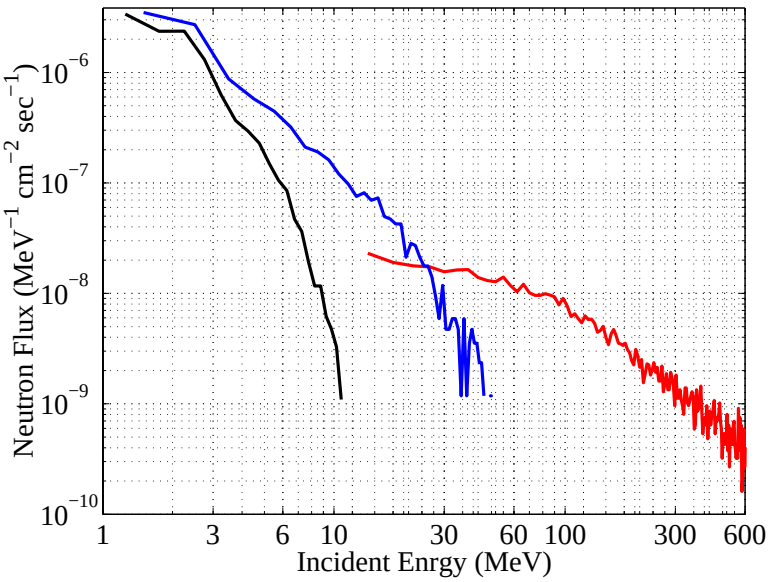

Figure 5.1: Flux-normalized neutron spectra at the SUF from simulations of neutron production mechanisms external to the shield. As described in the text, the high-energy spectrum is due to primary neutrons from hadron showers. The evaporative spectrum is due to negative muon capture, electromagnetic showers, and low-energy virtual photons in direct muon-nuclear interactions. The natural radioactivity spectrum refers to neutrons from (α,n) reactions and fission.

5.2.3 Rates and Spectra of External Neutrons

The *standard* neutron production rates quoted above for the evaporative spectrum and natural radioactivity were used by Angela Da Silva to simulate the neutron flux in the SUF. The good agreement between measurements with a BF_3 counter and these simulations indicates that the production rates given above are reasonable. Based on older literature, a higher rate of shower neutrons than quoted above was used in these simulations (19 neutrons/kg/day). However, they did not contribute significantly to the data-to-simulation comparison in [4] because the BF_3 counter is insensitive to neutrons above a few tens of MeV.

Using these production rates for the evaporative and natural

	Natural radioactivity	Evaporative	Shower
Production Rate in Rock (n/kg/day)	34±3	41±4	4.14±0.03
Flux in SUF $\times 10^6$ (n/cm^2/sec)	5.7±0.5	9.9±1.0	2.14±0.02
Detection Rate (n/day)	$(2.1 \pm 0.6) \times 10^{-4}$	0.017±0.002	1.1±0.1

Table 5.1: Production rates, fluxes and detection rates for the three possible sources of external neutrons. The third row corresponds to the detection rate when the whole detector mass of BLIPs 3 through 6 are used. Uncertainties given for shower neutrons are simply the statistical errors in the methods used to arrive at these estimates. The systematic uncertainty, due to lack of knowledge about the production rate, is described in the text.

radioactivity components and the new value (4.14 neutrons/kg/day) for shower neutrons, the flux and spectrum of neutrons in the SUF were simulated with a GEANT Monte Carlo. Neutrons from each source were generated isotropically according to the above spectra in a 5-m shell of rock surrounding a cavity representing the SUF tunnel. The resulting flux-normalized spectra are shown in figure 5.1. The first and second rows of table 5.1 summarizes production rates and fluxes from the three possible sources of external neutrons. It is the third row of this table that clearly indicates the importance of shower neutrons over the other sources. I will now describe the simulations that were used to make this estimate.

5.3 Studies of Neutron Shielding and Detection in CDMS I

5.3.1 Importance of Neutrons from Hadron Showers

In the simulations described below, an artificial spectrum of neutrons was used to study the shield performance at various neutron energies. A

(a)

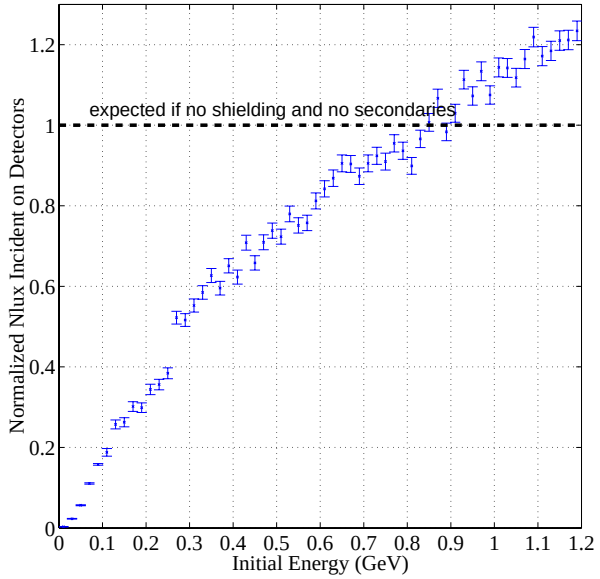

(b)

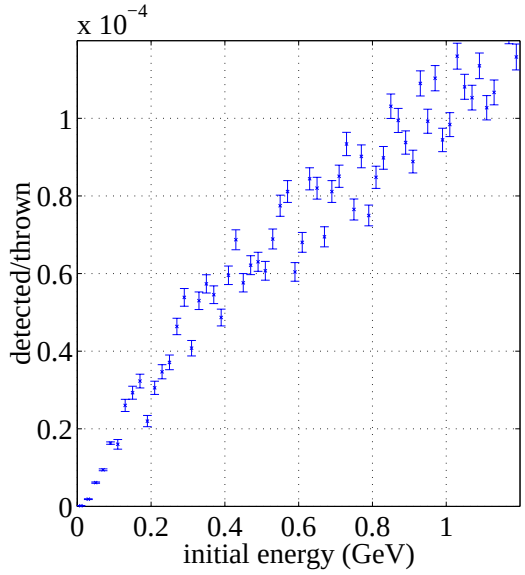

Figure 5.2: Penetration and detection probability of neutrons as a function of neutron energy outside the shield. (a) The penetration probability is normalized to yield unity when no shielding material is present. The "apparent excess penetration" above 800 MeV is due to production of secondaries. (b) the fraction of neutrons giving rise to detector interactions as a function of neutron energy outside the shield.

spectrum of isotropic neutrons was thrown from the surface of a $220 \times 220 \times 220$ cm cube surrounding the shield. Internal to the shield, the full Run 19 geometry including the germanium BLIP detectors was used. For each initial neutron energy at the throwing surface, the resulting flux of neutrons at the detectors was obtained. At a given initial neutron energy, the ratio of the resulting internal flux to the total thrown at that energy is proportional to the probability that neutrons of this energy will penetrate the shield. The solid curve of figure 5.2(a), obtained from these simulations, is proportional to this probability. Figure 5.2(a) is normalized so that the dashed line at unity represents the expected flux of neutrons at the detectors in the absence of intervening material.

As expected, the rise of this curve with initial neutron energy indicates that higher energy neutrons are more successful at penetrating the shield. The slope of this curve is steepest below 100 MeV. This indicates that evaporative and natural-radioactivity neutrons are well shielded. Although high-energy neutrons are more likely to penetrate the shield, figure 5.2(a) by itself does not imply that they will yield a higher interaction rate in detectors; these highly penetrative neutrons may pass through the detectors without interacting. However, figure 5.2(a) does provide a hint that the interaction rates are also higher for initial neutrons of high energy. For initial neutrons with energy greater than 800 MeV, the solid curve lies above the dashed line. This is due to the production of secondaries by high-energy neutrons. As explained above, the final generation of neutrons from hadron showers is expected to follow a evaporative spectrum. If secondaries from high energy neutrons form such an evaporative spectrum within the shield, a significant fraction of these will interact in detectors, as evidenced by the veto-coincident neutrons described in Chapter 3. Later, I will show that secondaries of high energy

primary neutrons do indeed form an evaporative spectrum within the shield.

Figure 5.2(b) shows the probability of a detector interaction for a neutron of given energy at the throwing surface described above. Interactions in any part of BLIPs 3 through 6 are accepted. This plot clearly indicates that high-energy neutrons yield higher interaction rates. The third row of table 5.1 was obtained by scaling the fluxes in the second row by the throwing-surface area and convolving the corresponding spectra in figure 5.1 with the detection probability of figure 5.2(b). According to this simulation and the arguments presented above, neutrons from hadron showers are found to dominate the veto-anticoincident neutron rate in detectors.

5.3.2 Spectrum Independence of Results

Figure 5.3 shows the energy spectra of neutrons incident on detectors for a range of initial neutron energies. The three plots show the incident spectra in three energy ranges. These spectra have been arbitrarily normalized to allow for a visual comparison between spectral shapes. The dashed lines show the neutron production spectrum used for evaporative neutrons generated in the lead and copper by low energy muon interactions. This is the spectrum given in Chapter 3 with regard to the veto-coincident neutron simulations. Details on the shape and physics of this spectrum can be found in Angela Da Silva's dissertation [4].

The three plots of figure 5.3 show that the low-energy parts of neutron spectra incident on detectors is independent of the initial neutron energy. This feature is especially clear for incident energies below 10 MeV where the interaction cross section for germanium and silicon is highest. While this low-energy spectrum is dominated by secondary neutrons, the flat spectrum above 20 MeV or so is presumably due to down-scattered

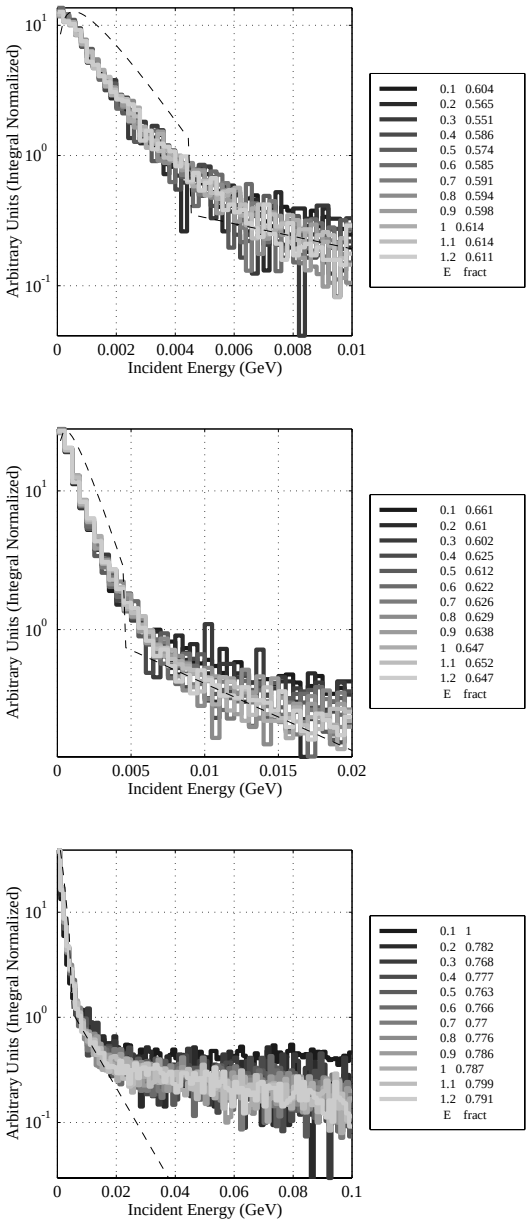

Figure 5.3: Spectra of neutrons incident on detectors for a range of initial neutron energies. The three plots correspond to three incident energy ranges. The first two columns of each legend defines the color coding where the initial neutron energy is expressed in GeV. For each near-detector incident-energy spectrum, the third column gives the fraction falling within the energy range of each plot. These spectra have been arbitrarily normalized to allow for a visual comparison between spectral shapes. The dashed line shows an the muon-coincident evaporative spectrum in lead and copper.

primaries. The good agreement between the dashed line and simulation results indicate that high-energy neutrons do indeed produce secondaries with an evaporative distribution. This part of the GEANT-FLUKA-MICAP simulation is handled by the FLUKA code since it is used for propagating neutrons above 20 MeV. In the version of FLUKA distributed with the GEANT Monte Carlo package, nuclear excitations and subsequent particle emission in the energy range of interest (< 2.5 GeV) is handled by the PEANUT (PreEquilibrium Approach to NUclear Thermalization) and EVAP codes [18]. Figure 5.3 shows good agreement between the results from these codes and the expected evaporative spectrum. For each initial energy, the figure legends give the fraction of near-detector neutrons falling within the energy range of that plot. These numbers indicate that for all initial energies considered, a significant fraction of resulting neutrons lie at low energy. In particular, more than 50% of neutrons caused by high energy primaries have energies below 10 MeV.

Due to the uniformity of incident spectra from initial neutrons of various energies, the resulting recoil energy spectra, singles/multiples ratios, and Ge/Si ratios will be independent of the initial energy to a good approximation. The recoil energy spectra are roughly exponential. Figure 5.4(a) shows the means of these recoil energy spectra as a function of initial neutron energy. Figure 5.4(b) shows the fraction of multiple scatters as a function of initial neutron energy. These plots show that the normalization-independent quantities used in the neutron subtraction are robust with respect to the primary energy of penetrating neutrons. Therefore, inaccuracies in the spectrum used for primary neutrons from hadron showers (equation 5.3) will have very little effect on the dark matter limits set by CDMS I. Note however, that the absolute event rate, not used

(a)

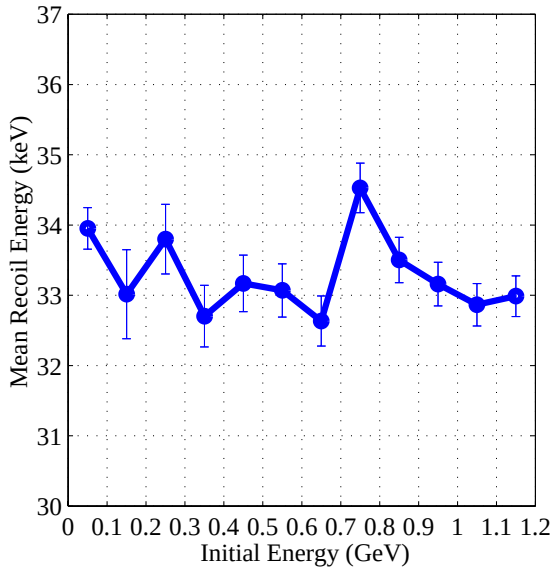

(b)

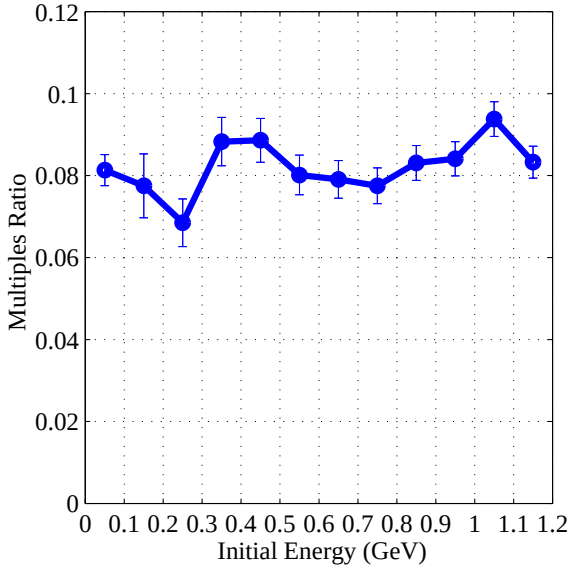

Figure 5.4: The dependence of mean recoil energy and multiples fraction on initial neutron energy.

in obtaining the final results, does depend on the external energy spectrum as evidenced by figure 5.2.

The similarity between low-energy incident spectra from high energy primaries, and the veto-coincident neutron generation spectrum is also important. This similarity implies that the reliability of Monte Carlo predictions can be tested by data-to-Monte Carlo comparisons for veto-coincident neutrons since both are based on the evaporative spectrum incident on detectors. As shown in Chapter 3, the recoil-energy spectrum and singles/multiples ratio, which are the normalization independent quantities, are well predicted by the Monte Carlo for this data set as well as the lower energy ^{252}Cf neutron calibration data.

5.4 Predictions of External Neutron Monte Carlo and Comparisons with Data

Even though the predictions of the above simulation are quite robust, an explicit Monte Carlo of neutrons from hadron showers is performed to obtain the spectrum, singles/multiples ratio, and Ge/Si ratio for the CDMS I neutron background. As in the Monte Carlo used for the study described above, neutrons are thrown from the surface of a $220 \times 220 \times 220$ cm cube external to the shield. As mentioned before, the flux and spectrum of neutrons at the cube surface is obtained by generating neutrons in a 5 m shell of rock surrounding the experimental volume. The production rate quoted in table 5.1 and the production spectrum of equation 5.3 are used. This production spectrum is shown by the solid curve of figure 5.5. The resulting flux is given in table 5.1. The resulting spectrum incident on the throwing surface is given by the histogram in figure 5.5. This spectrum is also shown in figure 5.1. The dashed line in figure 5.5 represents the evaporative neutron spectrum in lead and copper

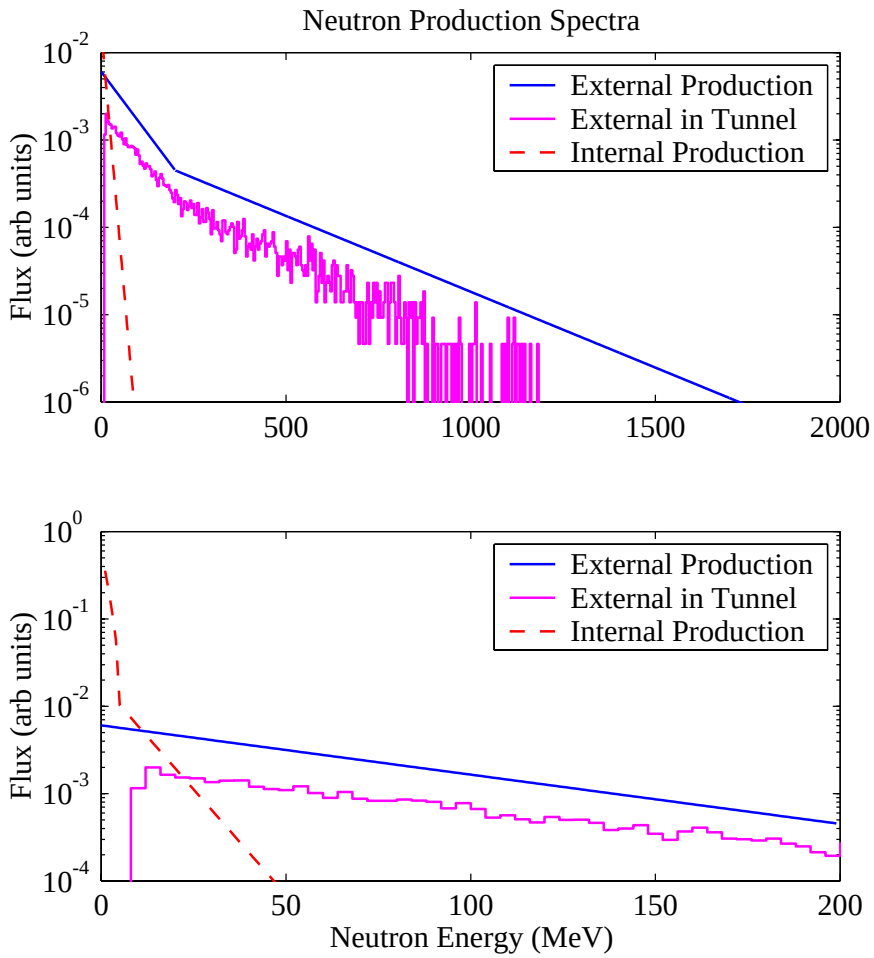

Figure 5.5: Production and ambient spectra of external neutrons at the SUF. The internal neutron production spectrum is also included for comparison.

used in the veto-coincident neutron simulations described in Chapter 3. It is included here for comparison. In the figure legend and below, this spectrum is referred to as the "internal neutron" spectrum because it represents the dominant muon-induced neutron population internal to the shield. Neutrons from hadron showers in the rock are usually referred to as "external neutrons". Thus, the Monte Carlo described here is called the "external neutron Monte Carlo".

Inside the shield, the Run 19 geometry is used to obtain the

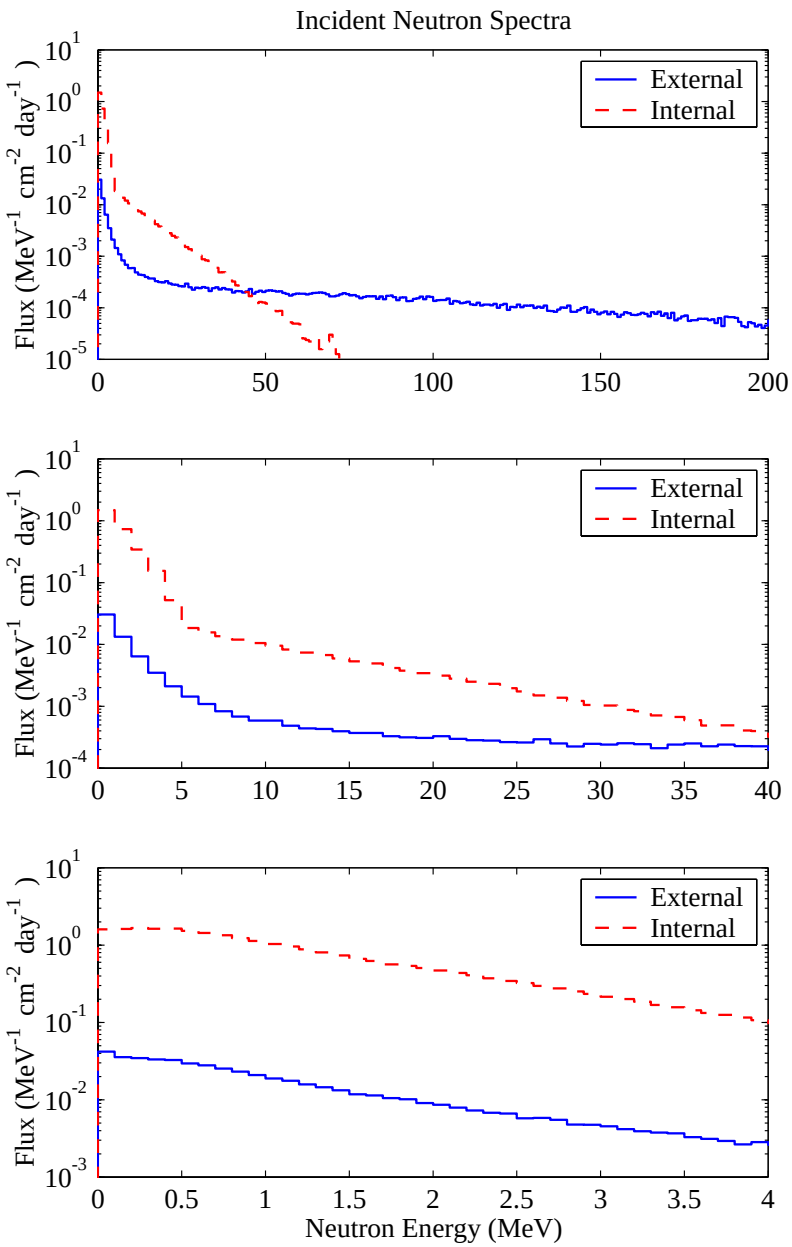

Figure 5.6: The neutron spectra incident on detectors due to external and internal neutrons. The three plots correspond to three energy ranges. At low energy, the two spectra are in good agreement.

	Data	Monte Carlo
Inner Ge Singles Rate (events/kg/day)	1.26±0.35	3.66
Inner + Shared Ge Singles Rate (events/kg/day)	1.57±0.30	3.19
Inner Ge multiples fraction	$0.24^{+0.15}_{-0.11}$	0.09
Inner + Shared Ge multiples fraction	$0.13^{+0.09}_{-0.06}$	0.08
Inner Si events / Ge events	$0.24^{+0.15}_{-0.11}$	0.26
Inner + Shared Si events / Ge events	$0.13^{+0.09}_{-0.06}$	0.16

Table 5.2: Comparison of rates and ratios between the external neutron Monte Carlo and the veto-anticoincident nuclear recoils. See text for details.

germanium recoil-energy spectrum and singles/multiples ratio. Results from this simulation are combined with those from a separate Monte Carlo run with the Run 18 geometry to get the Ge/Si ratio. Figure 5.6 shows neutron spectra incident on detectors in these simulations, for several energy ranges. As obtained in the previous section, the incident neutron spectra closely resemble the internal neutron spectrum (dashed curve) at low energy. Several predictions of this Monte Carlo and the corresponding quantities from the veto-anticoincident nuclear recoils seen in the data are given in table 5.2. Results for both the inner and inner + shared fiducial volumes are included.

Note that the Live-time and efficiency corrections of runs 18 and 19 have been applied to the Monte Carlo numbers appearing in this table. As explained in Chapter 4, BLIP3 is excluded from the final Run 19 data set. The inner and inner + shared data sets correspond to 10.3 and 17.2 kg-days respectively. The number of single scatters observed in these data sets are

13 and 27 respectively. The same 4 multiple scatters are seen in both data sets. The silicon data set, which corresponds to 1.5 kg-days, has 4 nuclear recoil candidates. The data rates and ratios in table 5.2 are obtained from these numbers. Here, unlike in the dark matter analysis (see Chapter 4) where 0.76 silicon nuclear recoils were conservatively assumed to be due to electron misidentification, all four nuclear recoil candidates are treated as neutrons. The multiple scatters refer to double scatters where both hits are required to be in the inner or shared volumes. For the inner multiples, one of the hits is required to be in the inner volume. The multiples fractions in the third and fourth rows refer to the number of double scatters over the total number of events. Uncertainties are higher in the data due to the low statistics. Therefore, only the statistical uncertainties from data are given. Poisson errors are used in the first two rows. Errors given in the other rows correspond to binomial intervals.

Absolute rates from data and Monte Carlo in the first two rows of table 5.2 are not expected to show good agreement for two reasons. The first reason is the large uncertainty in the neutron production rate explained in previous sections. A certain fraction of external neutron are also expected to be coincident with the veto due to the associated muons and shower particles as well as neutron interactions within the scintillator. A preliminary estimate [13] indicates that about 40% of external neutrons will be vetoed due to neutron interactions in the scintillator.

Figure 5.7 shows the recoil energy distribution of veto-anticoincident nuclear recoils in the Run 19 germanium data and the recoil energy spectrum predicted by the external neutron Monte Carlo. The two plots are for the inner and inner + shared fiducial volumes respectively. A better estimate of the agreement between predicted and observed spectra can be obtained from a Kolmogorov-Smirnov (KS) test. Figure 5.8 shows the

(a)

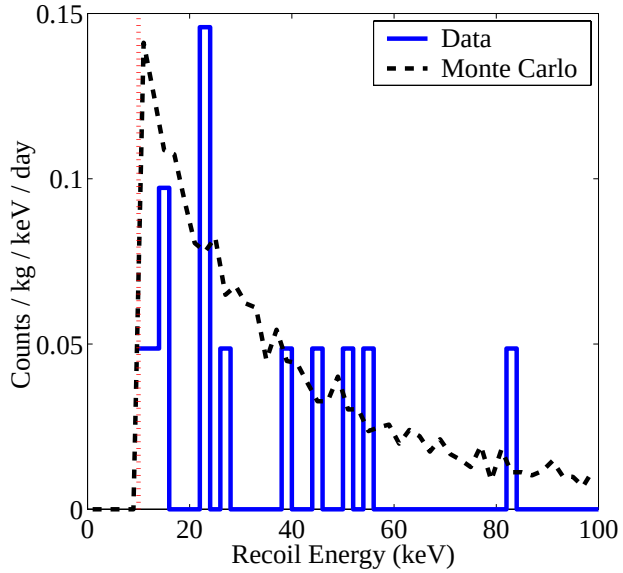

(b)

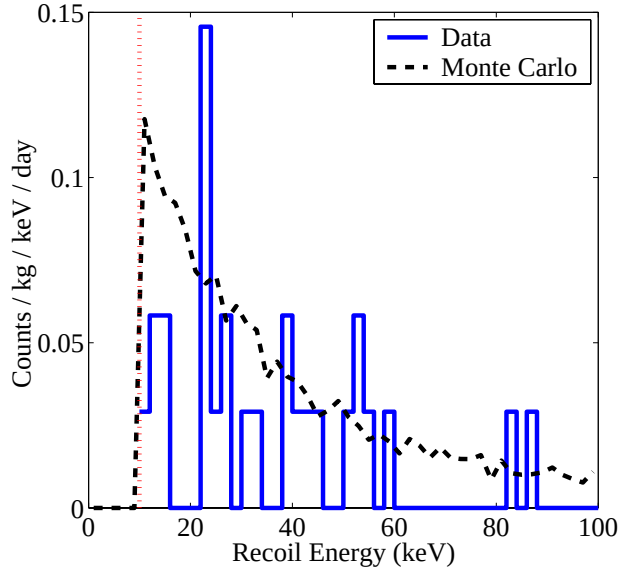

Figure 5.7: Recoil energy spectra from the veto-anticoincident germanium data set and the corresponding external neutron Monte Carlo. (a) inner data set. (b) inner + shared data set.

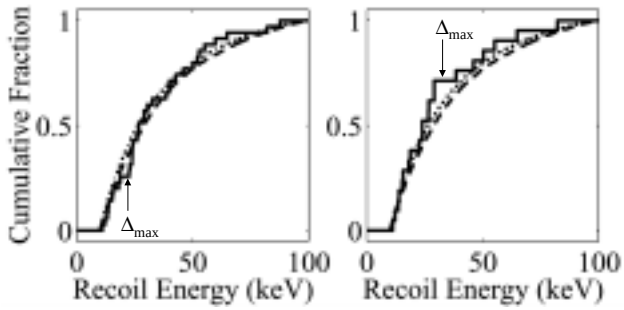

Figure 5.8: Comparison of observed and predicted cumulative spectra for veto-anticoincident neutrons. The left and right plots correspond to the inner + shared and inner data sets respectively. The agreement is good between data (solid) and the external (dashed) and internal (dotted) Monte Carlo predictions. Again, the internal spectra are included here for comparison. Results of KS tests for agreement between data and the external neutron Monte Carlo spectra are given in the text. Figure taken from [19].

integral plots used in these tests. The KS tests indicate that worse agreement is expected 32% and 69% of the time for inner and inner + shared spectra respectively [19].

5.5 Additional Shielding of External Neutrons in CDMS I

As evidence of the residual neutron background in CDMS I was solidified during Run 19, a new shielding scheme has been put in place to attenuate this background. The additional shielding consists of several slabs of polyethylene in the overall shape of a cylinder placed within the inner lead shield. This polyethylene cylinder is 27.5 cm in diameter and 27.5 cm in height with three hexagonal shaped cutouts to accommodate towers. According to a Monte Carlo simulation with a similar geometry, this

configuration will result in a factor of 2.3±0.1 reduction in the in the neutron background.

Although this polyethylene is contained within the base temperature stage of the cryostat, it is thermally anchored to the 600 mK stage of the refrigerator in order to avoid the large heat traps associated with cooling down hydrogenous materials to low temperatures [20]. Heat is conducted away from the polyethylene via 10 mil sheets of copper tightly sandwiched between individual blocks of polyethylene. The "inner" polyethylene layer was successfully cooled down in Run 20 of CDMS I. Due to the small exposures obtained during Run 20, which served mainly as an engineering run, no conclusive results are available yet about the effectiveness of the inner polyethylene. Run 21 which started in July 2001 should provide information on this issue and hopefully an improved dark matter limit due to the reduced background.

5.6 Neutron Background for CDMS II

The dominant backgrounds in CDMS II will be uncovered as data are acquired over the next few years. The present understanding indicates that high-energy neutrons from muon-induced hadron showers may again play an important role. This background has influenced the shielding strategy for CDMS II.

At the approximately 2000 m.w.e depth of the CDMS II site in the Soudan Mine, the muon intensity is 1.8×10^{-3} muons/m^2/sec integrated over all angles [21]. This flux is about a factor 2.5×10^4 lower than the corresponding intensity at the SUF. Therefore, initial neutron studies for CDMS II were focused on natural radioactivity since it dominates neutron production in the rock and the ambient neutron flux [22]. The relatively low-radioactivity Ely greenstone surrounding the Soudan mine is estimated

to produce neutrons at a rate of (1.7 ± 0.2) neutrons/kg/day from (α,n) reactions and 0.2 neutrons/kg/day from fission. The shotcrete lining the cavern is known to have a higher level of radioactivity [21]. The production rates in rock result in an ambient neutron flux of about 2×10^{-6} neutrons/cm^2/sec [22]. Simulations using a shield similar to the CDMS I shield give a neutron interaction rate in germanium of 2×10^{-5} events/keV/kg/day near 10 keV from this source [23].

To assess the significance of this interaction rate, one must consider the acceptable background level for CDMS II. Given a photon interaction rate of 0.5 events/keV/kg/day and a conservative misidentification factor of 0.5%, CDMS II will reach its expected sensitivity in 5000 kg-days of exposure, at which point the systematics are expected to dominate [24]. Therefore, a neutron background level below 1×10^{-4} events/keV/kg/day is desirable. Thus, the interaction rate from natural-radioactivity neutrons, given above, is at an acceptably low level.

However, neutrons from muon-induced hadron showers yield a higher interaction rate. Due to the high muon energies ($<E_\mu> \simeq 250$ GeV) at the CDMS II depth, neutrons from negative muon capture are negligible [9]. At this depth, muon-induced neutron production is approximately equally divided between electromagnetic and hadron showers [9]. In the following, the shower neutron spectrum given by equation 5.3 and shown in figure 5.5 is assumed for all muon-induced neutrons. These neutrons are produced in rock at a rate of $(5.2 \pm 1.0) \times 10^{-3}$ neutrons/kg/day [21, 16, 23] giving an ambient flux of about 2.7×10^{-9} neutrons/cm^2/sec. Before tuning the shield geometry, this background resulted in a simulated interaction rate significantly greater than the acceptable level quoted above.

This problem was compounded by the original shield-design plan for CDMS II. In CDMS I, the polyethylene is contained within the outer lead

shield to moderate and absorb muon-induced neutrons from the lead. Such a design is necessary due to the high-muon rate at shallow depth, in spite of the high veto-efficiency. In CDMS II, where the muon rate is greatly reduced, it is desirable to have the polyethylene outside the lead to avoid the high cost of a large lead shield. However, this design poses two problems for shielding high energy neutrons. First, at typical shower neutron energies of hundreds of MeV, the neutron interaction length in polyethylene exceeds 40 cm, the planned thickness of the moderator. Therefore most high-energy neutrons will penetrate the polyethylene. Interactions of these neutrons in the lead shield will then yield an evaporative spectrum with low enough energy to cause a significant detector interaction rate. Secondly, due to reflection by the lead shield, these neutrons will pass though the near-detector region many times before escaping, which greatly increases the interaction probability. Simulations indicate that a $\sim$10 cm thick layer of polyethylene within the lead is very effective at attenuating this evaporative neutron spectrum. The final CDMS II shield design consists of 40 cm polyethylene on the outside, followed by a 22 cm lead shield and another 8 cm polyethylene layer between the lead and the cryostat cans. According to previous Monte Carlo studies, this shielding scheme would result in a neutron interaction rate of $(2.0 \pm 0.5)\times10^{-4}$ events/keV/kg/day near 10 keV. With the full 42 detector installment planned for CDMS II, 35-45% of these interactions can be rejected due to multiple scattering. The scintillator muon veto makes up the outermost layer of the CDMS II shield. A modest veto efficiency of 99% is required for sufficient rejection of muon-induced neutrons from within the shield.

According to the numbers quoted above, the event rate due to muon-induced external neutrons in CDMS II is marginally acceptable with this shield design. It may be possible to further reduce this background

using a vetoing scheme that detects the associated muons and hadron showers [25] within the rock.

5.7 Direct Simulation of External Neutrons Through Muon Transport in Rock

The Monte Carlo results presented in previous sections were generated using a neutron production rate and spectrum obtained from the literature [15, 9, 16]. Because of the difficulties mentioned in section 5.2.1, the production rate of neutrons in rock is uncertain by about a factor of four. Inaccuracies in the production spectrum also lead to an uncertainty in the normalization of absolute detected rates although normalization-independent quantities like the multiple-scatter fraction should be spectrum independent, as shown in section 5.3.2. It is desirable to obtain a better absolute normalization for the detected rate, in order to assure ourselves that external neutrons are indeed the cause of the residual background seen in CDMS I. Because it is difficult to perform measurements on such a low-rate source, a simulation strategy was developed for obtaining the absolute rate. This strategy involves the simulation of primary muons that give rise to high-energy external neutrons.

A Monte Carlo that begins with the primary muons has several advantages. If muon interactions are accurately simulated, the true production rate and spectrum of neutrons will automatically emerge from such a simulation. If all secondaries of muon interactions are followed, the fraction of vetoed events due to the primary muon and other shower particles can also be estimated. Using information on production rate, production spectrum, and vetoed fraction, the absolute rate of veto-anticoincident neutrons seen in the detectors can be predicted. In addition to giving the absolute rate, such a simulation would allow the

identification of possible veto signatures associated with *vetoed* external-neutron events. For instance, the veto-energy distribution for such events may be different from that of the usual veto triggers. Since the rate of upward-going muons is negligible, nuclear recoils with a veto signal in only the bottom scintillator paddles may be due to external neutrons with an associated scatter in the bottom scintillators [1]. A detailed simulation containing directional information on neutrons can be used to predict the rate of such events. Note that in the simulations described in previous sections, external neutrons are thrown isotropically for lack of a better model.

Accurate simulation of high-energy muon interactions is essential for the success of such a Monte Carlo. The cross-sections for muon-nuclear interactions in the energy range of interest (hundreds of MeV) have been calculated by Bezrukov and Bugaev [26]. These cross-sections are not incorporated in the GEANT [27] treatment of muons. They are, however, included in the "standalone" FLUKA [28] Monte Carlo package. This is *not* the distribution of FLUKA included with GEANT (version 3.21). Comparisons of GEANT and standalone-FLUKA results with experimental data indicate that the cross-section approximations used in GEANT for direct muon-nuclear interactions are too low by about an order of magnitude [29, 30]. On the other hand, several authors have verified that the standalone-FLUKA results are in good agreement with available data [31, 29, 30]. Therefore, we have started using the standalone version of FLUKA (2000 release) for simulating the production of external neutrons. I describe below the setup for the FLUKA simulation.

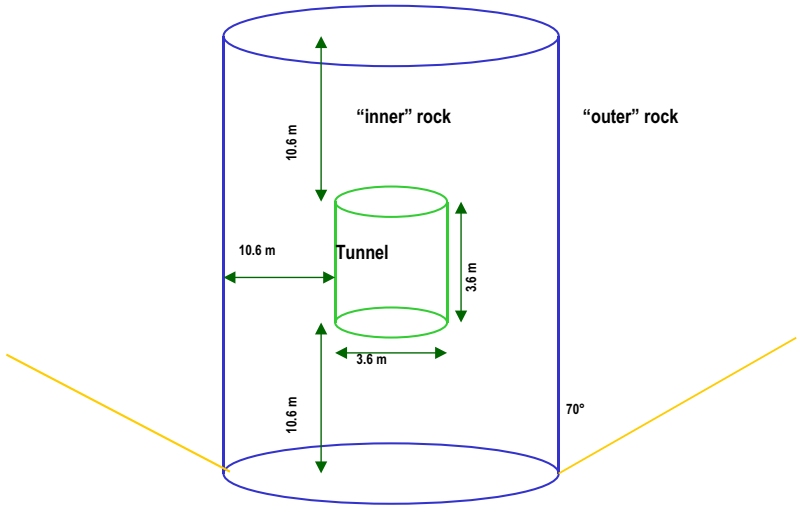

Figure 5.9: Geometry setup for the FLUKA Monte Carlo.

5.7.1 Monte Carlo Setup

As indicated in figure 5.9, the SUF tunnel is modeled as a 3.6 ×3.6 m cylindrical cavity inside a cylinder of rock. The "inner" rock cylinder shown in figure 5.9 is surrounded by another cylinder of rock (not shown) that extends out to a 90 m radius. The flat surfaces of both rock cylinders are aligned. The top surface of these cylinders is taken to be the ground level (i.e. earth surface). The SUF tunnel is placed at a realistic depth of 10.6 m.

Muons are thrown from the ground level according to the following distribution in energy E and zenith angle θ [32].

$$\frac{dN}{dEd\Omega} \propto \frac{372}{E\cos\theta + 80}(5E + 10\sec\theta)^{-2.57}\frac{E+15}{E+15\sec\theta} \tag{5.5}$$

An overall normalization is applied later, using the integrated muon flux at the surface. Angles up to 70° are sampled. Beyond 70°, the intensity becomes very small. The radius of the outer rock cylinder was chosen so that it would subtend a 70° angle at the bottom edge of the inner rock, as indicated in figure 5.9. Muons are thrown uniformly from the surface of both the inner and outer rock cylinders. Instead of sampling energies and spectra according to equation 5.5, a flat distribution in energy and solid angle are used. However, each muon is assigned a weight according to equation 5.5. Since all histograms are filled according to this weighting, the plotted quantities represent normalized spectra. This method is used here, since rare processes like high-energy neutron production are more relevant and require good sampling. Muons thrown from the top of the outer cylinder are not transported unless their initial angle and energy would allow them to reach the inner cylinder. All muons originating from the top of the inner cylinder are transported. This distinction between inner and outer cylinders does not introduce a bias because earlier simulations show that neutrons produced outside the inner cylinder do not reach the tunnel

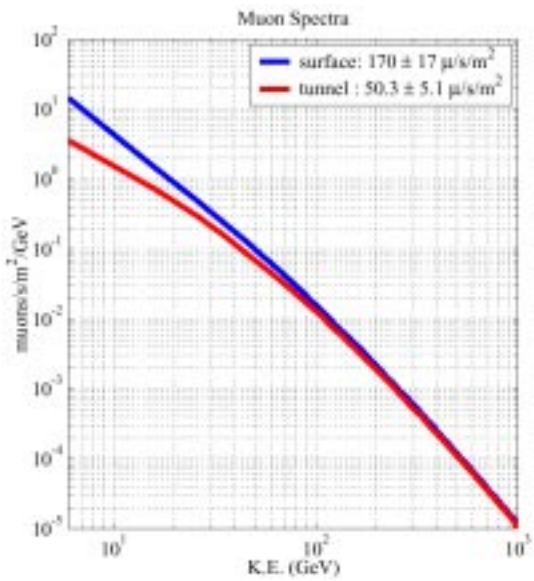

Figure 5.10: Muon spectra at ground level and at the SUF tunnel from FLUKA simulations. These are the integrated spectra over all angles. The absolute fluxes are given in the legend.

cavity. Muons that will not reach the inner rock are ignored (not thrown) for this reason.

For the rock, we have used the chemical composition that was supplied with the FLUKA distribution. However, the rock density was tuned in order to get the effective depth of 16 m.w.e. as obtained from muon-flux measurements [4] at the actual depth of 10.6 m. First results from FLUKA simulations indicate that the tuned density is in the correct range. This can be seen in figure 5.10 which shows the surface and tunnel muon spectra, integrated over all angles. The figure legend shows the integral flux of muons at the surface and tunnel, from these simulations. The simulated tunnel muon flux of (50.3±5.1) muons/sec/m^2 is in reasonable agreement with the measured range of 44-46 muons/m^2/sec [4].

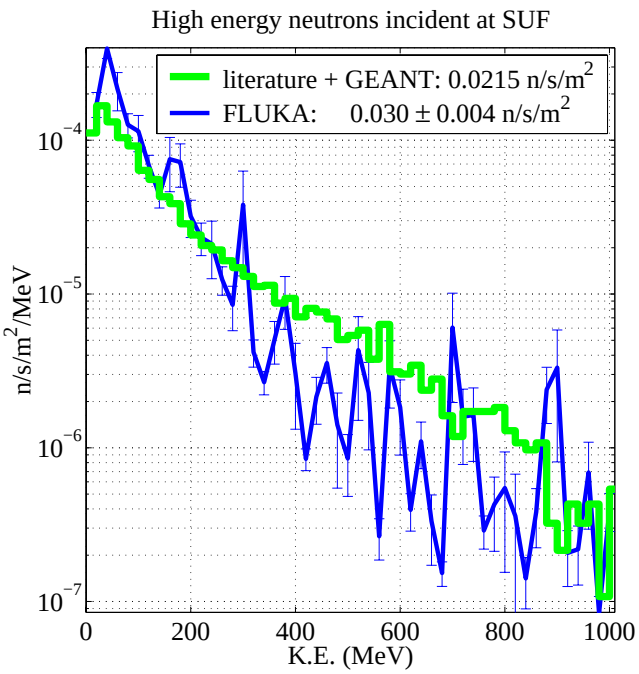

Figure 5.11: Ambient neutron spectra inside the SUF tunnel from GEANT and FLUKA simulations. The light and dark curves represent the GEANT and FLUKA simulations, respectively. Statistical errors are shown for the FLUKA output.

5.7.2 Results

The dark line in figure 5.11 shows the ambient spectrum of neutrons in the "SUF tunnel" as simulated by the standalone FLUKA Monte Carlo. As indicated by the error bars, the apparent fluctuations in the spectrum are due to poor statistics in these initial studies. The light curve (histogram) represents the ambient neutron flux obtained from the GEANT-FLUKA-MICAP simulation by throwing muons within a 5 m shell of rock according to the spectrum in equation 5.3. This is the same spectrum shown in figure 5.1 and figure 5.5 (histogram), with regard to external neutrons. The absolute flux resulting from these two simulations are given in the figure legend. The spectrum obtained from the FLUKA

simulation is softer than the GEANT-FLUKA-MICAP spectrum. However, the total ambient flux predicted by FLUKA is higher. Convolution of the FLUKA spectrum with the "detection-probability" curve of figure 5.2(b) results in a detection rate of 1.1±0.4 neutrons/day. This rate is consistent with the detection rate of 1.1±0.1 shower neutrons (from GEANT-FLUKA-MICAP) per day given in table 5.1.

The good agreement between rates builds confidence that the external neutron background is indeed dominant. However, the vetoed fraction must be obtained before estimating the rate of veto-anticoincident neutrons in detectors. Note that there is room for a significant vetoed fraction since the rate predicted by the GEANT-FLUKA-MICAP Monte Carlo is significantly higher than the observed rate of veto-anticoincident nuclear recoils (see table 5.2). Note also that the simple convolution performed here does not account for angular correlations because the "detection probability" curve was obtained using an isotropic flux. There may also be other correlations associated with the veto. For instance, the predicted rate may change if higher energy neutrons are more like to have associated veto triggers.

Further simulations are necessary for obtaining the vetoed fraction and for taking account of all correlations. The next phase of FLUKA simulations includes a skeletal form of the CDMS veto and shield within the rock cavity of figure 5.9. Information on neutrons reaching a certain "cloning" boundary (see Chapter 3) are saved along with information on veto energy depositions in that event. The saved information is then used as input to a GEANT-FLUKA-MICAP Monte Carlo[2]. The saved veto information will be retained with each thrown neutron. Future results from

[2]At present, the GEANT based Monte Carlo is used as the second stage since the full CDMS geometry has not yet been coded in FLUKA format. In future it may be better to use FLUKA for the second stage since it is expected to have more accurate neutron interaction cross-sections.

this two-stage Monte Carlo will allow us to estimate the veto-anticoincident event rate due to external neutrons in CDMS I, which was the original aim of this work.

References

[1] Richard Schnee. Efficiency of Veto for Rejecting Internally Produced Neutrons. Memo to the CDMS collaboration, May 2001.

[2] Andrew Sonnenschein. *A Search for Weakly Interacting Dark Matter Particles with Low Temperature Detectors Capable of Simultaneously Measuring Ionization and Heat*. PhD thesis, University of California, Santa Barbara, July 1999.

[3] T. Florkowski, L. Morawska, and K. Rozanski. Natural Production of Radionuclides in Geological Formations. *Nuclear Geophysics*, 2:1, 1988.

[4] Angela Da Silva. *Development of a Low Background Environment for the Cryogenic Dark Matter Search*. PhD thesis, The University of British Columbia, April 1996.

[5] Eric J. Weinberg and D.L. Nordstrom, editors. *Physical Review D, Particles and Fields*, volume 54, chapter 26, page 154. American Physical Society, July 1996. Updated in November 1993 by E. Brown.

[6] P. Singer. *Springer Tracts in Modern Physics*, 71:38, 1974.

[7] R.M. Sudelin and R.M. Edelstein. *Physical Review C*, 7(3):1037, 1973.

[8] B. Macdonald et al. *Physics Review*, 139:5B, 1965.

[9] F.F. Khalchukov et al. *Nuovo Cimento*, 18C:5, 1995.

[10] J.C. Barton. In *Proceedings of the 19th International Cosmic Ray Conference*, 1985.

[11] O.C. Allkofer and R.D. Andersen. *Nuclear Physics*, B8:402, 1968.

[12] F.F. Khalchukov et al. *Nuovo Cimento*, 6C:3, 1983.

[13] Steve Yellin. Private communication.

[14] G.T. Zatsepin and O.G. Ryazhskaya. In *Proceedings of the 9th International Cosmic Ray Conference*, 1966.

[15] M. Chen et al. *Nucl. Inst. and Meth. in Phys. Res.*, A 336:232, 1993.

[16] M. Aglietta et al. *Nuove Cimento*, 12C(4):467, 1989.

[17] E. Segrè. *Nuclei and Particles*. Benjamin and Cummins Publ. Co., second edition, 1977.

[18] A. Fassò et al. Presented at the Specialist's Meeting on Shielding Aspects of Accelerators, Targets, and Irradiation Facilities in Arlington, Texas, April 1994.

[19] D. Abrams et al. Exclusion Limits on the WIMP-Nucleon Cross-Section from the Cryogenic Dark Matter Search. Will appear in Physical Review D., 2001.

[20] F. Pobell. *Matter and Methods at Low Temperatures*. Springer-Verlag, Berlin, 1992.

[21] K. Ruddick. Underground Particle Fluxes in the Soudan Mine. MINOS internal note NuMI-L-210, 1996.

[22] Steve Eichblatt. Neutron Studies for the CDMS II site at Soudan. In cdmsnotes (cdmsnote 9701011)., January 1997.

[23] Steve Yellin. Design Considerations for the CDMS II Shield. In cdmsnotes (cdmsnote 9704003)., April 1997.

[24] The Cryogenic Dark Matter Search Collaboaration. Proposal for a Second Generation Experiment to Search For Cold Dark Matter: CDMS II. February 1997.

[25] Moshe Katz-Hyman and Daniel S. Akerib. Simulated Detection and Veto of High Energy Neutrons in the CDMS II Experiment. In cdmsnotes (cdmsnote 0106002)., April 1997.

[26] L.B. Bezrukov and E.V. Bugaev. *Sov. J. Nucl. Phys.*, 35(5):635, 1981.

[27] Geant version 3.21.04, released March 1995. Copyright CERN, Geneva.

[28] A. Fassò, A. Ferrari, J. Ranft, and P.R. Sala. Fluka: present status and future developments. In Menzione and A. Scribano, editors, *Proc. IV Int. Conf. on Calorimetry in High Energy Physics*, pages 493–502, La Biodola, Italy, 21-26 September 1993. World Scientific.

[29] G. Battistoni for the MACRO collaboration. hep-ph/9809006., 1998.

[30] G. Battistoni et al. *Nucl. Instr. Meth. Phys. Res., Sect. A*, 394:136, 1997.

[31] Y-F. Wang et al. hep-ex/0101049., 2001.

[32] S. Miyake. In *Proceedings of the 19th International Cosmic Ray Conference*, 1973.

Chapter 6

Tests of a Z-sensitive Ionization and Phonon mediated Detector

6.1 Introduction

The second phase of the CDMS experiment (CDMS II) will be located at a depth of about 2000 m.w.e. in the Soudan mine in northern Minnesota. As described in Chapter 2, it will be a longer-duration, larger-detector-mass experiment which will benefit from lower background rates due to the deep site. First detector operation in CDMS II is scheduled to commence in early 2002. The detectors used in CDMS II will be Z-sensitive Ionization and Phonon (ZIP) mediated detectors. In these detectors, the ionization measurement is carried out using the same technique introduced in Chapter 2 with regard to BLIP detectors. However, BLIP and ZIP detectors differ in the phonon measurement. This novel phonon detection technology was initially developed by Blas Cabrera's group at Stanford. In recent years, the CDMS collaboration as a whole has spent much time and effort in characterizing and refining this technology for fruitful use in CDMS II.

In the next section, I will briefly outline the working principles and design constraints of the ZIP phonon technology. In the following sections,

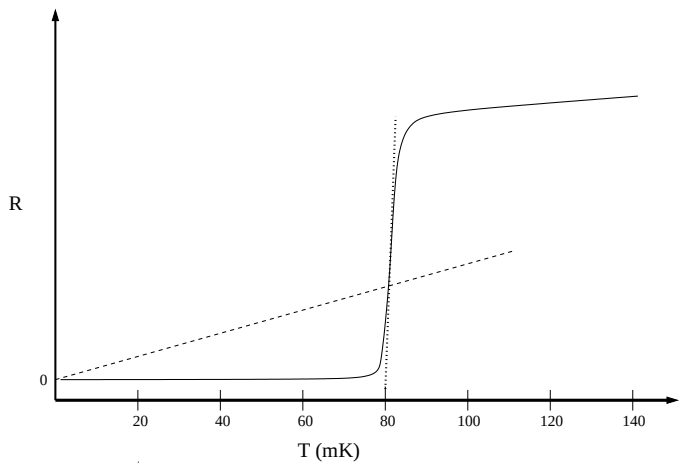

Figure 6.1: Resistance versus temperature for a Transition Edge Sensor (TES). The dimensionless parameter α ($= \frac{dR}{dT}/\frac{R}{T}$) is given by the slope of the dotted line ($\frac{dR}{dT}$) over the slope of the dashed line ($\frac{R}{T}$), shown here for a point within the transition. Note that a linear rescaling of the temperature axis has no effect on α.

I will describe the detector testing facility at Case Western Reserve University (C.W.R.U.) and tests of a germanium ZIP detector at this facility.

6.2 The ZIP Phonon Technology

6.2.1 Transition Edge Sensors

Transition edge sensors (TESs) are used in a wide variety of applications requiring sensitive calorimetry [1]. In ZIP detectors, tungsten TESs are used in the phonon measurement. When biased in the superconducting transition, a small change in the temperature T of the TES's electron system results in a large change in resistance R (see figure 6.1). These temperature changes are caused by particle interactions within the detector, as described in the following sections. The dimensionless parameter $\alpha = \frac{dR}{dT}/\frac{R}{T}$ is useful in quantifying the sharpness of the

transition. In general, α is a function temperature given by the ratio of the slopes of the dotted and dashed lines in figure 6.1. Thus, it is the fractional change in resistance induced by a unit fractional change in temperature. The tungsten TESs used in ZIP detectors have transition temperatures of order 100 mK, and transition widths of order 1 mK. The electron temperature T, of a TES is governed by the equation

$$C\frac{dT}{dt} = P_J + P_E - \Sigma V(T^n - T_\phi^n) \tag{6.1}$$

where the r.h.s. is simply the difference between the power into the sensor and the heat loss of the sensor. Here, C is the heat capacity of the sensor, given by $C = V\gamma T$ where V is the volume of the sensor and $\gamma \sim 0.14$ fJ/K$^2/\mu$m^3 [2] is an intrinsic property of the material. The Joule heating due to current in the sensor is denoted by P_J. External power entering the sensor due to particle interactions or thermal fluctuations (phonon noise) is denoted by P_E. The last term in the r.h.s. of equation 6.1 is the rate of heat loss from the TES's electron system. The dominant thermal impedance between the TES's electron system and the refrigerator's base temperature stage arises due to the decoupling of the electron and phonon systems within a TES. Therefore, in the following, the phonon temperature T_ϕ and detector temperature are assumed to be equal to the refrigerator temperature while the phonon and electron temperatures are different. The exponent n is about 5 for heat flow from the electron to the phonon system [3]. In this last term, V is again the volume of the TES and $\Sigma \simeq 0.4 \times 10^{-9}$ W/K$^5/\mu$m^3 [2] is an intrinsic property of the material.

In equilibrium, the temperature is constant and $<P_E> = 0$. The temperature can therefore be controlled by the Joule power P_J and the refrigerator temperature T_ϕ. When biased in the transition, a small amount of power P_E injected into the system will cause a small temperature change δT. Once P_E returns to zero, the behavior of δT can be obtained by a

linear expansion of equation 6.1 about T

$$C\frac{d\delta T}{dt} = \delta P_J - g\delta T \begin{cases} \delta P_J = P_J\alpha\frac{\delta T}{T} & \text{for current bias} \\ \delta P_J = -P_J\alpha\frac{\delta T}{T} & \text{for voltage bias} \end{cases} \tag{6.2}$$

where $g = n\Sigma V T^{n-1}$. For stable operation, δT must return to zero, which requires that the r.h.s. of equation 6.2 be negative. A negative r.h.s. is ensured for a voltage bias. For a current bias, the bias power and hence the bias current must be maintained below a critical value to obtain a negative r.h.s. This *latching* current I_l is calculated to be $\sqrt{gT/R\alpha}$ from equation 6.2 and $P_J = I_l^2 R$. For a current bias, the voltage change due to δR will be measured using a FET. Because of the restriction on bias current, the signal to noise ratio in such a measurement will be poor, as reported in [4]. More importantly, due to the low bias current and hence the low Joule power, T stays very close to the refrigerator temperature. However, the transition temperature of TESs on a detector face varies on the order of 10% [5]. Thus, with a current bias, only a small fraction of TESs can be maintained within the transition at one time. This is the main problem with a current bias technique. In ZIP detectors, the TESs are voltage biased to overcome these limitations.

6.2.2 Voltage Bias and Electrothermal Feedback

A voltage bias has other advantages in addition to the stability implied by equation 6.2. These include tolerance of T_c variations across the detector face, a self-calibrating energy measurement, and pulse shortening. Each of these features will be described below starting with the adaptability to T_c variations, the most important feature.

The phonon collection side of the ZIP detector is divided into four quadrants, each containing 888 TESs wired in parallel. For a single voltage biased TES in equilibrium, equation 6.1 reduces to

$$\frac{V_b^2}{R} = \Sigma V(T^n - T_\phi^n). \tag{6.3}$$

In the following, the r.h.s. of equation 6.3 can be treated as a constant for a TES in its transition because of the small transition width. As the bias voltage V_b is decreased from a high value, suppose that the individual TES with the highest transition temperature $T_{\rm hi}$ enters its superconducting transition at a bias voltage $V_{\rm hi}$. Assuming a constant transition temperature, this TES's resistance can be reduced to 20% of its normal resistance by setting $V_b = \sqrt{0.2 V_{\rm hi}}$. For a parallel TES, still in its normal state, the Joule power is reduced to 20% of its value at $V_{\rm hi}$, due to the above reduction in voltage. At $V = V_{\rm hi}$, the temperature of such a TES would also be $T_{\rm hi}$ given the same R_{normal}, V, and Σ for all TESs. For $T^n \gg T_\phi^n$, the new temperature of the normal TES is $0.2^{1/n} T_{\rm hi} \simeq 0.72 T_{\rm hi}$. Therefore, by biasing the TES with the highest T_c (transition temperature) at 20% of its normal resistance, other TESs with T_c within 28% of this value can be biased in their respective transitions. This example shows that a voltage bias allows simultaneous biasing of TESs with a large variation in T_c. The refrigerator is usually operated at a few tens of mK below the lowest T_c. Therefore, $T^n \gg T_\phi^n$.

Self calibration and pulse shortening are among the other advantages of using a voltage biased array of TESs. For the usual mode of operation where $T^n \gg T_\phi^n$, the r.h.s. of equation 6.3 can be approximated by $\Sigma V T^n$. Then, equation 6.2 for a voltage bias may be recast as

$$C\frac{d\delta T}{dt} = -\frac{P_J}{T}(\alpha + n)\delta T. \tag{6.4}$$

Both terms on the r.h.s. facilitate the return of δT to zero. The second term represents the usual heat transfer from the electron system to the phonon system. The first term is due to the reduction in Joule heating induced by an increase in resistance. This mechanism is called electrothermal feedback (ETF). In a ZIP detector, the TESs work in the extreme electrothermal feedback limit where $\alpha \gg n$. In this case almost all the external power

injected into the system is eventually removed through δP_J, the reduction in Joule heating. As described later, a SQUID array is used to measure the change in current flow δI_s through the TESs. Since $\delta P_J = V\delta I_s$, essentially all the external energy injected into the TESs is given by

$$E = V_b \int \delta I_s dt \tag{6.5}$$

Note that the above energy measurement is self-calibrating. For instance, if the bias point within a transition has changed due to temperature drifts, equation 6.5 will still yield the correct energy as long as $\alpha \gg n$. Also note that the solution to equation 6.4 is a decaying exponential with time constant $\tau_{\mathrm{ETF}} = \tau_0/(1+\alpha/n)$ where $\tau_0 = C/g$ is the intrinsic relaxation time due to heat transfer away from the electron system. With electrothermal feedback, pulses are shorter by about a factor of α/n due to the reduction in Joule heating. Note that equation 6.5 is a good energy estimate even for saturated pulses if they decay on short time scales compared to τ_0, because the reduction in Joule heating still dominates in this case.

Despite the many practical advantages they bring (eg. less pileup during testing and calibrations), short pulses are not essential for a low-count-rate experiment like CDMS. However, as demonstrated in [4], the fundamental energy resolution of the phonon measurement goes as the square root of pulse duration. Therefore, energy resolution is improved by the shortening of pulses. In the present ZIP design, the pulse duration is longer than τ_{ETF} due to the long life time of athermal phonons in a detector.

6.2.3 Production and Trapping of Quasiparticles

ZIP detectors are disk shaped crystals of germanium or silicon with diameters and thicknesses of about 7.6 cm and 1 cm, respectively. Particle interactions in these crystals cause high frequency optical phonons of tens

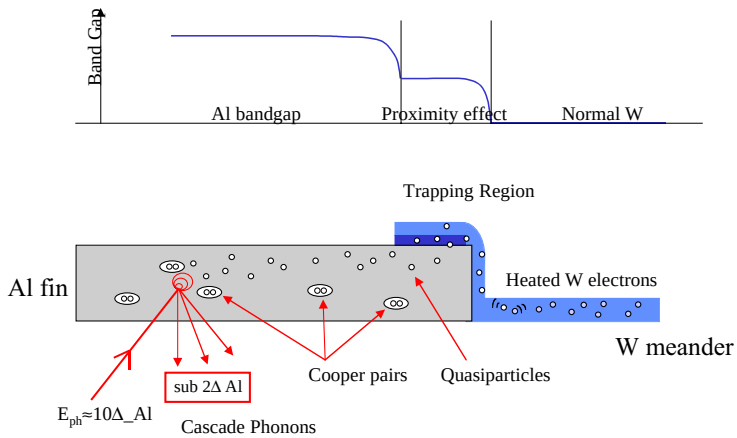

Figure 6.2: Pictorial representation of quasiparticle trapping and diffusion in ZIP detectors. Figure taken from [9].

of THz [6]. These phonons decay to lower energy acoustic phonons through anharmonic decay and isotopic scattering [7]. In a few microseconds a roughly gaussian distribution of phonons is formed around 1.6 THz ($\sim$ 4 meV) [8]. Once the phonon energies are at this level, they have large enough interaction lengths to reach the detector surface. Further phonon down-conversion yields ballistic phonons ($\sim$ 0.5 THz) with interaction lengths on the order of detector dimensions. Eventually, after several milliseconds there is enough down-conversion to form a thermal phonon distribution.

The BLIP detectors are sensitive to these low energy phonons. In ZIP detectors, only phonons of energy above $2\Delta_{Al} \simeq 120$ GHz, the superconducting gap of aluminium, are detected. Once these phonons reach the aluminium collector fins on the phonon side of the detector, they will scatter off Cooper pairs producing quasiparticles and sub-gap ($E < 2\Delta_{Al}$) phonons. The quasiparticles diffuse within the aluminium fins until they

reach a region of overlap between tungsten and aluminium, where the gap energy is smaller. Quasiparticles will be trapped into this region once they lose energy through an inelastic scatter and fall below the aluminium gap [10]. Through further loss of energy, these quasiparticles are trapped into the pure tungsten region where the gap is lower still. The heated electrons in tungsten will then diffuse out of the spurs and into the current carrying parts. The resulting increase in the TES's resistance is measured. Figure 6.2 contains a pictorial representation of the diffusion and trapping of quasiparticles. Phonon sensitive elements that operate as described above are called QETs, or Quasiparticle-trap-assisted (QTA) Electrothermal-feedback (ETF) Transition edge sensors (TES). In what follows, I will refer to the parallel array of QETs in each quadrant as a phonon sensor.

6.2.4 Biasing and Readout Scheme

As depicted in figure 6.3, a phonon sensor is voltage biased using R_b, a 20 mΩ bias resistor. The constant voltage across the sensor is obtained by driving a constant current through R_b which is much smaller than R, the sensor resistance, during regular operation. This constant current is established using a 12-bit voltage DAC spanning a ± 5 V range and a 10 kΩ load resistor R_l. This results in a $\pm$ 500 μA bias current (I_b) range through R_b and a ± 10 μV voltage (V_b) across the sensor.

Figure 6.3 also shows the scheme used to measure I_s, the current through the sensors. For each sensor, a SQUID array consisting of 100 individual SQUID elements is used. The use of SQUIDs ensures a low-noise high-bandwidth measurement. The feedback circuit shown in figure 6.3 works to keep the magnetic flux coupled to the SQUID array at a constant value. Since the inductive coupling between the input coil and the SQUID

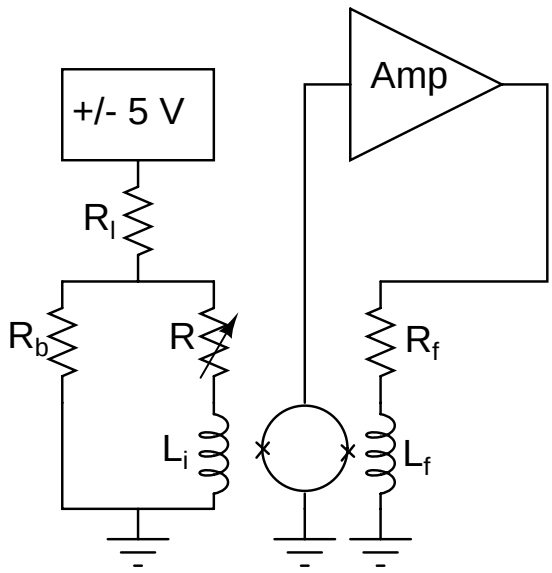

Figure 6.3: The biasing and readout scheme for phonon sensors in ZIP detectors. The single SQUID element shown here represents a 100-element SQUID array. Typical values of R_l, R_b, and R_f are 10 kΩ, 20 mΩ, and 1 kΩ respectively. The sensor resistance R ranges from hundreds of mΩ, when biased in the transition, to a few Ω when normal.

array is 10 times greater than the corresponding coupling of the feedback coil, the current in the feedback coil must change 10 times as much as I_s to keep the flux unchanged. The resulting voltage change across the 1 kΩ feedback resistor is digitized and later converted to an energy using equation 6.5 and the above gain factors.

6.2.5 Design Considerations for ZIP Detectors

In previous designs, the SQUID chips were mounted with the FETs at the 4.2 K stage of the detector tower described in Chapter 2. To reduce low frequency noise the SQUID chips are now attached to the 600 mK stage of the tower and electrically connected to the FET card through a superconducting "flyover" cable. Now, noise in the phonon measurement is dominated by thermal fluctuations (phonon noise) and Johnson noise in the sensors. At frequencies below $1/\tau_{\mathrm{ETF}}$, the Johnson noise is suppressed by electrothermal feedback as explained in [4]. The phonon noise dominated energy resolution for small pulses is calculated to be [4]

$$\Delta E_{\mathrm{FWHM}} = 2.355\sqrt{4kT^2C\sqrt{n/2}/\alpha} \tag{6.6}$$

This is the ideal resolution that would be obtained using a optimal filtering technique using an array of templates to account for pulse shape variations [2] induced by phonon physics. Since the heat capacity C is linear in T, the resolution goes as $T^{3/2}$. The same temperature dependence is true when the simple integral in equation 6.5 is used without templates to estimate the energy. Therefore, lower temperatures improve detector performance[1]. When tungsten films are deposited on the now required amorphous silicon layer (see Chapter 2), transition temperatures of about 130 mK are observed [5]. Ion implantation with ^{56}Fe has been used to lower

[1]Note however that the temperature cannot be reduced indefinitely without making other changes. This is because an energy of TC/α will saturate the sensor. Therefore, TC/α must be maintained above the energy range of interest.

T_c's to the 60-90 mK range [11]. The lower limit on T_c is imposed by the refrigerator temperatures attainable in the experiment and testing facilities.

Subject to the constraints discussed below, the number of TESs per quadrant is always maximized in the phonon sensor design. To avoid electrothermal oscillations, the L/R time constant due to the SQUID input coil must be smaller than $\tau_{\mathrm{ETF}}/5.83$ [3]. Since τ_{ETF} is on the order of tens of μsec, an L/R of about 1 μsec is preferable. The input coil inductance is about 0.25 μH. Therefore, an operating sensor resistance (for one parallel array quadrant) of about 200 mΩ is chosen. In order to have a high α, this operating point is chosen to be about 20% of the normal sensor resistance. This puts the normal sensor resistance at 1 Ω. In order to maximize the number of TESs while maintaining a 1 Ω parallel resistance, the resistance of an individual TES must be maximized. However, the width and thickness of TESs are constrained by fabrication issues to be no smaller than 1 μm and 35 nm respectively. The length of a TES should be no longer than 250 μm to avoid superconducting/normal phase separation within a TES, as reported in [12]. Given the $5\Omega/\square$ resistance of 35 nm tungsten film, an individual TES with these dimensions will have a 1.25 kΩ resistance. To obtain a normal sensor resistance close to 1 Ω, as discussed above, 888 parallel TESs are included in each quadrant.

The aluminium fins have film thickness of 300 nm. With this thickness, the quasiparticle diffusion length is expected to be 360 μm [9]. The fin width is chosen to be 50 μm to minimize magnetic field trapping which limits the quasiparticle diffusion process [9]. Therefore, the amount of surface coverage depends on fin length. Since phonons have a 30% absorption probability each time they are incident on the aluminium, interacting in aluminium is the dominant phonon absorption process. Longer fins and therefore more surface coverage will speed up the phonon

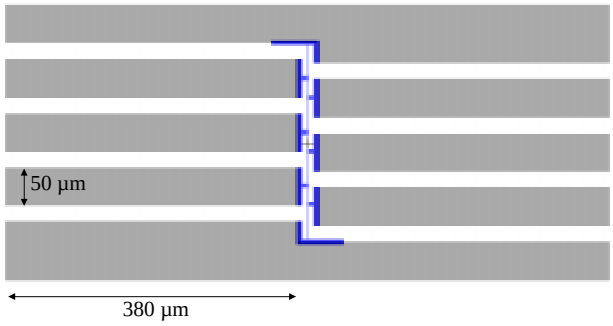

Figure 6.4: Present aluminium fin and TES design in ZIP detectors. The light shaded shaded region represent the aluminium fins. The darker regions represent the tungsten overlap (trapping) regions and the TESs. Figure taken from [9].

absorption process. However, most of the absorbed energy will not reach the TESs due to the finite quasiparticle diffusion length [9]. Shorter fins, while increasing the quasiparticle collection efficiency, will not significantly reduce phonon energy collection because phonons will reflect many times at bare crystal surfaces without significant energy loss and eventually be absorbed in the fins. Therefore, in the present phonon sensor design, the fin length is chosen to be 380 μm, not much greater than the quasiparticle diffusion length. Figure 6.4 shows the design surrounding a single TES. With this geometry, about 23% of the surface is covered by aluminium fins. Based on simulations, the quasiparticle collection efficiency is estimated to be about 25% [9].

Since the phonon absorption efficiency is high in aluminium, the surface area of uninstrumented aluminium due to features like alignment marks and voltage rails must be minimized. For the same reason, the charge electrodes on the opposite side of the detector are patterned as grids

with a 20 μm pitch and a small ($\sim$1%) filling factor. The electric field at the detector is believed to be sufficiently uniform for such a grid pattern. On the phonon side, the thicknesses of the amorphous silicon, aluminium and tungsten are 40 nm, 300 nm, and 35 nm, respectively. The trapping (overlap) regions have 70 nm of tungsten atop the 300 nm of aluminium. On the ionization side, the amorphous silicon, aluminium, and tungsten thicknesses are 40 nm, 20 nm, and 20 nm respectively. While the amorphous silicon covers an entire detector face, the aluminium and tungsten features described above are photolithographically patterned.

Figure 6.5 shows the dimensions of a ZIP detector and the geometry of the phonon sensors. Phonon collection may be poor for events on the outer edge of the detector since the sensors do not cover this region. However, partition of the ionization signal between the inner and outer electrodes may be used to define a fiducial volume that excludes such events. In ZIP detectors, the outer electrode, which covers the annular region at the very edge of the detector, has a small area compared to the inner electrode.

On average phonons will be absorbed on time scales of order 15 μsec after several (about 7-8 on average) reflections [9]. However, pulse fall times of hundreds of μsec are observed since this is the characteristic time scale for phonon energies falling below $2\Delta_{Al}$. It estimated that about 5% of the energy released in a particle interaction is collected in the phonons sensors[2] [13]. The dominant loss mechanisms are the creation of sub-gap phonons in the aluminium ($\sim$ 50%) and the quasiparticle collection inefficiency (efficiency $\sim$ 25%) mentioned above [9]. Uninstrumented aluminium regions, scattering in amorphous silicon, and down-conversion during reflection also contribute to energy losses.

[2]As noted in Chapter 2, the energy utilized in liberating charge pairs is believed to be returned to the phonon system after recombination in the electrodes.

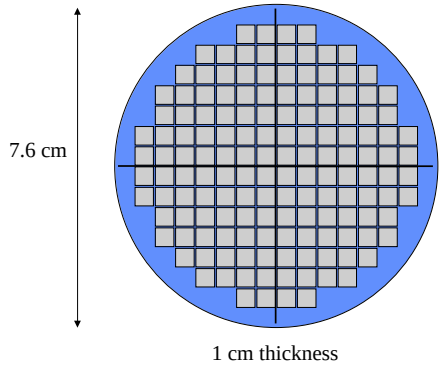

Figure 6.5: Phonon side of a ZIP detector. The squares within the phonon sensors represent 5 mm × 5 mm unit cells containing 24 of the individual elements shown in figure 6.4, at a 20% fill factor. Figure taken from [9].

6.2.6 Advantages of Using ZIP Detectors

As in BLIP detectors, ZIP detectors have sub-keV charge and phonon resolutions at low energy and good charge yield separation between electron and nuclear recoils [14]. Because phonon energy is collected before thermalization, there are several other advantages to ZIP detectors. The relative pulse start times among the four phonon sensors can be used to obtain information about the position of an interaction in the xy-plane of the detector. Figure 6.13 is a plot of these "xy-delays" for a data set obtained with two collimated ^{241}Am sources (see the figure caption for details). Information on xy-position is useful for identifying localized backgrounds because they are likely to yield a non-uniform distribution of hits within the detector. As demonstrated in Roland Clarke's thesis [15], the shapes of phonon pulses can be used to get information about the z-position of an interaction. In particular, events near surfaces show a faster pulse rise time. As described in [15], this information can be

combined with the ionization-yield to improve the rejection of surface electron-recoils[3]. Further studies are under way to ascertain what other position dependent information may be available [16].

6.3 Tests of a CDMS II ZIP Detector

6.3.1 Detector Characterization at C.W.R.U.

ZIP detectors are fabricated at the Center for Integrated Systems (CIS) at Stanford University. Once the packaging is complete and the appropriate wirebonds are made, these detectors are sent to the test facilities at UCB or CWRU. At the test facilities, the basic performance of the detector and the distribution of tungsten T_c's are measured. If a detector passes the necessary checks, it is sent back to the CIS for ion implantation which lowers T_c's to the required range. After ion implantation, the detector is tested again to confirm that the T_cs are indeed lower with sufficiently narrow transitions, and to check for electrical connectivity and basic performance before deployment in a physics run. To minimize radioactive contamination of detectors, they are kept in a radon and dust free environment during storage and transport. Ground transport is preferred due to the higher rate of cosmic-ray induced spallation at high altitudes. When not in use, the detectors are stored underground to minimize exposure to cosmic rays and thermal neutrons. In addition to the radon and dust free storage already present, a new scheme to shield against thermal neutrons will be implemented at the test facilities soon by surrounding the detectors by 10 cm of hydrocarbon. Detector mounting and installation are performed under radon-free clean-room conditions. In addition to these precautions, the first batch of detectors for CDMS II will be operated at

[3]The evolution of ZIP detectors since this result may have reduced the effectiveness of the *rise-time* effect. The smaller surface coverage and the addition of amorphous silicon may be responsible for this.

the SUF in the CDMS I cryostat. The background rates inside the CDMS I shield are low enough to establish whether there is significant contamination of detectors. Such low background testing will continue until it is clear that the contamination introduced during fabrication, transport, and testing of detectors is comparable to CDMS I levels.

While the UCB test facility has been used for detector operation since the inception of CDMS, the CWRU test facility started detector testing in mid 2000. Initially the CWRU test facility consisted of a Kelvinox 400 dilution refrigerator made by Oxford Instruments housed inside a "Faraday cage" for RF shielding. The first few cool-downs of the refrigerator served to test it performance, and the performance and reliability of the plumbing and thermometry. Base temperatures below 10 mK and cooling powers of about 160 μW at 100 mK were measured[4]. Reliability of the pre-installed RuO_2 thermistors and the lowest achievable temperature were established using nuclear-orientation thermometry [17] with a ^{60}Co radiation source. Subsequent cool-downs were used to measure T_c distributions on test wafers processed alongside detectors. An LR 700 AC resistance bridge was used for four-wire resistance measurements of individual pieces cut from these test wafers. Since up to 60 samples can be operated simultaneously, detailed T_c maps of test wafers were obtained [18]. These measurements provided important feedback for detector fabrication at a time when tungsten-film uniformity was a major concern. These cool-downs were also used for the calibration of several new RuO_2 resistors to be used in CDMS II and the test facilities.

The next stage of development at the CWRU test facility involved the installation and testing of hardware and electronics needed for detector operation. Several parts of the refrigerator were custom designed to

[4]The 400μW rating applies if a roots booster pump is installed. Without this option, which has not been purchased, the system is rated at 160μW at 100 mK.

facilitate installation of the tower, and striplines. Initially, several test devices were used with a SQUET (SQUID+FET) card, readout electronics, and a custom low-noise GPIB control interface. These components and the whole electronics chain are organized and used in the same manner described in Chapter 2 with regard to CDMS I. As described in Chapter 2, raw signals are brought out of the refrigerator through a hermetically sealed vacuum feedthrough and processed in two electronics crates before digitization with Joerger cards installed in a VXI crate. The front-end rack is the only electronics within the Faraday cage. Its power supply is kept outside to minimize noise pickup. Signals are brought out of the RF enclosure using bulkhead connectors and appropriate low-pass filtering.

The first detector operated at the CWRU test facility was a Ge detector which was rejected for use in Run 20 of CDMS I due to problematic T_cs in two of the phonon sensors. Operation of this detector served to further improve the control and readout chains as well as initiate work on data acquisition and analysis. The rest of this chapter describes data and results from *99GSA6*, the second detector operated at the CWRU Test Facility. It is one of the germanium detectors that will be deployed in Run 21 of CDMS I and possibly in "tower one" of CDMS II. These data were obtained in CWRU Runs 10 and 11 which took place during January and February of 2001.

6.3.2 Diagnostics and Testing of a ZIP Detector

The *99GSA6* detector, or "G6" as it is commonly known, was tested at CWRU after ion implantation. Most of the diagnostic tests involve only the four phonon sensors, labeled A through D according to their orientation relative to the detector interface board (DIB). First, the transition temperature of each sensor is measured. This is done by using voltage a

Phonon Sensor Test Results				
	A	B	C	D
T_c (mK)	81-101	93-100	85-91	88-100
R_{normal} (Ω)	1.08	1.56	1.32	1.09
I_{crit} (μA)	121	131	125	126

Table 6.1: Transition temperature, normal resistance, and critical current at base temperature for the four phonon sensors. The measurement errors on normal resistance and critical current are less than 5%. However, a systematic error may be present in normal resistance estimates due to parasitic resistances.

tringle wave instead of the DAC shown in figure 6.3 to obtain a variable current through R_l and the parallel combination of R and R_b. The current through R, the phonon sensor, is measured using a SQUID array as shown in figure 6.3. The ratio of sensor current (I_s) to bias current ($I_b = V/R_l$) depends on sensor resistance. This ratio is low when the sensor is normal, high when the sensor is superconducting, and in a intermediate range during the transition. Therefore, the transition temperature (T_c) is measured by studying the sensor current as the refrigerator temperature is varied. The measured range of the transition and the normal resistance of each sensor are given in the first two rows of table 6.1. The width of a T_c range indicates the measurement resolution, given a finite excitation current, and does not reflect the true transition width of a sensor. However, this current is small enough to ensure that the refrigerator temperature accurately reflects the electron temperature of the TESs.

The third row of this table gives the current required to drive each sensor normal (critical current) at the base refrigerator temperature, which was about 20 mK during these measurements. The measured values of critical current are high enough to conclude that there are no significant

dead regions within a sensor, where TESs remain normal even at base temperature. Measurements of critical current as a function of refrigerator temperature can be used to estimate the variation of T_c within a sensor. While critical current measurements made during runs 10 and 11 were inconclusive low-resolution in temperature sampling, later measurements indicate that most of the TESs in all four sensors have T_cs in the 60-70 mK range [19]. Note that the T_c measurements described above and reported in table 6.1 reflect the highest T_c's in a sensor because only a few TES transitions are necessary for the sensor as a whole to superconduct a $\sim$2 μA current. A thermometry offset of about 10 mK between Run 11 and later runs may also explain why the T_cs of table 6.1 are higher than the numbers from later critical current and T_c measurements.

Measurements of sensor current (I_s) versus bias current (I_b) at base temperature provide a powerful sensor diagnostic. These "IbIs" data for the four sensors are shown in figures 6.6, 6.7, 6.8, and 6.9. They were obtained by using a triangle wave voltage in place of the DAC in figure 6.3 as described above. A very low frequency (mHz) triangle wave was used in order to keep the voltage drop across L_i, the SQUID pickup (input) coil, negligible and to ensure that the sensor is close to thermal equilibrium at each point in time. In later fridge runs, IbIs data have been acquired using an automated procedure developed by Tarek Saab which slowly changes the bias current using the $\pm$5 V DAC.

The top plots in these figures show I_s versus I_b for each sensor. The linear region at small I_b corresponds to the superconducting phase of a sensor while the linear region at higher I_b corresponds to the normal regime. The hyperbolic behavior at intermediate I_b is due to the superconducting-to-normal transition. Since the transition is narrow, the

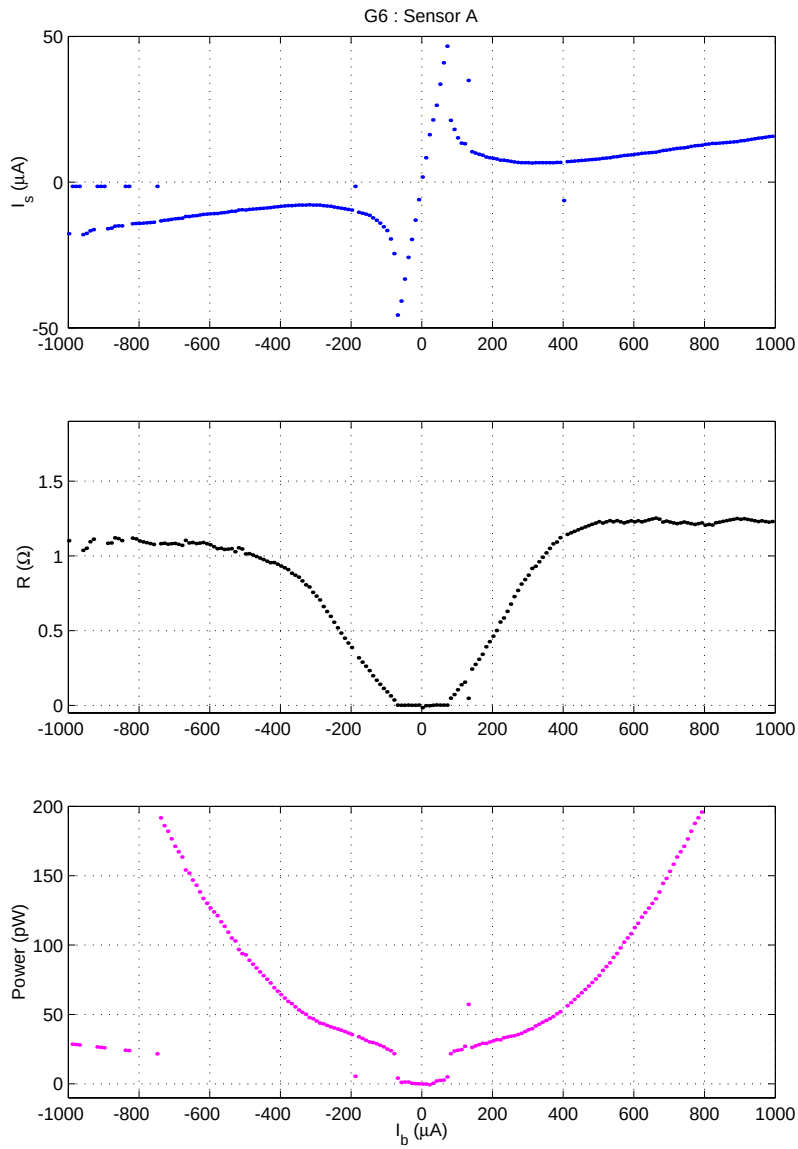

Figure 6.6: IbIs data from sensor A. The three plots correspond to sensor current I_s, sensor resistance, and Joule power dissipation in the sensor as a function of the bias current I_b. See the text for details on the expected shapes of these curves. The few points that deviate from smooth behavior in these curves are artifacts due to "SQUID lock-point jumps", and therefore are of no significance.

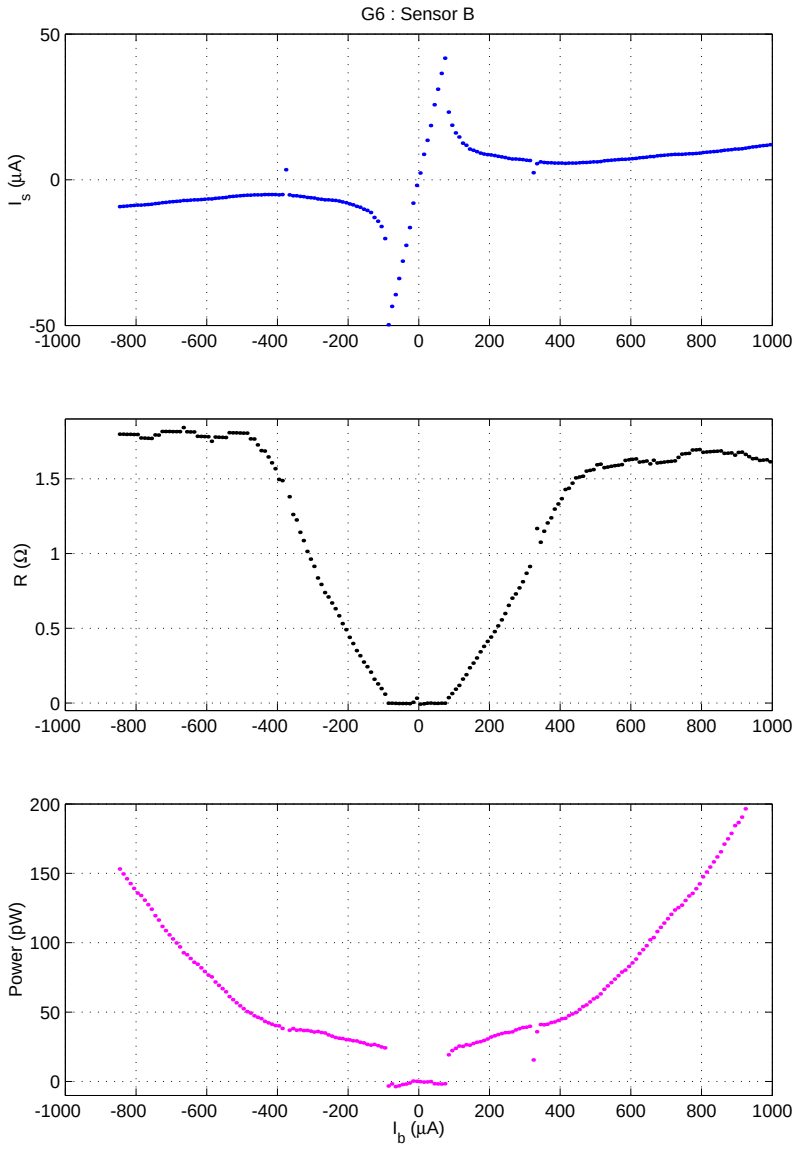

Figure 6.7: IbIs data from sensor B.

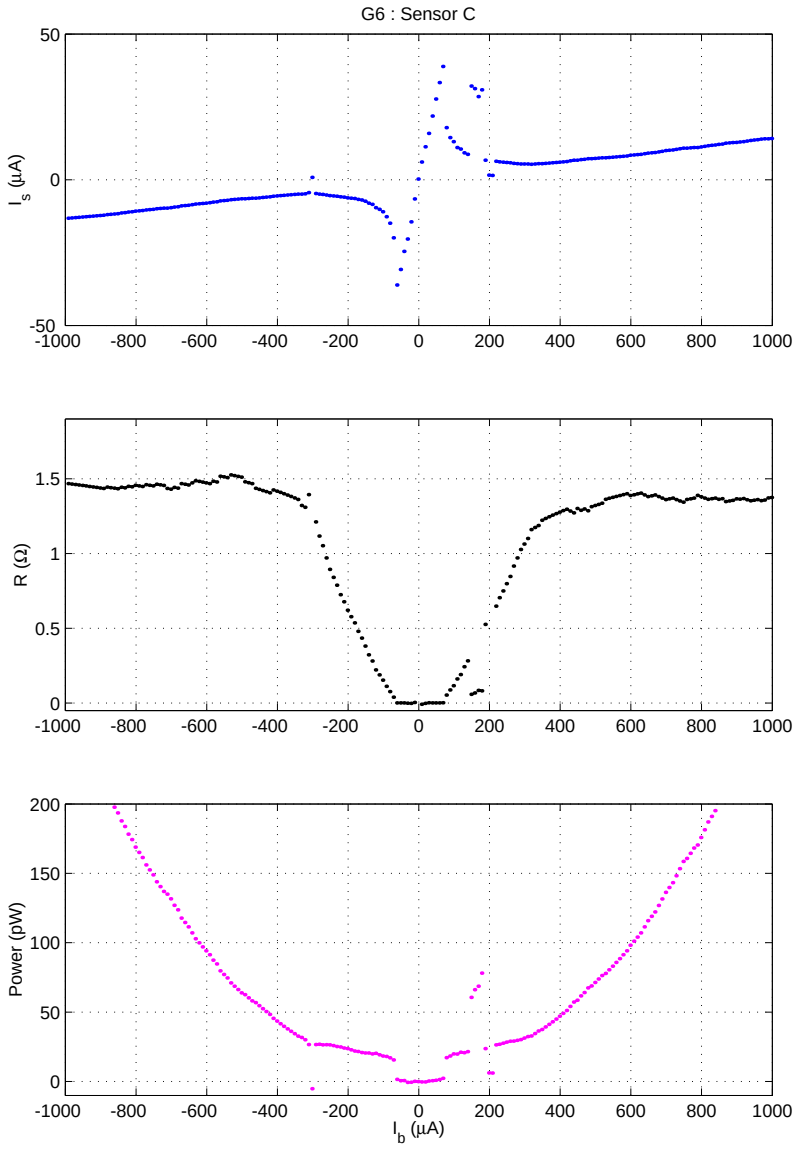

Figure 6.8: IbIs data from sensor C.

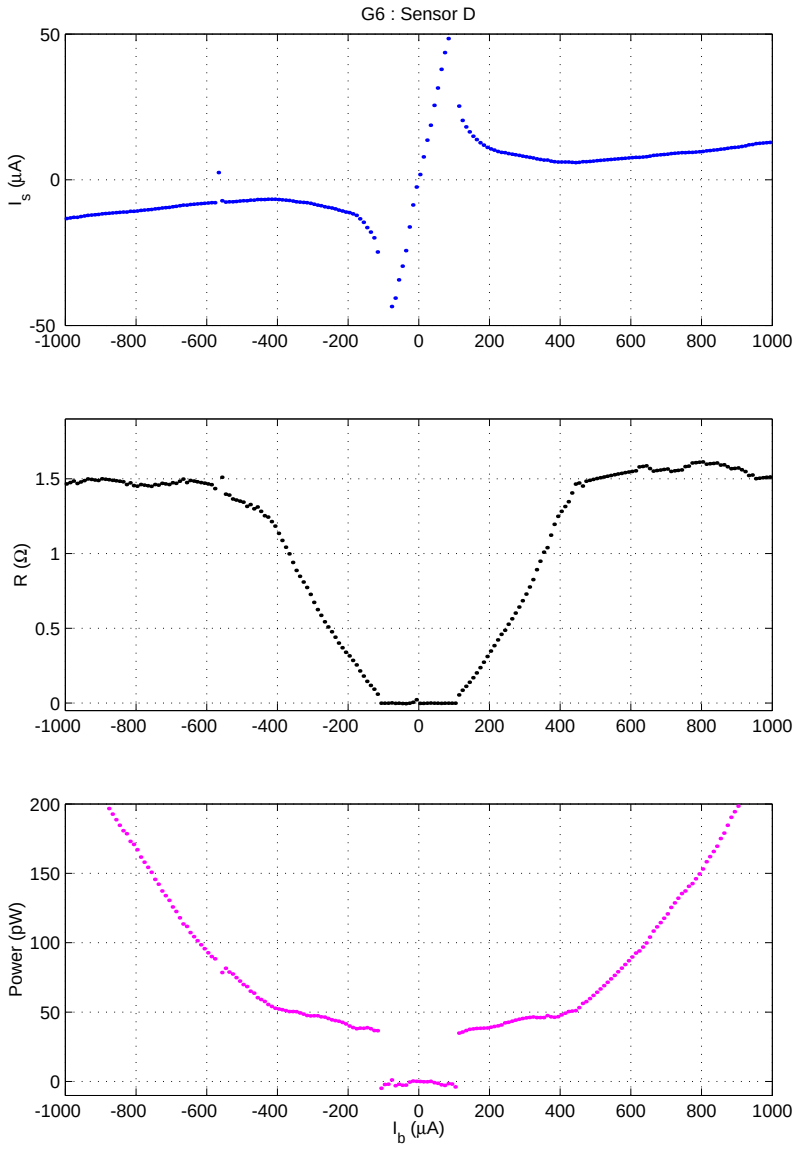

Figure 6.9: IbIs data from sensor D.

r.h.s. of equation 6.3, repeated here, can be regarded as a constant.

$$\frac{V_b^2}{R} = \Sigma V(T^n - T_\phi^n). \tag{6.7}$$

Since the l.h.s. is equal to $I_b R_b I_s$ $(= V_b I_s)$, the sensor current goes as $1/I_b$ in the transition. The sensor resistance, shown in the middle plots are obtained from I_b and I_s. The resistance behavior in the transition can be understood by writing the l.h.s. of equation 6.7 as $I_b^2 R_b^2/R$. Since the r.h.s. in equation 6.7 is treated as a constant, R will then be a parabolic function in I_b as seen in these plots. The lower plots, showing the Joule Power dissipated in the sensor as a function of I_b are usually the most useful diagnostics in these sequence of plots, as explained below.

In the normal regime, the power is quadratic in I_b. As expected, the power dissipated within the transition is reasonably flat. The value of Joule power within this flat region is called the bias power. Deviations from flat behavior are due to non-zero transition widths. This effect is dominated by T_c variations within a sensor and not by the transition widths of individual TESs. If the sensors are biased near the low I_b end of the transition, the bias power is approximately equal to the external power (P_E) needed to saturate the sensor. Therefore, the bias power reflects the dynamic range of a sensor. A high bias power is also preferable for high signal-to-noise since the change in sensor current (δI_s) induced by particle interactions is given by

$$\delta I_s = \delta\left(\frac{V_b}{R}\right) = -\sqrt{\frac{P}{R}}\frac{\alpha}{T}\delta T \tag{6.8}$$

whereas the contribution from phonon and Johnson noise goes as $\sqrt{kT/R}$ [4].

Since the sensor transition temperature and refrigerator temperature are known, the bias power may be used in equation 6.7 to find ΣV and hence V the total volume of a sensor. An unexpectedly low bias power my

be due to low T_c within a sensor, a high refrigerator temperature, or a low V, which may be due to over-etching of tungsten. The shape of the power curve within the transition may also be used to determine if the sensor undergoes phase separation. A detailed description on the diagnostic power of IbIs data is contained in [12].

6.3.3 SQUID and QET biasing

As described before, the feedback circuit of figure 6.3 keeps the magnetic flux coupled to the SQUID array at a constant value. In order to ensure the best noise performance, the quiescent flux coupled to the SQUID is chosen to be at the point of maximum responsivity. Here, the responsivity is the change in voltage drop across the SQUID for a unit current change in the feedback coil. In other words, the quiescent current through the feedback coil is chosen to maximize the slope of the SQUID V-ϕ curve. This setting minimizes the output voltage change needed to cancel out noise at the input of the amplifier shown in figure 6.3 [20]. The SQUID array and room temperature electronics contribute to noise at the input of the room temperature amplifier. Maximizing the responsivity also maximizes the bandwidth of the feedback circuit.

The QET bias current (I_b) is also chosen to maximize signal-to-noise. Since V_b^2/R is approximately constant in the transition, V_b is proportional to $\sqrt{R}$. Therefore phonon and Johnson noise, which are proportional to $1/\sqrt{R}$, will go as $1/V_b$. When the sensor is biased, a given external power results in a current change (δI_s) equal to P_E/V_b. Therefore the signal also goes as $1/V_b$. Thus, a naive estimate indicates that signal-to-noise is independent of the bias voltage. However, since both signal and noise are lower at high bias voltages, the constant SQUID noise starts to dominate. Therefore, the QETs are biased at the low end of the

transition. A more detailed calculation involving only phonon and Johnson noise also indicates that signal-to-noise is slightly better at a lower bias within the transition [15]. A low bias also results in a higher dynamic range as explained above. However, a very low bias current is undesirable because the high value of α that results may make the system susceptible to electrothermal oscillations. Therefore the bias current is lowered within the transition until there is evidence of electrothermal oscillations. In principle, the the ideal bias point should be empirically determined by studying signal-to-noise at a sequence of bias points.

For the data described below, the QET bias currents in sensors A, B, C, and D were 58.5 μA, 79.9 μA, 72.1 μA, and 88.2 μA, respectively. The charge bias on the inner and outer channels was 1 V. The noise power spectral densities (PSDs) at these settings for all six channels are shown in figure 6.10. Noise in the four phonon sensors is referred to the SQUID input coil. In other words, all noise is quoted in terms of current noise in the sensor. Noise in the phonon channels is dominated by phonon and Johnson noise. The measured values are close to the expectation of about 10 pA/$\sqrt{\text{Hz}}$ for a sensor resistance of 200 mΩ and a transition temperature of 100 mK. The noise fall-off at tens of kHz is due to the L/R time constant of the circuit. The rise in PSD just below the fall-off, especially in sensor A, indicates the onset of electrothermal oscillations. When the sensor is superconducting, the Johnson noise of the bias resistor (R_b) dominates. When normal, the noise is at the few pA/$\sqrt{\text{Hz}}$ level and dominated by SQUID noise.

Noise in the charge channels is referred to the output of the first stage charge amplifier. This is the output of charge measurement circuit shown in Chapter 2. Charge noise is dominated by FET-gate noise above 1 kHz or so [21], and is calculated to be 150 nV/$\sqrt{\text{Hz}}$ at the first stage

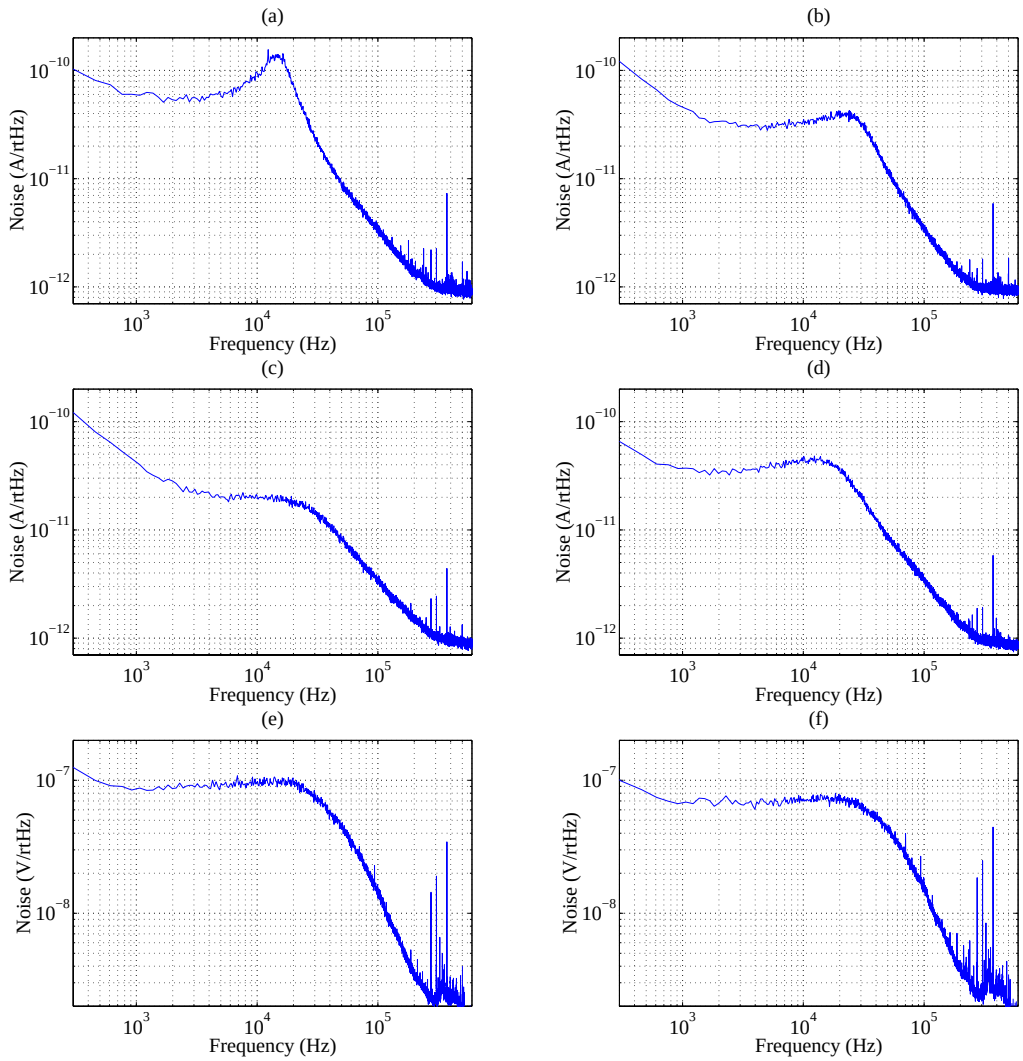

Figure 6.10: The noise power spectral density for the four phonon channels and two charge channels of a ZIP detector. Plots (a), (b), (c), and (d) correspond to the phonon sensors A, B, C, and D respectively. Plots (e) and (f) show the noise in the inner and outer ionization channels respectively.

output given a typical FET gate noise of 1 nV/$\sqrt{\text{Hz}}$ and assuming standard values for the feedback (1 pF), detector (50 pF), and parasitic (100pF [22]) capacitances. At low frequency, charge noise is dominated by microphonics, as discussed in [21]. The knee at about 30 kHz is due to the low-pass filtering employed to stabilize the ionization circuit (see Chapter 2).

6.3.4 Description of Data

Two collimated ^{241}Am sources, each with a 0.2 μCi nominal source strength were included with the detector package. The two sources were separated by about 1.6 cm and placed over phonon sensors B and C at an approximate radius of 1.9 cm. In addition to alphas, these sources emit 14 keV, 18 keV, 21 keV, and 60 keV photons. Of the photons, the 60 keV line has the highest intensity. Aluminium foil was used to shield the detector from alphas. However, it was later found that the aluminium thickness was insufficient to completely attenuate the alphas. Because of this, the event rate was about twice as large as the 60 Hz value that was aimed for, taking only the 60 keV photons into account. For the data described below, a ^{137}Cs gamma source, external to the refrigerator, was also used. No gamma line is expected from this source since the 662 keV gammas are mostly expected to Compton scatter uniformly within the detector depositing a fraction of their energy.

In the data presented below, the ionization energy is proportional to the sum of pulse heights in the inner and outer charge channels. It has been calibrated to yield electron-recoil equivalent energy using the 60 keV gamma line. The phonon energy is also a linear combination of signal heights from the phonon channels. Before summing, individual pulse heights from each channel are multiplied by pre-factors to account for differences in bias voltage (V_b) and sensor transition temperature (T_c). For

both the phonon and charge measurements, an optimal-filter technique is used to find the pulse height. A pulse height measurement is used to obtain phonon energy because the simple integral of equation 6.5 yields worse energy resolution due to low frequency noise. However, a pulse height estimate is not self-calibrating like the integral estimate. In particular, the pulse height for a given energy deposition depends on T_c, the transition temperature, which varies across the detector face. There may also be a slight position dependence in the phonon pulse shapes. Therefore, in addition to the sensor-by-sensor pre-factors mentioned above, a position dependent calibration is necessary to obtain a good phonon energy estimate. I will first present data prior to this calibration.

All events with significant energy in the outer ionization electrode have been excluded from the following plots and analysis. A large number of events are subject to pileup due to the high event rate. These events must also be excluded to ensure that phonon and charge pulse height estimates are accurate. This is done by using a χ^2 cut on charge pulses as described in Chapter 4. Such a cut removes most of the pileup in both phonon and charge since all 6 channels were digitized for equal amounts of time.

Figure 6.11 shows ionization energy versus phonon energy for events passing these cuts. Note that the phonon energy is in arbitrary units since the position dependent calibration has not yet been performed. The 60 keV gamma line is evident in this plot as a narrow band in ionization energy. This indicates that the broad distribution of events in charge energy versus phonon energy is due to poor phonon energy resolution. As shown below, the phonon energy resolution can be improved with a position dependent calibration. The dense band of events to the right of the vertical dashed line are due to alphas.

A histogram of the ionization energy is shown in figure 6.12. It

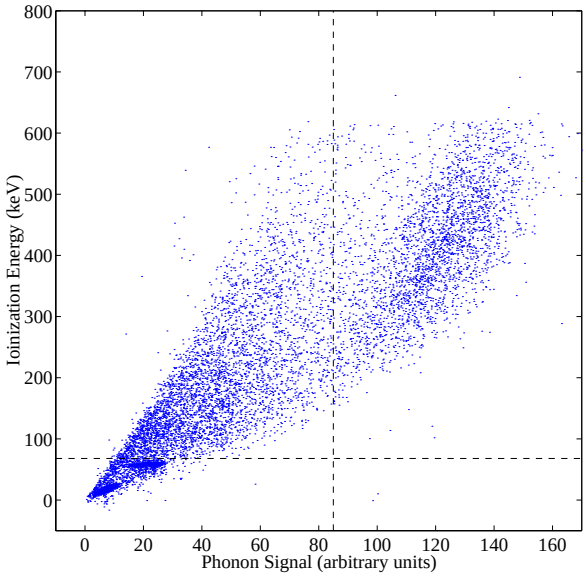

Figure 6.11: Ionization energy versus phonon energy from detector *G6* before applying the position dependent phonon energy calibration. Only points to the left of the vertical dashed lines and above the horizontal dashed line are used for the position dependent calibration.

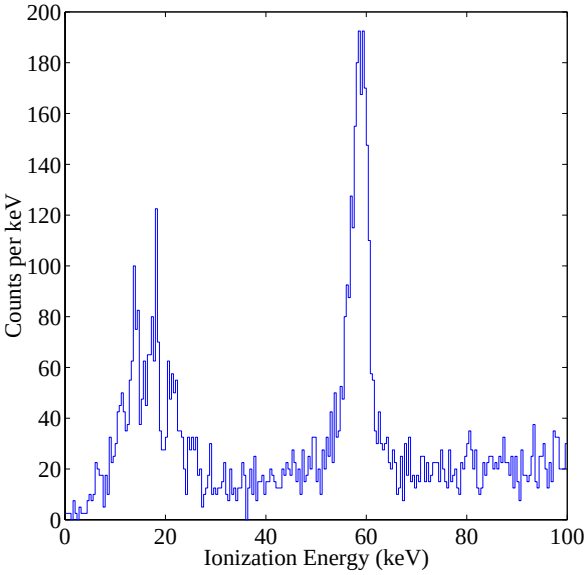

Figure 6.12: Histogram of ionization energy in *G6*.

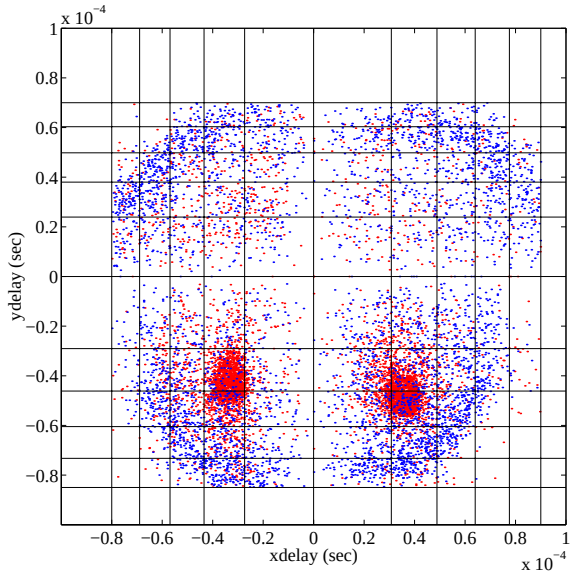

Figure 6.13: *Xdelay* vs. *ydelay* for ^{241}Am and ^{137}Cs photons in *G6*. Note that alphas are not included here because only events to the left of the vertical dashed line in figure 6.11 have been used. However, similar plots for the alpha events show that they are also concentrated at the two dense spots seen here due to photons from ^{241}Am . The more uniform distribution of events is mostly due to the ^{137}Cs source.

shows the expected photon lines. The low energy tail of the 60-keV line is wider than the high-energy tail because of diminished charge yield for surface events. Note that a 60-keV gamma has a mean interaction length of about 1 mm in germanium. The high-energy tail measures the charge energy resolution. This plot indicates a charge energy resolution of about 3 keV full-width at half-maximum.

The x and y positions of interactions can be inferred from the relative pulse start times among the four phonon sensors. The quantities *xdelay* and *ydelay* in figure 6.13, which have units of time, were obtained from a triangulation algorithm devised by Vuk Mandic. They are expected to be single valued and monotonic in the x and y position of an interaction within the detector. All points to the right of the vertical dashed line in

figure 6.11 have been excluded from figure 6.13. Therefore most of the events in this figure are from ^{241}Am and ^{137}Cs photons. The dense spots within the two lower quadrants are due to the collimated ^{241}Am sources. The spread of these patches indicates the x-y position resolution of the detector. Most of the other events in this plot are from the ^{137}Cs source. The variables *xdelay* and *ydelay* are clearly not linear in position since the distribution of these points is non-uniform in figure 6.13. However, since they are expected to be monotonic in x and y, they can be used to parametrize other position dependencies, as demonstrated below.

6.3.5 Position Dependent Phonon Energy Calibration

Events associated with the ^{241}Am sources are excluded from the position dependent phonon calibration. These events are removed by including only those events that appear to the left of the vertical dashed line and above the horizontal dashed line in figure 6.11. For events passing these cuts figure 6.14(a) shows P/Q, the phonon energy over the ionization energy, as a function of *xdelay* and *ydelay*. Since the charge is much better resolved than phonons, P/Q can be used as an energy-independent measure of how phonon pulse height changes with position. Figure 6.14(a) hints that phonon pulse height is a single-valued smooth function of position. Figure 6.14(b) shows the average values of P/Q for rectangular cells in *xdelay* and *ydelay*. Next, the calibration must be carried out to test whether position dependence is the dominant cause of the poor phonon energy resolution. Figure 6.15 contains the same mesh used in figure 6.14(b) and shown in figure 6.13. The numbers inside each rectangle are $<P/Q> \times 100$ for points contained within that rectangle in *xdelay* and *ydelay*. The calibration consists of dividing the uncalibrated phonon energy for points within the i th rectangle by $<P/Q>_i$.

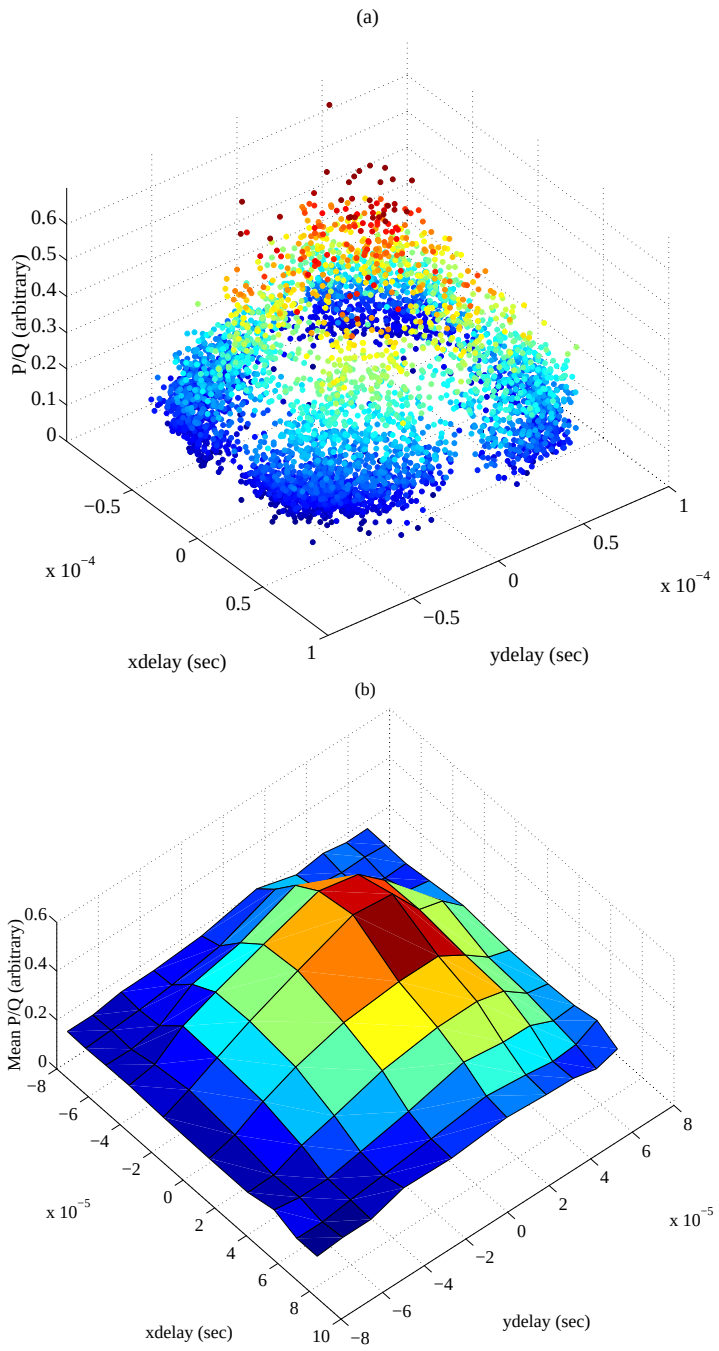

Figure 6.14: Position dependence of phonon pulse height. (a) phonon energy over ionization energy (P/Q) versus *xdelay* and *ydelay* for events passing cuts described in the text. (b) Surface plot showing the average values of P/Q given in figure 6.15.

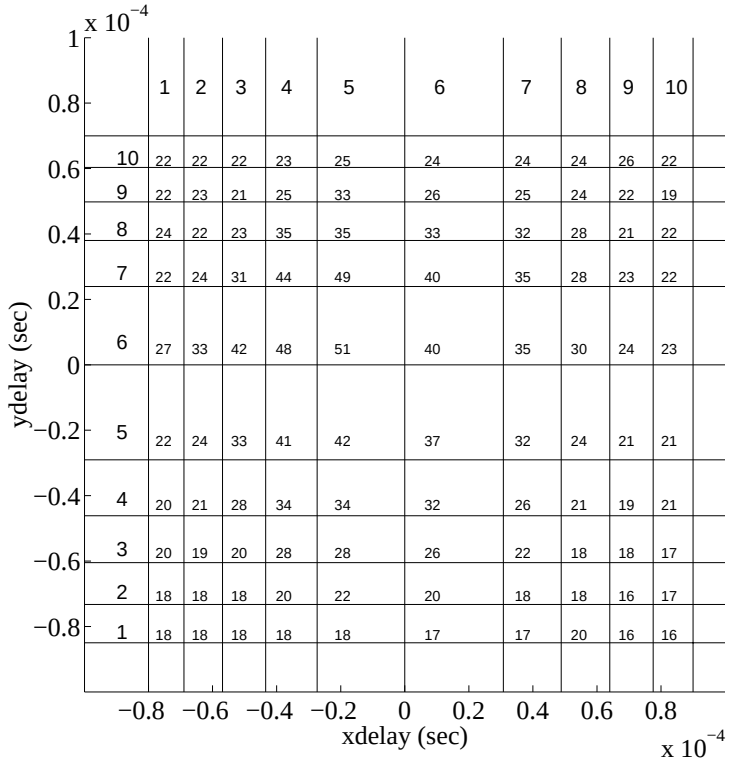

Figure 6.15: $<P/Q> \times 100$ for a grid in $xdelay$ and $ydelay$

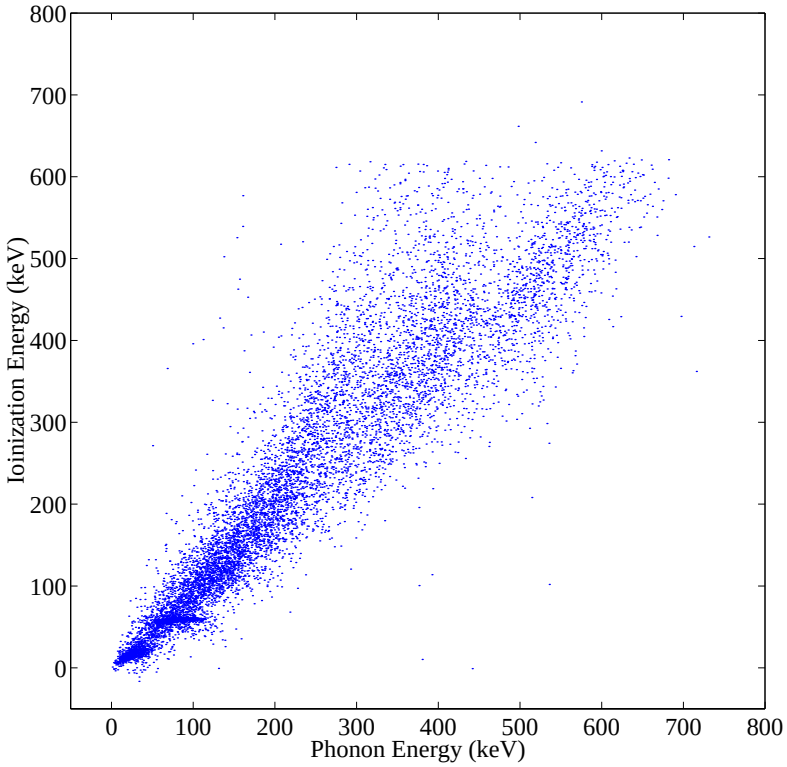

Figure 6.16: Ionization energy vs. *calibrated* phonon energy. Comparison of this plot with figure 6.11 clearly shows the success of the phonon calibration.

The ionization energy versus *calibrated* phonon energy is shown in figure 6.16. The distribution of points is significantly narrower than in figure 6.11. Most importantly, points excluded from the calculation of $<P/Q>_i$ also form a narrower distribution. This is clearly evident for events below 60 keV in ionization energy. For instance, in a 5 keV slice of ionization energy around 40 keV, the standard deviation of phonon energy is reduced by a factor of 1.7±0.3. Of course, the resolution of the 60 keV gamma line is not improved because these events are localized within the detector. Figure 6.16 indicates the success of the phonon calibration, and therefore confirms that position dependence is the main cause for poor resolution in the *raw* phonon data. Here, the improvement due to the calibration is limited by the poor statistics that result from cutting out a large number of pileup events. Better statistics will allow for better estimates of $<P/Q>_i$ and a finer grid size than the one shown in figure 6.15. Therefore, it should be possible to obtain better resolution in phonon energy.

References

[1] N.E. Booth, B. Cabrera, and E. Fiorini. *Annu. Rev. Nucl. Part. Sci.*, 46:471, 1996.

[2] B. Cabrera. In *Proceedings of the VIII international Workshop on Low Temperature Detectors*, 1999. In cdmsnotes (cdmsnote 9909012).

[3] Sae Woo Nam. *Development of Phonon-Mediated Cryogenic Particle Detectors with Electron and Nuclear Recoil Descrimination.* PhD thesis, Stanford University, December 1998.

[4] Kent D. Irwin. *Phonon Mediaterd Particle Detection Using Superconducting Tungsten Transition-Edge Sensors.* PhD thesis, Stanford University, February 1995.

[5] P. Brink. In *Proceedings of the IDM 2000 Conference*, 2000. In cdmsnotes (cdmsnote 0012003).

[6] A.T. Lee et al. *Phys. Rev. B*, 54(5):3244, 1996.

[7] S. Tamura and M.J. Harris. *Phys. Rev. B*, 31:2595, 1985.

[8] S. Tamura. *Phys. Rev. B*, 56:13630, 1997.

[9] T. Saab et al. In *Proceedings of the VIII international Workshop on Low Temperature Detectors*, 1999. In cdmsnotes (cdmsnote 9909004).

[10] N.E. Booth. *App. Phys. Lett.*, 50:293, 1987.

[11] B. Young et al. In *Proceedings of the VIII international Workshop on Low Temperature Detectors*, 1999. In cdmsnotes (cdmsnote 9909006).

[12] T. Saab. In cdmsnotes (cdmsnote 9911004)., November 1999.

[13] T. Saab. Private communication.

[14] T. Saab et al. In *Proceedings of the IX international Workshop on Low Temperature Detectors*, 2001.

[15] Roland Clarke. *An Athermal Phonon Mediated Dark Matter Detector with Surface Event Discrimination.* PhD thesis, Stanford University, May 1999.

[16] V. Mandic et al. In *Proceedings of the IX international Workshop on Low Temperature Detectors*, 2001.

[17] O.V. Lounasmaa. *Experimental Principles and Methods Below 1 K.* Academic Press, 1974.

[18] D. Driscoll. In cdmsnotes (cdmsnote 9909008)., September 1999.

[19] P. Brink. Private communication.

[20] Jochen Hellmig. FLIP Setup Procedure. July 1999.

[21] Thomas A. Shutt. *A Dark matter Detector Based on the Simultaneous Measurement of Phonons and Ionization at 20 mK.* PhD thesis, The University of California at Berkeley, 1993.

[22] V. Mandic, P. Meunier, and D. Seitz. In cdmsnotes (cdmsnote 0011001)., October 2000.

Chapter 7

Conclusion

At present, the CDMS collaboration in a transitional state with focus shifting from CDMS I to CDMS II. The final results from Run 19 of CDMS I will be published soon [8]. The physics results from CDMS I may improve with new data from Run 21 which started in July 2002. In addition to physics data, this run will hopefully provide a clean bill of health for the first tower of detectors planned for use in CDMS II. The projected sensitivity of CDMS II is shown in figure 7.1 along with the WIMP upper limits set by several recent experiments including CDMS I (Run19). While there is no general consensus on preferred regions of supersymmetric parameter space, most experts agree that the region between the CDMS I and CDMS II contours is very promising. To provide a general idea, I have indicated in figure 7.1 the parameter space for a set of minimal supersymmetric models proposed by Baltz and Gondolo [6].

In this work, I have described in detail the background studies and simulation tools used in CDMS I. Detailed studies into the limiting background of CDMS I indicate that the source of the background is well understood. These studies also indicate that the predictions of simulations are reliable and robust. I hope that background issues will not reach the forefront in CDMS II for a long time to come. If and when they do, I hope

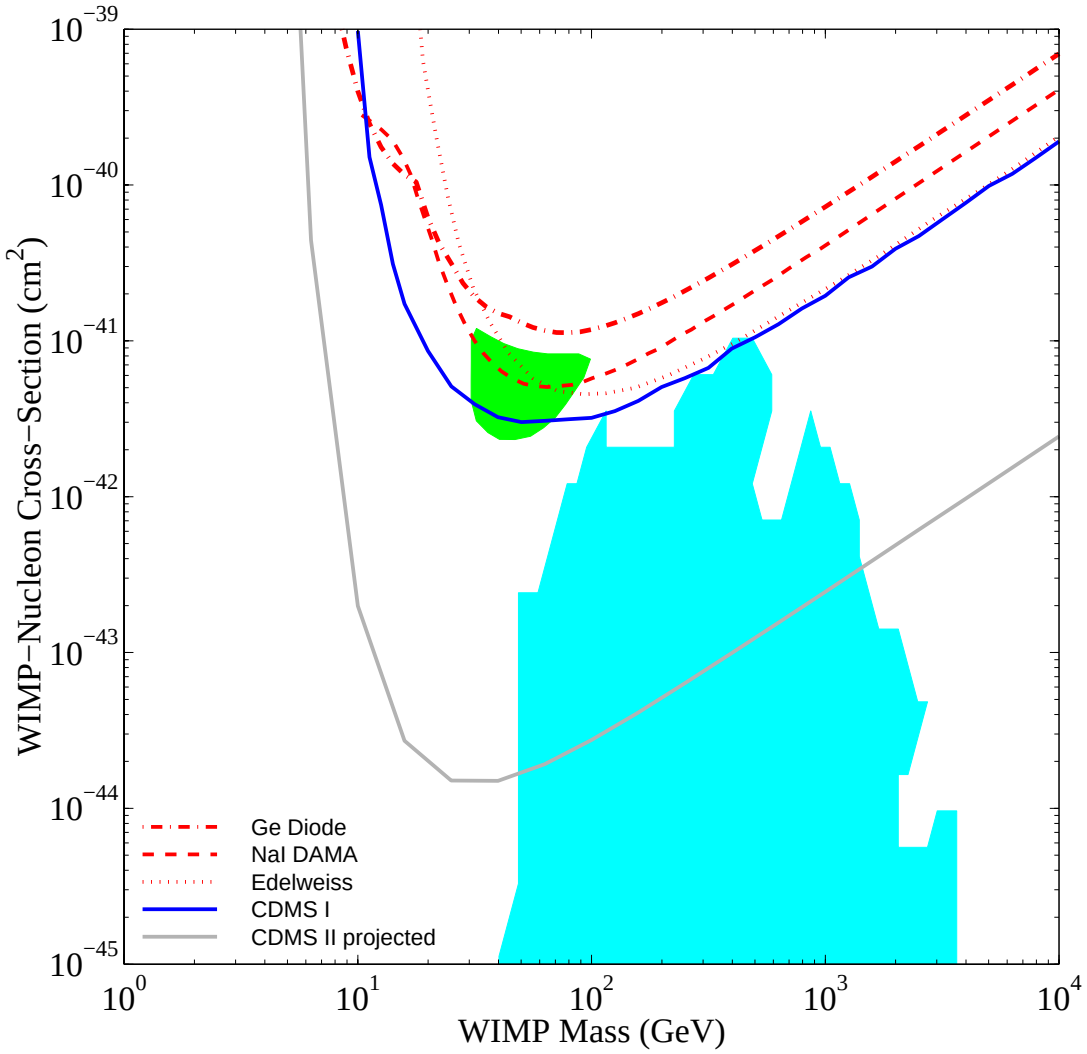

Figure 7.1: Projected sensitivity of CDMS II and WIMP upper limits from recent experiments. Limit contours are shown for Ge diode experiments [1, 2], DAMA [3], Edelweiss [4], and CDMS I [5]. The small shaded region corresponds to the annual modulation signal claimed by the DAMA experiment. The larger shaded region shows the parameter space for a set of minimal supersymmetric (MSSM) models proposed by Baltz and Gondolo [6]. Plot obtained from resources in [7].

that the studies and tools described here will be of some use.

References

[1] L. Baudis et al. *Phys. Rev. D*, 59:022001, 1999.

[2] A. Morales et al. hep-ex/0002053. Submitted to Phys. Lett. B, 2000.

[3] R. Bernabei et al. *Phys. Lett. B*, 389:757, 1996.

[4] A. Benoit et al. astro-ph/0106094 Submitted to Phys. Lett. B., 2001.

[5] R. Abusaidi et al. Exclusion Limits on the WIMP-Nucleon Cross-Section from the Cryogenic Dark Matter Search. *Physical Review Letters*, 84:5699, 2000.

[6] E.A. Baltz and P. Gondolo. *Phys. Rev. Lett.*, 86:5004, 2001.

[7] R.J. Gaitskell and V. Mandic. http://dmtools.berkeley.edu/limitplots/.

[8] D. Abrams et al. Exclusion Limits on the WIMP-Nucleon Cross-Section from the Cryogenic Dark Matter Search. Will appear in Physical Review D., 2001.

Appendix A

Output of the GEANT Based Monte Carlo

Most of the simulations discussed in this dissertation make use of a GEANT based Monte Carlo transport code. As explained in Chapter 3, neutron simulations are performed using the combination GEANT-FLUKA-MICAP. Neutrons above 20 MeV are handled by the FLUKA interface of GEANT while lower energy neutrons are handled by the MICAP interface. GEANT does not use any external interfaces for the transport of photons.

Information is saved in a "ntuple" format for all events that give rise to energy deposition in detectors. All information presented here on Monte Carlo simulations is obtained from this raw ntuple. To give an idea of what information is available from these GEANT based simulations, I provide below a detailed description of all the raw output quantities from neutron Monte Carlos. Similar information is available from the photon Monte Carlos. All energies and momenta are saved in units of GeV and Gev/c^2. All lengths and positions are in cm. The particle identities discussed below are defined in the GEANT manual.

Figure A.1 contains a list of the quantities output for each saved event as displayed by PAW, the analysis package used for plotting raw quantities. The variable names are listed on the last column of this output.

```
*      1   * I*4  *         *              * DETECTS  * IP_ORIG
*      2   * R*4  *         *              * DETECTS  * E_ORIG
*      3   * R*4  *         *              * DETECTS  * E_INIT
*      4   * I*4  *         * [ 0,18]      * DETECTS  * NDTS
*      5   * R*4  *         *              * DETECTS  * ENERGY_DEPE(NDTS)
*      6   * R*4  *         *              * DETECTS  * ENERGY_DEPN(NDTS)
*      7   * R*4  *         *              * DETECTS  * VERTEX(3)
*      8   * I*4  *         *              * DETECTS  * LOWP
*      9   * I*4  *         *              * DETECTS  * ICAPT
*     10   * I*4  *         * [ 0,10]      * DETECTS  * NVP
*     11   * I*4  *         *              * DETECTS  * IDVP(NVP)
*     12   * R*4  *         *              * DETECTS  * VE(NVP)
*     13   * I*4  *         *              * DETECTS  * ISSAME
*     14   * R*4  *         *              * DETECTS  * UVAR(5)
*     15   * I*4  *         * [ 0,50]      * DETECTS  * NMHITS
*     16   * I*4  *         *              * DETECTS  * IDP(NMHITS)
*     17   * R*4  *         *              * DETECTS  * EN_INCID(NMHITS)
*     18   * R*4  *         *              * DETECTS  * ANUCL(NMHITS)
*     19   * R*4  *         *              * DETECTS  * DEPHITN(NMHITS)
*     20   * R*4  *         *              * DETECTS  * DEPHITE(NMHITS)
*     21   * R*4  *         *              * DETECTS  * XHIT(NMHITS)
*     22   * R*4  *         *              * DETECTS  * YHIT(NMHITS)
*     23   * R*4  *         *              * DETECTS  * ZHIT(NMHITS)
*     24   * R*4  *         *              * DETECTS  * DIFF(NMHITS)
*     25   * I*4  *         *              * DETECTS  * IPNOW(NMHITS)
*     26   * I*4  *         *              * DETECTS  * IMI(NMHITS)
*     27   * I*4  *         *              * DETECTS  * NSCAT(NMHITS)
*     28   * I*4  *         *              * DETECTS  * NDS(NMHITS)
*     29   * R*4  *         *              * DETECTS  * P1IN(NMHITS)
*     30   * R*4  *         *              * DETECTS  * P2IN(NMHITS)
*     31   * R*4  *         *              * DETECTS  * P3IN(NMHITS)
```

Figure A.1: Raw output of GEANT based Monte Carlo.

The other columns, separated by "*"s, from left to right contain the quantity number, variable type and number of bytes used, range of the quantity, and the name of the ntuple containing this quantity. These quantities naturally fall into two categories.

A.1 Event-by-event Quantities

As defined in Chapter 3, an event refers to all that transpires between successive throws of particles in GEANT.

IP_ORIG : Identity of "original" particle. When cloning is used (see Chapter 3), this need not be the thrown particle that causes an ntuple

entry. It is the identity of the user-specified primary particle used at the beginning of the simulation. This information is propagated through each cloning step.

E_ORIG : Kinetic energy of "original" particle as defined above.

E_INIT : Kinetic energy of particle thrown in present cloning step. It is always equal to E_ORIG when no cloning is used.

NDTS : Number of detectors in present simulation.

ENERGY_DEPE : Total energy deposited in a detector by particles other than neutrons. This is an array indexed by NDTS. Therefore the non-neutron energy deposition is saved for each detector.

ENERGY_DEPN : Neutron energy deposition. Otherwise same as ENERGY_DEPE.

LOWP : Flag which is set to 1 if a neutron associated with this event falls below 10 keV of kinetic energy while in the polyethylene. Otherwise 0.

ICAPT : Flag which is set to 1 if a neutron associated with this event is captured onto hydrogen in the polyethylene. Otherwise 0. This variable is only useful in rare cases when the neutron transport threshold is set to zero. Usually, this threshold is set to 10 keV in order to save CPU time. The quantity LOWP can be used in this case to get an approximate estimate of neutron captures in polyethylene.

NVP : Number of different particle types associated with this event that deposited energy in the veto. Can save up to ten particle types.

IDVP : Array indexed by NVP containing the identity of the above particle types.

VE : Array indexed by NVP containing the energy deposited by each particle type. For example, if two photons deposit energy in the veto, the sum of the two energies is saved in the array element corresponding to photons. The energy deposited in the veto by a neutron in the same event

is saved in a separate array element reserved for neutrons.

ISSAME : Flag indicating whether current event is related to previous event. For instance, when simulating a radioactive source that emits two or more particles in quick succession, the user may chose to throw them in separate iterations of the GEANT event generator. This variable is then useful for keeping track of whether the current event is related to the previous one. This affects the estimation of multiple scatters.

UVAR : User variables that will be carried through all cloning steps.

NMHITS : Number of detector hits associated with current event. Note that two hits within the same detector are counted as two separate hits.

A.2 Hit-by-hit Quantities

Each of the quantities listed below pertain to individual detector hits. They are indexed by NMHITS, the last quantity defined in the previous section.

IDP : Identity of particle causing present hit.

EN_INCID : Kinetic energy of particle causing present hit.

ANUCL : Mass number of the recoiling nucleus in case of a nuclear recoil. Zero otherwise.

DEPHITN : Neutron energy deposition associated with present hit.

DEPHITE : Non-neutron energy deposition associated with present hit.

XHIT, YHIT, ZHIT : Position of hit.

DIFF : Deficit energy going into nuclear excitations etc. in the case of inelastic nuclear recoils. Zero otherwise.

IPNOW : Redundant. Same as IDP.

IMI : Flag indicating which transport code handled this hit; 1–MICAP, 0–FLUKA.

NSCAT : Total number of scatters of interacting particle prior to this hit.

NDS : Number of detector scatters of interacting particle prior to this hit.

P1IN, P2IN, P3IN, : Three momentum of incident particle.

Bibliography

http://www.nndc.bnl.gov. National Nuclear Data Center.

Geant version 3.21.04, released March 1995. Copyright CERN, Geneva.

Abrams, D., et al. Exclusion Limits on the WIMP-Nucleon Cross-Section from the Cryogenic Dark Matter Search. Will appear in Physical Review D., 2001.

Abusaidi, R., et al. Exclusion Limits on the WIMP-Nucleon Cross-Section from the Cryogenic Dark Matter Search. *Physical Review Letters 84* (2000), 5699.

Aglietta, M., et al. *Nuove Cimento 12C*, 4 (1989), 467.

Aguirre, A., Schaye, J., and Quataert, E. astro-ph/0105184. Submitted to Astrophys. J., 2001.

Akerib, D., et al. *Nucl. Instr. Meth. Phys. Res., Sect. A 400* (1997), 181.

Alcock, C., et al. astro-ph/0001272, 2000.

Allkofer, O., and Andersen, R. *Nuclear Physics B8* (1968), 402.

Backenstoss, G., et al. *Nuclear Physics A162* (1971), 541.

Bahcall, N., Lubin, L., and Dorman, V. *Astrophys. J. 447* (1995), L81–L85.

Baltz, E., and Gondolo, P. *Phys. Rev. Lett. 86* (2001), 5004.

Barnes, P. PhD thesis, The University of California at Berkeley, 1996.

Barton, J. In *Proceedings of the 19th International Cosmic Ray Conference* (1985).

Battistoni, G., et al. *Nucl. Instr. Meth. Phys. Res., Sect. A 394* (1997), 136.

Baudis, L., et al. *Phys. Rev. D 59* (1999), 022001.

Benoit, A., et al. astro-ph/0106094 Submitted to Phys. Lett. B., 2001.

Bernabei, R., et al. *Phys. Lett. B 389* (1996), 757.

Bernabei, R., et al. *Phys. Lett. B 480* (2000), 23.

Bezrukov, L., and Bugaev, E. *Sov. J. Nucl. Phys. 35*, 5 (1981), 635.

Boesgaard, A., and Steigman, G. *Ann. Rev. Astron. Astro. 23* (1985), 319.

Booth, N. *App. Phys. Lett. 50* (1987), 293.

Booth, N., Cabrera, B., and Fiorini, E. *Annu. Rev. Nucl. Part. Sci. 46* (1996), 471.

Brink, P. Private communication.

Brink, P. In *Proceedings of the IDM 2000 Conference* (2000). In cdmsnotes (cdmsnote 0012003).

Burles, S., et al. *Astrophys. J. 483* (1997), 778.

Cabrera, B. In *Proceedings of the VIII international Workshop on Low Temperature Detectors* (1999). In cdmsnotes (cdmsnote 9909012).

Carlberg, R., et al. *Astrophys. J. 462* (1996), 32.

Carlstrom, J. astro-ph/9905255, 1999.

Carr, B. *Ann. Rev. Astron. Astro. 32* (1994), 531.

Chen, M., et al. *Nucl. Inst. and Meth. in Phys. Res. A 336* (1993), 232.

Clarke, R. *An Athermal Phonon Mediated Dark Matter Detector with Surface Event Discrimination*. PhD thesis, Stanford University, May 1999.

Coles, P., and Ellis, G. *Is the Universe Open or Closed*. Cambridge University Press, 1997.

Collaboaration, T. C. D. M. S. Proposal for a Second Generation Experiment to Search For Cold Dark Matter: CDMS II.

Copi, C. Private communication.

Copi, C., Schramm, D., and Turner, M. *Science 276* (1995), 192.

David, L., et al. *Astrophys. J. 445* (1995), 578.

de Bernardis, P., et al. *Nature 404* (2000), 955.

Driscoll, D. In cdmsnotes (cdmsnote 9909008)., September 1999.

Eichblatt, S. Neutron Studies for the CDMS II site at Soudan. In cdmsnotes (cdmsnote 9701011)., January 1997.

Eichblatt, S. Estimating the Neutron Background for SUF Run 18. In cdmsnotes (cdmsnote 9802001)., February 1998.

Engel, J., and Vogel, P. *Phys. Rev. D61* (2000), 63503.

Evrard, A., Metzler, A., and Navarro, J. *Astrophys. J. 469* (1996), 494.

Fassò, A., et al. Presented at the Specialist's Meeting on Shielding Aspects of Accelerators, Targets, and Irradiation Facilities in Arlington, Texas, April 1994.

Fassò, A., Ferrari, A., Ranft, J., and Sala, P. Fluka: present status and future developments. In *Proc. IV Int. Conf. on Calorimetry in High Energy Physics* (La Biodola, Italy, 21-26 September 1993), Menzione and A. Scribano, Eds., World Scientific, pp. 493–502.

Feldman, G., and Cousins, R. *Physical Rev. D 57* (1998), 3873.

Fields, B., Freese, K., and Graff, D. *Astrophys. J. 534* (2000), 265.

Florkowski, T., Morawska, L., and Rozanski, K. Natural Production of Radionuclides in Geological Formations. *Nuclear Geophysics 2* (1988), 1.

for the MACRO collaboration, G. B. hep-ph/9809006., 1998.

Fukugita, M., and Hogan, C. *Euoro. Phys. J. C, Review of Particles and Fields 15* (2000), 136.

Gaitskell, R. Observation of Inelastic Neutron Scattering and thermal Neutron Capture in Ge BLIP data from First Neutron Calibrations of Run 18. In cdmsnotes (cdmsnote 9805001)., May 1998.

Gaitskell, R., and Mandic, V. http://dmtools.berkeley.edu/limitplots/.

Golwala, S. *Exclusion Limits on the WIMP-Nucleon Elastic-Scattering Cross-Section from the Cryogenic Dark Matter Search*. PhD thesis, The University of California at Berkeley, Fall 2000.

Griest, K., and Sadoulet, B. Model Independence of Constraints on Particle Dark Matter, Erice, Italy. In *Second Particle Astrophysics School on Dark Matter* (1988).

Hanany, S., et al. *Astrophys. J. 545* (2000), L5–L9.

Harris, G., and Shanley, T. *Physical Review 85*, 5 (1952), 983.

Hellmig, J. FLIP Setup Procedure. July 1999.

III, H. C. F. Gheisha version 7.03, released September 1985.

Irwin, K. D. *Phonon Mediaterd Particle Detection Using Superconducting Tungsten Transition-Edge Sensors*. PhD thesis, Stanford University, February 1995.

Jochum, J. Spectrum of deposited energies from Tritium beta decay. In cdmsnotes (cdmsnote 9705005)., May 1997.

Johnson, J. O., and Gabriel, T. A. Micap: A Monte Carlo Ionization Chamber Analysis Package, February 1993.

Jungman, G., Kamionkowski, M., and Griest, K. *Phys. Rep. 267* (1996), 195.

Katz-Hyman, M., and Akerib, D. S. Simulated Detection and Veto of High Energy Neutrons in the CDMS II Experiment. In cdmsnotes (cdmsnote 0106002)., April 1997.

Khalchukov, F., et al. *Nuovo Cimento 6C* (1983), 3.

Khalchukov, F., et al. *Nuovo Cimento 18C* (1995), 5.

Klimenko, A., et al. *JETP Letters 67* (1998), 837.

Knoll, G. F. *Radiation Detection and Measurement*, second ed. John Wiley and Sons, 1989.

Kolb, E., and Turner, M. *The Early Universe*. Addison-Wesley, 1990.

Krauss, L. In *Proceedings of the Second International Workshop on The Identification of Dark Matter* (1999), N. Spooner and V. Kundryavtsev, Eds. hep-ph/9807376.

Lee, A., et al. *Phys. Rev. B 54*, 5 (1996), 3244.

Lee, B., and Weinberg, S. *Phys. Rev. Lett. 38* (1977), 165.

Leitch, E., et al. astro-ph/0104488. Submitted to Astrophys. J., 2001.

Lewin, J., and Smith, P. *Astropart. Phys. 6* (1996), 87.

Lounasmaa, O. *Experimental Principles and Methods Below 1 K*. Academic Press, 1974.

Luke, P. *Journal of Applied Physics 64* (1988), 6858.

Macdonald, B., et al. *Physics Review 139* (1965), 5B.

Mandic, V., et al. In *Proceedings of the IX international Workshop on Low Temperature Detectors* (2001).

Mandic, V., Meunier, P., and Seitz, D. In cdmsnotes (cdmsnote 0011001)., October 2000.

Miyake, S. In *Proceedings of the 19th International Cosmic Ray Conference* (1973).

Morales, A., et al. hep-ex/0002053. Submitted to Phys. Lett. B, 2000.

Nam, S. W. *Development of Phonon-Mediated Cryogenic Particle Detectors with Electron and Nuclear Recoil Descrimination.* PhD thesis, Stanford University, December 1998.

Neganov, B., and Trofimov, V. *JETP Letters 28* (1978), 328.

Netterfield, C., et al. astro-ph/0104460, 2001.

Pages, L., Bertel, E., Joffre, H., and Sklavenitis, L. Energy loss, range, and bremsstrahlung yield for 10-keV to 100-MeV electrons in various elements and chemical compounds. *Atomic Data 4* (1972), 1–127.

Peacock, J. *Cosmological Physics.* Cambridge University Press, 1999.

Peccei, R., and Quinn, H. *Phys. Rev. Lett. 38* (1977), 1440.

Peebles, P. *Principles of Physical Cosmology.* Princeton University Press, 1993.

Perlmutter, S., et al. *Astrophys. J. 517* (1999), 565.

Pobell, F. *Matter and Methods at Low Temperatures.* Springer-Verlag, Berlin, 1992.

Riess, A., et al. *Astron. J. 116* (1998), 1009.

Ruddick, K. Underground Particle Fluxes in the Soudan Mine. MINOS internal note NuMI-L-210, 1996.

Saab, T. Private communication.

Saab, T. In cdmsnotes (cdmsnote 9911004)., November 1999.

Saab, T., et al. In *Proceedings of the VIII international Workshop on Low Temperature Detectors* (1999). In cdmsnotes (cdmsnote 9909004).

Saab, T., et al. In *Proceedings of the IX international Workshop on Low Temperature Detectors* (2001).

Salucci, P., and Persic, M. In *Dark and Visible Matter in Galaxies* (1997), P. Salucci and M. Persic, Eds. asto-ph/9703027.

Sancisi, R., and van Albada, T. Dark Matter in the Universe. J. Kormandy and G. Knapp, Eds., Dordrecht, Holland.

Schnee, R. Private communication.

Schnee, R. Calculating Limits Following Feldman and Cousins. Memo to the CDMS collaboration, April 2001.

Schnee, R. Calculation of Neutron Multiple Scatter Fraction. Memo to the CDMS collaboration, July 2001.

Schnee, R. Efficiency of Veto for Rejecting Internally Produced Neutrons. Memo to the CDMS collaboration, May 2001.

Scott, D., et al. astro-ph/0104435. Submitted to Mon. Not. R. Astron. Soc., 2001.

Segrè, E. *Nuclei and Particles*, second ed. Benjamin and Cummins Publ. Co., 1977.

Seitz, D. Private communication.

Shutt, T., et al. In *Proceedings of the Seventh International Workshop on Low Temperature Detectors* (1997).

Shutt, T., et al. *Nucl. Instrum. Methods Phys. Res., Sect A 444* (2000), 340.

Shutt, T. A. *A Dark matter Detector Based on the Simultaneous Measurement of Phonons and Ionization at 20 mK*. PhD thesis, The University of California at Berkeley, 1993.

Silva, A. D. *Development of a Low Background Environment for the Cryogenic Dark Matter Search*. PhD thesis, The University of British Columbia, April 1996.

Singer, P. *Springer Tracts in Modern Physics 71* (1974), 38.

Smail, I., et al. *Astrophys. J. 479* (1996), 70.

Sonnenschein, A. *A Search for Weakly Interacting Dark Matter Particles with Low Temperature Detectors Capable of Simultaneously Measuring Ionization and Heat*. PhD thesis, University of California, Santa Barbara, July 1999.

Stockwell, W. PhD thesis, The University of California at Berkeley, 1996.

Sudelin, R., and Edelstein, R. *Physical Review C 7*, 3 (1973), 1037.

Tamura, S. *Phys. Rev. B 56* (1997), 13630.

Tamura, S., and Harris, M. *Phys. Rev. B 31* (1985), 2595.

Walker, T., et al. *Astrophys. J. 376* (1991), 51.

Wang, Y.-F., et al. hep-ex/0101049., 2001.

Weinberg, D., et al. *Astrophys. J. 490* (1997), 564.

Weinberg, E. J., and Nordstrom, D., Eds. *Physical Review D, Particles and Fields*, vol. 54. American Physical Society, July 1996, ch. 26, p. 154. Updated in November 1993 by E. Brown.

Yellin, S. Private communication.

Yellin, S. Design Considerations for the CDMS II Shield. In cdmsnotes (cdmsnote 9704003)., April 1997.

Young, B., et al. In *Proceedings of the VIII international Workshop on Low Temperature Detectors* (1999). In cdmsnotes (cdmsnote 9909006).

Zatsepin, G., and Ryazhskaya, O. In *Proceedings of the 9th International Cosmic Ray Conference* (1966).